USC
UNIVERSIDADE DE SANTIAGO DE COMPOSTELA

INTERNATIONAL DOCTORAL SCHOOL OF THE USC

Yaiza
Bugallo Codeseira

PhD Thesis

Structural characterization of recombinant PrPSc prions using biochemical and biophysical techniques

Santiago de Compostela, 2022

Doctoral Programme in Molecular Medicine

TESE DE DOUTORAMENTO

STRUCTURAL CHARACTERIZATION OF RECOMBINANT PrP^{Sc} PRIONS USING BIOCHEMICAL AND BIOPHYSICAL TECHNIQUES

YAIZA BUGALLO CODESEIRA

ESCOLA DE DOUTORAMENTO INTERNACIONAL DA UNIVERSIDADE DE SANTIAGO DE COMPOSTELA

PROGRAMA DE DOUTORAMENTO EN MEDICINA MOLECULAR

SANTIAGO DE COMPOSTELA

ANO 2022

I, Yaiza Bugallo Codeseira declare that I have no conflict of interest with this thesis.

DECLARACIÓN DEL AUTOR/A DE LA TESIS

D./Dña. **Yaiza Bugallo Codeseira**

Título de la tesis: **Structural characterization of recombinant PrPSc prions using biochemical and biophysical techniques**

Presento mi tesis, siguiendo el procedimiento adecuado al Reglamento y declaro que:

1) La tesis abarca los resultados de la elaboración de mi trabajo.
2) De ser el caso, en la tesis se hace referencia a las colaboraciones que tuvo este trabajo.
3) Confirmo que la tesis no incurre en ningún tipo de plagio de otros autores ni de trabajos presentados por mí para la obtención de otros títulos.
4) La tesis es la versión definitiva presentada para su defensa y coincide la versión impresa con la presentada en formato electrónico.

Y me comprometo a presentar el Compromiso Documental de Supervisión en el caso que el original no esté depositado en la Escuela.

En **Bueu**, **05 de mayo de 2022**.

Firma electrónica

AUTORIZACIÓN DEL DIRECTOR/TUTOR DE LA TESIS

D./Dña. **Jesús Rodríguez Requena**

En condición de: **Director/a**

Título de la tesis: **STRUCTURAL CHARACTERIZATION OF RECOMBINANT PrPSc PRIONS USING BIOCHEMICAL AND BIOPHYSICAL TECHNIQUES**

INFORMA:

Que la presente tesis, se corresponde con el trabajo realizado por D/Dña **Yaiza Bugallo Codeseira**, bajo mi dirección/tutorización, y autorizo su presentación, considerando que reúne los requisitos exigidos en el Reglamento de Estudios de Doctorado de la USC, y que como director/tutor de esta no incurre en las causas de abstención establecidas en la Ley 40/2015.

En **Santiago, 05 de mayo de 2022**

Vincit qui patitur.
To all my loved ones.

ACKNOWLEDGMENTS

Now that I have finished writing this thesis and I am writing these words at 7 a.m., while my husband sleeps, listening to music and looking at the sunrise over the sea, it is ,without a doubt, one of the happiest moments of my life.

I feel very fortunate for having had the opportunity of doing a PhD in Galicia, financed by a Xunta de Galicia PhD fellowship, right out of Pharmacy school in my early 20s. It is been over four and a half year since I first walked into Requena's lab and I am no longer the same person I was back then. I have grown older, my life has changed for the better and, which was the whole point of this experience, I believe I have become a scientist.

Briefly, I thank everyone who loves me, everyone I love and everyone who has ever supported me. Especially my thesis advisor, collaborators, husband, family, in laws, labmates and friends.

The following poem by my favorite Galician writer, Rosalía de Castro, is technically sad as the "black shadow" figure of speech refers to depression. Though the reader can always give the poem a different meaning and I choose to think of it as a positive being.

When I think that you have parted,
Black shadow that overshades me,
At the foot of my head pillows
You return making fun of me.

When I fancy that you've gone,
From the very sun you taunt me
And you are the star that shines
And you are the wind that moans.

If there's singing it's you who sings,
If there's weeping it's you who weeps,
And you are the river's rumor
And the night—and the dawn.

Everywhere you are in everything,
For and within me you live
Nor will you ever leave me,
Shadow that always shades me.

SUMMARY

Prions are infectious proteins which cause rare fatal neurodegenerative diseases, in animals and humans, called transmissible spongiform encephalopathies (TSE) because the brains of the patients, when analyzing postmortem, show extreme vacuolation which makes them look like a sponge. They may present as genetic, infectious, or sporadic disorders, all of which involves refolding of the host prion protein, PrP^{C}, which is a normal constituent of mammalian cells, into its infectious isoform, PrP^{Sc}, through a process which involves its α-helical and coil structure being refolded into β-sheets, with PrP^{Sc} acting as a template for PrP^{C}. Prions were discovered in the early 80s by Stanley Prusiner who won the Nobel Prize in Physiology or Medicine in 1997 for it. There are other non-mammalian prions such as the prions of fungi and yeast but these are usually functional not pathologic.

Prion diseases became widely known due to the "mad cow disease" zoonosis, which is technically referred as bovine spongiform encephalopathy (BSE). There was a widespread outbreak in the United Kingdom in the 80's and 90's, causing 231 human deaths, due mainly to the feeding of meat and bone meal (MBM), which contains central nervous system tissues, and others that are known to host prions, to cattle. Currently, the worrisome zoonosis is chronic wasting disease (CWD) that affects cervids and is killing them massively in Canada, The United States and also in Norway and Sweden. Luckily, research says that it is not transmissible to humans but it does seem unstoppable and will probably be more well known in the near future.

There are distinct strains of prions which are defined by differences in a heritable phenotype under controlled experimental transmission conditions. Prion strains can differ in incubation period, clinical signs of disease, tissue tropism, and host range. The prevailing hypothesis for this phenomenon is that prion strain diversity is encoded by different conformations of PrP^{Sc}, although some cofactors have been identified *in vitro* that may also contribute to prion strain diversity

The elucidation of the PrP^{C} structure was possible in 1997 because of the improvements in the expression of recombinant PrP, in sufficient amount to permit NMR studies. However, PrP^{Sc} was much more complicated and it was not achieved until 2021 about which we will go further into detail but for now we can mention that it presents a PIRIBS architecture (parallel-in-register-intermolecular-β-sheets). The reason why it was so difficult is because PrP^{Sc} forms insoluble aggregates that resist the solubilization in nondenaturing detergents, hampering the gathering of suitable preparations from brains of infected animals for high-resolution techniques like NMR spectroscopy and X-ray crystallography. Furthermore, PrP^{Sc} has high heterogeneity derived from the GPI anchor and the carbohydrates contained in its C-terminal region, which makes very difficult the interpretation of data. The rising of recombinant prions, such us recombintat GPI-less PrP^{Sc}, was very helpful in this regard.

The structure of PrP^{Sc} was still unknown at the beginning of my PhD in November 2017, but there were many constrains available obtained through different techniques: (i) Electron microscopy (EM), (ii) Fourier-Transform Infrared Spectroscopy (FTIR), (iii) Electron crystallography, (iv) Fiber X-ray diffraction, (v) Hydrogen-deuterium exchange (HDX) coupled to mass spectrometry (MS), (vi) Limited proteolysis coupled to mass spectrometry (MS), (vii) Cryogenic electron microscopy (cryo-EM). Briefly, it was

believed that PrP^{Sc} formed amyloid fibers and that its secondary structure was composed of parallel β-sheets connected by loops.

Electron microscopy is a technique for obtaining high resolution images of biological and non-biological specimens. The high resolution of EM images results from the use of electrons (which have very short wavelengths) as the source of illuminating radiation. Through negative stain EM the first observation of PrP^{Sc} fibrils was obtained forty years ago by Merz, which showed abnormal fibrillary structures, designated "scrapie-associated fibrils" (SAF), in subfractions of brains from scrapie-affected animals. They concluded that SAF consisted either of two or four filaments and that they bared a resemblance to amyloid. A couple of years later, Prusiner also observed such structures and called them “rods” measuring 10 to 20 nm in diameter and 100 to 200 nm in length. Moreover, he performed birefringence studies with Congo red proving that PrP^{Sc} fibrils are amyloids. However, the amount of structural information that could be gathered was greatly limited by the highly aggregated nature of the protein. In 2010, Sim and colleagues employed severely under-glycosylated prion protein fibrils from scrapie infected transgenic mice expressing anchorless prion protein since heavy surface glycosylation may obscure visualization of prion fibrillar cores. Dimensions and morphological information about prion protein core protofilaments which variably intertwined to form scrapie fibrils were obtained. These fibers extended around 100-150 nm in length and were apparently formed by two intertwined protofilaments with a width of around 4-5 nm per protofilament. Occasional isolated protofilaments were observed, suggesting that the lateral association of protofilaments is neither essential nor invariant in prion protein polymerization.

FTIR is a non-invasive, label-free spectroscopic technique which uses infrared radiation to probe the secondary structure of proteins due to the absorption of its polar bonds, mainly the amide one. FTIR studies were among the first to be carried out given that they can be applied to an insoluble, disordered sample. They showed that the conversion of PrPSc from PrPC is associated with a loss of α-helix and a large increase of β-sheets in the secondary structure. However, in 2011, it was proved that there is no presence of α-helix in PrP^{Sc} by Smirnovas et al. when it was shown that the 1660 cm^{-1} band, region that covers different wavelengths, in the FTIR spectra of PrP^{Sc} and PrP27-30 which had been attributed to α-helices, based on calibration using globular proteins, is also present in the spectrum of recombinant PrP amyloid fibers which exhibit exclusively a parallel-in-register-intermolecular-β-sheet architecture. Therefore, it was concluded that a misinterpretation had been made and that PrP^{Sc} had about 50% of β-sheet content and 50% of turns and coils.

Electron crystallography is similar to X-ray crystallography in that a protein crystal scatters a beam to produce a diffraction pattern. However, the interactions between the electrons in the beam and the crystal are much stronger than those between the X-ray photons and the crystal. This means that meaningful amounts of data can be collected from much smaller crystals. Then, two-dimensional (2D) crystals of PrP27-30 and PrP106 (Δ23–88, Δ141–176), which is the minimum PrP construct that can support the propagation of prions, were analyzed. PrP^{Sc}106 lacks residues 141–176 but it is consistently diglycosylated. By comparison, PrP 27-30 has a longer peptide chain and it is a mix of un-, mono-, and diglycosylated forms. As these crystals display a complex mixture of negative and positive staining, it is important to consider the staining behavior of the different constructs. PrP^{Sc}106 lacks many of the negatively charged residues that

are present in PrP 27-30 and hence binds fewer uranyl cations at the center of the subunits. Therefore, subtracting the PrP 27-30 density from the PrP^{Sc}106 density should highlight residues 141–176 in positive density, whereas subtracting PrP^{Sc}106 from PrP 27-30 should place the extra glycosylation sites in positive density. As expected, PrP 27-30 minus PrP^{Sc}106 showed differences that were nearly identical to the location of the sugars determined by Nanogold labeling. Here the difference signal for the N-linked sugars was found in all three-fold symmetry axes around the oligomer. PrP^{Sc}106 minus PrP 27-30 revealed differences around the center of each oligomer, which were interpreted as being representative of the amino acids in the internal deletion of PrP106 (141–176). The authors concluded that PrP^{Sc} is formed by a parallel β-helix, since such structure would be the only one to fit to the hexagonal lattice dimensions. The resolution of this technique is about 2 nm, which is just the diameter of the proposed β-helix. Therefore, it was not possible to provide any detail of higher resolution, just that their architecture might correspond to a solenoid.

Fiber X-ray diffraction is a phenomenon in which the atoms of a crystal, by virtue of their uniform spacing, cause an interference pattern of the waves present in an incident beam of X rays; the atomic planes of the crystal act on the X rays in exactly the same manner as does a uniformly ruled grating on a beam of light. The fiber formation property of PrP^{Sc} makes possible to determine additional information about the three-dimensional structure of PrP27-30 molecule by fiber X-ray diffraction technique. The earliest studies with X-ray fiber diffraction on the structure of PrP^{Sc} confirmed the amyloid nature of the prion rods. The meridional diffraction at 4,8 Å indicates the typical cross-β structure corresponding with the distance between β-sheet in which the hydrogen bonds run parallel to the fiber axis. In 2009, Wille et al prepared fibers of $MoPrP^{Sc}$ purified from the brains of mice inoculated with RML prions using PTA precipitation, which is a selective method for the precipitation of PrP^{Sc} since at neutral pH and in the presence of Mg^{+2} PTA forms complexes with oligomers of PrP^{Sc} and PrP 27-30 but no with PrP^{C}. The MoPrP 27–30(RML) patterns contained at least 11 meridional intensity maxima which could be classified into three groups, ‘‘l’’ ‘‘u’’ and ‘‘p’’. Group ‘‘l,’’ showed relatively sharp maxima at resolutions close to 4.1 Å and 8.2 Å which most probably came from lipid or lipid-detergent assemblies, reflecting the spacing between hydrocarbon chains. Group ‘‘u’’had a pair of relatively sharp intensities at 7.7 Å and 7.4 Å that seemed to be protein contaminats from other organs. Group ‘‘p,’’ in contrast, could be interpreted in terms of protein structure. This group contains three maxima: very weak, broad cross-diffraction at 4.8 Å and moderately broad arcs at 9.6 Å and 6.4 Å. These maxima correspond to the second, third, and fourth orders of a 19.2 Å vertical repeat, meaning half, one third and one fourth of the 19.2 Å vertical repeat whose absence can be accounted for by disorder in the filament. 19.2 Å happens to be the size of a four-stranded ß-sheet whose presence would be consistent with the amyloid properties of the fibers and their high ß-sheet content. The weakness of the 4.8 Å diffraction may reflect irregularity in the spacing of the four strands. Although these data support the presence of a four-strand β-structure they are unable to determine whether that structure consists of an isolated sheet, stacked sheets, β-helices or any other form of ß-structure.

HDX-MS protocol takes advantage of the labile nature of protons present on protein backbone amides, and is a powerful tool in the study of protein structure. When dissolved in solution, proteins exchange these protons with hydrogen groups present in a deuterated buffer, and protons from the protein are exchanged with deuterium. Only the protons present on the backbone amides are measured. The rate of hydrogen to deuterium

exchange provides solvent accessibility data, which can be used to infer information on protein structure and conformation. Mass spectrometry can be used to measure the rate of deuterium uptake after pepsin treatment. Some studies have been performed with this technique analyzing the structure of recombinant PrP amyloid. Finally, a paper was published which studied GPI-less PrP^{Sc} and it was showed that the C-terminal part of GPI-less PrP^{Sc} exhibits extremely low rates of H/D exchange, which is typical of stretches with extensive H-bonding (β-sheets) and the whole 90-215 stretch is relatively resistant to exchange. Some other stretches exhibit a higher exchange rate corresponding to partially overlap with turns or loops, such as 133-148 and 81-118. Therefore, it was concluded that GPI-less PrP^{Sc} consists of a series of β-sheets connected by short loops and/or loops with no native α-helices which was consistent with the FTIR reinterpretation of results.

The principle of limited proteolysis is that a protein is incubated with a relatively low concentration of different proteases, which cut at recognition sites throughout the protein, normally at exposed regions such as loops and other flexible regions. In 2012 GPI-anchorless PrP^{Sc} was entirely analyzed by Vázquez-Fernández and collaborators due to the lack of GPI and almost complete lack of glycosylation. It revealed cleavage sites at positions 81, 85, 89, 116, 118, 133, 134, 141,152, 153, 162, 169 and 179. These results showed the actual PK cleavage sites for the entire PrP^{Sc} monomer. Such cleavage sites coincide with those previously identified in hamster PrP^{Sc}, up to where the analysis of that molecule was possible (~N154), suggesting that the architecture of GPI−PrP^{Sc}, 263 K $SHaPrP^{Sc}$, and $DySHaPrP^{Sc}$ share a common structure. The authors concluded that the structure of PrP^{Sc} consists of a series of high PK-resistant β-sheet strands that are connected through loops and turns in agreement with the previous results. Since no cleavage sites were detected beyond position 170 it was also concluded that the C-terminal stretch of GPI- PrP^{Sc} was particularly resistant to PK, being probably mainly composed of β-sheets.

Cryogenic electron microscopy is a cryomicroscopy technique applied on samples cooled to cryogenic temperatures and embedded in an environment of vitreous water which is liquid ethane; it makes the sample freeze so fast that ice crystals are not able to form. Vázquez-Fernández and colleagues in 2016 used for the first time a GPI-anchorless PrP^{Sc} since its fibers inherently present a repetitive organization. Further details are provided in the main text. In short, the 3D reconstruction of one of these individual GPI-anchorless PrP 27–30 fibrils, with a maximum width of 9.1 nm and a crossover distance of 95 nm, showed two approximately 50 x 29 Å oval-shaped protofilaments. One important implication is that PrP^{Sc} subunits can only fit into protofilaments with the observed dimensions if they are folded up onto themselves. Based on the routine observation of regular 4.8 Å cross-β signals in individual GPI-anchorless PrP 27–30 fibrils, a β-solenoid arrangement is the easiest way to accommodate the peptide into the available protofilament volume.

Over the years several models had been proposed but at the time in 2017 only two were left standing: (i) the PIRIBS (parallel-in-register-intermolecular-β-sheets) which states that PrP^{Sc} amyloid fibers are made by a single protofilament where each monomer is parallel in register stacked along the fibrillar axes and argues that PrP^{Sc} monomers are flat, with rPrP amyloid-like β-strand rich cores extending up to position ~90; and (ii) the 4RβS (4-rung-β-solenoid) which, in contrast, states that the fibers are made by two intertwined protofilaments.

The main objective of this thesis is to challenge both models in order to elucidate which is the real structure of PrP^{Sc}. Furthermore, the specific objectives are: (i) preparation of non-infectious recPrP amyloid and infectious recBVPrP^{Sc}(109I) and analysis by FTIR to compare their secondary structures; (ii) acquisition and comparison of different ssNMR spectra (CP-HSQC, DREAM, DARR, INEPT-HSQC) of (U-^{13}C, ^{15}N)-recBVPrP^{Sc}(109I) to be able to distinguish between PIRIBS and 4RβS architectures; (iii) acquisition and comparison of PITHIRDS-CT spectra of ^{13}CO-Phe PrP amyloid, ^{13}CO-Tyr-Het-s (218-289) and ^{13}CO-Phe-recBVPrP^{Sc}(109I) as well as of ^{13}CO-Leu PrP amyloid, ^{13}CO-Tyr-Het-s (218-289) and ^{13}CO-Leu-recBVPrP^{Sc}(109I) to assess their intermolecular distances to be able to distinguish between PIRIBS and 4RβS architectures; (iv) acquisition and comparison of 1D-^{13}CP-MAS and PARIS spectra of ^{13}CO-Phe-PrP amyloid, ^{13}CO-Tyr-Het-s (218-289) and ^{13}CO-Phe-recBVPrP^{Sc}(109I) to obtain information about flexibility/rigidity of the samples; (v) acquisition and comparison of $T_1\rho$ spectra of ^{13}CO-Phe-PrP amyloid, ^{13}CO-Tyr-Het-s (218-289) and ^{13}CO-Phe-recBVPrP^{Sc}(109I) to obtain information about flexibility/rigidity of the samples (vi) acquisition of ^{13}C-^{13}C DARR spectra of U-(^{13}C, ^{15}N)-Phe-recBVPrP^{Sc}(109I) to probe the chemical shifts of each one of the three Phe residues present in the sample.

For the purpose of this thesis, we expressed recombinant bank vole PrP in *E.coli*, non-labelled and also labelled, in different ways, depending on the experiment which would be performed, and then we subjected the samples to PMSA in order to obtain the infectious material. The development of this technique was key to the quest of elucidating recombinant bank vole PrP^{Sc} structure since this method allowed, for the first time, the production of large enough quantities of labelled recBVPrP^{Sc} from PrP^{C}, with attack rates of 100%, needed for solid state nuclear magnetic resonance measurements (ssNMR). Moreover, we also prepared non-labelled and labelled non-infectious PrP amyloid, by a spontaneous nucleation method using denaturing conditions, for comparison reasons.

Firstly, to fulfill objective number one, we prepared non-labelled recBVPrP amyloid and non-labelled recBVPrP^{Sc} and subjected them to FTIR analysis. There were differences in the minimum peaks and shoulders of both structures indicating differences in their secondary structure, most likely such differences are due to different levels of rigidity of the β-sheets of their PIRIBS architectures.

Subsequently, in order to fulfill objective number two, we prepared (U-^{13}C, ^{15}N)-recBVPrP^{Sc}(109I) and subjected it to solid state nuclear magnetic resonance experiments acquiring several different kinds of spectra: CP-HSQC, DREAM, DARR, INEPT-HSQC. Although we obtained relevant and new at the time information about the secondary structure of some residues, the data was compatible with both models thus not allowing us to accomplish our objective.

After this small disappointment we knew that acquiring spectra of the whole uniformly labelled recBVPrP^{Sc} we would not be able to solve the structure nor to distinguish between the two proposed models. Therefore, we needed a different kind of experiment that would yield a "yes or no" answer to the question that if PrP^{Sc} had the structure of one or the other model. Luckily, we found right what we needed: an experiment named PITHIRDS-CT that measures mean ^{13}C-^{13}C intermolecular distances and if the result is 5 Å that means that the architecture of the sample is a PIRIBS, or at least in theory. For instance, non-infectious recPrP amyloid is known to present a PIRIBS architecture,

solved two years ago by cryo-EM, but its ^{13}CO-^{13}CO PITHIRDS-CT acquired with ^{13}CO-Phe yielded an answer of 5.5 Å. This is because one of the Phe, Phe141, is located outside of the rigid β-core thus it is more flexible.

We performed PITHIRDS-CT experiments of ^{13}CO-Phe PrP amyloid, ^{13}CO-Tyr-Het-s (218-289) and ^{13}CO-Phe-recBVPrP^{Sc}(109I) as well as of ^{13}CO-Leu PrP amyloid, ^{13}CO-Tyr-Het-s (218-289) and ^{13}CO-Leu-recBVPrP^{Sc}(109I) and the results we obtained were completely unexpected. As already stated, we believed throughout the entire spam of my thesis, until last year when the structure of brain-derived PrP^{Sc} was published, that the secondary structure of PrP^{Sc} was a 4RβS. However, we obtained a mean intermolecular distance of 6.5 Å for both ^{13}CO-Phe and ^{13}CO-Leu-recBVPrP^{Sc}(109I), whereas we obtained the expected results of 5.5 Å and way longer than 7 Å for non-infectious ^{13}CO-Phe and ^{13}CO-Leu PrP amyloid and for ^{13}CO-Tyr-Het-s, respectively.

After this result of 6.5 Å, the 4RβS model was ruled out because if it were so the mean intermolecular distance should be of way longer than 7 Å, as for Het-s which is known to feature a 2RβS secondary structure. However, we still needed to explain why we had not obtained the canonical 5 Å distance. One plausible explanation is that some of the Phe and Leu residues were in loops as it was the case for one of the Phe residues from BVPrP amyloid and also for several residues from Sup35p prion domain.

Therefore, in order to assess the flexibility of our recBVPrP^{Sc} sample in the ms time scale, we performed CP-MAS and PARIS experiments with ^{13}CO-Phe-PrP amyloid, ^{13}CO-Tyr-Het-s (218-289) and ^{13}CO-Phe-recBVPrP^{Sc}(109I). We were expecting to obtain that recBVPrP^{Sc} was the most flexible, however that was not the case, indicating that Phe residues in recBVPrP^{Sc} are not flexible in the ms time scale.

Afterwards, since we still believed that recBVPrP^{Sc} had residues in flexible regions hence that it had to show flexibility at some time scale, we performed $T_1\rho$ experiments with ^{13}CO-Phe-PrP amyloid, ^{13}CO-Tyr-Het-s (218-289) and ^{13}CO-Phe-recBVPrP^{Sc}(109I) in orfer to assess their flexibility at the us time scale, which is where the loop's movements occur. As expected, these experiments yielded the resul that recBVPrP^{Sc} had faster tumbling in the us time scale, meaning that it is more flexible than the others in such time scale.

Finally, since we wanted to prove that some Phe residues presented chemical shits characteristic of coil, meaning that some of them are located in loops, we acquired ^{13}C-^{13}C DARR spectra of U-(^{13}C, ^{15}N)-Phe-recBVPrP^{Sc}(109I) to probe the chemical shifts of each one of the three Phe residues present in the sample. We expected to see three signals, one for each Phe residue. However, we obtained two sets of three signals, one set characteristic of coil and the other one of β-sheet secondary structure. Since we dismissed the possibility of a mixture of conformers due to our recBVPrP^{Sc} being perfectly stable throughout several PMSA passages, we concluded that Phe residues present micro static heterogeneity in recBVPrP^{Sc}.

To sup up, we generated uniformly labelled recBVPrP^{Sc} in large enough quantities which allowed us to extensively characterize it by solid state nuclear magnetic resonance for the first time. The most important result we obtained is that recBVPrP^{Sc} presents a PIRIBS architecture, although it is a PIRIBS with looser loops, meaning more flexible, than others; for instance the non-infectious PrP amyloid. This information is in line with the

structure of brain-derived PrP^{Sc} published last year which is a PIRIBS where only 33% of all residues are located in canonical β-sheets.

RESUMEN

Los priones son proteínas infecciosas que causan enfermedades neurodegenerativas raras y fatales, en animales y humanos, llamadas encefalopatías espongiformes transmisibles (TSE) porque los cerebros de los pacientes, cuando se analizan post mortem, muestran una vacuolización extrema que los hace parecer una esponja. Pueden presentarse como trastornos genéticos, infecciosos o esporádicos, todos los cuales implican el replegamiento de la proteína priónica del huésped, PrP^{C}, que es un componente normal de las células de mamíferos, en su isoforma infecciosa, PrP^{Sc}, a través de un proceso que involucra a su hélice α y estructura de muelle replegándose en hojas β, con PrP^{Sc} actuando como plantilla para PrP^{C}. Los priones fueron descubiertos a principios de los años 80 por Stanley Prusiner, quien ganó el Premio Nobel de Fisiología o Medicina en 1997 por ello. Hay otros priones no mamíferos, como los priones de hongos y levaduras, pero estos suelen ser funcionales, no patológicos.

Las enfermedades priónicas se hicieron ampliamente conocidas debido a la zoonosis de la "enfermedad de las vacas locas", que técnicamente se conoce como encefalopatía espongiforme bovina (BSE). Hubo un brote generalizado en el Reino Unido en los años 80 y 90, que causó 231 muertes humanas, debido principalmente a la alimentación con harina de carne y huesos (HCH), que contiene tejidos del sistema nervioso central, y otros que se sabe que albergan priones, al ganado. Actualmente, la zoonosis preocupante es la caquexia crónica (CWD, por sus siglas en inglés) que afecta a los cérvidos y los está matando masivamente en Canadá, Estados Unidos y también en Noruega y Suecia. Afortunadamente, la investigación dice que no es transmisible a los humanos, pero parece imparable y probablemente será más conocida en un futuro próximo.

Hay distintas cepas de priones que se definen por diferencias en un fenotipo heredable en condiciones de transmisión experimental controlada. Las cepas de priones pueden diferir en el período de incubación, los signos clínicos de la enfermedad, el tropismo tisular y el rango de huéspedes. La hipótesis predominante para este fenómeno es que la diversidad de cepas de priones está codificada por diferentes conformaciones de PrP^{Sc}, aunque se han identificado algunos cofactores *in vitro* que también pueden contribuir a la diversidad de cepas de priones.

La elucidación de la estructura de la PrP^{C} fue posible en 1997 debido a las mejoras en la expresión de la PrP recombinante, en cantidad suficiente para permitir los estudios de RMN. Sin embargo, la de la PrP^{Sc} fue mucho más complicada y no se logró hasta el 2021, sobre la cual profundizaremos, pero por ahora podemos mencionar que presenta una arquitectura PIRIBS (parallel-in-register-intermolecular-β-sheets). La razón por la que resultó tan difícil es que la PrP^{Sc} forma agregados insolubles que resisten la solubilización en detergentes no desnaturalizantes, lo que dificulta la obtención de preparaciones adecuadas a partir de cerebros de animales infectados para técnicas de alta resolución como la espectroscopia de RMN y la cristalografía de rayos X. Además, la PrP^{Sc} tiene una alta heterogeneidad derivada del anclaje GPI y los carbohidratos contenidos en su región C-terminal, lo que dificulta mucho la interpretación de los datos. El surgimiento de los priones recombinantes, como la PrP^{Sc} recombinante sin GPI, fue muy útil en este sentido.

La estructura de la PrP^{Sc} aún se desconocía al comienzo de mi doctorado en noviembre de 2017, pero había muchos datos disponibles obtenidos a través de diferentes técnicas: (i) Microscopía electrónica (EM), (ii) Espectroscopía infrarroja de transformada de Fourier (FTIR), (iii) cristalografía electrónica, (iv) difracción de rayos X de fibras, (v) intercambio de hidrógeno-deuterio (HDX) acoplado a espectrometría de masas (MS), (vi) proteólisis limitada acoplada a espectrometría de masas (MS), (vii) microscopía electrónica criogénica (crio-EM). Resumiendo, se creía que la PrP^{Sc} formaba fibras amiloides y que su estructura secundaria estaba compuesta por láminas β paralelas conectadas por bucles.

La microscopía electrónica es una técnica para obtener imágenes de alta resolución de especímenes biológicos y no biológicos. La alta resolución de las imágenes EM resulta del uso de electrones (que tienen longitudes de onda muy cortas) como fuente de radiación de iluminación. A través de EM de tinción negativa, Merz obtuvo la primera observación de fibrillas de PrP^{Sc} hace cuarenta años, que mostró estructuras fibrilares anormales, denominadas "fibrillas asociadas a scrapie" (SAF), en subfracciones de cerebros de animales afectados por scrapie. Llegaron a la conclusión de que SAF constaba de dos o cuatro filamentos y que mostraban un parecido con el amiloide. Un par de años más tarde, Prusiner también observó tales estructuras y las llamó "rods" que medían de 10 a 20 nm de diámetro y de 100 a 200 nm de longitud. Además, realizó estudios de birrefringencia con rojo Congo demostrando que las fibrillas de PrP^{Sc} son amiloides. Sin embargo, la cantidad de información estructural que se pudo recopilar estuvo muy limitada por la naturaleza altamente agregada de la proteína. En 2010, Sim y sus colegas emplearon fibrillas de proteína priónica gravemente subglucosiladas de ratones transgénicos infectados con scrapie que expresan proteína priónica sin ancla, ya que la glicosilación de la superficie pesada puede oscurecer la visualización de los núcleos fibrilares priónicos. Se obtuvieron las dimensiones y la información morfológica sobre los protofilamentos del núcleo de proteína priónica que se entrelazaron de forma variable para formar fibrillas de tembladera. Estas fibras se extendían alrededor de 100-150 nm de longitud y aparentemente estaban formadas por dos protofilamentos entrelazados con un ancho de alrededor de 4-5 nm por protofilamento. Se observaron protofilamentos aislados ocasionales, lo que sugiere que la asociación lateral de protofilamentos no es esencial ni constante en la polimerización de proteínas priónicas.

FTIR es una técnica espectroscópica no invasiva y sin etiquetas que utiliza radiación infrarroja para sondear la estructura secundaria de las proteínas debido a la absorción de sus enlaces polares, principalmente el amida. Los estudios FTIR fueron de los primeros en realizarse dado que se pueden aplicar a una muestra insoluble y desordenada. Demostraron que la conversión de PrP^{Sc} de PrP^{C} está asociada con una pérdida de hélice α y un gran aumento de láminas β en la estructura secundaria. Sin embargo, en 2011 se demostró que no hay presencia de hélice α en PrP^{Sc} por Smirnovas et al. cuando se demostró que la banda de 1660 cm-1, región que cubre diferentes longitudes de onda, en los espectros FTIR de PrPSc y PrP27-30 que había sido atribuida a hélices α, con base en la calibración usando proteínas globulares, también está presente en el espectro de fibras de amiloide PrP recombinante que exhiben exclusivamente una arquitectura de lámina β intermolecular paralela en registro. Por lo tanto, se concluyó que se había hecho una interpretación errónea y que PrP^{Sc} tenía alrededor del 50 % de contenido de láminas β y el 50 % de bucles.

La cristalografía electrónica es similar a la cristalografía de rayos X en que un cristal de proteína dispersa un haz para producir un patrón de difracción. Sin embargo, las interacciones entre los electrones en el haz y el cristal son mucho más fuertes que aquellas entre los fotones de rayos X y el cristal. Esto significa que se pueden recopilar cantidades significativas de datos de cristales mucho más pequeños. Luego, se analizaron cristales bidimensionales (2D) de PrP27-30 y PrP106 (Δ23–88, Δ141–176), que es la construcción mínima de PrP que puede soportar la propagación de priones. $PrP^{Sc}106$ carece de los residuos 141–176 pero está constantemente diglicosilado. En comparación, la PrP 27-30 tiene una cadena peptídica más larga y es una mezcla de formas sin, mono y diglicosiladas. Como estos cristales muestran una mezcla compleja de tinción negativa y positiva, es importante considerar el comportamiento de tinción de las diferentes construcciones. $PrP^{Sc}106$ carece de muchos de los residuos cargados negativamente que están presentes en PrP 27-30 y, por lo tanto, se une a menos cationes de uranilo en el centro de las subunidades. Por lo tanto, restar la densidad de PrP 27-30 de la densidad de $PrP^{Sc}106$ debería resaltar los residuos 141–176 en densidad positiva, mientras que restar $PrP^{Sc}106$ de PrP 27-30 debería colocar los sitios de glicosilación adicionales en densidad positiva. Como era de esperar, PrP 27-30 menos $PrP^{Sc}106$ mostró diferencias que eran casi idénticas a la ubicación de los azúcares determinada por el etiquetado con Nanogold. Aquí, la señal de diferencia para los azúcares unidos por N se encontró en todos los ejes de simetría triple alrededor del oligómero. $PrP^{Sc}106$ menos PrP 27-30 reveló diferencias alrededor del centro de cada oligómero, que se interpretaron como representativas de los aminoácidos en la eliminación interna de PrP106 (141-176). Los autores concluyeron que la PrP^{Sc} está formada por una β-hélice paralela, ya que tal estructura sería la única que encajaría en las dimensiones de la red hexagonal. La resolución de esta técnica es de unos 2 nm, que es justo el diámetro de la hélice β propuesta. Por lo tanto, no fue posible brindar ningún detalle de mayor resolución, solo que su arquitectura podría corresponder a un solenoide.

La difracción de rayos X de fibra es un fenómeno en el que los átomos de un cristal, en virtud de su espaciamiento uniforme, provocan un patrón de interferencia de las ondas presentes en un haz incidente de rayos X; los planos atómicos del cristal actúan sobre los rayos X exactamente de la misma manera que una rejilla reglada uniformemente sobre un haz de luz. La propiedad de formación de fibra de PrP^{Sc} hace posible determinar información adicional sobre la estructura tridimensional de la molécula PrP27-30 mediante la técnica de difracción de rayos X de fibra. Los primeros estudios con difracción de fibra de rayos X sobre la estructura de PrP^{Sc} confirmaron la naturaleza amiloide de los bastones priónicos. La difracción meridional a 4,8 Å indica la típica estructura β cruzada correspondiente a la distancia entre láminas β en las que los enlaces de hidrógeno corren paralelos al eje de la fibra. En 2009, Wille et al prepararon fibras de MoPrPSc purificadas a partir de cerebros de ratones inoculados con priones RML mediante precipitación con PTA, que es un método selectivo para la precipitación de PrPSc ya que a pH neutro y en presencia de Mg^{+2} el PTA forma complejos con oligómeros de PrPSc y PrP 27-30 pero no con PrPC. Los patrones MoPrP 27-30 (RML) contenían al menos 11 máximos de intensidad meridional que podrían clasificarse en tres grupos, "l", "u" y "p". El grupo "l" mostró máximos relativamente nítidos en resoluciones cercanas a 4,1 Å y 8,2 Å que muy probablemente provenían de ensamblajes de lípidos o detergentes lipídicos, lo que refleja el espacio entre las cadenas de hidrocarburos. El grupo "u" tenía un par de intensidades relativamente agudas de 7,7 Å y 7,4 Å que parecían ser contaminantes de proteínas de otros órganos. El grupo "p", por el contrario, podría interpretarse en términos de estructura de proteína. Este grupo contiene tres máximos:

difracción cruzada amplia y muy débil a 4,8 Å y arcos moderadamente amplios a 9,6 Å y 6,4 Å. Estos máximos corresponden al segundo, tercer y cuarto orden de una repetición vertical de 19,2 Å, es decir, la mitad, un tercio y un cuarto de la repetición vertical de 19,2 Å cuya ausencia puede explicarse por el desorden en el filamento. 19,2 Å tiene el tamaño de una lámina ß de cuatro hebras cuya presencia sería consistente con las propiedades amiloides de las fibras y su alto contenido de lámina ß. La debilidad de la difracción de 4,8 Å puede reflejar una irregularidad en el espaciado de las cuatro hebras. Aunque estos datos respaldan la presencia de una estructura β de cuatro hebras, no pueden determinar si esa estructura consiste en una lámina aislada, láminas apiladas, hélices β o cualquier otra forma de estructura ß.

El protocolo HDX-MS aprovecha la naturaleza lábil de los protones presentes en las amidas del esqueleto de la proteína y es una poderosa herramienta en el estudio de la estructura de la proteína. Cuando se disuelven en solución, las proteínas intercambian estos protones con grupos de hidrógeno presentes en un tampón deuterado, y los protones de la proteína se intercambian con deuterio. Solo se miden los protones presentes en las amidas del esqueleto. La tasa de intercambio de hidrógeno a deuterio proporciona datos de accesibilidad de solventes, que se pueden usar para inferir información sobre la estructura y conformación de las proteínas. La espectrometría de masas se puede utilizar para medir la tasa de absorción de deuterio después del tratamiento con pepsina. Se han realizado algunos estudios con esta técnica analizando la estructura del amiloide PrP recombinante. Finalmente, se publicó un artículo que estudió la PrPSc sin GPI y mostró que la parte C-terminal de la PrP^{Sc} sin GPI exhibe tasas extremadamente bajas de intercambio H/D, lo cual es típico de tramos con extensos enlaces H (β- hojas) y todo el tramo 90-215 es relativamente resistente al cambio. Algunos otros tramos exhiben una tasa de cambio más alta correspondiente a la superposición parcial con giros o bucles, como 133-148 y 81-118. Por lo tanto, se concluyó que la PrP^{Sc} sin GPI consta de una serie de láminas β conectadas por bucles cortos y/o bucles sin hélices α nativas, lo que concuerda con la reinterpretación de los resultados de FTIR.

El principio de la proteólisis limitada es que una proteína se incuba con una concentración relativamente baja de diferentes proteasas, que cortan en los sitios de reconocimiento a lo largo de la proteína, normalmente en regiones expuestas como bucles y otras regiones flexibles. En 2012, Vázquez-Fernández y colaboradores analizaron por completo la PrP^{Sc} sin anclaje de GPI debido a la falta de GPI y la falta casi total de glicosilación. Reveló sitios de escisión en las posiciones 81, 85, 89, 116, 118, 133, 134, 141, 152, 153, 162, 169 y 179. Estos resultados mostraron los sitios de escisión PK reales para el monómero PrPSc completo. Dichos sitios de clivaje coinciden con los previamente identificados en PrPSc de hámster, hasta donde fue posible el análisis de esa molécula (~N154), lo que sugiere que la arquitectura de GPI−PrP^{Sc}, 263 K SHaPrPSc y DySHaPrPSc comparten una estructura común. Los autores concluyeron que la estructura de PrPSc consiste en una serie de hebras de hoja β de alta resistencia a PK que están conectadas a través de bucles y vueltas de acuerdo con los resultados anteriores. Dado que no se detectaron sitios de escisión más allá de la posición 170, también se concluyó que el tramo C-terminal de GPI-PrP^{Sc} era particularmente resistente a PK, estando probablemente compuesto principalmente por láminas β.

La microscopía electrónica criogénica es una técnica de criomicroscopía aplicada en muestras enfriadas a temperaturas criogénicas e incrustadas en un ambiente de agua vítrea que es etano líquido; hace que la muestra se congele tan rápido que no se pueden formar

cristales de hielo. Vázquez-Fernández y sus colegas en 2016 utilizaron por primera vez una PrPSc sin anclaje GPI ya que sus fibras presentan inherentemente una organización repetitiva. Se proporcionan más detalles en el texto principal. En resumen, la reconstrucción 3D de una de estas fibrillas individuales de PrP 27–30 sin anclaje GPI, con un ancho máximo de 9,1 nm y una distancia de cruce de 95 nm, mostró dos protofilamentos de forma ovalada de aproximadamente 50 x 29 Å. La implicación es que las subunidades de PrPSc solo pueden caber en protofilamentos con las dimensiones observadas si se doblan sobre sí mismas. Según la observación de rutina de señales β cruzadas regulares de 4,8 Å en fibrillas PrP 27–30 sin anclaje GPI individuales, una disposición de solenoide β es la forma más fácil de acomodar el péptido en el volumen de protofilamento disponible.

A lo largo de los años, se habían propuesto varios modelos, pero en ese momento, en 2017, solo quedaban dos: (i) el PIRIBS (parallel-in-register-intermolecular-β-sheets) que establece que las fibras de amiloide PrP^{Sc} están hechas por un solo protofilamento donde cada monómero tiene un registro paralelo apilado a lo largo de los ejes fibrilares y argumenta que los monómeros de PrP^{Sc} son planos, con núcleos ricos en cadenas β similares a amiloide de rPrP que se extienden hasta la posición ~90; y (ii) el 4RβS (4-peldaño-β-solenoide) que, por el contrario, establece que las fibras están formadas por dos protofilamentos entrelazados.

El objetivo principal de esta tesis es desafiar ambos modelos para dilucidar cuál es la estructura real de PrP^{Sc}. Además, los objetivos específicos son: (i) preparación de amiloide recPrP no infeccioso y recBVPrP^{Sc}(109I) infeccioso para analizarlos mediante FTIR con el fin de comparar sus estructuras secundarias; (ii) adquisición y comparación de diferentes espectros ssNMR (CP-HSQC, DREAM, DARR, INEPT-HSQC) de (U-^{13}C, ^{15}N)-recBVPrP^{Sc}(109I) para poder distinguir entre arquitecturas PIRIBS y 4RβS; (iii) adquisición y comparación de espectros PITHIRDS-CT de amiloide no infeccioso ^{13}CO-Phe PrP, ^{13}CO-Tyr-Het-s (218-289) y ^{13}CO-Phe-recBVPrPSc(109I), así como de amiloide no infeccioso ^{13}CO-Leu PrP, ^{13}CO-Tyr-Het-s (218-289) y ^{13}CO-Leu-recBVPrP^{Sc}(109I) para evaluar sus distancias intermoleculares con el fin de distinguir entre arquitecturas PIRIBS y 4RβS; (iv) adquisición y comparación de espectros 1D-13CP-MAS y PARIS de amiloide no infeccioso ^{13}CO-Phe-PrP, ^{13}CO-Tyr-Het-s (218-289) y ^{13}CO-Phe-recBVPrP^{Sc}(109I) para obtener información sobre flexibilidad/ rigidez de las muestras; (v) adquisición y comparación de espectros $T_{1\rho}$ de amiloide no infeccioso ^{13}CO-Phe-PrP, ^{13}CO-Tyr-Het-s (218-289) y ^{13}CO-Phe-recBVPrPSc(109I) para obtener información sobre la flexibilidad/rigidez de las muestras (vi) adquisición de espectros ^{13}C-^{13}C DARR de U-(^{13}C,^{15}N)-Phe-recBVPrP^{Sc}(109I) para sondear los desplazamientos químicos de cada uno de los tres residuos de Phe presentes en la muestra.

Para el propósito de esta tesis, expresamos PrP recombinante de topillo rojo (bank vole) en *E.coli*, no marcada y también marcada, de diferentes formas, dependiendo del experimento a realizar, y luego sometimos las muestras a PMSA para obtener el material infeccioso. El desarrollo de esta técnica fue clave para la búsqueda de la estructura de PrP^{Sc} recombinante, ya que este método permitió, por primera vez, la producción de cantidades suficientemente grandes de recBVPrP^{Sc} marcada a partir de PrP^{C}, con tasas de ataque del 100%, necesarias para las mediciones de resonancia magnética nuclear de estado sólido (ssNMR). Además, también preparamos amiloide PrP no infeccioso marcado y no marcado, mediante un método de nucleación espontánea utilizando condiciones desnaturalizantes, por razones de comparación.

En primer lugar, para cumplir el objetivo número uno, preparamos amiloide recBVPrP no marcado y recBVPrP^{Sc} no marcados y los sometimos a análisis FTIR. Hubo diferencias en los picos y hombros mínimos de ambas estructuras que indican diferencias en su estructura secundaria, lo más probable es que tales diferencias se deban a diferentes niveles de rigidez de las hojas β de sus arquitecturas PIRIBS.

Posteriormente, para cumplir el objetivo número dos, preparamos (U-^{13}C, ^{15}N)-recBVPrP^{Sc}(109I) y lo sometimos a experimentos de resonancia magnética nuclear en estado sólido adquiriendo varios tipos de espectros: CP-HSQC, DREAM, DARR, INEPT -HSQC. Aunque obtuvimos información relevante y nueva en ese momento sobre la estructura secundaria de algunos residuos, los datos eran compatibles con ambos modelos, por lo que no nos permitieron lograr nuestro objetivo.

Después de esta pequeña decepción, supimos que adquiriendo espectros de recBVPrP^{Sc} uniformemente marcada, no seríamos capaces de resolver la estructura ni distinguir entre los dos modelos propuestos. Por lo tanto, necesitábamos un tipo diferente de experimento que diera una respuesta de "sí o no" a la pregunta de si PrP^{Sc} tenía la estructura de uno u otro modelo. Por suerte, encontramos justo lo que necesitábamos: un experimento llamado PITHIRDS-CT que mide distancias intermoleculares medias ^{13}C-1^{3}C y si el resultado es 5 Å eso significa que la arquitectura de la muestra es una PIRIBS, o al menos en teoría. Por ejemplo, se sabe que el amiloide recPrP no infeccioso presenta una arquitectura PIRIBS, resuelta hace dos años por cryo-EM, pero su ^{13}CO-^{13}CO PITHIRDS-CT adquirida con ^{13}CO-Phe produjo una respuesta de 5,5 Å. Esto se debe a que una de las Phe, Phe141, está ubicada fuera del núcleo β rígido, por lo que es más flexible.

Realizamos experimentos PITHIRDS-CT de amiloide 13CO-Phe PrP, ^{13}CO-Tyr-Het-s (218-289) y ^{13}CO-Phe-recBVPrP^{Sc}(109I), así como de amiloide ^{13}CO-Leu PrP, ^{13}CO-Tyr-Het-s (218-289) y ^{13}CO-Leu-recBVPrP^{Sc}(109I) y los resultados que obtuvimos fueron completamente inesperados. Como ya se dijo, creímos durante toda la duración de mi tesis, hasta el año pasado cuando se publicó la estructura de la PrP^{Sc} derivada de cerebro, que la estructura secundaria de la PrP^{Sc} era un 4RβS. Sin embargo, obtuvimos una distancia intermolecular media de 6,5 Å tanto para ^{13}CO-Phe como para ^{13}CO-Leu-recBVPrP^{Sc}(109I), mientras que obtuvimos los resultados esperados de 5,5 Å y mucho más de 7 Å para ^{13}CO-Phe y ^{13}CO-Leu PrP amiloide y para ^{13}CO-Tyr-Het-s, respectivamente.

Después de este resultado de 6,5 Å, se descartó el modelo 4RβS porque, de ser así, la distancia intermolecular media debería ser mucho mayor que 7 Å, como para Het-s, que se sabe que presenta una estructura secundaria 2RβS. Sin embargo, todavía necesitábamos explicar por qué no habíamos obtenido la distancia canónica de 5 Å. Una explicación plausible es que algunos de los residuos de Phe y Leu estaban en bucles, como fue el caso de uno de los residuos de Phe del amiloide BVPrP y también de varios residuos del dominio del prión Sup35p.

Por lo tanto, para evaluar la flexibilidad de nuestra muestra recBVPrPSc en la escala de tiempo de ms, realizamos experimentos CP-MAS y PARIS con amiloide ^{13}CO-Phe-PrP, ^{13}CO-Tyr-Het-s (218-289) y ^{13}CO-Phe-recBVPrP^{Sc}(109I). Esperábamos obtener que recBVPrP^{Sc} fuera la más flexible, sin embargo, ese no fue el caso, lo que indica que los residuos de Phe en recBVPrP^{Sc} no son flexibles en la escala de tiempo de ms.

Posteriormente, dado que todavía creíamos que recBVPrP^{Sc} tenía residuos en regiones flexibles, por lo que tenía que mostrar flexibilidad en alguna escala de tiempo, realizamos experimentos $T_{1\rho}$ con amiloide ^{13}CO-Phe-PrP, ^{13}CO-Tyr-Het-s (218-289) y ^{13}CO-Phe-recBVPrP^{Sc}(109I) para evaluar su flexibilidad en la escala de tiempo de microsegundos (us), que es donde se producen los movimientos de los bucles. Como era de esperar, estos experimentos arrojaron el resultado de que recBVPrP^{Sc} tiene una caída más rápida en la escala de tiempo de us, lo que significa que es más flexible que los demás en dicha escala de tiempo.

Finalmente, dado que queríamos probar que algunos residuos de Phe presentaban desplazamientos químicos propios de bucles, es decir, que algunos de ellos se encuentran en bucles, adquirimos espectros ^{13}C-^{13}C DARR de U-(^{13}C, ^{15}N)-Phe-recBVPrP^{Sc}(109I) para averiguar los desplazamientos químicos de cada uno de los tres residuos de Phe presentes en la muestra. Esperábamos ver tres señales, una para cada residuo de Phe. Sin embargo, obtuvimos dos conjuntos de tres señales, un conjunto característico de bucles y el otro de estructura secundaria de hoja β. Dado que descartamos la posibilidad de una mezcla de confórmeros debido a que nuestro recBVPrP^{Sc} es perfectamente estable a lo largo de varios pasajes de PMSA, concluimos que los residuos de Phe presentan heterogeneidad microestática en recBVPrP^{Sc}.

En resumen, hemos sido capaces de generar recBVPrP^{Sc} marcada en cantidades lo suficientemente grandes que nos permitieron caracterizarla ampliamente por resonancia magnética nuclear de estado sólido por primera vez. El resultado más importante que obtuvimos es que recBVPrP^{Sc} presenta una arquitectura PIRIBS, aunque es un PIRIBS con bucles más sueltos, es decir, más flexible, que otros; por ejemplo, el amiloide PrP no infeccioso. Esta información está en línea con la estructura de PrP^{Sc} derivada del cerebro publicada el año pasado, que es un PIRIBS donde solo el 33% de todos los residuos se encuentran en hojas β canónicas.

RESUMO

Os prións son proteínas infecciosas que causan enfermidades neurodexenerativas raras e mortais, en animais e humanos, chamadas encefalopatías esponxiformes transmisibles (EET) porque o cerebro dos pacientes, cando se analiza post mortem, mostra unha vacuolización extrema que os fai parecer unha esponxa. Poden presentarse como trastornos xenéticos, infecciosos ou esporádicos, todos os cales implican o replegamento da proteína priónica do hóspede, PrP^{C}, que é un compoñente normal das células de mamíferos, na súa isoforma infecciosa, PrP^{Sc}, mediante un proceso que implica o plegamento da súas hélices α e bucles en follas β, coa PrP^{Sc} actuando como molde para a PrP^{C}. Os prións foron descubertos a principios dos anos 80 por Stanley Prusiner, que gañou o Premio Nobel de Fisioloxía ou Medicina en 1997 por iso. Hai outros prións non mamíferos, como de fungos e lévedos, pero estes adoitan ser funcionais, non patolóxicos.

As enfermidades priónicas fixéronse moi coñecidas debido á zoonose da "enfermidade das vacas tolas", que se coñece tecnicamente como encefalopatía esponxiforme bovina (EEB). Houbo un brote xeneralizado no Reino Unido nas décadas de 1980 e 1990, que causou 231 mortes humanas, principalmente debido á alimentación con fariña de carne e ósos (MBM), que contén tecido do sistema nervioso central, e outros coñecidos por albergar prións, ao gando vacún. Actualmente, a zoonose preocupante é a enfermidade de emaciación crónica (CWD) que afecta aos cérvidos e está a matalos en masa en Canadá, Estados Unidos e tamén en Noruega e Suecia. Afortunadamente, a investigación di que non é transmisible aos humanos, pero parece imparable e probablemente se fará máis coñecida nun futuro próximo.

Existen distintas cepas de prións que se definen por diferenzas nun fenotipo herdable en condicións de transmisión experimental controlada. As cepas de prións poden diferir no período de incubación, os signos clínicos da enfermidade, o tropismo dos tecidos e o rango de hóspede. A hipótese predominante para este fenómeno é que a diversidade de cepas de prións está codificada por diferentes conformacións de PrP^{Sc}, aínda que se identificaron algúns cofactores *in vitro* que tamén poden contribuír á diversidade de cepas de prións.

A elucidación da estrutura da PrP^{C} foi posible en 1997 debido a melloras na expresión da PrP recombinante, en cantidade suficiente para permitir estudos de RMN. Porén, a PrP^{Sc} foi moito máis complicada e non se conseguiu ata 2021, no que afondaremos, pero de momento podemos mencionar que conta cunha arquitectura PIRIBS (parallel-in-register-intermolecular-β-sheets). A razón pola que isto resultou tan difícil é que a PrP^{Sc} forma agregados insolubles que resisten a solubilización en deterxentes non desnaturalizantes, o que dificulta a obtención de preparados axeitados do cerebro dos animais infectados para técnicas de alta resolución como a espectroscopia de RMN e a cristalografía de raios X. Ademais, a PrP^{Sc} ten unha alta heteroxeneidade derivada da áncora GPI e dos hidratos de carbono contidos na súa rexión C-terminal, o que dificulta moito a interpretación dos datos. O surximento dos prións recombinantes, como a PrPSc recombinante esgotada en GPI, foi moi útil neste sentido.

A estrutura de PrP^{Sc} aínda era descoñecida ao comezo do meu doutoramento en novembro de 2017, pero estaban dispoñibles moitos datos obtidos a través de diferentes técnicas: (i) Microscopía electrónica (EM), (ii) Espectroscopia de infravermellos por transformada de Fourier (FTIR), (iii) cristalografía electrónica, (iv) difracción de raios X de fibra, (v) intercambio hidróxeno-deuterio (HDX) acoplado a espectrometría de masas (MS), (vi) proteólise limitada acoplada a espectrometría de masas (MS), (vii) microscopía electrónica crioxénica (crio-EM). Resumindo, pensábase que a PrP^{Sc} formaba fibras amiloides e que a súa estrutura secundaria estaba composta por follas β paralelas conectadas por bucles.

A microscopía electrónica é unha técnica para a obtención de imaxes de alta resolución de mostras biolóxicas e non biolóxicas. A alta resolución das imaxes EM resulta do uso de electróns (que teñen lonxitudes de onda moi curtas) como fonte de radiación iluminadora. Mediante a tinción negativa EM, Merz obtivo a primeira observación de fibrillas de PrP^{Sc} hai corenta anos, que mostraban estruturas fibrilares anormais, denominadas "fibrillas asociadas á scrapie" (SAF), en subfraccións dos cerebros de animais afectados por scrapie. Concluíron que SAF constaba de dous ou catro filamentos e que mostraban un parecido co amiloide. Un par de anos despois, Prusiner tamén observou este tipo de estruturas e chamounas "rods" que medían entre 10 e 20 nm de diámetro e entre 100 e 200 nm de lonxitude. Ademais, realizou estudos de birrefringencia co vermello Congo que mostran que as fibrillas de PrP^{Sc} son amiloides. Non obstante, a cantidade de información estrutural que se podía recoller estaba moi limitada pola natureza altamente agregada da proteína. En 2010, Sim e os seus colegas utilizaron fibrillas de proteína priónica gravemente subglicosiladas de ratos transxénicos infectados con tembladera que expresaban proteínas priónicas sen ancora, xa que a glicosilación superficial pesada pode ocultar a visualización dos núcleos fibrilares priónicos. Obtivéronse dimensións e información morfolóxica dos protofilamentos do núcleo de proteínas priónicas que se entrelazaron de forma variable para formar fibrillas de scrapie. Estas fibras abarcaban uns 100-150 nm de lonxitude e aparentemente estaban formadas por dous protofilamentos entrelazados cunha anchura duns 4-5 nm por protofilamento. Observáronse ocasionalmente protofilamentos illados, o que suxire que a asociación lateral de protofilamentos non é esencial nin constante na polimerización da proteína priónica.

FTIR é unha técnica espectroscópica non invasiva e sen etiquetas que utiliza radiación infravermella para sondar a estrutura secundaria das proteínas debido á absorción dos seus enlaces polares, principalmente amida. Os estudos FTIR foron dos primeiros en realizarse xa que se poden aplicar a unha mostra insoluble e desordenada. Mostraron que a conversión de PrP^{Sc} en PrP^{C} está asociada cunha perda de hélice α e un gran aumento das follas β na estrutura secundaria. Porén, en 2011, Smirnovas et al demostrou que non hai hélice α presente na PrP^{Sc}. cando se demostrou que a banda de 1660 cm-1, unha rexión que abarca diferentes lonxitudes de onda, nos espectros FTIR de PrPSc e PrP27-30 que fora atribuída ás hélices α, baseada na calibración mediante proteínas globulares, tamén está presente no espectro. de fibras amiloides de PrP recombinantes que presentan exclusivamente unha arquitectura de folla β intermolecular paralela en log. Polo tanto, chegouse á conclusión de que se fixo unha interpretación errónea e que PrP^{Sc} tiña preto do 50% de contido de folla β e un 50% de bucles.

A cristalografía de electróns é semellante á cristalografía de raios X en que un cristal de proteína dispersa un feixe para producir un patrón de difracción. Non obstante, as

interaccións entre os electróns do feixe e o cristal son moito máis fortes que as entre os fotóns de raios X e o cristal. Isto significa que se poden recoller cantidades significativas de datos a partir de cristais moito máis pequenos. Despois, analizáronse cristais bidimensionais (2D) de PrP27-30 e PrP106 (Δ23-88, Δ141-176), que é a construción mínima de PrP que pode soportar a propagación de prións. A PrP^{Sc}106 carece de residuos 141-176 pero está constantemente diglicosilada. En comparación, a PrP 27-30 ten unha cadea peptídica máis longa e é unha mestura de formas syn, mono e diglicosiladas. Como estes cristais mostran unha complexa mestura de coloración positiva e negativa, é importante ter en conta o comportamento da cor dos diferentes construtos. A PrP^{Sc}106 carece de moitos dos residuos cargados negativamente que están presentes na PrP 27-30 e, polo tanto, únese a menos catións de uranilo no centro das subunidades. Polo tanto, restar a densidade de PrP 27-30 da densidade de PrP^{Sc}106 debería destacar os residuos 141-176 en densidade positiva, mentres que restar PrP^{Sc}106 da PrP 27-30 debería situar os sitios adicionais de glicosilación en densidade positiva. Como era de esperar, PrP 27-30 menos PrP^{Sc}106 mostrou diferenzas que eran case idénticas á localización dos azucres determinada pola etiquetaxe Nanogold. Aquí, o sinal de diferenza para os azucres ligados a N atopouse en todos os eixes de triple simetría ao redor do oligómero. PrP^{Sc}106 menos PrP 27-30 revelaron diferenzas ao redor do centro de cada oligómero, que foron interpretadas como representativas dos aminoácidos na deleción interna de PrP106 (141-176). Os autores concluíron que a PrP^{Sc} está formada por unha hélice β paralela, xa que tal estrutura sería a única que se axustaría ás dimensións da rede hexagonal. A resolución desta técnica é duns 2 nm, que é só o diámetro da hélice β proposta. Polo tanto, non foi posible proporcionar ningún detalle de maior resolución, só que a súa arquitectura podería corresponder a un solenoide.

A difracción de raios X da fibra é un fenómeno no que os átomos dun cristal, en virtude da súa separación uniforme, provocan un patrón de interferencia das ondas presentes nun feixe incidente de raios X; os planos atómicos do cristal actúan sobre os raios X exactamente do mesmo xeito que unha reixa regulada uniformemente nun feixe de luz. A propiedade de formación de fibras da PrPSc permite determinar información adicional sobre a estrutura tridimensional da molécula de PrP27-30 mediante a técnica de difracción de raios X de fibras. Os primeiros estudos de difracción de fibras de raios X da estrutura da PrPSc confirmaron a natureza amiloide das varillas priónicas. A difracción meridional a 4,8 Å indica a típica estrutura cruzada β correspondente á distancia entre as follas β na que os enlaces de hidróxeno corren paralelos ao eixe da fibra. En 2009, Wille et al prepararon fibras de MoPrPSc purificadas a partir de cerebros de ratos inoculados con prións RML mediante precipitación con PTA, que é un método selectivo para a precipitación de PrPSc xa que a pH neutro e en presenza de Mg+2 PTA forma complexos con oligómeros de PrPSc. e PrP 27-30 pero non con PrPC. Os patróns MoPrP 27-30 (RML) contiñan polo menos 11 máximos de intensidade meridional que se podían clasificar en tres grupos, "l", "u" e "p". O grupo "l" mostrou máximos relativamente nítidos en resolucións próximas a 4,1 Å e 8,2 Å que probablemente proviñan de conxuntos lipídicos ou deterxentes lipídicos, reflectindo o espazo entre cadeas de hidrocarburos. O grupo "u" tiña un par de intensidades relativamente nítidas de 7,7 Å e 7,4 Å que parecían ser contaminantes proteicos doutros órganos. O grupo "p", pola contra, podería interpretarse en termos de estrutura da proteína. Este grupo contén tres máximos: difracción cruzada ampla e moi débil a 4,8 Å e arcos moderadamente anchos a 9,6 Å e 6,4 Å. Estes máximos corresponden á segunda, terceira e cuarta orde dunha repetición vertical de 19,2 Å, é dicir, a metade, un terzo e un cuarto da repetición vertical de 19,2 Å cuxa ausencia pode explicarse pola desorde no filamento. 19,2 Å é o tamaño dunha folla

ß de catro cadeas cuxa presenza sería consistente coas propiedades amiloides das fibras e o seu alto contido en folla ß. A debilidade de difracción de 4,8 Å pode reflectir unha irregularidade na separación das catro cadeas. Aínda que estes datos apoian a presenza dunha estrutura β de catro cadeas, non poden determinar se esa estrutura consiste nunha única folla, follas apiladas, hélices β ou calquera outra forma de estrutura β.

O protocolo HDX-MS aproveita a natureza lábil dos protóns presentes nas amidas da columna vertebral das proteínas e é unha poderosa ferramenta no estudo da estrutura das proteínas. Cando se disolven en solución, as proteínas intercambian estes protóns con grupos hidróxeno presentes nun tampón deuterado, e os protóns da proteína intercambian con deuterio. Só se miden os protóns presentes nas amidas da columna vertebral. A taxa de cambio de hidróxeno ao deuterio proporciona datos de accesibilidade aos disolventes, que se poden usar para inferir información sobre a estrutura e conformación das proteínas. A espectrometría de masas pódese usar para medir a taxa de absorción de deuterio despois do tratamento con pepsina. Realizáronse algúns estudos con esta técnica que analizan a estrutura do amiloide PrP recombinante. Finalmente, publicouse un artigo que estudou PrPSc sen GPI e mostrou que a parte C-terminal da PrP^{Sc} sen GPI presenta taxas extremadamente baixas de intercambio H/D, o que é típico dos tramos con enlaces H extensas (follas β) e todo o tramo 90-215 é relativamente resistente ao cambio. Algúns outros tramos presentan unha maior taxa de cambio correspondente á superposición parcial con torsións ou bucles, como 133-148 e 81-118. Polo tanto, concluíuse que a PrPSc GPI-negativa consiste nunha serie de follas β conectadas por bucles curtos e/ou bucles sen hélices α nativas, o que é consistente coa reinterpretación dos resultados do FTIR.

O principio da proteólise limitada é que unha proteína é incubada cunha concentración relativamente baixa de diferentes proteases, que cortan nos sitios de recoñecemento de toda a proteína, xeralmente en rexións expostas como bucles e outras rexións flexibles. En 2012, Vázquez-Fernández e os seus colegas analizaron completamente a PrP^{Sc} sen ancoraxe do GPI debido á falta de GPI e á case total falta de glicosilación. Revelou sitios de escisión nas posicións 81, 85, 89, 116, 118, 133, 134, 141, 152, 153, 162, 169 e 179. Estes resultados mostraron os sitios de escisión PK reais para todo o monómero PrPSc. Estes sitios de clivaxe coinciden cos identificados anteriormente no PrPSc do hámster, na medida en que foi posible a análise desa molécula (~N154), o que suxire que a arquitectura de GPI−PrPSc, 263 K SHAPrPSc e $DySHaPrP^{Sc}$ comparten unha estrutura común. Os autores concluíron que a estrutura de PrPSc consiste nunha serie de cadeas de folla β de alta resistencia a PK que están conectadas mediante bucles e voltas de acordo cos resultados anteriores. Dado que non se detectaron sitios de escisión máis aló da posición 170, tamén se concluíu que o tramo C-terminal de GPI-PrP^{Sc} era particularmente resistente á PK, estando probablemente composto principalmente por follas β.

A microscopía electrónica crioxénica é unha técnica de criomicroscopia aplicada a mostras arrefriadas a temperaturas crioxénicas e incrustadas nun ambiente de auga vítrea que é etano líquido; fai que a mostra se conxele tan rápido que non se poidan formar cristais de xeo. Vázquez-Fernández e os seus compañeiros utilizaron en 2016 unha PrP^{Sc} sen ancoraxe GPI por primeira vez desde que as súas fibras presentan de forma inherente unha organización repetitiva. No texto principal ofrécense máis detalles. En resumo, a reconstrución en 3D dunha destas fibrillas de PrP individuais 27-30 sen áncora GPI, cunha anchura máxima de 9,1 nm e unha distancia de cruce de 95 nm, mostrou dous protofilamentos de forma oval de aproximadamente 50 x 29 A. A implicación é que as

subunidades PrP^{Sc} só poden encaixar en protofilamentos coas dimensións observadas se se replegan sobre si mesmas. Baseándose na observación rutineira de sinais cruzados β regulares de 4,8 Å en fibrillas de PrP 27-30 sen unir a GPI, unha disposición β-solenoide é a forma máis sinxela de acomodar o péptido no volume do protofilamento dispoñible.

Ao longo dos anos propuxéronse varios modelos, pero no seu momento, en 2017, só quedaban dous: (i) o PIRIBS (parallel-in-register-intermolecular-β-sheets) que establece que as fibras amiloides PrP^{Sc} están feitas por un protofilamento único onde cada monómero ten un rexistro paralelo apilado ao longo dos eixes fibrilares e argumenta que os monómeros PrP^{Sc} son planos, con núcleos ricos en cadeas β de tipo amiloide de rPrP que se estenden ata a posición ~90; e (ii) o 4RβS (4-run-β-solenoid) que, pola contra, afirma que as fibras están formadas por dous protofilamentos entrelazados.

O obxectivo principal desta tese é desafiar ambos modelos para dilucidar cal é a estrutura real da PrP^{Sc}. Ademais, os obxectivos específicos son: (i) preparación de recPrP non infeccioso e análise de amiloide recBVPrP^{Sc}(109I) mediante FTIR para comparar as súas estruturas secundarias; (ii) adquisición e comparación de diferentes espectros ssNMR (CP-HSQC, DREAM, DARR, INEPT-HSQC) de (U-^{13}C, ^{15}N)-recBVPrP^{Sc}(109I) para distinguir entre arquitecturas PIRIBS e 4RβS; (iii) adquisición e comparación de espectros PITHIRDS-CT de amiloide ^{13}CO-Phe PrP, ^{13}CO-Tyr-Het-s (218-289) e ^{13}CO-Phe-recBVPrP^{Sc} (109I), así como amiloide ^{13}CO-Leu PrP, ^{13}CO -Tyr-Het-s (218-289) e ^{13}CO-Leu-recBVPrPSc(109I) para avaliar as súas distancias intermoleculares co fin de distinguir entre arquitecturas PIRIBS e 4RβS; (iv) adquisición e comparación dos espectros 1D-13CP-MAS e PARIS de amiloide ^{13}CO-Phe-PrP, ^{13}CO-Tyr-Het-s (218-289) e ^{13}CO-Phe-recBVPrPSc(109I) para obter información sobre flexibilidade/ rixidez da mostra; (v) adquisición e comparación de espectros $T_{1\rho}$ do amiloide ^{13}CO-Phe-PrP, ^{13}CO-Tyr-Het-s (218-289) e ^{13}CO-Phe-recBVPrP^{Sc}(109I) para obter información sobre a flexibilidade/rixidez das mostras (vi) adquisición de espectros DARR 13C-13C de U-(^{13}C, ^{15}N)-Phe-recBVPrP^{Sc}(109I) para probar os desprazamentos químicos de cada un dos tres residuos de Phe presentes na mostra.

Para os efectos desta tese, expresamos PrP recombinante de topillo vermello en *E.coli*, sen marcar e tamén marcada, de diferentes xeitos, dependendo do experimento a realizar, e despois sometemos as mostras á PMSA para obter o material infeccioso. O desenvolvemento desta técnica foi clave na procura de dilucidar a estrutura da PrP^{Sc} recombinante, xa que este método permitiu, por primeira vez, a produción de cantidades suficientemente grandes de recBVPrP^{Sc} a partir de PrP^{C}, con taxas de ataque do 100 %, necesarias para as medidas de resonancia magnética nuclear de estado sólido (ssNMR). Ademais, tamén preparamos amiloide PrP non infeccioso marcado e non marcado, mediante un método de nucleación espontánea utilizando condicións desnaturalizantes, por motivos de comparación.

En primeiro lugar, para lograr o obxectivo número un, preparamos o amiloide recBVPrP sen marcar e a recBVPrPSc sen marcar e sometémolos á análise FTIR. Houbo diferenzas nos picos e ombreiros mínimos de ambas estruturas que indican diferenzas na súa estrutura secundaria, o máis probable é que estas diferenzas se deban a diferentes niveis de rixidez das follas β das súas arquitecturas PIRIBS.

Posteriormente, para cumprir o obxectivo número dous, preparamos (U-^{13}C, ^{15}N)-recBVPrP^{Sc}(109I) e sometémolo a experimentos de resonancia magnética nuclear en estado sólido, adquirindo varios tipos de espectros: CP-HSQC, DREAM, DARR, INEPT-HSQC). Aínda que nese momento obtivemos información relevante e nova sobre a estrutura secundaria dalgúns residuos, os datos eran compatibles con ambos modelos, non permitíndonos así acadar o noso obxectivo.

Despois desta pequena decepción, soubemos que ao adquirir espectros de recBVPrP^{Sc}, uniformemente marcada, non seríamos capaces de resolver a estrutura nin distinguir entre os dous modelos propostos. Polo tanto, necesitabamos un tipo diferente de experimento que dese unha resposta "si ou non" á pregunta de se PrP^{Sc} tiña a estrutura dun ou doutro modelo. Afortunadamente, atopamos xusto o que necesitabamos: un experimento chamado PITHIRDS-CT que mide distancias intermoleculares medias ^{13}C-^{13}C e se o resultado é 5 Å significa que a arquitectura da mostra é un PIRIBS, ou polo menos en teoría. Por exemplo, sábese que o amiloide recPrP non infeccioso presenta unha arquitectura PIRIBS, resolta hai dous anos mediante cryo-EM, pero o seu ^{13}CO-^{13}CO PITHIRDS-CT adquirido con ^{13}CO-Phe produciu unha resposta de 5,5 Å. Isto débese a que unha das Phe, Phe141, está situada fóra do núcleo β ríxido, o que a fai máis flexible.

Realizamos experimentos PITHIRDS-CT en amiloide ^{13}CO-Phe PrP, ^{13}CO-Tyr-Het-s (218-289) e ^{13}CO-Phe-recBVPrP^{Sc} (109I), así como amiloide ^{13}CO-Leu PrP, ^{13}CO-Tyr-Het-s (218-289) e ^{13}CO-Leu-recBVPrP^{Sc}(109I) e os resultados que obtivemos foron completamente inesperados. Como dixen, crimus ao longo da miña tese, ata o ano pasado cando se publicou a estrutura da PrP^{Sc} derivada do cerebro, que a estrutura secundaria da PrP^{Sc} era un 4RβS. Non obstante, obtivemos unha distancia intermolecular media de 6,5 Å tanto para ^{13}CO-Phe como para ^{13}CO-Leu-recBVPrP^{Sc}(109I), mentres que obtivemos os resultados esperados de 5,5 Å e moito máis de 7 Å para ^{13}CO-Phe e ^{13}CO-Leu PrP amiloide e para 13CO-Tyr-Het-s, respectivamente.

Despois deste resultado de 6,5 Å, o modelo 4RβS foi descartado porque, de ser así, a distancia intermolecular media debería ser moito maior que 7 Å, como para Het-s, que se sabe que ten unha estrutura secundaria 2RβS. Non obstante, aínda necesitabamos explicar por que non obtivemos a distancia canónica de 5 Å. Unha explicación plausible é que algúns dos residuos Phe e Leu estaban en bucles, como foi o caso dun dos residuos Phe do amiloide BVPrP e tamén de varios residuos do dominio priónico Sup35p.

Polo tanto, para avaliar a flexibilidade da nosa mostra de recBVPrP^{Sc} na escala de tempo dos ms, realizamos experimentos CP-MAS e PARIS con amiloide ^{13}CO-Phe-PrP, ^{13}CO-Tyr-Het-s (218-289) e ^{13}CO-Phe-recBVPrP^{Sc}(109I). Agardabamos que recBVPrPSc fose o máis flexible, pero este non foi o caso, o que indica que os residuos Phe en recBVPrP^{Sc} non son flexibles na escala de tempo ms.

Posteriormente, como aínda críamos que recBVPrP^{Sc} tiña residuos en rexións flexibles, polo que tiña que mostrar flexibilidade nalgunha escala de tempo, realizamos experimentos $T_{1\rho}$ con amiloide ^{13}CO-Phe-PrP, ^{13}CO-Tyr-Het-s (218-289) e ^{13}CO-Phe-recBVPrP^{Sc}(109I) para avaliar a súa flexibilidade na escala de tempo dos microsegundos (us), que é onde se producen os movementos dos bucles. Como era de esperar, estes experimentos deron o resultado de que a recBVPrP^{Sc} ten un decaemento máis rápido na

escala temporal dos us, o que significa que é máis flexible que os demais nesa escala temporal.

Finalmente, dado que queriamos demostrar que algúns residuos de Phe presentan desplazamentos químicos propios de bucles, é dicir, que algúns deles se atopan en bucles, adquirimos os espectros DARR ^{13}C-^{13}C de U-(^{13}C, ^{15}N)-Phe-recBVPrP^{Sc}(109I) para averiguar os desprazamentos químicos de cada un dos tres residuos de Phe presentes na mostra. Esperabamos ver tres sinais, un por cada residuo Phe. Non obstante, obtivemos dous conxuntos de tres sinais, un conxunto característico de bucles e outro de estrutura secundaria de folla β. Dado que descartamos a posibilidade dunha mestura de confórmeros porque a nosa recBVPrP^{Sc} é perfectamente estable a través de múltiples pasaxes de PMSA, chegamos á conclusión de que os residuos de Phe presentan heteroxeneidade microstática na recBVPrP^{Sc}.

En resumo xeramos recBVPrP^{Sc} marcada en cantidades suficientemente grandes como para poder caracterizala extensamente por resonancia magnética nuclear de estado sólido por primeira vez. O resultado máis importante que obtivemos é que recBVPrP^{Sc} presenta unha arquitectura PIRIBS, aínda que é un PIRIBS con bucles máis soltos, é dicir, máis flexible que outros; por exemplo, o amiloide non infeccioso PrP. Esta información está en liña coa estrutura da PrP^{Sc} derivada do cerebro publicada o ano pasado, que é un PIRIBS onde só o 33% de todos os residuos se atopan en follas β canónicas.

LIST OF ABBREVIATURES

BV: Bank vole (*Myodes glareolus*).
CJD: Creutzfeldt-Jakob Disease
CP-HSQC: Cross polarization- Heteronuclear single quantum coherence.
CP-MAS: Cross polarization-Magic angle spinning
Cryo-EM: Cryo-electron microscopy.
CWD: Chronic wasting disease.
Da: Dalton.
DARR: Dipolar assisted rotational resonance.
DNase: deoxyribonuclease.
DREAM: Dipolar recoupling enhanced by amplitude modulation.
Dy: Drowsy strain.
EDTA: Ethylenediaminetetraacetic acid.
EM: Electron microscopy.
ESI-TOF: Electrospray ionization-time of flight mass analyzer.
E. coli: *Escherichia coli.*
FFI: Fatal familial insomnia.
FFT: Fast Fourier transform
FTIR: Fourier-transform infrared spectroscopy.
g: Centrifuge force.
Gdn: Guanidine.
GPI: Glycosylphosphatidylinositol
GSS: Gerstmann-Sträussler-Scheinker disease.
h: Hours
HDX: Hydrogen-deuterium exchange.
HPLC: High-performance liquid chromatography.
Hy: Hyper prion strain.
IPTG: Isopropyl β-d-1-thiogalactopyranoside.
IR-MSP: Infrared microspectroscopy.
MAS: Magic angle spinning.
MALDI-TOF: matrix-assisted laser desorption/ionization-time of flight.
MBM: Meat and bone meal.
MES: 2-(N-morpholino) ethanesulfonic acid.
MeOH: Methanol.
Min: Minutes.
Mo: Mouse.
MQ: Milli-Q water.
MS: Mass spectrometry.
MW: Molecular weight.
Nano-HPLC: Nano-high performance liquid chromatography.
Ni-NTA: Nickel-nitrilotriacetic acid.
NMR: Nuclear magnetic resonance.
OD: Optical density.
PBS: Phosphate-buffered saline.
PIRIBS: Parallel-in-register-intermolecular-β-sheets.
PITHIRDS: Nonacronymic. A ssNMR experiment that allows measurement of distances between 13CO labelled amino acid residues in amyloid samples.
PK: Proteinase K.
PMCA: Protein misfolding cycling amplification.

PMSA: Protein misfolding shaking amplification.
PMSF: Phenylmethylsulfonyl fluoride.
PrP: Prion protein.
PrP^{Sc}: Prion protein, scrapie isoform.
PrP 27-30: Prion protein, scrapie isoform PK treated.
PrP^{C}: Prion protein, cellular isoform.
RecPrP: Recombinant prion protein.
RML: Rocky Mountain Laboratory prion strain.
rpm: Revolutions per minute.
RT-QUiC: Real-time quaking-induced conversion.
s: Seconds.
SAF: Scrapie associated fibers.
SDS-PAGE: Sodium dodecyl sulfate polyacrylamide gel electrophoresis.
ssNMR: Solid state nuclear magnetic resonance.
T: Tesla.
TEM: Transmission electron microscopy.
TFA: Tri-fluoroacetic acid.
Tg: Transgenic.
ThT: Thioflavin-T.
TOCSY: Total correlation spectroscopy.
TRIS: Tris (Hydroxymethyl)aminomethane.
TSE: Transmissible Spongiform Encephalopathy.
4RβS: 4-rung-β-solenoid.

GGGTHNQWNKPSKPKTNMKHVAGAAAAGAVVGGLGGYMLGSAMSR
PMIHFGNDWEDRYYRENMNRYPNQVYYRPVDQYNNQNNFVHDCVNI
TIKQHTVTTTTKGENFTETDVKMMERVVEQMCVTQYQKESQAYYEGRSS

Figure 0.1 BV PrP^{Sc} sequence

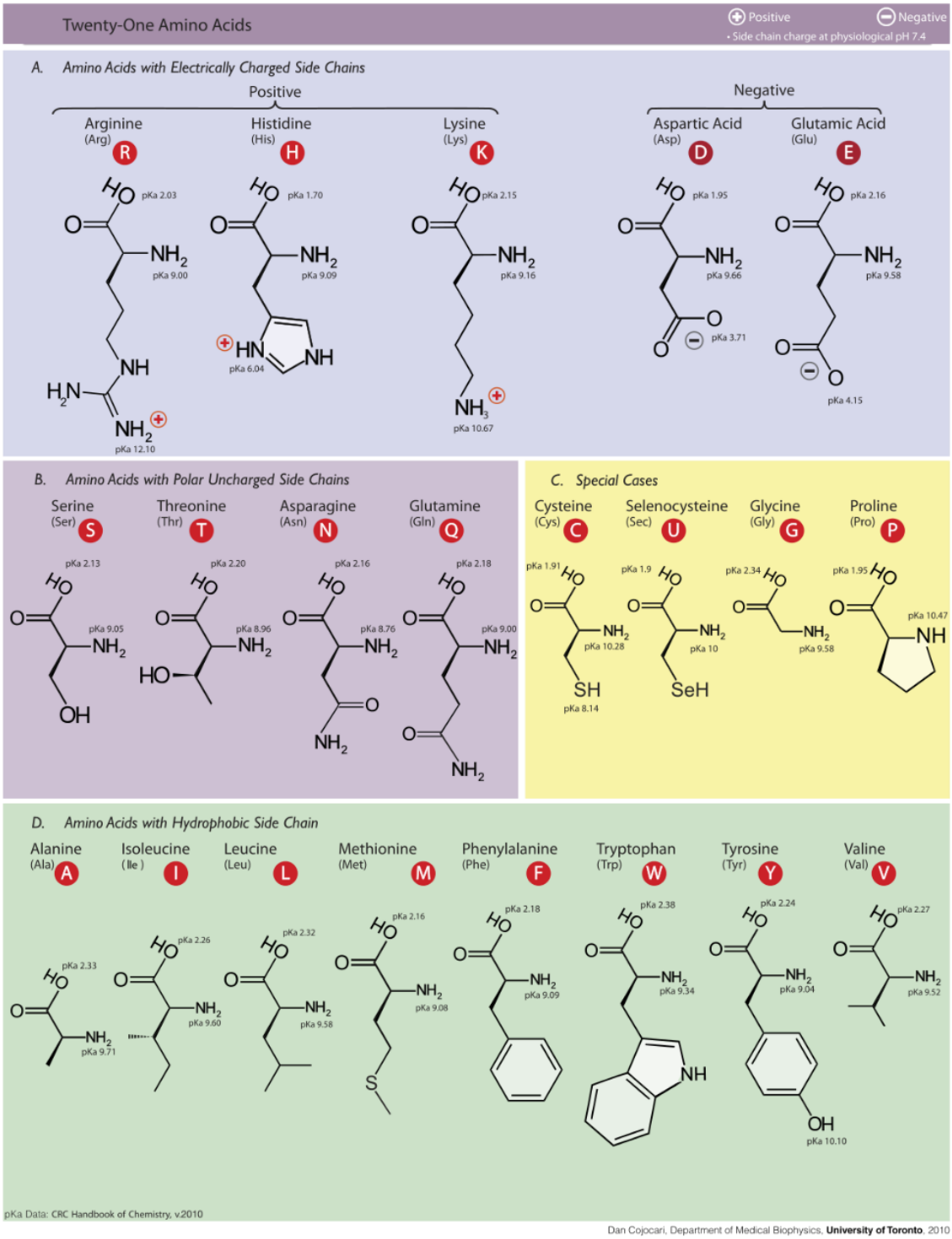

Figure 0.2 Amino acids

GLOSSARY OF NMR TERMS AND CONCEPTS

Adiabatic pulse: a class of amplitude- and frequency-modulated radiofrequency (RF)-pulses that are relatively insensitive to B1 inhomogeneity and frequency offset effects.

Assignment (**resonance assignment**): the process by which the signals in a spectrum are correlated to the NMR-active nuclei that give rise to them.

B_1 field: field perpendicular to the magnetic field which is created by radiofrequency (RF) pulses.

Cross-polarization: technique to transfer nuclear magnetization from different types of nuclei via heteronuclear dipolar interactions.

Cross polarization contact time: time during which the cross-polarization technique is applied.

Chemical shift (δ): the resonance frequency (the characteristic frequency of a nucleus) of NMR signals is most commonly given as chemical shift in units of ppm.

Chemical shift anisotropy (CSA): non-spherical distribution of electron density (e.g. occurring for sp^2 hybridized carbon nuclei) will cause a fluctuating field upon rotation of the nucleus which serves as a efficient source for relaxation (CSA relaxation mechanism).

Correlation time (**τc**)**:** a time constant that is a measure of how fast a molecule tumbles in solution. It depends on the size and the shape of a molecule (and also on many other parameters such as temperature, viscosity …). Small domains (5-10kDa) have correlation times in the range of 4-8ns.

COSY: COrrelation SpectroscopY. The *COSY* experiment correlates two spins that are connected via a single J-coupling.

DARR: Dipolar Assisted Rotational Resonance. Magnetization is transferred from hydrogen to ^{13}C nuclei. From here it is transferred to other ^{13}C nuclei which are close in space.

Decoupling: eliminate fully or partially the effect of coupling between certain nuclei.

Diamagnetic: a substance with only paired electrons.

Direct polarization: it enables selectively polarizing specific moieties or polarizing systems which have low levels of protonation.

DREAM: Dipolar recoupling enhanced by amplitude modulation.

Exchange (intermediate, fast, slow, chemical and conformational): Exchange is a kinetic process between two (or more) states that is characterized by a rate constant. In NMR spectroscopy, exchange is classified into fast, intermediate and slow depending on the size of the rate constant with respect to chemical shift (which is measured in the same units (Hz) as the rate constant). In the fast exchange regime, the rate is much larger than

the difference in chemical shift between the two states and the NMR signal will be at the weighted average position of the two states. In slow exchange, signals for both states are observable and the intensities are proportional to the populations of the two states. In intermediate exchange, the transition between the signals seen for slow and fast exchange takes place, resulting in very broad and often non-observable signals. Conformational exchange occurs when a structural element has more than one possible conformation. Chemical exchange is given when a chemical reaction is taking place, e.g. a ligand binds to the molecule that is measured or protons exchange with the solvent.

Exchangeable proton: A ^{1}H atom of a macromolecule that under mild conditions (neutral pH, ambient temperature and pressure) is replaced by a ^{1}H atom from the solvent (water) after a certain time. The time constant is important, since it is used to classify protons into: a) non-exchangeable: all carbon-bound protons, that do not exchange at all with the solvent even over very long periods (years); b) exchangeable: all OH, SH and NH protons that exchange within seconds or minutes; c) slowly exchanging: protons that are in principle exchangeable, but have much slower rate (hours, days, weeks) than the other protons of the same type. Slowly-exchanging protons are in some way shielded from the solvent, for example HN in hydrogen bonds in secondary structure elements; d) fast-exchanging: OH and SH which exchange so fast with water that their signal is normally not observable.

Evolution period: the pulse sequence element that enables frequency labelling in the indirect dimension

Free induction decay (FID): the observable NMR signal generated by non-equilibrium nuclear spin magnetization precessing about the magnetic field (conventionally along z). This non-equilibrium magnetization can be created generally by applying a pulse of radio-frequency close to the Larmor frequency of the nuclear spins.

Fourier Transform (FT): a mathematical operation that transforms time-domain data (intensities measured at discrete time intervals) into a frequency-domain spectrum and vice versa.

Heteronuclear: between nuclei that are not of the same isotope.

Heteronucleus: a nucleus that is not of the same isotope as another. Very often, it means "other than ^{1}H", i.e. ^{15}N or ^{13}C.

Homonuclear: between nuclei of the same isotope, e.g. ^{1}H-^{1}H or ^{13}C-^{13}C. Very often, it refers to experiments with unlabeled proteins that only deal with 1H.

HSQC: heteronuclear single-quantum correlation. This type of experiment correlates ^{1}H to a heteronucleus, for example to ^{15}N.

INEPT: Insensitive nuclei enhanced by polarization transfer.

Inter-scan relaxation delay or relaxation delay: time between end of sampling of the FID and start of the next experiment.

Isotopic labelling (isotopic enrichment): enrichment of the abundance of a particular isotope in a macromolecule by (bio)synthesis from isotopically enriched precursors, e.g. $^{15}NH_4Cl$, $^{13}C_6$-glucose, heavy water ("D_2O").

J-coupling (scalar coupling): a through-bond interaction between nuclear spins. One manifestation of the J-coupling is the splitting of resonance lines. J-couplings can also be used to transfer magnetization between two coupled spins. J-couplings in proteins are measured either as line-splitting or as peak intensity ratios which depend on the size of the coupling (quantitative J experiment). ^{3}J-couplings (J-couplings over 3 bonds) contain torsion angle information.

Linebroadening: the linewidth of a NMR signal (resonance line) is dependent on T2, the transverse relaxation rate. If T2 is increased, the signals are broader. Since the peak volume (the integral over all points of the signal) stays constant, a broader signal has a lower intensity. This means that very strongly broadened peaks have such a low intensity that they disappear in the noise of the baseline, i.e. they are no longer detectable.

Linewidth: width of a NMR resonance line, measured at half-height.

Lorentzian: a function that is obtained by Fourier transformation of an decaying exponential function.

Mixing time (t_2) : in two-dimensional NMR, time period, that comes after the preparation time, when the sample is excited by one or more pulses after which the signal is recorded.

NMR-active nucleus: a nucleus with spin $I > 0$.

Nuclear Overhauser effect (NOE): transfer of nuclear spin polarization from one population of spin-active nuclei (e.g. ^{1}H, ^{13}C, ^{15}N etc.) to another via cross-relaxation.

Peak: NMR signal. A signal in a 1D NMR spectrum is typically a Lorentzian line. 2D signals are the convolution of two of these lines. Since 2D (and also 3D) NMR experiments are represented as contour plots in a similar manner as topographic maps, a 2D signal has the appearance of a peak.

Pulse sequence: a series of radio frequency pulses applied to the sample, such that the free induction decay is related to the characteristic frequencies of the desired signals

ppm: parts per million, units of chemical shift.

PARIS: Phase Alternated Recoupling Irradiation Schemes

Preparation time (t_1): in two-dimensional NMR, time period, that comes prior to the mixing time, when the sample is excited by one or more pulses and allow to evolve for the first time.

Relaxation: a process by which a system returns to thermal equilibrium.

Relaxation rates (T1, T2): relaxation of magnetization is governed by exponential decay rates. There are two important relaxation rate constants: T1, the longitudinal relaxation

and T2, the transverse relaxation rate. T1 and T2 depend on the correlation time and hence on the size of the molecule, e.g. larger proteins have higher T2 rates. Both T1 and T2 also depend on local dynamics.

Residual dipolar couplings (RDCs): dipolar couplings are a through-space interaction between NMR active nuclei. In solution NMR, these couplings are averaged to zero due to the fast rotation of the molecule. In solid state, they also average out to zero when used the magic angle spinning.

Resonance frequency: the resonance frequency of a NMR-active nucleus is the frequency at which its signal appears in the spectrum.

Resonance line: NMR signal of a 1D (or a 1D trace in a 2D or 3D). A resonance line is characterised by its position in the spectrum (resonance frequency), its height (signal intensity) and its width (linewidth). Cf. Lorentzian.

Restraint (structural R.): structural information of NMR spectra is stored in a format called restraint. A restraint defines a geometric value (a distance between two atoms, an angle between two bonds) with appropriate upper and lower bounds. In a structure calculation, the molecule is forced to fulfil the restraint, i.e. the value of the distance or the angle is restrained to stay within the upper and lower bounds of the restraint.

Recoupling period: time during which spin-spin interactions are reintroduced.

Rotating frame: coordinate frame of reference that rotates with the magnetization vector spinning at a Larmor frequency, in contrast to a reference point in a fixed Cartesian coordinate system

Scalar coupling: the isotropic part (independent on the molecular orientation) of the J coupling.

Spin: quantum-mechanical property of a nucleus. In NMR, only nuclei with spin I>0 are observable. In conventional NMR jargon “spin” often means “NMR active nucleus”.

Spin-lock field: an additional field applied along a transverse axis (x- or y-axis) during a rotating frame NOE experiment.

Spin-lock pulse (t_{SL}): a pulse sequence that allows to keep magnetization in the transverse plane for certain amount of time.

Spin-lock time: time during which spins relax with a $T_{1\rho}$ mechanism.

States-TPPI technique: technique that achieves achieves two effects for a given indirect dimension (say, dimension F1): (1) signal frequency discrimination and (2) displacement of the unmodulated artefact signal from an inconvenient location in the middle of spectrum to the edge.

Spin-system: all nuclei of the same isotope type that are connected via J-couplings. For example, all protons in an aromatic ring belong to a spin system. More importantly, the

amino acid residue constitutes a spin-system for both carbon and proton, because there are no homonuclear J-couplings across the peptide bond.

Structure calculation: a NMR structure calculation combines structural restraints with known geometric information (bond lengths, atom radii, etc.). It is a molecular dynamics simulated annealing calculation that enforces the structural restraints to drive an initial random structure towards a final structure. Usually, a large number of structures (an ensemble) are calculated from different random seeds in parallel, so as to judge how well the restraints define the structure of a molecule.

Time-scale: order of magnitude of time (cf. dynamics).

TOCSY: TOtal Correlation SpectroscopY. The TOCSY experiment transfers magnetization via J-couplings. All nuclei in a spin-system are correlated (hence "total correlation"). For proteins, this means that all nuclei of the same isotope of a residue can be assigned conveniently with TOCSY experiments. TOCSY experiments are used for protein sidechain assignment.

ω_O: Larmor frequency or precession frequency. The frequency of the precessing spins.

ω_r: MAS frequency.

π pulse: a pulse of a longer duration that can flip the net magnetization completely.

INDEX

1. INTRODUCTION

1.1 Prion diseases

A prion was originally defined by Stanley Prusiner as "a small proteinaceous infectious particle which is resistant to inactivation by most procedures that modify nucleic acids" (Prusiner 1982). Although recently, the concept has been expanded to: "prions are composed of host-encoded proteins that adopt alternative conformations, which are self-replicating" (Prusiner 2017). Anyhow, prions are unparalleled infectious proteins that cause a group of fatal neurodegenerative diseases mediated by a completely unique mechanism.

Prion diseases, also known as transmissible spongiform encephalopathies (TSEs) may present as genetic, infectious, or sporadic disorders (see table 1.1), all of which involve refolding of the host prion protein, PrP^{C}, which is a normal constituent of mammalian cells, into its infectious isoform, PrP^{Sc}, through a process which involves its α-helical and coil structure being refolded into β-sheets, with PrP^{Sc} acting as a template for PrP^{C} (Prusiner 1991, Pan et al. 1993); with this structural transition comes deep changes in the physicochemical properties of PrP. The amino acid sequence of PrP^{Sc}, its primary structure, corresponds to that of the PrP^{C} of the mammalian host in which it last replicated. Interestingly, prions do not have a nucleic acid genome like other pathogens, but they do present strain specific properties, thought to be encoded in the tertiary structure of PrP^{Sc} (Bessen et al., Telling et al., Prusiner Science 1997, Prusiner Science 1998).

There are other non-mammalian prions such as the prions of fungi and yeast. *Saccharomyces cerevisiae* is an occasional host to an array of prions, most based on self-propagating, self-templating amyloid filaments of a normally soluble protein. [URE3] is a prion of Ure2p, a regulator of nitrogen catabolism, while [PSI+] is a prion of Sup35p, a subunit of the translation termination factor Sup35p. In contrast to the functional prions, [Het-s] of *Podospora anserina* and [BETA] of yeast, the amyloid-based yeast prions are rare in wild strains, arise sporadically, have an array of prion variants for a single prion protein sequence, have a folded in-register parallel β-sheet amyloid architecture, are detrimental to their hosts, arouse a stress response in the host, and are subject to curing by various host anti-prion systems. These characteristics allow a logical basis for distinction between functional amyloids/prions and prion diseases (Wickner et al.).

Scrapie, a prion disease of sheep and goats, has been known to the scientific community for over 200 years. This condition causes animals to constantly itch ("scraping" against fences with subsequent loss of fleece) and comes with anorexia, emaciation, and subsequent death. Earlier than the 18th century, the agricultural community in Europe knew that scrapie was contagious (Cuillè & Chelle. 1936). Thus, when shepherds identified a member of their flock with signs of the disease, they would isolate it from the healthy animals. Transmission by inoculation was assessed during the first half of the 20th century (Cuillè & Chelle 1936, Cuillè & Chelle 1939). This discovery started the microbiological viewpoint in studies on scrapie, and later on related human diseases, along with a focus on isolating and characterizing the agent that caused the mysterious spongiform degeneration of the brain. Logically, scientists started to look for a nucleic

acid core in the scrapie agent. However, Alper and colleagues demonstrated that the scrapie agent was extremely resistant to inactivation by ultraviolet light and ionizing radiation, estimating its size to be about 90% smaller than the smallest known virus (Alper et al. 1966, Alper et al. 1967, Latarjet et al.), which led to the idea that the scrapie agent did not have a functional nucleic acid (Alper 1967). This proposal was widely rejected until it was ultimately demonstrated to be true by the discovery of prions (Prusiner 1982, Prusiner 1989).

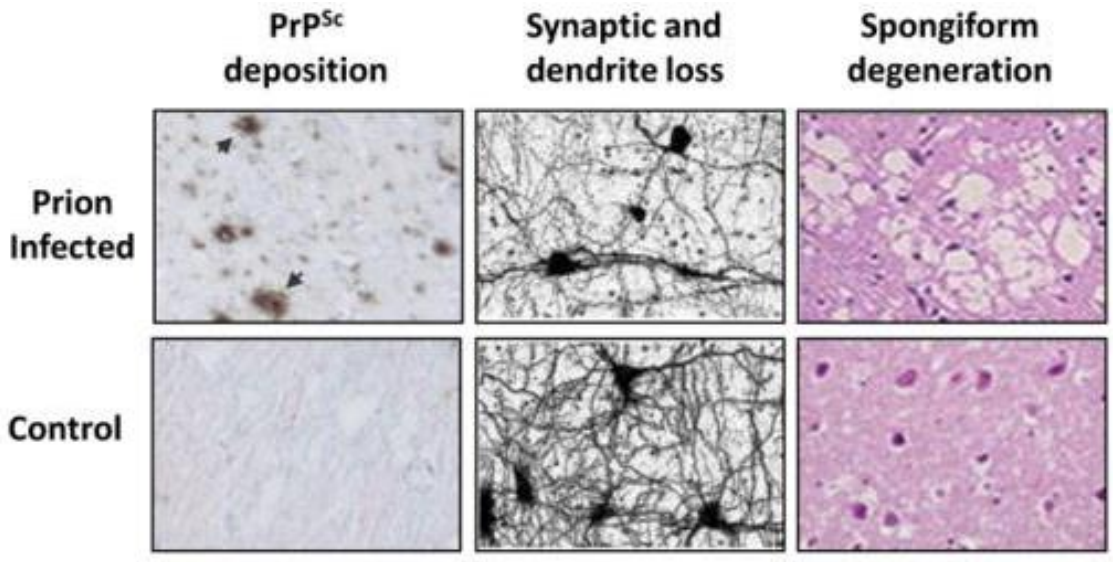

Fig 1.1 Abnormalities observed in the brain of the affected individuals of TSE. Accumulation of PrP^{Sc} deposits was determined by anti-PrP antibodies. Hematoxylin and eosin staining are used to evaluate the vacuolation. Astrogliosis is detected by the use of anti-GFAP antibodies. (Figure adapted from Soto and Satani 2011).

As the quest to identify the scrapie agent was taking place, a novel neurodegenerative disease called kuru was described among the Fore people in Papua New Guinea (Gajdusek and Zigas 1957, Gajdusek and Zigas 1959). The affected individuals presented with headache and joint pain that rapidly progressed to ataxia in 6 to 12 weeks and to death within 12 months. Hadlow, who realized that kuru and scrapie had indistinguishable histopathologies, proposed that both shared an infectious etiology (Hadlow 1959). Similarly, Igor Klatzo made a connection between kuru and Creutzfeldt-Jakob Disease (CJD) due to the fact that the both of them presented brain spongiosis (Klatzo 1959). A few years later, in 1968 the transmission of CJD to chimpanzees after intracerebral inoculation was reported (Gibbs 1968). Gajdusek and coworkers inoculated kuru brain homogenates into the brains of non-human primates that thereafter developed progressive neurological impairment and pathology similar to kuru within three years (Gajdusek 1966). Kuru, which had very long asymptomatic periods as well as scrapie, was attributed to ritualistic cannibalism during funeral rites which were eradicated in 1964 by the Australian government which at the time controlled that territory (Zigas 1990)

Regarding the etiology of scrapie and kuru, as reproducible data began to accumulate indicating that scrapie infectivity was resistant to procedures that alter nucleic acids, but sensitive to those that hydrolyze or modify proteins, a family of hypotheses about the etiology of the scrapie agent emerged, such as the protein only hypothesis (Prusiner 1982). For the first time, the data indicated that a particular macromolecule was required for infectivity and that it was a protein which was named "prion". A few more years were to pass until the scientific community accepted a new class of pathogens without genome that would culminate with Stanley Prusiner receiving The Nobel Prize in Physiology or Medicine in 1997 (Prusiner 1998).

Fig 1.2. Stanley Prusiner during the Prion 2018 conference in Santiago de Compostela and me (Permission granted by Stanley Prusiner).

Prion diseases became widely known due to the "mad cow disease" zoonosis, which is technically referred as bovine spongiform encephalopathy (BSE). There was a widespread outbreak in the United Kingdom in the 80's and 90's, causing ~230 human deaths, due mainly to the feeding of meat and bone meal (MBM), which contains central nervous system tissues and others that are known to host prions, to cattle. (Greenlee et al.)

Human prion diseases (see table 1 below) present a clinical diagnostic problem in themselves because they do not have unique clinical profiles although they are relatively characteristic. Moreover, the initial symptoms, such as unsteadiness, confusion and mood changes are common to other, potentially treatable, neurological disorders, which complicates the differential diagnosis. Another problem lies in distinguishing among different forms of prion disease, especially between sporadic and variant CJD, with the long-term public health and policy implications that it has. Moreover, sporadic CJD itself

has been divided into subtypes which is of importance on clinical diagnosis. Diagnostic tests can be divided into: 1. non-specific supportive tests, such as electroencephalogram, brain magnetic resonance imaging and certain cerebrospinal fluid protein tests (mainly detection of protein 14-3-3) which are usually used combined; and 2. specific tests which consist on the detection of PrP^{Sc} through capture/concentration techniques and protein amplification techniques, such as RT-Quick and PMCA (see point 1.4). (Legname)

Table 1.1 The human forms of prion disease. Adapted from Legname.

Causal group	Human diseases	Notes
Sporadic disease	Sporadic CJD	Found world-wide. Cause unknown but regarded as a spontaneously developing disease in affected individuals. Been divided into subtypes according to clinical phenotype/PRNP-129 genotype/prion protein type.
	Variably Protease Sensitive Prionopathy (VPSPr)	Nosological status a little uncertain. Probably best regarded as a type of sCJD.
Genetic disease	Various phenotypic terms in use: Genetic CJD, Fatal Familial Insomnia, Gerstmann Straussler Scheinker Syndrome.	Caused by underlying PRNP mutations. Many now identified. Autosomal Dominant inheritance.
Acquired disease	Kuru	Confined to Papua New Guinea. Related to mourning ritualistic cannibalism.
	Iatrogenic CJD	Accidental human-to-human transmission by surgery or certain medical treatments (use of cadaveric-derived dura mater and human pituitary hormones).
	Variant CJD	Originally caused by BSE contamination of diet; some secondary transmission via blood/blood products. Most cases in UK and France.

Regarding animal prion diseases, BSE and scrapie have already been discussed, although there are others described and in particular there is one that has been gaining importance for the last few years which is chronic wasting disease (CWD) of the Cervidae family, for its rapid and unstoppable spread throughout the U.S. and Canada.

CWD is highly infectious and contagious and efficiently transmitted among cervids by both direct and environmental contacts (Houston et al.). An important difference with BSE is that CWD prions (PrP^{CWD}) are distributed throughout the body of the sick animal, including the peripheral and central nervous system, muscles, antler velvet and blood (Daus et al. 2012). PrP^{CWD} is also shed in saliva, feces and urine (Houston et al., Sakudo et al.) and can persist in the environment for many years thus the risk to all animal species within the ecosystem increases. With BSE, banning MBM and the specific risk material was enough to reduces cases (Gough et al., Osterholm et al.); however, PrP^{CWD} are shed

in high numbers by migrating animals which makes its management harder. Attempts to control the spread of CWD include non-selective culling of the animals in endemic areas, regulations on the number of animals to be raised in a farm, guidance on carcass handling, mandatory testing of hunter harvested animals, feed bans, and prohibitions in importing cervids (Uehlinger et al.). Despite these measures, CWD incidence continues to rise (Fig. 1.3). In 2016, CWD was diagnosed for the first time in Europe, in reindeer and European moose. Both were diagnosed in Norway, and, subsequently, more cases were detected in a semi-isolated wild reindeer population in the Nordfjella area, in which the first case was identified. This population was culled, and all reindeer (approximately 2400) were tested for CWD; 18 positive animals, in addition to the first diagnosed case, were found (Tranulis et. al).

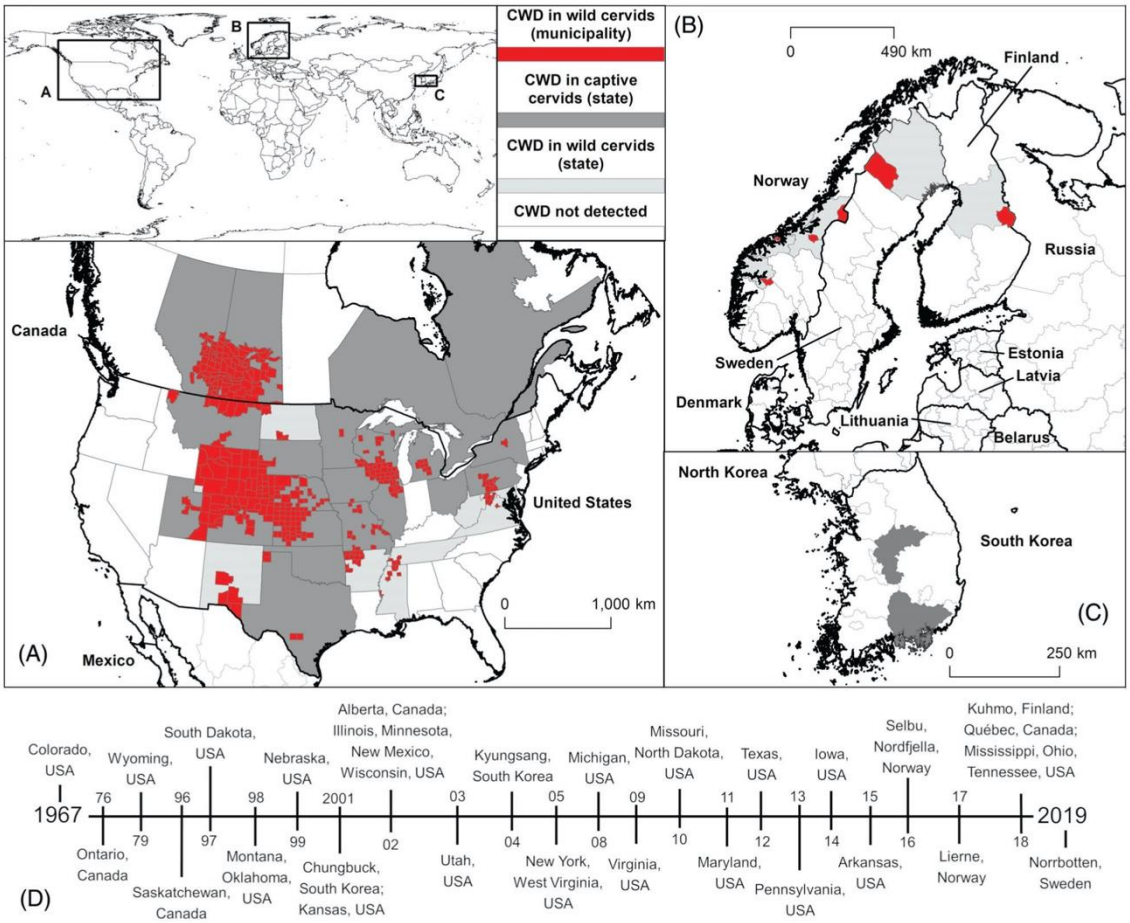

Fig 1.3. Geographic distribution of Chronic Wasting Disease (CWD) reports. (A) The region with the most cases and areas infected with CWD is North America; (B) Europe has reported CWD in Norway, Sweden, and Finland; (C) Asia reported CWD in South Korea. Red: counties (in USA) and wildlife management areas (in Canada) with reports of CWD in wild cervids; dark grey: states/provinces reporting CWD in captive cervids; light grey: states with CWD detection in wild cervids; white: areas with no reports of CWD; (D) Timeline denoting the first detections of CWD in specified regions for each country. Data derived from CDC (2019) and CWD Alliance (2019).

Currently, there is no cure or treatment available for prion diseases, although there are some compounds which are effective *in vivo* and *in vitro* (Zattoni et al.) The targets of anti-prion therapeutics are mainly PrP^{Sc}, being this the infectious agent, and PrP^{C}, with the idea of halting prion replication. However, recent approaches are focused on different targets thought to be involved in prion pathogenesis mechanism (see figure 1.4 below) (Zattoni et al.).

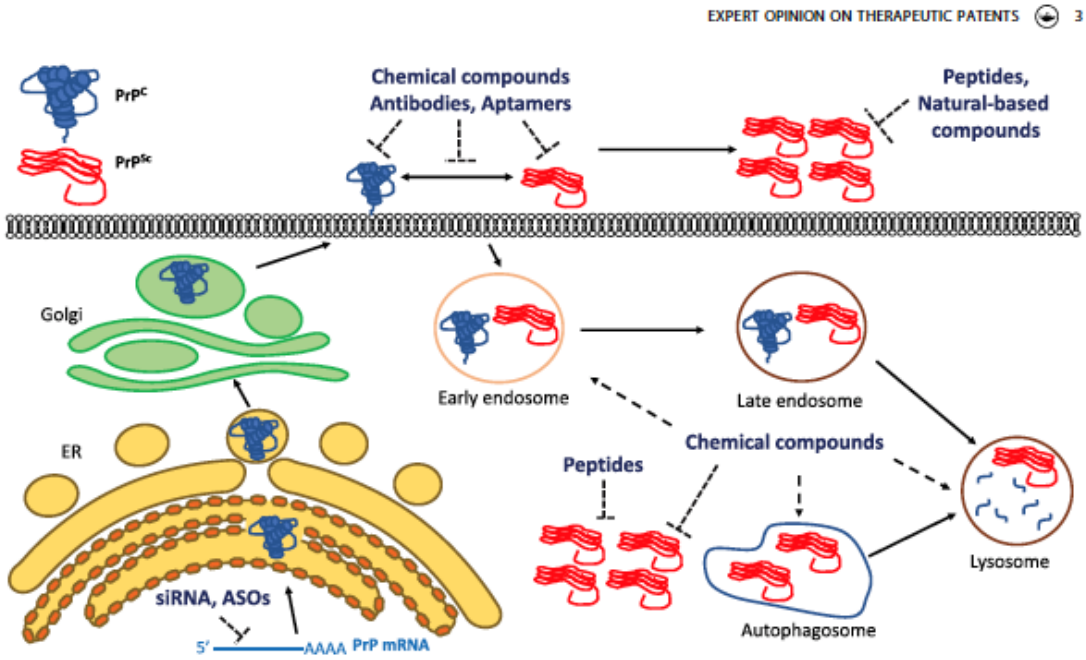

Fig 1.4 Schematic representation of prion conversion mechanism and anti-prion therapeutic strategies. Adapted from Zattoni et al (Permission granted personally by the autor).

1.2 The prion protein, cellular isoform (PrP^{C})

The PRNP gene was discovered and cloned at the end of the 80's, proving that both PrP^{C} and PrP^{Sc} are encoded in the same gene (Basker et al.), which is a single copy gene and its open reading frame is located in one exon in all mammal species studied.

PrP^{C} has a single polypeptide chain of approximately 254 amino acids (aa), depending on the species. It has an amino-terminal signal peptide and in the N-terminal region there are five copies of an octarepeat PHGGGWGQ (residues 51-90, in mouse sequence). There is a single disulphide bond between cysteines 178 and 213 and two N-glycosylation sites at asparagines 180 and 196 (mouse numbering). Furthermore, in the residue 231 it has a hydrophobic carboxy-terminal domain to be attached to the cell membrane by a glycosylphosphatidylinositol (GPI) anchor. PrP polypeptide is post-translationally processed, being shortened to 209 residues (numbered 23-231) removing the 22 aa of the signal peptide and 23 C-terminal aa that are replaced by a GPI anchor (Stahl et al.). Once it is detached from the cell membrane, it is water soluble and protease K (PK)-sensitive, unlike PrP^{Sc}, and circular dichroism (CD) spectroscopy indicates a high content of α-helix (Caughey et al., Pan et al.)

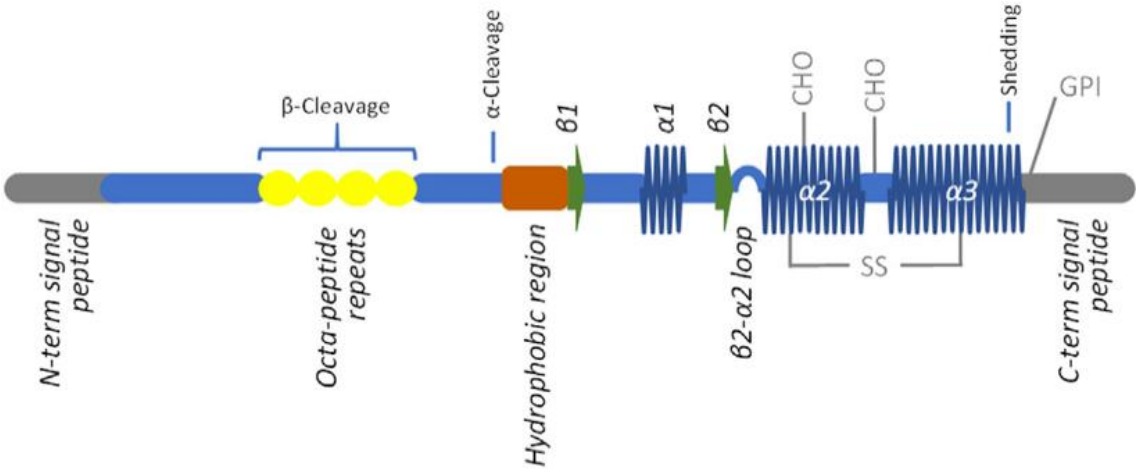

Fig 1.5. NMR structure of mouse PrP23-231. Secondary structure elements, and sites of glycosylation and GPI attachment are indicated. Adapted from Gill et al. 2018.

The elucidation of the PrP^C structure was possible because of the improvements in the expression of recombinant PrP, in sufficient amount to permit NMR studies. The first determination of the structure was in mouse recombinant PrP comprising the residues 121-231, NMR showed that MoPrP(121-231) is a globular region that contains three α-helices and two-stranded antiparallel β-sheet (Riek et al. 1996). Subsequently, this study was completed characterizing the full-length mouse prion protein, MoPrP(23-231) and it was determined that the N-terminal region 23-120 is flexible and disordered (Riek et al. 1997).

The function of PrP^C has been of interest for a long time since its disruption may play a key role in prion disease pathogenesis (Leighton and Allison, 2016; Allison et al., 2017). However, knockout of PrP^C expression in mice produced animals that were normal and did not appear to suffer from detrimental phenotypes in the CNS or elsewhere (Bueler et al., 1992; Manson et al., 1994). However, in 2010 it was proved that axonal prion protein is required for peripheral myelin maintenance (Bremer 2010). Moreover, a more detailed study of knockout mice, PrP^C-null goats and PrP^C expressing and non-expressing cell lines allowed for the identification of a range of phenotypes and potential functions for the protein (Castle and Gill, 2017); at the same time, molecular studies produced a large and varied putative interactome of PrP^C (Rutishauser et al. 2009). Over time, the deluge of functions of this protein has grown, some of which are outlined on figure 1.6

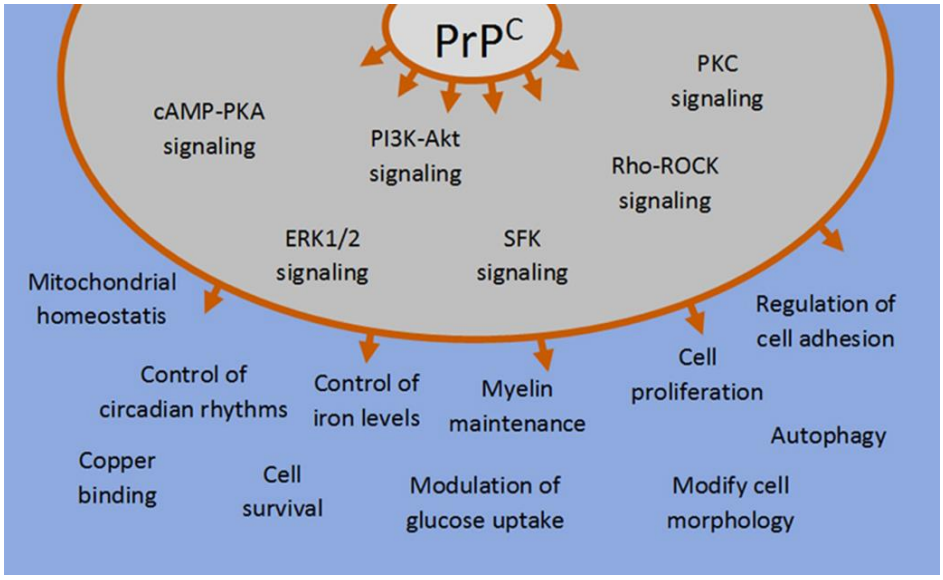

Fig 1.6. Putative functions of the prion protein. PrP^C has been postulated to impact directly or indirectly a range of signaling pathways. Through these biochemical pathways, or others, PrP^C expression causes various downstream measurable effects, including, but not limited to, those shown on the figure. Adapted from Castle and Gill 2017 (Open access).

1.2.1 PrP amyloid

PrP^C has a high tendency to forming amyloids *in vitro* which is dependent on the reaction conditions. Ideal reaction conditions for fibril formation combine neutral or slightly acidic pH (between 5.0 and 7.5) and moderate concentrations of denaturants such as guanidine hydrochloride (up to 2 M) or urea (up to 4 M). (Makarava 2012). A structural characteristic shared by all amyloid fibrils is the cross-β-fold, an architecture featuring a ladder of stacked β-strands aligned perpendicularly to the fibril axis. The resulting β-sheet displays the typical repeating length of 4.8 Å, corresponding to the hydrogen bond distance between paired amide and carbonyl groups in the backbone of adjacent strands (Sunde et. al). These strands can be additionally stabilized by the presence of characteristic interactions, such as steric-zippers and asparagine (or glutamine) ladders. Steric zippers are tight interfaces of interdigitated hydrophobic side-chains that are established between amino acids located in laterally-interacting β-strands (Sawaya et. al). Instead, asparagine (or glutamine) ladders consist in a repetitive pattern of hydrogen bonds between the sidechain groups of residues located in vertically-interacting β-strands (Wiegand et. al). Amyloid fibrils have been shown to consist of one or more protofilaments. In the case of multiple protofilaments assemblies, the resulting fibrils have morphologies ranging from twisted-rope structures to flat tapes (Smith et. al.)

The amyloid state of a protein is intrinsically misfolded and so is inherently prone to interact inappropriately within the crowded and complex environment of a living system, thereby generating toxicity. Many proteins are prone to forming amyloids whose deposits are involved in different clinical conditions named amyloidosis such as Alzheimer's disease (amyloid β), Parkinson's disease (tau) and Huntington's disease (huntingtin) (Dobson 2017). Moreover, the involvement of only a handful of proteins in amyloid diseases has commonly been thought to be associated with some particular conformational character of the protein sequences involved.

However, compelling evidence has accumulated that the ability to form amyloid is not a peculiarity of this small group of proteins. A clue came, fortuitously, from an NMR study of the SH3 module of PI3 kinase, which has no connection with any known disease. At low pH, where the protein is at least partially unfolded, the solution turned into a viscous gel after several hours. When this gel was examined by electron microscopy and other techniques it was found to contain well-defined fibrils with all the characteristics of those associated with the amyloid diseases.

Formation of similar fibrils has also been observed when a domain of fibronectin was heated to temperatures above that required for unfolding as well as this has also been reported for an increasing range of other proteins and fragments of proteins (Dobson 1999). In 1999, a study by Dobson's group proved right the hypothesis that amyloid could be a common state of all proteins, by designing solution conditions to see if fibrils could be deliberately formed from a soluble protein not associated with any disease. The selected method was to add trifluoroethanol – a solvent known to denature proteins but, unlike traditional denaturants such as urea, one that generates partially unfolded states where hydrogen bonds between peptide groups are still stable. After several days under the chosen conditions, the protein involved, acylphosphatase, duly formed amyloid fibrils with all the characteristics of those associated with disease. Therefore, it was concluded that any protein can convert to amyloid form under the right conditions of temperature, pH and denaturants (Chiti 1999).

In order to prove the protein only hypothesis, Baskakov and colleagues used recombinant full-length PrP (rPrP) to form amyloid fibrils *in vitro* in absence of PrP^{Sc}-template. This amyloid showed remarkable stability towards temperature-induced denaturation which analysis of FTIR spectra revealed that it was due to its β-sheets. Prolonged treatment with PK caused only minor conformational perturbations in the β-sheet-rich core and did not destroy the fibrillar assembly (Bocharova 2005a). In 2007, PrP amyloid was used in structural studies and it was concluded that it had a core of residues 160-220 and that and these residues formed single-molecule layers that stack on top of one another with parallel, in-register alignment of β-strands (Cobb 2007). Moreover, PrP amyloid was found to be non-infectious *in vivo,* only producing disease after two serial passages (Makarava 2011) and as judged by FTIR spectroscopy and X-ray diffraction analysis, the PrP folding pattern within amyloid fibrils produced in the absence of co-factors was fundamentally different from that of brain-derived PrP^{Sc} (Wille et. al 2009, Ostapchenko 2010). Moreover, using the sPMCA format (see section 1.5) that detects single PrP^{Sc} particles (González-Montalban et al.) the preparations of rPrP amyloid fibrils were found to be PrP^{Sc} free (Makarava et al. 2011). In 2020 the atomic structure of PrP amyloid fibers was solved by cryo-EM: each fibril is composed of two protofibrils intertwined in a left-handed helix and arranged in a staggered manner; the fibrils are morphologically homogeneous, showing a fibril core diameter or ~14 nm and width of ~25 nm (Wang et al. 2020). A comparison between PrP^{C} and amyloid PrP fibers can be seen on fig 1.7.

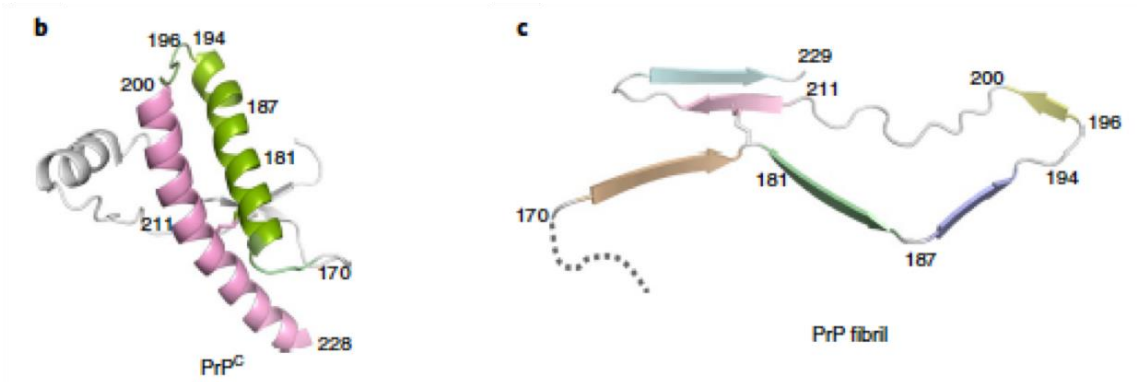

Fig 1.7. Comparison of the structures of PrP^C and PrP fibrils. (A) Ribbon representation of the structure of the C-terminal domain (residues 125–228) of PrP^C with a disulfide bridge linking α2 and α3 (B) Ribbon representation of the structure of a PrP fibril core containing one molecular layer and one subunit with a single disulfide bond. Adapted from Wang et al 2020.

1.3 The prion protein, scrapie isoform (PrP^{Sc})

PrP^{Sc} is the pathologic isoform of PrP^C which causes prion diseases. It was very complicated to elucidate its structure which was not done until 2021, since it forms insoluble aggregates that resist the solubilization in nondenaturing detergents hampering the gathering of suitable preparations from brains of infected animals for high-resolution techniques like NMR spectroscopy and X-ray crystallography. Furthermore, PrP^{Sc} has high heterogeneity derived from the GPI anchor and the carbohydrates contained in its C-terminal region, which make very difficult the interpretation of data; the rising of recombinant prions (see section 1.4) is being very helpful in this regard. It is very important to remember that PrP^{Sc} is PK resistant, unlike PrP^C which is not.

There are distinct strains of prions which are defined by differences in a heritable phenotype under controlled experimental transmission conditions. Prion strains can differ in incubation period, clinical signs of disease, tissue tropism, and host range. The prevailing hypothesis for this phenomenon is that prion strain diversity is encoded by different conformations of PrP^{Sc}, although some cofactors have been identified *in vitro* that may also contribute to prion strain diversity. (Bartz 2016).

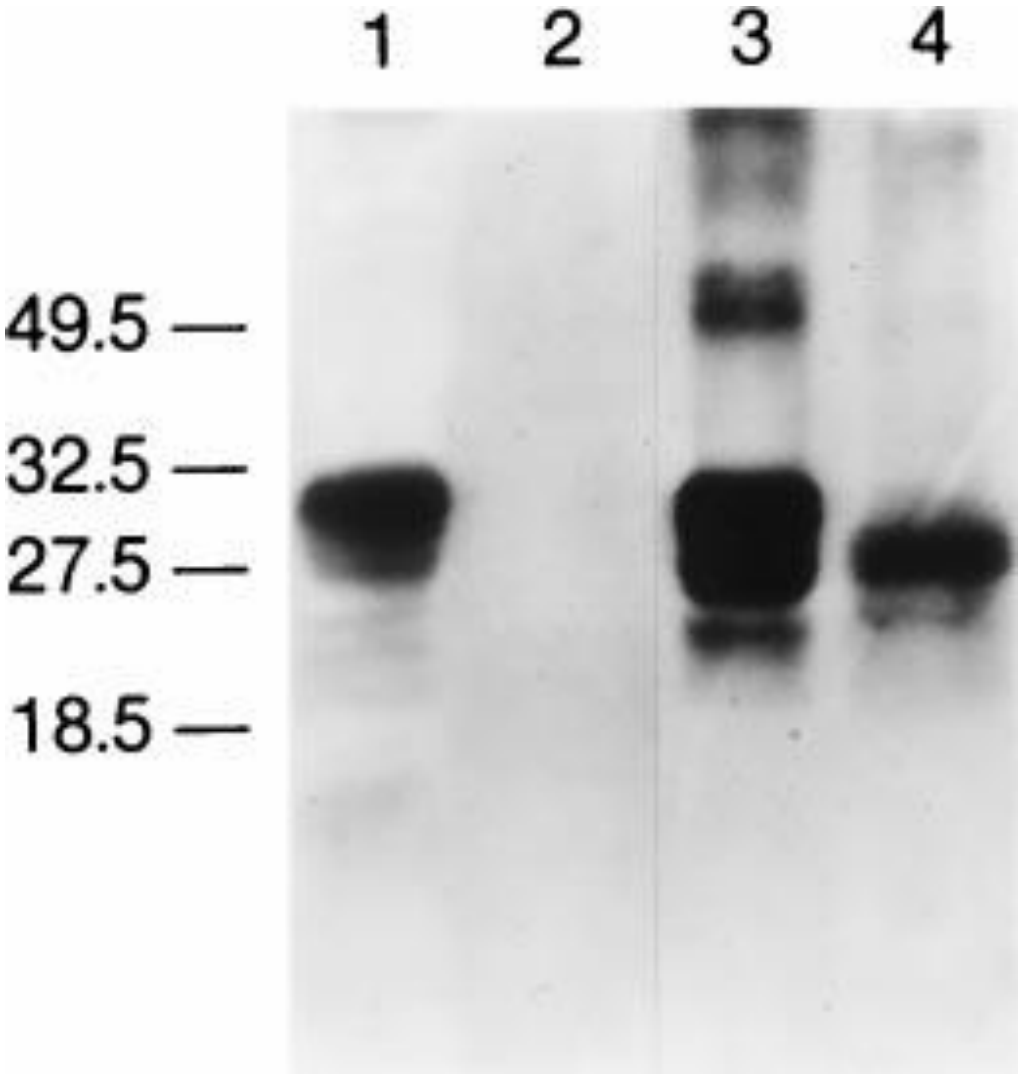

Fig 1.8. Immunoblotting of the Syriam Hamstar brain homogenates from uninfected (lanes 1-2) and prion infected (lanes 3-4). Lanes 2 and 4 show the migration of the product from the digestion with 50µg/ml of PK. Lanes 1 and 3 were used as proteolytic digestion control. While the western blot of the hamster infected with prions showed a band PK resistant around 27-30 KDa, no bands were observed in the western blotting from uninfected hamster. The decrease on the Molecular Weight observed in lane 4 indicated that around 67 amino acids were digested form the NH2-teminus of the PrP^{Sc} to generate the PrP27-30. Adapted from Prusiner 1998 (Open access).

In contrast to PrP^{Sc}, the structures of the fungal prion Het-s was early solved by ssNMR in 2008 (Wasmer et al.) being shown to contain a β-helical structure, being a 2-rung-β-solenoid.

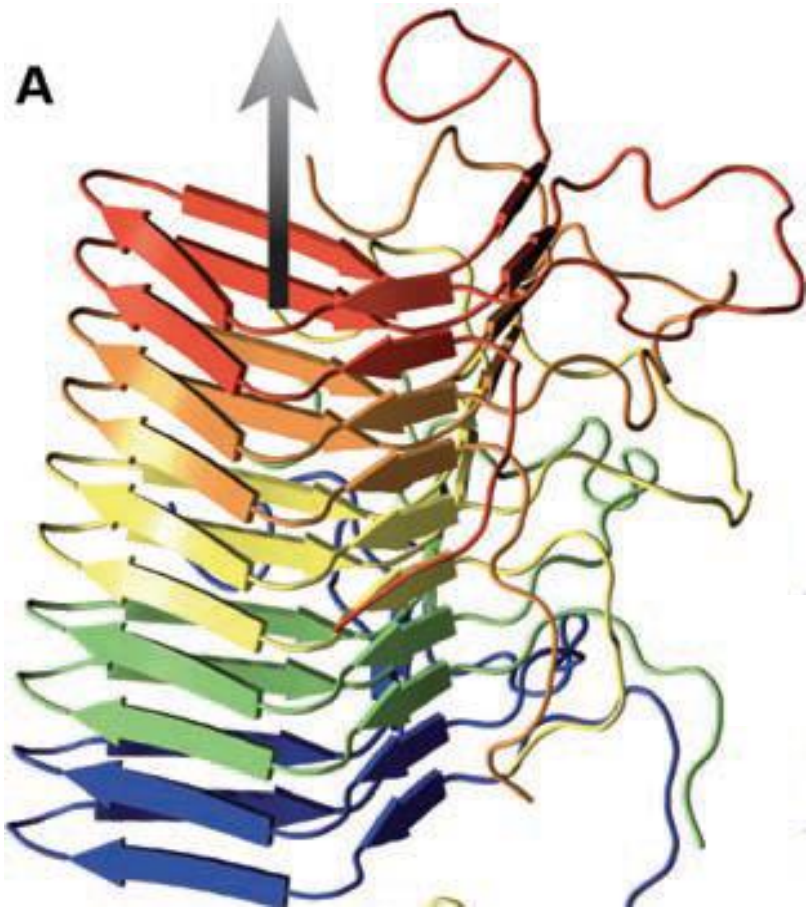

Fig 1.9. Structure of the HET-s(218-289) fibrils. The fibril axis is indicated by an arrow. Side view of the five central molecules of the lowest energy structure of the HET-s(218–289) heptamer calculated from the NMR restraints. Adapted from Wasmer 2008 (Open access).

The structure of PrP^{Sc} was still unknown at the beginning of my PhD, but there were many constrains available obtained through different techniques which I will describe consequently:

1.3.1 Electron microscopy (EM)

Electron microscopy is a technique for obtaining high resolution images of biological and non-biological specimens. The high resolution of EM images results from the use of electrons (which have very short wavelengths) as the source of illuminating radiation.

Indeed, the first observation of PrP^{Sc} fibrils was obtained by negative stain EM forty years ago by Merz, which showed abnormal fibrillary structures, designated "scrapie-associated fibrils" (SAF), in subfractions of brains from scrapie-affected animals. They concluded that SAF consisted either of two or four filaments and that they bared a resemblance to amyloid (Merz 1981). A couple of years later, Prusiner also observed such structures and called them “rods” measuring 10 to 20 nm in diameter and 100 to 200 nm in length. He also performed birefringence studies with Congo red proving that PrP^{Sc} fibrils are amyloids (Prusiner 1983). However, the amount of structural information that could be gathered was greatly limited by the highly aggregated nature of the protein.

Later on, Sim and colleagues’ observations provided measurements of scrapie-associated fibrils, revealing variations that differentiate the strains and provide constraints for improved structural modeling. Since heavy surface glycosylation may obscure visualization of prion fibrillar cores, severely under-glycosylated prion protein fibrils from scrapie infected transgenic mice expressing anchorless prion protein were purified along with wild type fibers. They used different strains: ME7, 22L and RML, which displayed overlapping fibril morphologies, providing evidence that prion fibril morphology is influenced, but not dictated, by strain-dependent differences in protofilament structure. Dimensions and morphological information about prion protein core protofilaments which variably intertwined to form scrapie fibrils were obtained. These fibers extended around 100-150 nm in length and were apparently formed by two intertwined protofilaments with a width of around 4-5 nm per protofilament. Occasional isolated protofilaments were observed, suggesting that the lateral association of protofilaments is neither essential nor invariant in prion protein polymerization (Sim et.al).

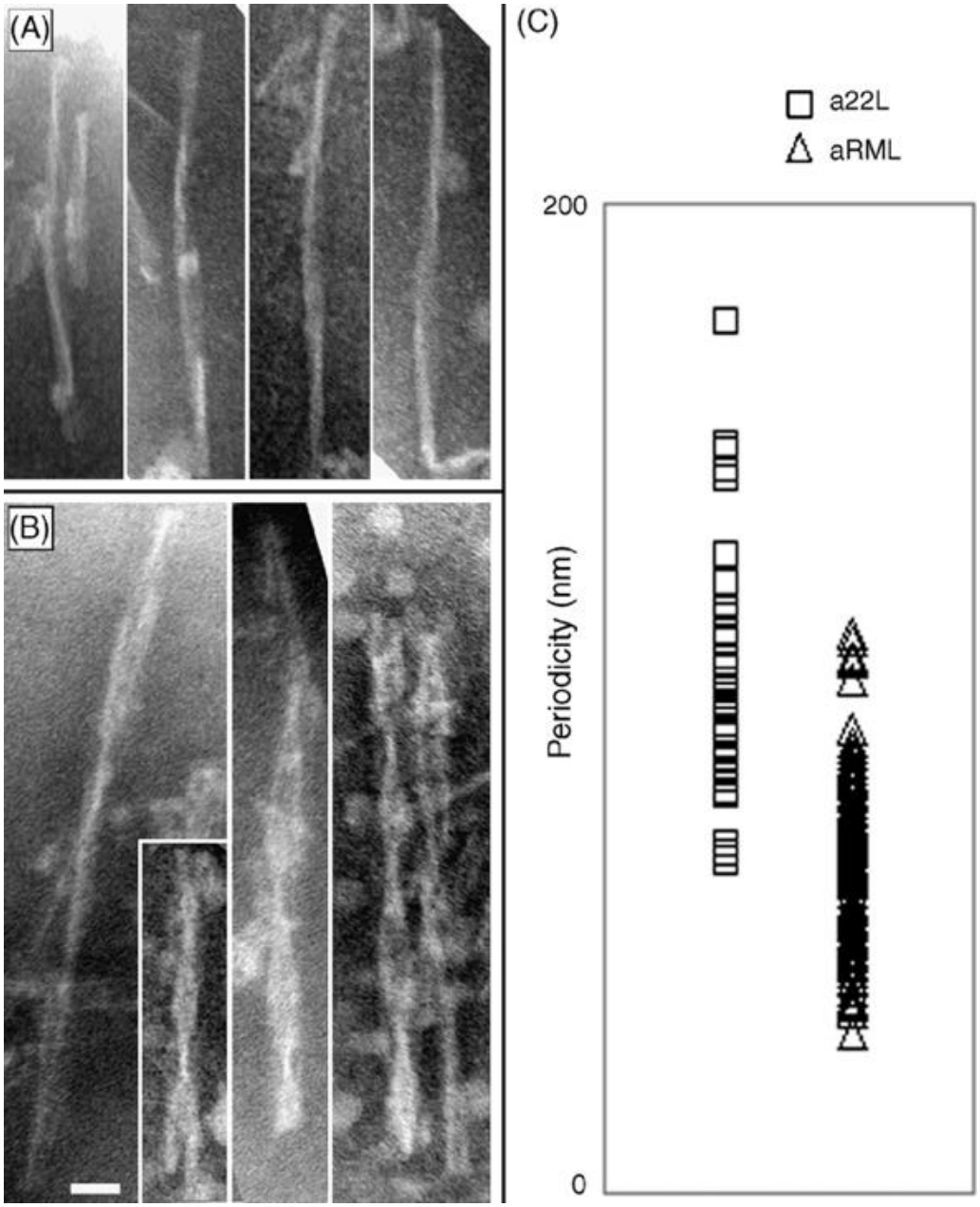

Fig 1.10. Periodicities of twists in anchorless 22L and RML fibrils. (A) Long anchorless 22L fibrils with multiple twists and (B) long anchorless RML fibrils with multiple twists. Direct magnification 100,000×. All panels were stained with methylamine tungstate. The scale bars are 20 nm. (C) Range of periodicities. Anchorless 22L (a22L) fibrils averaged 106 nm per half-turn, anchorless RML (aRML) fibrils 64 nm, $p < 0.001$. Adapted from Sim et al (Open access).

1.3.2 FTIR

FTIR is a non-invasive, label-free spectroscopic technique which uses infrared radiation to probe the secondary structure of proteins due to the absorption of its polar bonds, mainly the amide one.

FTIR studies were among the first to be carried out given that they can be applied to an insoluble, disordered sample. They showed that the conversion of PrP^{Sc} from PrP^{C} is associated with a loss of α-helix and a large increase of β-sheets in the secondary structure (Pan et al.; Caughey et al. 91; Baron et al. 2011). Specifically, data from PrP^{C}, PrP^{Sc}, and PrP 27-30 showed the proportions presented in the table 1.2.

Table 1.2. Secondary structure percentage determination from FTIR

Content of secondary structure, %			
Structure	PrP^{C}	PrP^{Sc}	PrP 27-30
α-helix	42	30	14
ß-sheet	3	43	48
Turn	32	11	34
Coil	23	16	4

However, in 2011, it was proved that there is no presence of α-helix in PrP^{Sc} by Smirnovas et al. when it was shown that the 1660 cm^{-1} band, region that covers different wavelengths, in the FTIR spectra of PrP^{Sc} and PrP27-30 which had been attributed to α-helices, based on calibration using globular proteins, is also present in the spectrum of recombinant PrP amyloid fibers which exhibit exclusively a parallel-in-register-intermolecular-β-sheet architecture (Smirnovas et al. 2011). Furthermore, the ~1660 cm^{-1} FTIR band overlaps with bands in the same region arising from turns and coils. Therefore, it was concluded that a misinterpretation had been made and that PrP^{Sc} had about 50% of β-sheet content and 50% of turns and coils (Wille & Requena 2018). Moreover, infrared (IR) spectroscopy studies have indicated strain-dependent differences in β-sheet content of PrP^{Sc} meaning that the strain phenomenon is encoded in its conformation (Baron et al.; Caughey 98) and it was observed that the glycans and the GPI anchor do not affect the secondary structure of PrP^{Sc} of a specific strain.

1.3.3 Electron crystallography

Electron crystallography is similar to X-ray crystallography in that a protein crystal scatters a beam to produce a diffraction pattern. However, the interactions between the electrons in the beam and the crystal are much stronger than those between the X-ray photons and the crystal. This means that meaningful amounts of data can be collected from much smaller crystals.

One PrP construct containing only 106 residues, PrP106 (Δ23–88, Δ141–176), supported the propagation of prions. Transgenic mice expressing only PrP106 developed a histologically accurate neurodegenerative prion disease after inoculation with prions, and the resulting prions could be serially passaged (Wille et al. 2002).

Then two-dimensional (2D) crystals of PrP 27-30 were found among the purified fibers (see Fig. 1.11). During the purification of PrP 27-30 most of the protein polymerized into "prion rods" which are typical amyloid polymers that revealed little structural detail. The final step of this purification procedure used a sucrose gradient purification and in some fractions there were both prion rods and 2D crystals, with an apparent hexagonal lattice (a and b = 69 Å; $\gamma = 120^{\circ}$, as determined by electron diffraction). Immunogold labelling with anti-PrP mAbs stablished that PrP is an integral part of such crystals and later on it was proved that they had high titers of infectivity. The 2D crystals could be visualized in EM with negative stains such as uranyl acetate. The dark areas in the center of the current 2D crystal subunits were caused by a complexation of uranyl ions or other heavy metal cations to negative charges within the crystal lattice, effecting a positive stain. The sequence of PrP 27-30 contains several negatively charged residues that may contribute to the observed complexation of heavy metal cations; the highest concentration of these residues lies between amino acids 143 and 177.

In order to obtain images suitable for digital processing, electron micrographs of the 2D crystals were taking at 200-300 nm of underfocus. However, the images were of bad quality and were processed with correlation methods that are used routinely for single-particle reconstructions. The amplitude R factors and phase residuals for a 2D crystal processed for the relevant plane groups indicate a p3 plane group as the most likely symmetry. Thus, p3 symmetry during crystallographic averaging was applied. Because rotational cross-correlation demonstrated six distinct densities within each subunit it was presupposed either a trimer of dimers arrangement for the unit cell with a noncrystallographic dimer axis or a trimeric arrangement, in which each subunit had two centers of density. The trimeric arrangement would give the unit cell a polarity that should be noticeable within the crystals and could result in a polar filament assembly. As neither of these features was observed, authors favored the trimer of dimers interpretation.

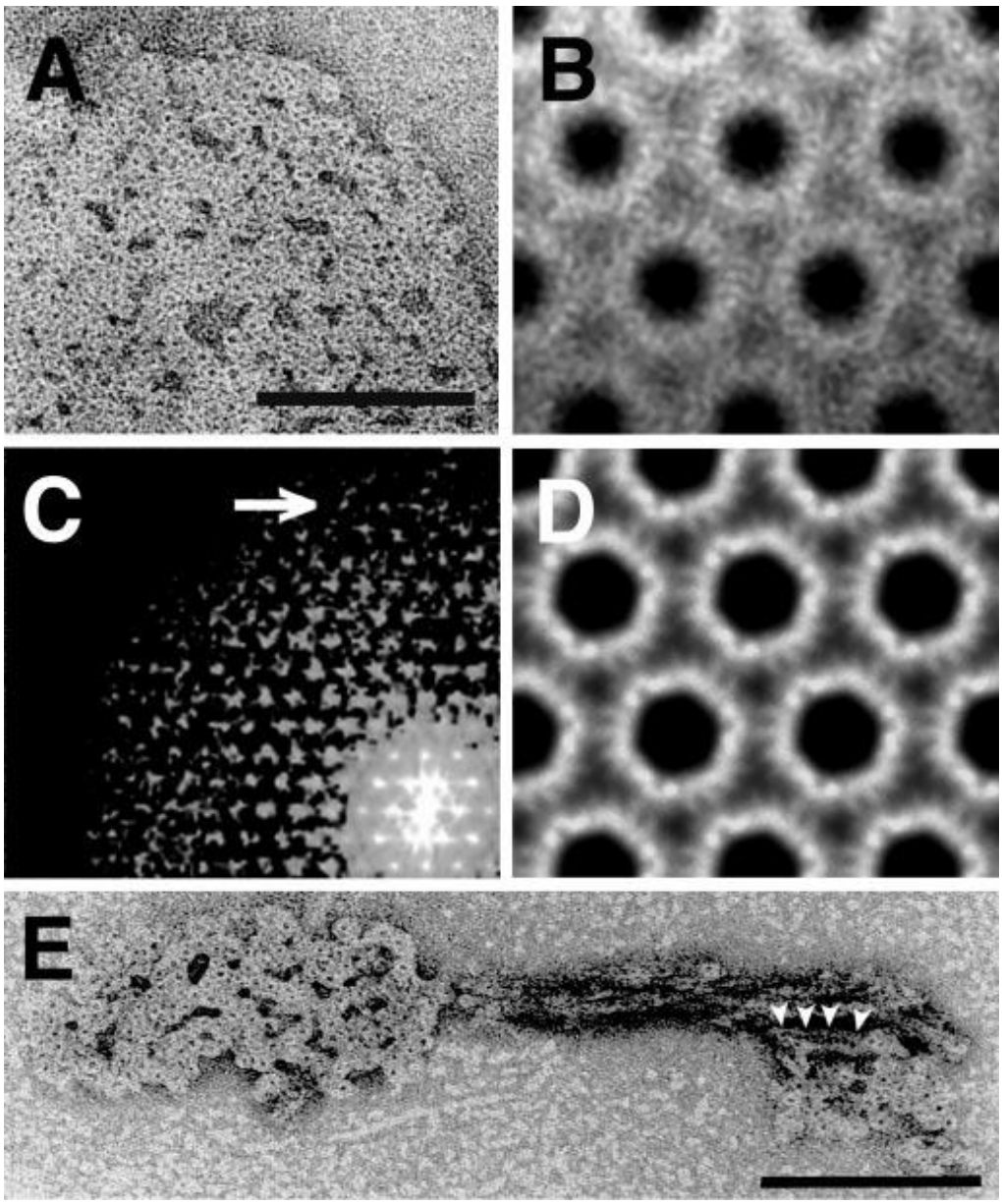

Fig 1.11. 2D crystals of PrP 27-30. (A) A 2D crystal of PrP 27-30 stained with 2% uranyl acetate showing an apparent hexagonal lattice. (B) High power view of a crystal after CTF correction and several rounds of correlation-mapping and averaging. (C) Section of a power spectrum after averaging showing spots out to the 11th order, corresponding to ~7 Å (arrow). (D) Crystallographic averaging further improved the amount of detail visible. A p3 plane group was used. (E) Typical prion rod with an aggregate of ''crystal'' subunits at each end. Some protofilaments reveal rows of dense stain accumulations, suggesting stacked subunits (arrowheads). [Bars = 100 nm.] Adapted from Wille 2002 (Open access).

To localize the N-linked sugars of PrP 27-30, the oligosaccharides were specifically labeled by 1.4 nm gold particles, which did not affect prion infectivity. The high contrast of uranyl acetate staining made it difficult to visualize the small label. The image processing on labeled crystals revealed some differences, but the procedure required additional refinements to detect the somewhat nonperiodic labels. Because the crystallographic averaging used p3 symmetry, the image processing procedure may have systematically underestimated the number of locations for the gold label by a factor of 2. The subtraction map did indeed show some weak differences at the second three-fold axis. By subtracting 3 times the value of the standard error map, statistically significant differences were obtained that when overlaid onto the average of an unlabeled crystal, showed the sugar side chains located toward the outside of the oligomers. This peripheral localization provides a constraint on the orientation of the protein molecules within the crystal lattice.

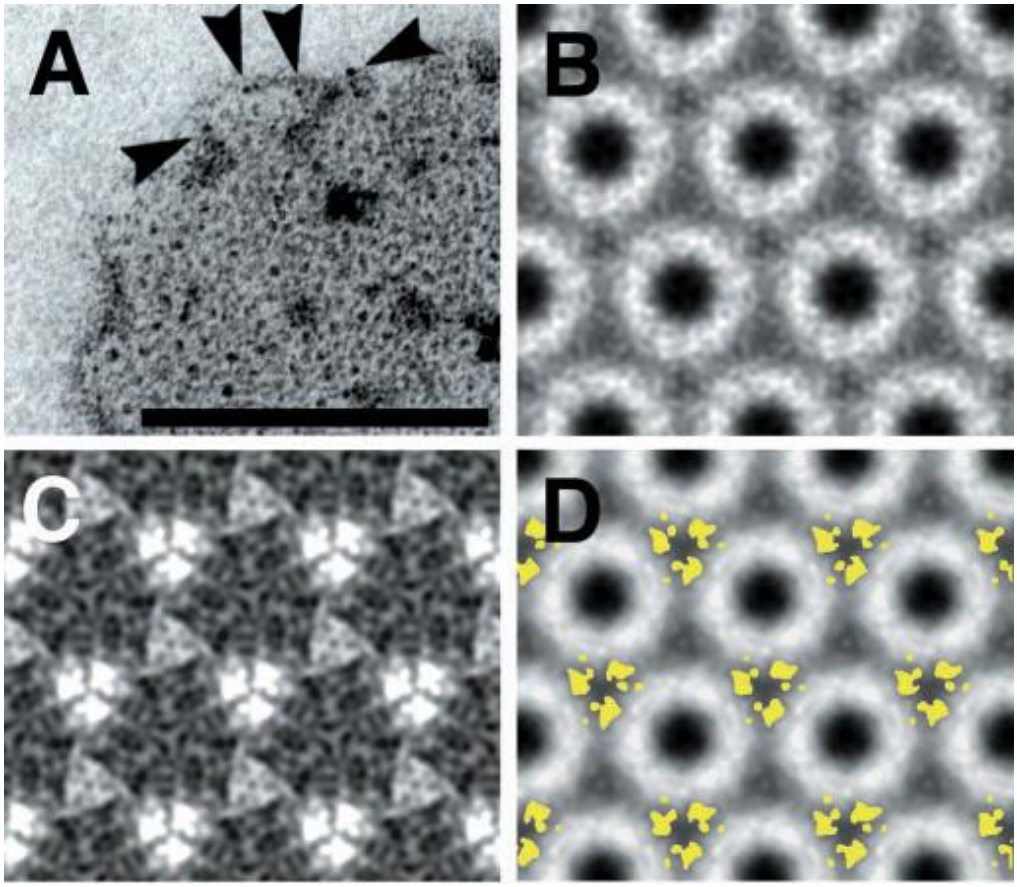

Fig 1.12 Nanogold labeling of the N-linked sugars. (A) Uranyl acetate-stained 2D crystal of Nanogold-labeled PrP 27-30. The high contrast of the uranyl stain obscures some of the labels, but others are clearly visible (arrowheads). [Bar 100 nm.] (B) Image processing result of a labeled crystal after correlation mapping and averaging followed by crystallographic averaging. (C) Subtraction map between labeled and unlabeled crystals showing major differences in lighter shades. (D) Overlay of the statistically significant differences calculated from C in yellow onto a projection map of PrP 27-30. Adapted from Wille et al. 2002 (Open access).

While analyzing preparations of $PrP^{Sc}106$ miniprions by negative stain EM both rod-like polymers and 2D crystals isomorphous to those seen with PrP 27-30 were observed. This finding enabled the researchers to use the same image processing strategies used for the PrP 27-30 crystals and map the differences between PrP 27-30 and $PrP^{Sc}106$.

$PrP^{Sc}106$ lacks residues 141–176 but it is consistently diglycosylated. By comparison, PrP 27-30 has a longer peptide chain and it is a mix of un-, mono-, and diglycosylated forms. As these crystals display a complex mixture of negative and positive staining, it is important to consider the staining behavior of the different constructs. $PrP^{Sc}106$ lacks many of the negatively charged residues that are present in PrP 27-30 and hence binds fewer uranyl cations at the center of the subunits. Therefore, subtracting the PrP 27-30 density from the $PrP^{Sc}106$ density should highlight residues 141–176 in positive density, whereas subtracting $PrP^{Sc}106$ from PrP 27-30 should place the extra glycosylation sites in positive density.

As expected, PrP 27-30 minus $PrP^{Sc}106$ showed differences that were nearly identical to the location of the sugars determined by Nanogold labeling. Here the difference signal for the N-linked sugars was found in all three-fold symmetry axes around the oligomer. $PrP^{Sc}106$ minus PrP 27-30 revealed differences around the center of each oligomer, which were interpreted as being representative of the amino acids in the internal deletion of PrP106 (141–176).

The authors concluded that PrP^{Sc} is formed by a parallel β-helix, since such structure would be the only one to fit to the hexagonal lattice dimensions. The resolution of this technique is about 2 nm, which is just the diameter of the proposed β-helix. Therefore, it was not possible to provide any detail of higher resolution, just that their architecture might correspond to a solenoid.

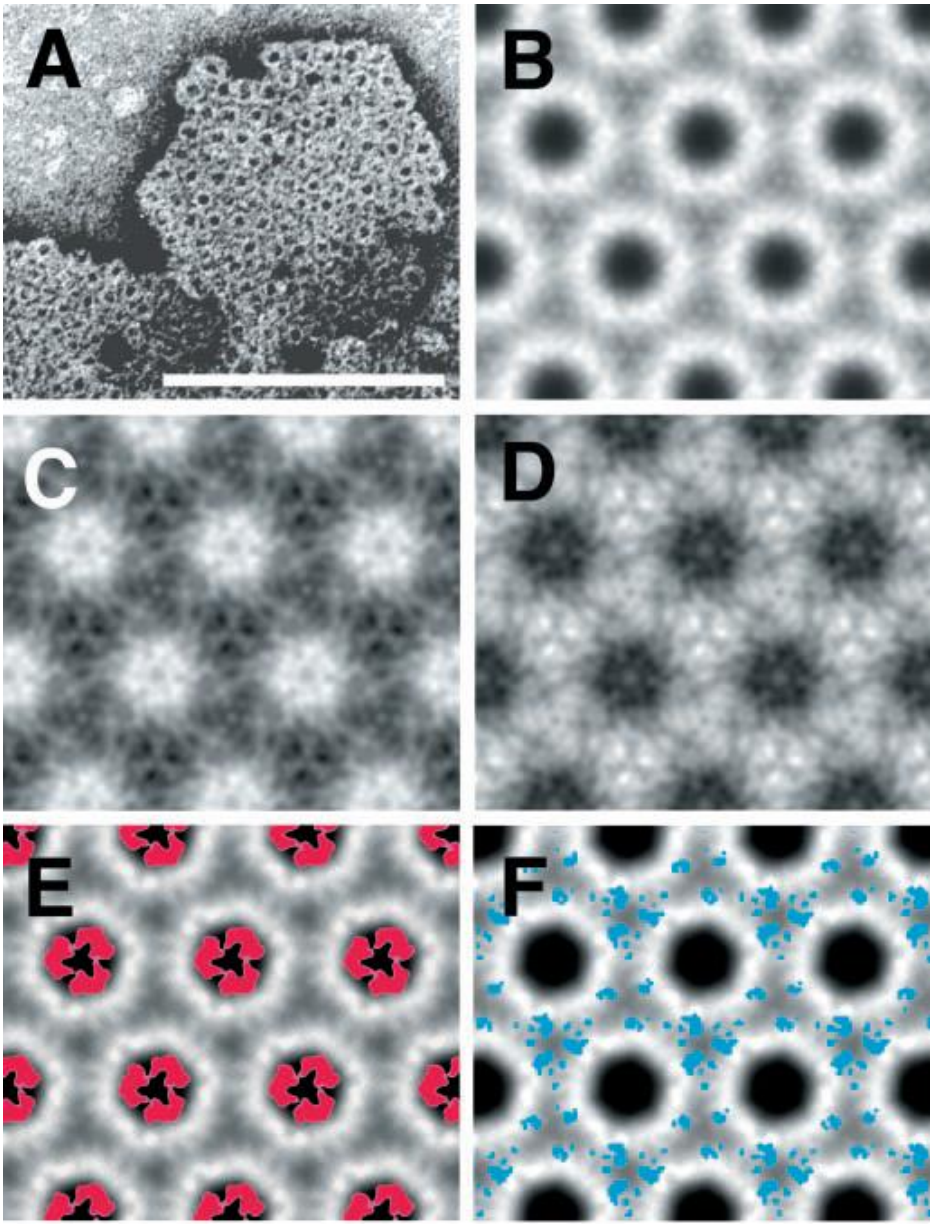

Fig 1.13 2D crystals of PrP^{Sc}106. (A) A2Dcrystal of PrP^{Sc}106 stained with uranyl acetate. [Bar 100 nm.] (B) Image processing result after correlation-mapping and averaging followed by crystallographic averaging. (C and D) Subtraction maps between the averages of PrP 27-30 (Fig. 1D) and PrP^{Sc}106 (B). (C) PrP^{Sc}106 minus PrP 27-30 and (D) PrP 27-30 minus PrP^{Sc}106, showing major differences in lighter shades. (E and F) The statistically significant differences between PrP 27-30 and PrP^{Sc}106 calculated from C and D in red and blue, respectively, overlaid onto the crystallographic average of PrP 27-30 (Fig. 1D). Adapted from Wille et al. 2002 (Open access).

The authors proposed models of the structure of PrP^{Sc} based on their 2D crystals data and also taking into account the EM, antibody-biding and FTIR information. However, in 2003 it was still believed due to a misinterpretation of the FTIR data that PrP^{Sc} had α-helices thus now we know that all their models are wrong. Although for the sake of historical recollection I will present them.

PrP^{Sc} was modelled as a parallel β-helical fold, placing the wrongly believed structurally conserved C-terminal α-helices and the glycosylation sites (N181 and N197) on the periphery of the oligomer and with the highly flexible N-linked sugars pointing above and below the plane of the oligomer. The deletion of 36 residues in PrP106 correlates favorably with exactly two turns of an average left-handed-β-helix. Therefore, the orientation of the α- and β-helices, the sugars, as well as the fold of the oligomeric face, could be retained in this deletion mutant.

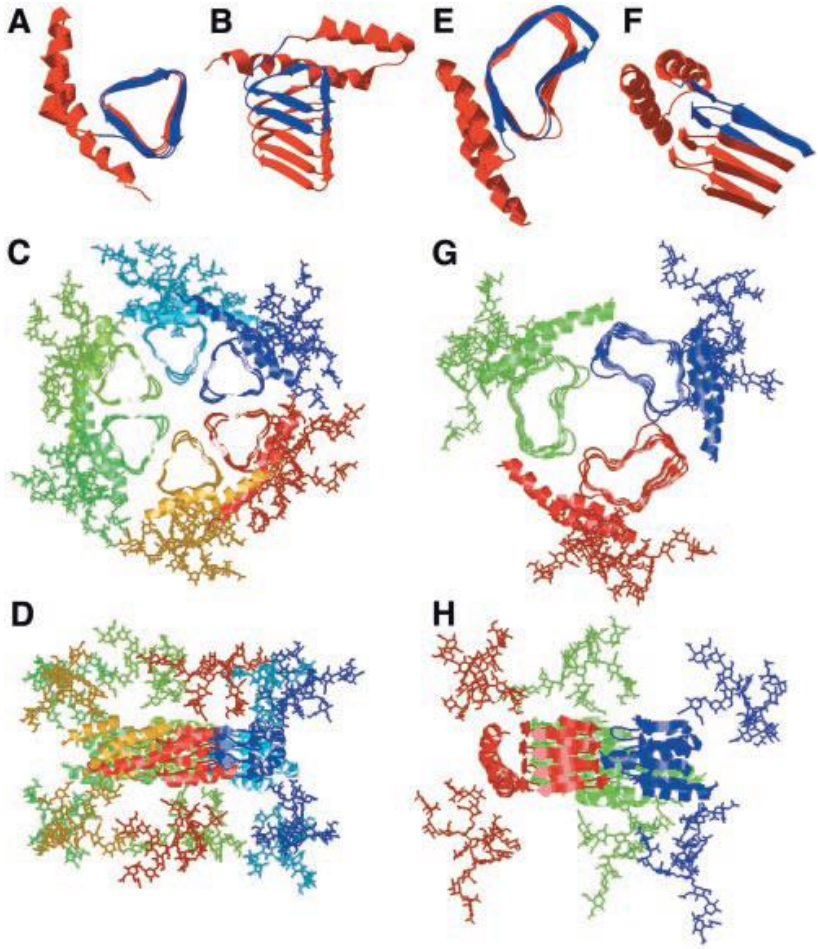

Fig **1.14 ß-Helical models of PrP 27-30. (A and B) Top and side views, respectively, of PrP 27-30 modeled with a left-handed ß-helix.** The ß-helical portion of the model is based on the Methanosarcina thermophila -carbonic anhydrase structure. (C and D) Top and side views, respectively, of the trimer of dimer model of PrP 27-30 with left-handed ß-helices. (E and F) Top and side views, respectively, of PrP 27-30 modeled with a right-handed ß-helix. The ß-helical portion of the model is based on the most regular helical turns of Bordetella pertussis P.69 pertactin. (G and H) Top and side views, respectively, of the trimer model of PrP 27-30 with right-handed -helices. The structure of the α-helices was derived from the solution structure of recombinant hamster PrP. In the single-molecule images (A, B, E, and F), residues 141–176 that are deleted in PrP106 are colored blue. Adapted from Wille et al. 2002 (Open access).

In 2004 Wille and Govaerts proposed a refined model based on more 2D crystals data which was a trimer formed by β-sheets and α-helices. From a study of 119 proteins of kwnown structure that featured β-folds observed in globular proteins they determined that, if PrP^{Sc} followed a known protein fold, it adopted either a β-sandwich or parallel β-helical architecture.

Since at the time there was already increasing evidence arguing for a parallel β-sheet organization in amyloids, they contended that the sequence of PrP was compatible with a parallel left-handed β-helical fold. Left-handed β-helices readily form trimers, providing a natural template for a trimeric model of PrP^{Sc}. This trimeric model accommodates the PrP sequence from residues 89–175 in a β-helical conformation with the C terminus (residues 176–227), retaining the disulfide-linked β-helical conformation observed in the normal cellular isoform.

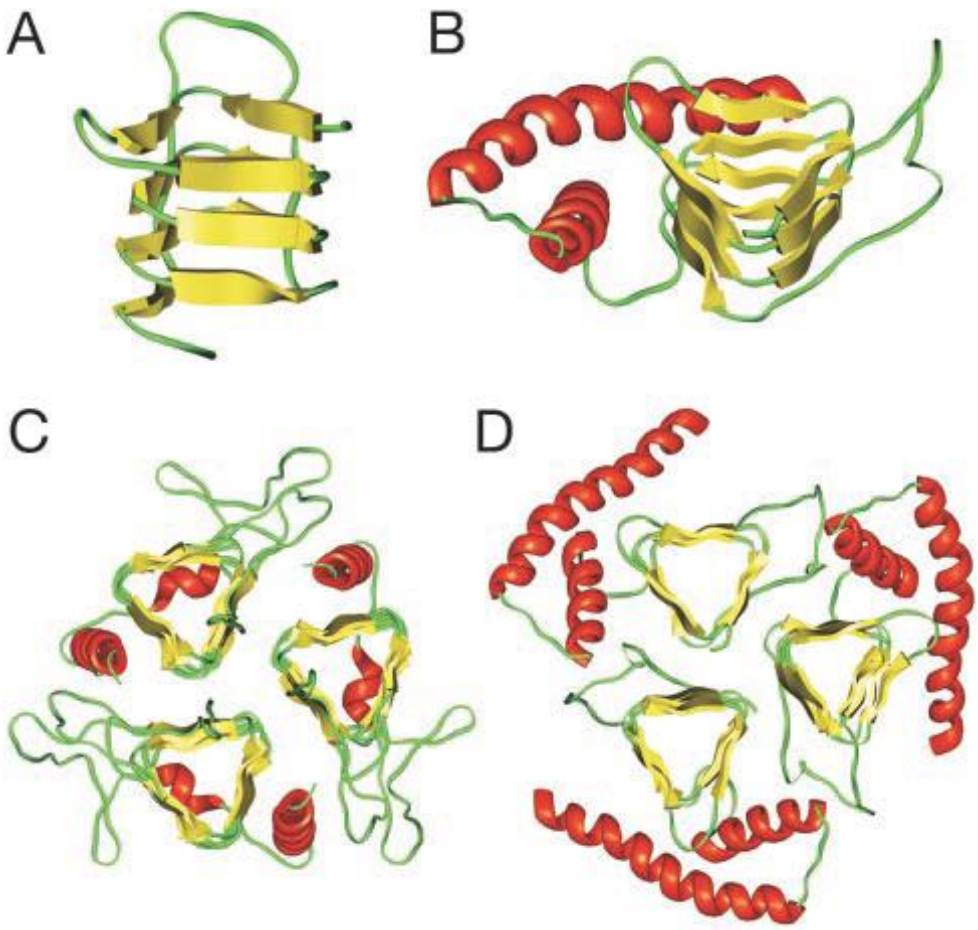

Fig 1.15 Modeling PrP residues 89-174 onto a left-handed ß-helical fold. (A) The β-helical model of the N-terminal part of PrP 27–30. (B) Model of the monomer of PrP 27–30. The α -helical region (residues 177–227) as determined by NMR spectroscopy (PDB ID code 1QM0) was linked to the β-helical model shown in A. (C) The crystal structure of the trimeric carbonic anhydrase from *Methanosarcina thermophila* (PDB ID code 1THJ). (D) Trimeric model of PrP 27–30 built by superimposing three monomeric models onto the coordinates of the C 's of the 1THJ structure. Adapted from Govaerts et al. 2004 (Open access).

1.3.4 Fiber X-Ray diffraction

Fiber X-ray diffraction is a phenomenon in which the atoms of a crystal, by virtue of their uniform spacing, cause an interference pattern of the waves present in an incident beam of X rays; the atomic planes of the crystal act on the X rays in exactly the same manner as does a uniformly ruled grating on a beam of light.

The fiber formation property of PrP^{Sc} makes possible to determine additional information about the three-dimensional structure of PrP27-30 molecule by fiber X-ray diffraction technique. The earliest studies with X-ray fiber diffraction on the structure of PrP^{Sc} confirmed the amyloid nature of the prion rods (Nguyen 1995). The meridional diffraction at 4,8 Å indicates the typical cross-β structure corresponding with the distance between β-sheet in which the hydrogen bonds run parallel to the fiber axis.

In 2009, Wille et al prepared fibers of $MoPrP^{Sc}$ purified from the brains of mice inoculated with RML prions using PTA precipitation, which is a selective method for the precipitation of PrP^{Sc} since at neutral pH and in the presence of Mg^{+2} PTA forms complexes with oligomers of PrP^{Sc} and PrP 27-30 but no with PrP^{C} (Safar 1998). In this procedure, small amounts of Sarkosyl (0.2%) from the purification procedure remain in the samples. The Sarkosyl concentration in the fibers after drying was considerably higher; it is likely to be 10–20 times the initial concentration.

Diffraction patterns from these samples included numerous intensities attributable to lipids or lipid-detergent assemblies; all of the MoPrP 27–30(RML) patterns included one or two series of strong, relatively sharp, crystalline equatorial intensities corresponding to spacings of about 40 Å. The spacings, relatively high orders, and sharpness of these intensities are characteristic of diffraction from lipid or lipid-detergent assemblies; reflections similar to these were seen in patterns from uninfected mouse brain controls, and even from high concentrations of pure Sarkosyl, although with much less orientation.

The MoPrP 27–30(RML) patterns contained at least 11 meridional intensity maxima which could be classified into three groups, ‘‘l’’ ‘‘u’’ and ‘‘p’’. Group ‘‘l,’’ showed relatively sharp maxima at resolutions close to 4.1 Å and 8.2 Å which most probably came from lipid or lipid-detergent assemblies, reflecting the spacing between hydrocarbon chains. Group ‘‘u’’had a pair of relatively sharp intensities at 7.7 Å and 7.4 Å that seemed to be protein contaminats from other organs. Group ‘‘p,’’ in contrast, could be interpreted in terms of protein structure. This group contains three maxima: very weak, broad cross-diffraction at 4.8 Å and moderately broad arcs at 9.6 Å and 6.4 Å. These maxima correspond to the second, third, and fourth orders of a 19.2 Å vertical repeat, meaning half, one third and one fourth of the 19.2 Å vertical repeat whose absence can be accounted for by disorder in the filament. 19.2 Å happens to be the size of a four-stranded ß-sheet whose presence would be consistent with the amyloid properties of the fibers and their high ß-sheet content. The weakness of the 4.8 Å diffraction may reflect irregularity in the spacing of the four strands.

Further, it was found that recPrP amyloid differed from highly infectious PrP^{Sc} fibers from infected brains. They also presented a strong equatorial intensity (approximately 10.5 Å) very typical of an amyloid structure, showing the existence of flat, parallel stacks of β-strands separated by this distance. Such equatorial reflection is absent in PrP^{Sc} preparations. This difference suggests that PrP^{Sc} from brain-derived prions could have a cross β-structure different from the classic amyloid β-conformation.

Although these data support the presence of a four-strand β-structure they are unable to determine whether that structure consists of an isolated sheet, stacked sheets, β-helices or any other form of ß-structure. The authors stated that Govaerts's model was compatible with this diffraction data but that other alternative models could not be ruled out (Wille et al 2009).

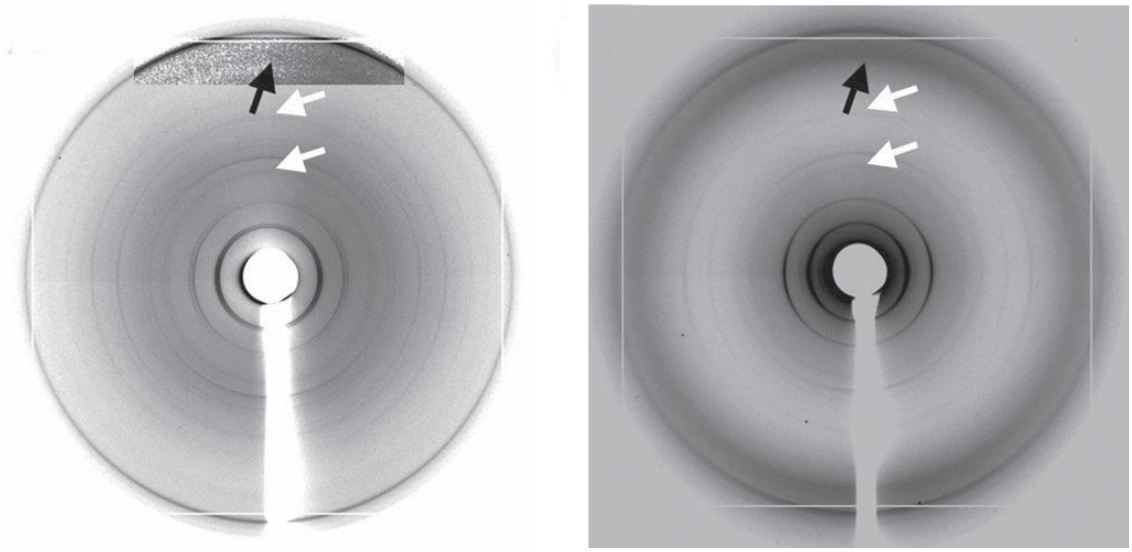

Fig 1.16. Fiber diffraction patterns from PTA-precipitated MoPrP amyloids. Black arrows indicate cross-meridional diffraction at close to 4.8 Å resolution. White arrows indicate second and third orders of meridional 19.2 Å diffraction. (A) MoPrP 27–30(RML). Inset uses a different color table to show the weak, broad 4.8 Å diffraction. (B) The synthetic prion strain, MoSP1, derived from recPrP (89–230) amyloid, passaged twice through Tg9949 mice and purified as in A. (Open access).

1.3.5 Hydrogen-deuterium exchange (HDX) coupled to MS

HDX-MS protocol takes advantage of the labile nature of protons present on protein backbone amides, and is a powerful tool in the study of protein structure. When dissolved in solution, proteins exchange these protons with hydrogen groups present in a deuterated buffer, and protons from the protein are exchanged with deuterium. Only the protons present on the backbone amides are measured. The rate of hydrogen to deuterium exchange provides solvent accessibility data, which can be used to infer information on protein structure and conformation. Mass spectrometry can be used to measure the rate of deuterium uptake after pepsin treatment.

Some studies have been performed with this technique analyzing the structure of recombinant PrP amyloid (Lu et al.; Nazabal et al.). Finally, a paper was published which studied GPI-less PrP^{Sc} (Smirnovas et al.) and it was showed that the C-terminal part of GPI-less PrP^{Sc} exhibits extremely low rates of H/D exchange, which is typical of stretches with extensive H-bonding (β-sheets) and the whole 90-215 stretch is relatively resistant to exchange. Some other stretches exhibit a higher exchange rate corresponding to partially overlap with turns or loops, such as 133-148 and 81-118.

Therefore, it was concluded that GPI-less PrP^{Sc} consists of a series of β-sheets connected by short loops and/or loops with no native α-helices which was consistent with the FTIR reinterpretation of results. These data favored Govaerts' model although they did not support the presence of C-terminal α-helices.

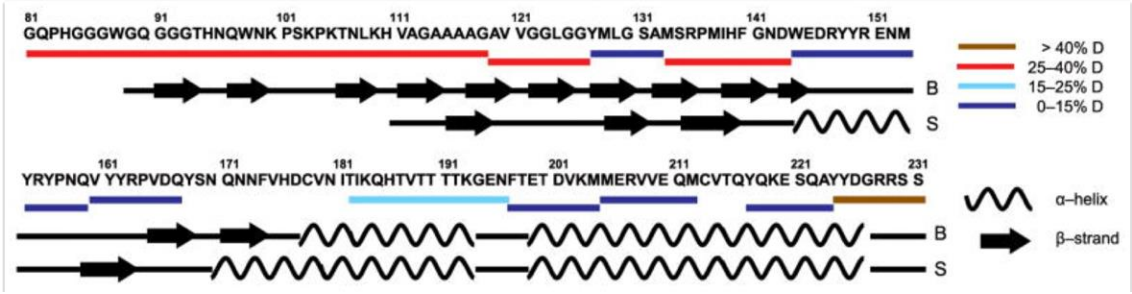

Fig 1.17. Schematic representation of prion protein secondary structure in the ß-helix (B) and spiral (S) models of PrP^{Sc}. Black arrows, curved lines and solid lines represent ß-strands,α-helices and loops/unordered segments, respectively. Colour bars immediately below the sequence represent the percentage of deuterium incorporation for GPI–22L PrP^{Sc} after 240 hours of exchange. Adapted from Smirnovas 2011(Permission granted by the journal).

1.3.6 Limited proteolysis coupled to Mass Spectrometry

The principle of limited proteolysis is that a protein is incubated with a relatively low concentration of different proteases, which cut at recognition sites throughout the protein, normally at exposed regions such as loops and other flexible regions.

The use of a non-specific protease like PK has been used for a long time in the prion field. While PrP^{Sc} is partially resistant to PK digestion, PrP^{C} is totally destroyed after incubation with PK. The PK-resistant peptide (PK-res PrP or PrP27-30) retains the infectivity of the full length PrP^{Sc}.

Limited proteolysis with PK was in fact the first technique employed and it allowed the discovery of the compact core of PrP^{Sc}. PK-resistant cores are variable in length depending on the species, the most abundant span the residues ~90-231. Therefore, it can be concluded that the PrP^{Sc} is formed by two domains: the N-terminal domain, which is unstructured and easily degraded by PK and the C-terminal domain, which its highly ordered and partially resists the proteolytic digestion of the PK (Gong et al; Bolton et al).

Nonetheless, additional studies have demonstrated the existence of a sensitive PrP^{Sc} to PK digestion ($sPrP^{Sc}$) that shares structural and biochemical features with the PK-resistant PrP^{Sc} (PK-res PrP) (Safar et al.; Pastrana et al; Sajnani et al.). The most noticeable difference is that whereas PK-res PrP consists of large aggregates, over 60 subunits, $sPrP^{Sc}$ consists of smaller aggregates of 12-15 subunits (Pastrana et al.).

In 2008, Sajnani and colleagues analyzed two hamster-adapted strains: 263K and Drowsy (Dy). PK cleavages at positions 86, 90, and 92 were observed for the 263 K strain and 86, 90, 92, 98,and 101 for the Dy strain. These results are consistent with Western blot analysis of PrP 27–30 from Dy and 263 K, which showed that PrP 27–30 from Dy had a lower molecular weight than that derived from 263 K. Additional PK cleavage at sites 117, 119, 135, 139, 142 and 154 were observed in both strains. However, the presence of asparagine-linked sugars and the GPI anchor impeded the analysis of the C-terminal portion of PrP^{Sc}.

In 2012 GPI-anchorless PrP^{Sc} was entirely analyzed by Vázquez-Fernández and collaborators due to the lack of GPI and almost complete lack of glycosylation. It revealed cleavage sites at positions 81, 85, 89, 116, 118, 133, 134, 141,152, 153, 162, 169 and 179. These results showed the actual PK cleavage sites for the entire PrP^{Sc} monomer. Such cleavage sites coincide with those previously identified in hamster PrP^{Sc}, up to where the analysis of that molecule was possible (~N154), suggesting that the architecture of GPI−PrP^{Sc}, 263 K $SHaPrP^{Sc}$, and $DySHaPrP^{Sc}$ share a common structure (Vázquez-Fernández 2012). The authors concluded that the structure of PrP^{Sc} consists of a series of high PK-resistant β-sheet strands that are connected through loops and turns in agreement with the previous results. Since no cleavage sites were detected beyond position 170 it was also concluded that the C-terminal stretch of GPI- PrP^{Sc} was particularly resistant to PK, being probably mainly composed of β-sheets.

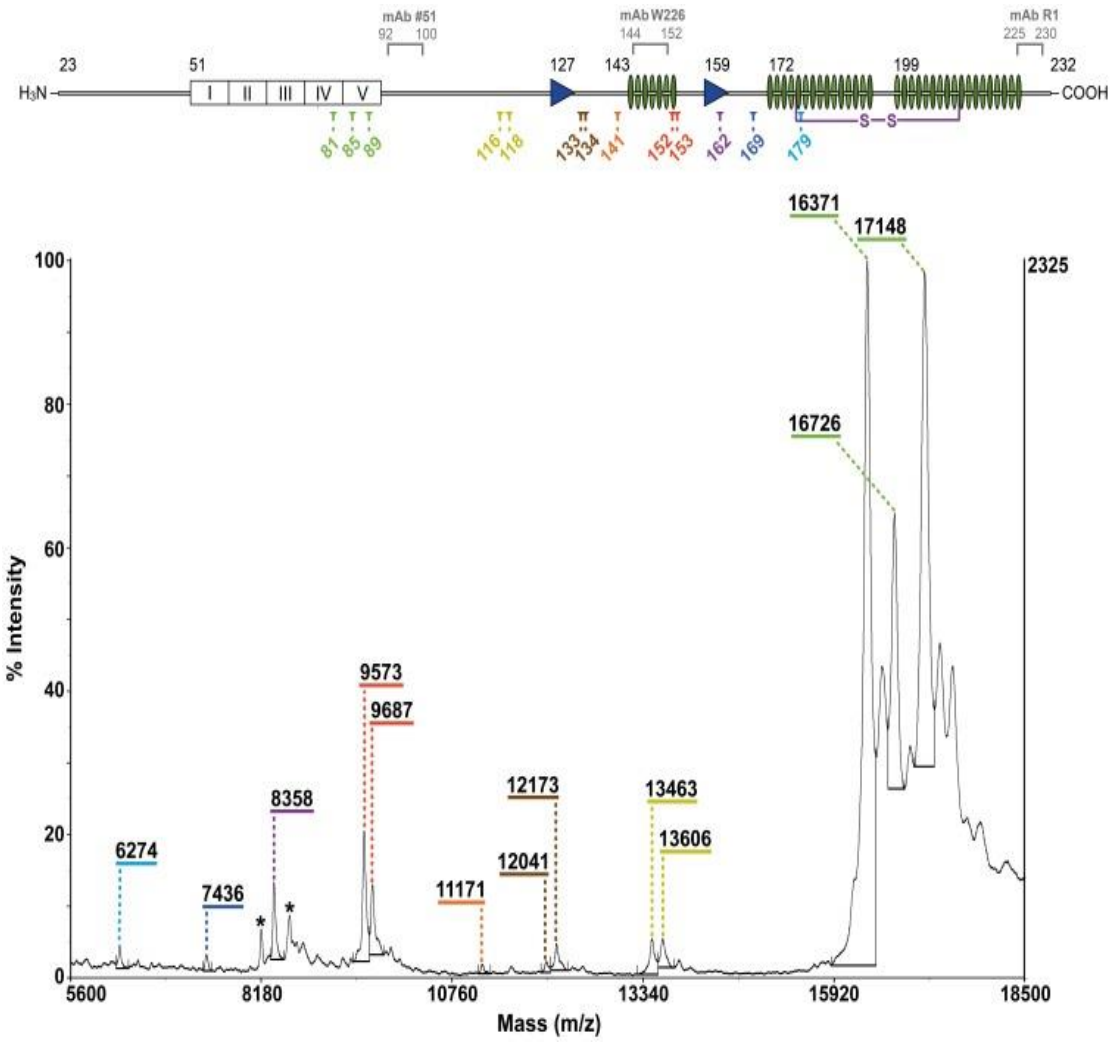

Fig 1.18. MALDI-TOF spectrum of PK-treated purified GPI− PrP^{Sc}. Doubly-charged ions from peptides with m/z 16371 and 17148 are indicated (*). Low resolution in the >16 kDa region precluded identifying unmarked peaks. A scheme of GPI- PrP sequence with PK cleavage points (color coded) and secondary structure of PrPC is included at the top: (octarepeats (□), ß-sheets (‣), and α-helices (‖)); epitopes of the mAbs used are also indicated. Adapted from Vázquez-Fernández et al. 2012 (Permission granted by the journal).

1.3.7 Cryogenic electron microscopy (Cryo-EM)

Cryogenic electron microscopy is a cryomicroscopy technique applied on samples cooled to cryogenic temperatures and embedded in an environment of vitreous water which is liquid ethane; it makes the sample freeze so fast that ice crystals are not able to form.

Vázquez-Fernández and colleagues used for the first time a GPI-anchorless PrP^{Sc} since its fibers inherently present a repetitive organization. GPI-archorless PrP^{Sc} was purified from the brains of transgenic mice expressing GPI-anchorless PrP that were infected with prions of the Rocky Mountain Laboratory (RML) strain.

Images showed fibrils ~10 nm wide, composed by two intertwined, twisting protofilaments of approximately 50 x 29 Å with a space between them. Separate fibrils were found to display either a left- or right-handed twist, or to be essentially straight.

Reconstructed tomograms allowed measurements of fibrils widths since they allowed a more facile visualization of individual fibrils, which were confirmed to be 9.55 ± 1.15 nm. The raw images contained high-resolution information, as surmised from Fourier-transform analyses of the fibrils routinely showing a 4.8 Å cross-β signal for individual fibrils along their axis that can be readily interpreted as originating from β-strands running perpendicular to the fibril axis. It is notable that the orientation of the cross-β signal is strictly dependent on the orientation of the individual amyloid fibrils, which proves its origin.

Furthermore, Fourier-transform analyses of nearby empty areas of ice or carbon film never showed a 4.8 Å signal, indicating that the 4.8 Å signal is indeed a cross-β signal similar to what was seen in X-ray fiber diffraction from PrP 27–30 (Wille 2002, Vázquez-Fernández et al. 2016).

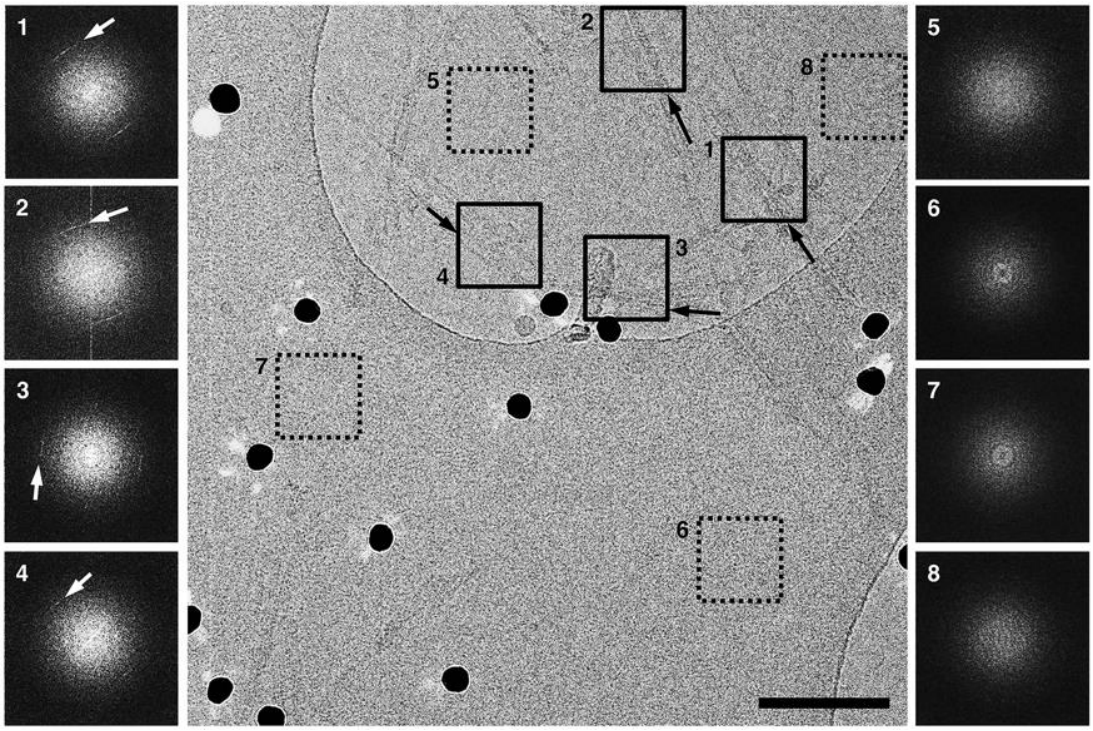

Fig 1.19. Raw cryo-EM images of GPI-anchorless prion fibrils show their basic features and 4.8 Å cross-ß signals. A high-resolution cryo-EM image showing individual GPI-anchorless PrP 27–30 fibrils or small bundles of fibrils (solid boxes). Fourier-transform (FT) analyses from the corresponding boxes show 4.8 Å cross-ß signals that originate from the ß-strand stacking along the fibril axis and which follow the orientation of the fibrils (black and white arrows). FT analyses of areas of ice or carbon film, that were devoid of amyloid fibrils (dotted boxes), and which did not show any noticeable signals at 4.8 Å. Scale bar, 100 nm. Adapted from Vázquez-Fernández et al. 2016 (Permission granted by the journal).

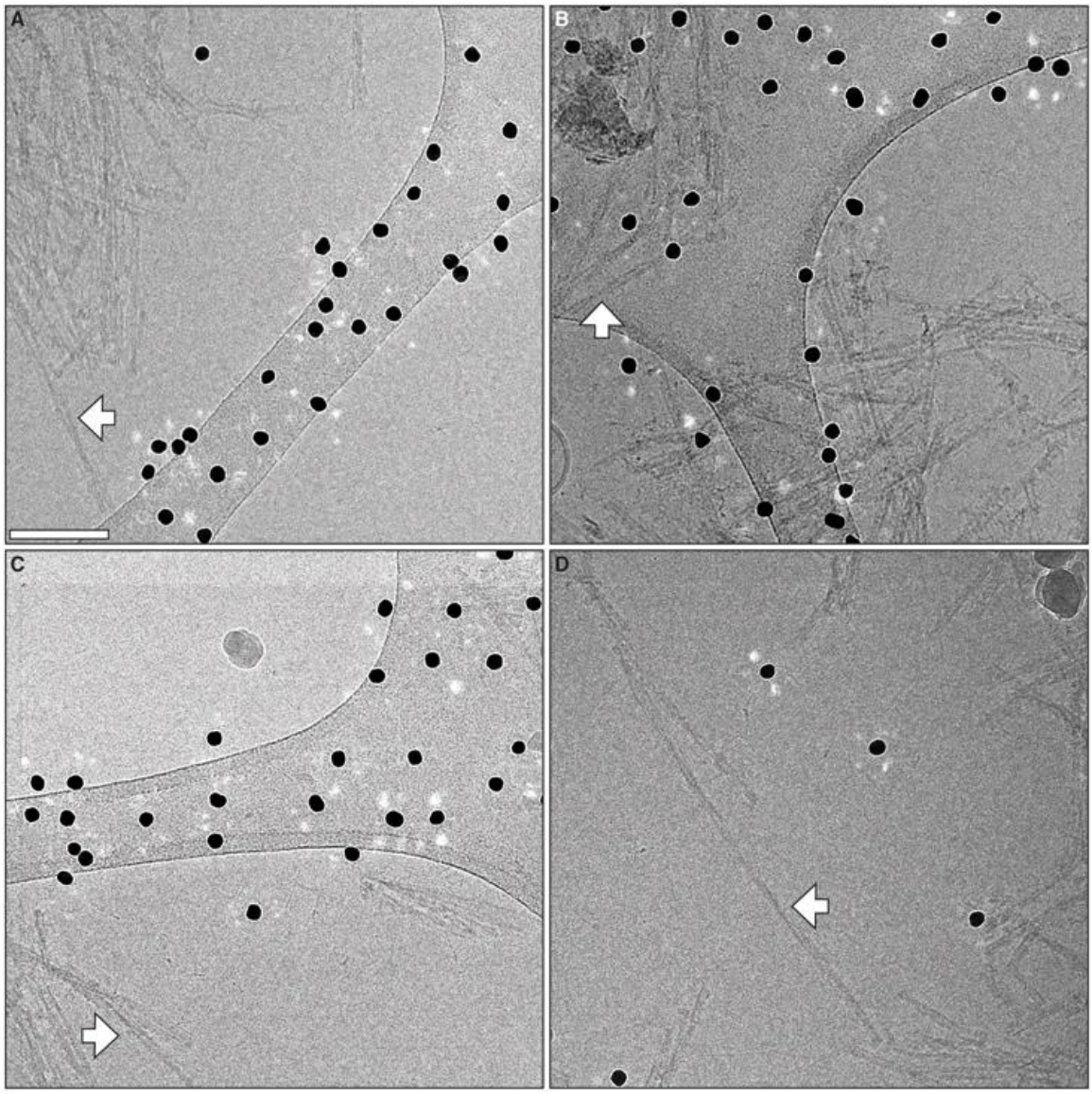

Fig 1.20. Raw cryo-EM images of GPI-anchorless prion fibrils show their basic features and 4.8 Å cross-ß signals. Additional cryo-EM micrographs of GPI-anchorless prion fibrils. Electron micrographs showing representative GPI-anchorless prion fibrils, including four isolated fibrils that were subsequently analyzed by image processing (white arrows). The labels (A to D) correspond to the lettering in the 3D fibril reconstruction figures (vide infra). Black dots originate from fiducial gold that was added for tomographic studies. Scale bar, 100 nm (Permission granted by the journal).

Single particle analysis is a technique which consists in selecting specific images, delimitated by boxes, rotate them so the fibers are in the same orientation or aligned, classify and average them treating them as single objects.

An averaged power spectrum of 1072 aligned segments showed a 4.8 Å intensity characteristic of the cross-β structure of amyloid fibrils, also detected in many raw images (Fig. 1.21). The arc-shape of the 4.8 Å signal was interpreted as indicative of an imperfect alignment of the fibrils.

To overcome this problem, each of the protofilaments that make up the fibril individually was analyzed, which revealed 19.1 Å and ~40 Å signals upon Fourier-transform analysis (Fig.1.21). These spacings correspond to 4 and 8 multiples of 4.8 Å β-strands, and indicate the existence of a structural subunit with a height of 4 β-strands, that associates vertically with another subunit to form a higher order dimeric structure.

Another feature, the absence of a strong ~10 Å signal on the equator of the Fourier-transforms is generally interpreted to indicate the presence of β-helical and β-solenoidal structures (Vázquez-Fernández et al. 2016).

The 3D reconstruction of one of these individual GPI-anchorless PrP 27–30 fibrils, with a maximum width of 9.1 nm and a crossover distance of 95 nm, showed two approximately 50 x 29 Å oval-shaped protofilaments (Fig. 1.22). One important implication is that PrP^{Sc} subunits can only fit into protofilaments with the observed dimensions if they are folded up onto themselves. Based on the routine observation of regular 4.8 Å cross-β signals in individual GPI-anchorless PrP 27–30 fibrils, a β-solenoid arrangement is the easiest way to accommodate the peptide into the available protofilament volume.

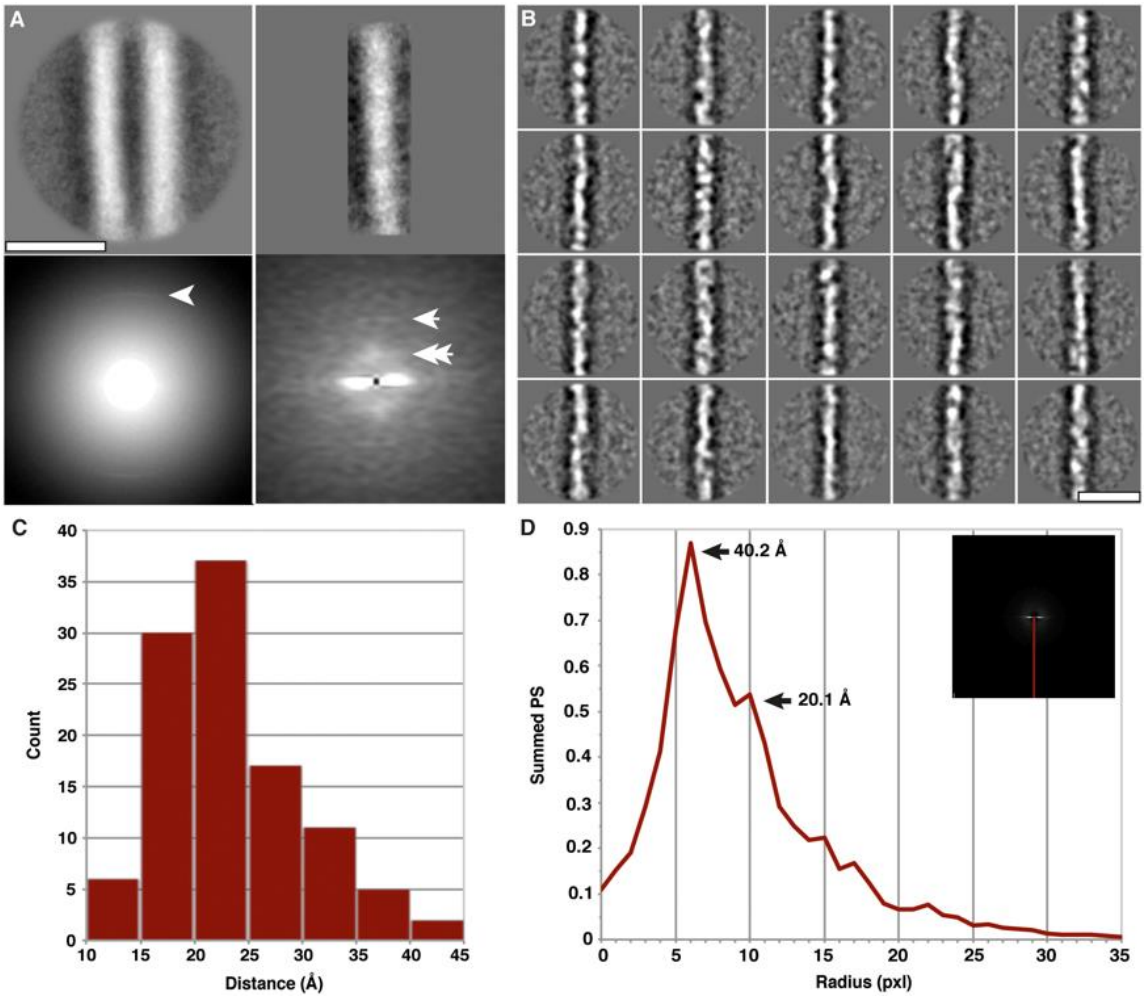

Fig 1.21. Single particle averaging of GPI-anchorless PrP 27–30 fibril images. (A) Average from 1072 fibril segments (top left) and the logarithm of their summed power spectrum (bottom left). The arrowhead indicates the characteristic 4.8 Å cross-β signal. Representative 2D class average of 100 single protofilaments (top right) and their averaged Fourier-transform (bottom right). Single and double arrows are pointing to intensities at 19.1 Å (single pixel) and ~40 Å (38.3 Å and 44.6 Å pixels), respectively. (B) Gallery of 2D class averages obtained from reference-free analysis of individual protofilaments. Box size is 150 by 150 pixels, equivalent to 20.1 by 20.1 nm. (C) Histogram of manually determined sizes of densities along the protofilament from the class averages in (B). The majority of densities fall into the classes between 15 and 25 Å. (D) The average over all amplitude spectra of all class averages. A plot of the meridian of the Fourier-transform (red line) reveals a broad peak around 40.2 Å and a smaller peak at 20.1 Å (arrows). The Nyquist frequency (2.68 Å) corresponds with the 75 pixel outer border of the spectra. Scale bars, 10 nm. Adapted from Vázquez-Fernández et al. 2016 (Permission granted by the journal).

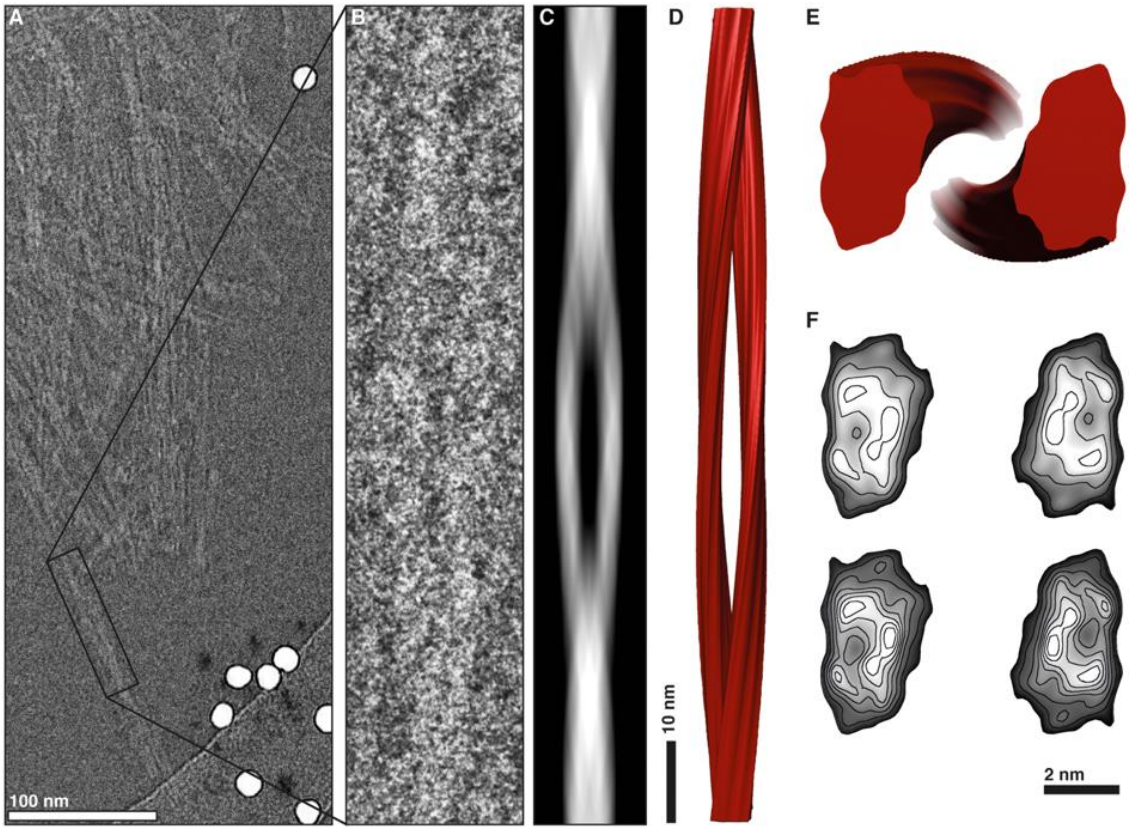

Fig 1.22. 3D reconstruction of a GPI-anchorless prion fibril. (A) Section of an electron micrograph showing GPI-anchorless prion fibrils. The single isolated and twisted fibril used for the 3D reconstruction is enclosed by a black box. (B) Close-up view of the prion fibril. (C) Re-projected image of the 3D fibril map. (D) Reconstruction of the GPI-anchorless prion fibril. (E) Cross-section of the reconstructed fibril. (F) Contoured density maps of the cross-sections. Lines are contoured at increasing levels of 0.25 σ and 0.125 σ (top and bottom, respectively) (Permission granted by the journal).

1.4. Two final structural models of PrP^{Sc}

Over the years many structural models of PrP^{Sc} have been proposed but I will only focus on the two left standing at the time of the start of my PhD studies in November 2017. They eventually emerged as the only plausible ones since they are compatible with most of the experimental restraints I have considered. These are: 1. The parallel-in-register-intermolecular-β-sheet (PIRIBS), and 2. The 4-rung- β-solenoid (4RβS).

1.4.1 Parallel-in-register-intermolecular-β-sheet (PIRIBS)

This model was proposed by Caughey's group in 2014 (Groveman 2014).

Recombinant PrP^{C} (90-231) was converted into seeded aggregates using the RT-QuIC method, which will be further explained, that generated non-infectious but propagative PrP amyloid fibrils. Such fibrils were labeled with either (1-^{13}C)-Ile, (1-^{13}C)-Phe or (1-^{13}C)-Leu in order to perform a ssNMR PITHIRDS experiment, which will be explained later in detail: basically it measures intermolecular distances and if it is of 5 Å it unequivocally means that the structure is a PIRIBS. This experiment yielded the result that the material employed was a PIRIBS.

Such information prompted the researchers to propose new detailed models of PrP(90-231) oligomers which were built on a previous schematic representation (Cobb 2007) of a limited amyloid core of PrP residues ~160-220 in which each monomer stacks with their polypeptide backbones being perpendicular to the fibril axis. Main constraints were considered: (i) Linearity of fibers: the parallel in-register β-sheet architecture that is evident for rPrP amyloid core residues 160–220 suggests that the more N-terminal residues that are also part of the resistant PrP amyloid core assume a configuration in which they are not only tightly packed but also lie roughly on the same plane and, on average, contribute 0.5 nm of axial thickness along the fibril axis perpendicular to the β-strands. Otherwise, the fibril would not be linear because the N-terminal residues of each monomer would contribute greater thickness than the C-terminal residues, forcing the fibril to be unstable or discontinuous with respect to native disulfide hairpin stacking. (ii). Cross-sectional dimensions: they collected dark field images using scanning transmission electron microscopy (STEM) of unstained, PK-treated GPI-anchorless PrP^{Sc} amyloid fibrils. Isolated fibrils were measured across their widths providing a distribution of 6–24 nm. Polypeptide β -strands are 0.3 nm long per residue, so a fully extended chain of residues 90–231 would be 42 nm (141 residues x 0.3 nm) long. Thus, the polypeptide backbone must fold back on itself multiple times in a "super-pleated sheet" to fit within the fibril cross-section. Distances between the backbone folds could vary depending upon the packing (or lack thereof) of side chains forming the faces of the β-sheets but is typically 1.0 nm in tightly packed amyloid fibrils containing steric zippers. As such, the native disulfide hairpin as depicted in the Cobb et al. model should be 5 x 2 nm incorporating 35 residues. A fibril cross-section of 5 x 9 nm could accommodate as many as 140 residues in four hairpins each with 35 residues, with 140 being the approximate number of residues in monomers of PK-treated PrP^{Sc}. Thus, the authors concluded that multiple hairpins (in addition to that defined by the native disulfide) are present within PrP. (iii). Glycans: the asparagine side chains to which glycans are often attached (Asn-181 and -197) should be oriented toward the outside of the native disulfide hairpin because it is impossible that bulky hydrophilic

glycans would fit inside the hairpin. The authors proposed a "glycan cleft" (see Fig. 1.23) where the glycans would be. (iv) Epitopes and proteolytic cleavage sites: the authors predicted further turn/loop positions based on known epitope exposures and sensitivities to proteolytic digestion since those residues are likely to be in more flexible turns or loops with exposure to the fibril surface, at least after partial unfolding and/or unbundling of fibrils. (v) Molecular dynamics simulations: they constructed assemblies of eight PrP molecules based on the aforementioned constraints and subjected them to energy minimization and molecular dynamics simulations: PIRIBS-A, PIRIBS-B and PIRIBS-C. The different parallel in-register-β-sheet models showed varying degrees of order (or disorder) in these simulations, each structure was able to maintain substantial order in the C-terminal region (residues 124–231) with much of the original β-sheet structure conserved, especially in the C-terminal 160–231 region. The flexibility in the N-terminal region (residues 90–125) was expected as it is consistent with that seen empirically in *in vitro* formed fibrils of pure rPrP without cofactors (Groveman 2014).

Therefore, Groveman's model was the first atomistic model of PrP^{Sc}. The advantages of this model are that its structure is simple and it resembles that of the non-infectious recombinant PrP amyloid, therefore that the conversion mechanism of PrP^{C} to PrP^{Sc} would be simple to explain, since PrP^{C} would pile up onto PrP^{Sc} and it would be misfolded. However, these conclusions were reached using a material which was non-infectious and the model is not able to accommodate glycans in the proposed glycan cleft because it is too narrow nor to undergone molecular dynamics simulations for a long enough time. Moreover, whereas Vázquez-Fernández saw two parallel protofilaments (see section 1.3.7), Groveman interpreted the electron micrographs to show a single protofilament composed of hairpins or combinations of hairpins connected by a hinge, giving a "celery stalk" or half-pipe appearance that would be deceitful to the eye.

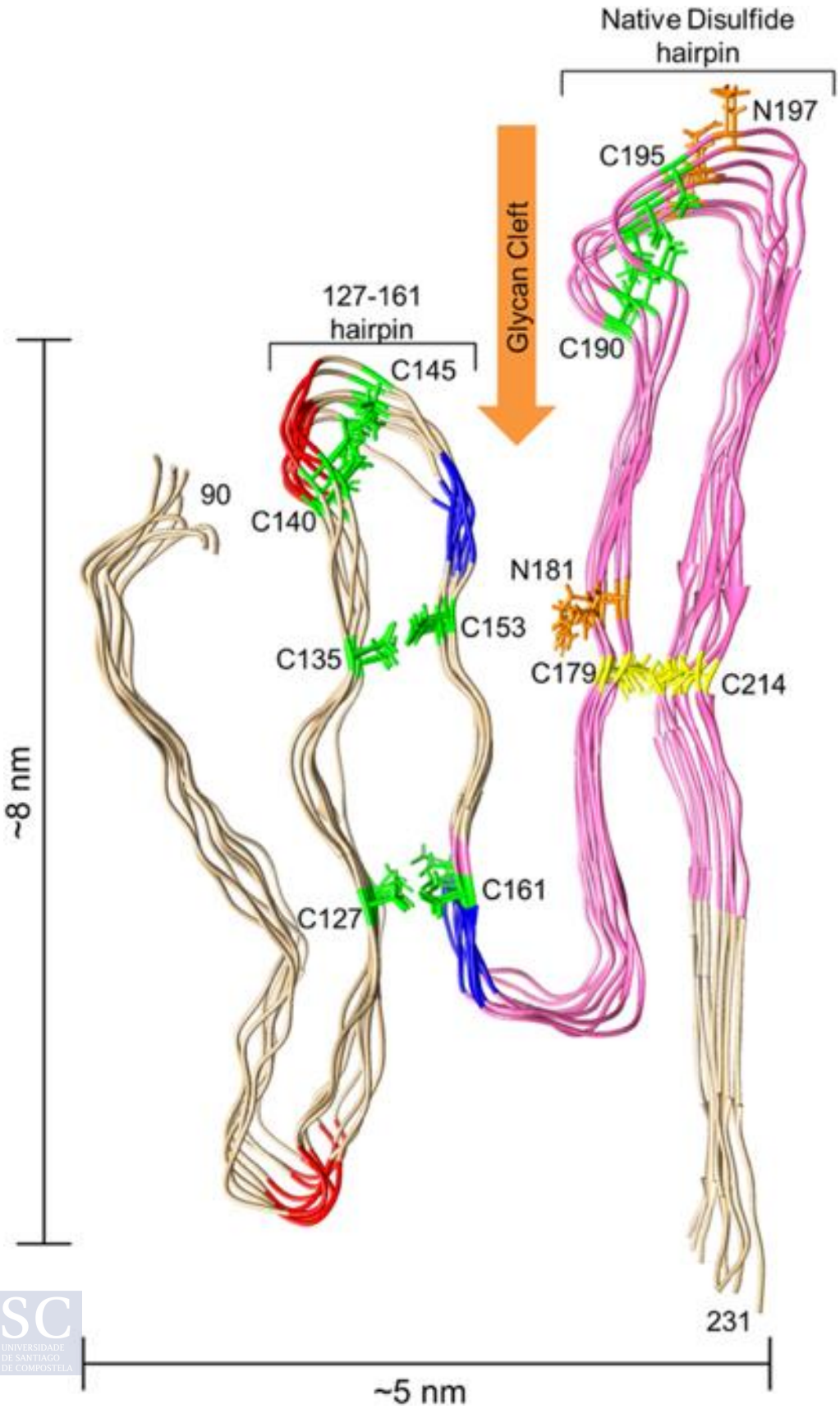

Fig 1.23 Model of an octameric PrP 27-30 amyloid segment subject to the experimental constraints. The view is looking down the axis of an energy-minimized octamer of mouse PrP(90 –231) molecules stacked parallel in-register and with the main hairpins (denoted on the model) defined by either the natural disulfide or the artificial disulfides (yellow or green, respectively) that have been shown to be compatible with PrPSc formation (Open acess).

1.4.2 4-rung-β-solenoid (4RβS)

A version of this model was proposed by Requena's and Wille's groups in 2016 based on several constrains gathered throughout the years already described. Three years later the first physically-plausible, atomic resolution model of mouse PrP^{Sc} was built using computational techniques (Spagnolli et al. 2019). Moreover, in 2020 a refined model compatible with deformed-templating (see section 1.5) was proposed (Spagnolli et al. 2020).

The 2019 4RβS atomistic model of mouse PrP^{Sc} was built based on the then available experimental evidence and theoretical structural constrains and its stability was tested by means of all-atom molecular dynamics (MD) simulations. Such model construction took into account an array of experimental data, including: (i) cryo-EM (Vázquez-Fernández 2016) and X-ray fiber diffraction studies (Wille et al. 2009) which showed that the fold of a mouse GPI-less infectious PrP^{Sc} is compatible with a 4RβS architecture with L- or T-shaped cross-section (Vázquez-Fernández 2016); (ii) CD and FTIR spectroscopy which excluded the presence of α-helices and suggested that PrP^{Sc} contains approximately 40-50% β-sheet and 50–60% coil/turns (Requena 2014); (iii): MS analysis indicating the presence of an intact disulphide bond between residues C178 and C213 (mouse sequence) (Welker 2002) as well as mapping Proteinase K (PK)-sensitive residues, which reflect amino acids likely excluded from the resistant core of the protein (Vázquez-Fernández 2012), (Sevillano 2018); and (iv) the possibility of accommodating complex glycans at positions N180 and N196 (Baskakov 2016, Spagnolli et al. 2019)

All these constraints were comprehensively included into a 2D threading scheme spanning mouse PrP (moPrP) residues 89–230 also considering the structural propensities of different residues: polyglycine tracts and prolines were positioned in loops due to their destabilizing effects on β-strands and charged sidechains were excluded from the inner core of the protein or counterbalanced by salt bridges. This scheme was then modelled onto the 3D arrangement of a naturally-occurring β-solenoid protein (*Dickeya dadantii* Pectate Lyase; PDB 1AIR). The resulting structure (depicted in Fig 1.24) features an inner core containing mainly hydrophobic or mildly polar side-chains (T94, T106, L108, V111, Y127, M128, W144, Y149, V165, Y168, I181, I183, V188, F197, T198 and T200), few polar side-chains involved in hydrogen bonding (N142-HB-Y168, H168-HB-T198, Q216-HB-T200 and Q218-HB-S221), and a salt bridge (R147-SB-D166). Conversely, the majority of the highly-polar residues (N and Q) including the glycosylation sites (N180 and N196) and charged side-chains (E, D, K and R) are exposed to the solvent. The structure also encompasses identified PK cleavage sites localized in loops/turns, or at the edge of the β-strands, and the intact disulphide bond between C178 and C213 (Spagnolli et al. 2019).

To test the physical consistency of the 4RβS model, the authors challenged its stability by all-atom MD simulations in explicit solvent, which rendered that the monomer was stable. Then, to mimic the fibrillary behavior of PrP^{Sc}, they built a tetrameric 4RβS model by stacking monomers in a head-to-tail fashion; this assembly showed a comparable MD stability to the monomer. Moreover, the 4RβS tetramer fits with the two main signals obtained by Fourier transform single particle analysis of cryo-EM data (19.1 Å and the ~40 Å) which reflect distances between the same

residues on two contiguous or alternate monomers, respectively, as well as with the observed volume of the protofilaments. Next, by introducing complex sugar precursors (GlcNAc2Man3Fuc) at positions N180 and N196 of each monomer, they observed the absence of steric clashes, confirming that the 4RβS model accommodates the presence of glycans (Spagnolli 2019).

The 4RβS model allowed Spagnolli and colleagues to develop an original scheme to perform for the first time a simulation of the conformational transition from PrP^{C} to PrP^{Sc} (Fig.1.26). In order to bridge the gap between the computationally-accessible and the biologically-relevant time scales, they employed a specific kind of biased dynamics called ratchet-and-pawl MD (rMD) in the framework of an all-atom realistic force field. The basic idea is that the algorithmic ratchet exerts a force on the protein when it is climbing the free-energy barrier, while it is inactive when it is descending. The transition state can be identified as the point of the trajectory where the ratchet changes regime (Tiana 2012). However, this scheme provides a sampling of the transition path ensemble only if the biasing force is applied along a reliable reaction coordinate.

Therefore, the first step towards developing their rMD simulation was to build a statistical model to identify the reaction coordinate of the process. Using the Markov State Mode formalism, they demonstrated that among all the possible misfolding patterns from PrP^{C} to PrP^{Sc} the prominent reaction mechanism is the sequential formation of rungs. A biasing coordinate was then built by coupling this dynamical information with the all atom 4RβS structure. The associated rMD simulations yielded a transition pathway with full atomistic resolution in which the C-terminal rung of the solenoid acts as a primary conversion surface for PrP^{C} unstructured N-terminus (residues 89–124). This first event initiates a cascade of conformational transitions in which each newly formed rung acts as a template for the formation of the following one, ultimately leading to the complete conversion of PrP^{C} into PrP^{Sc} (Spagnolli 2019).

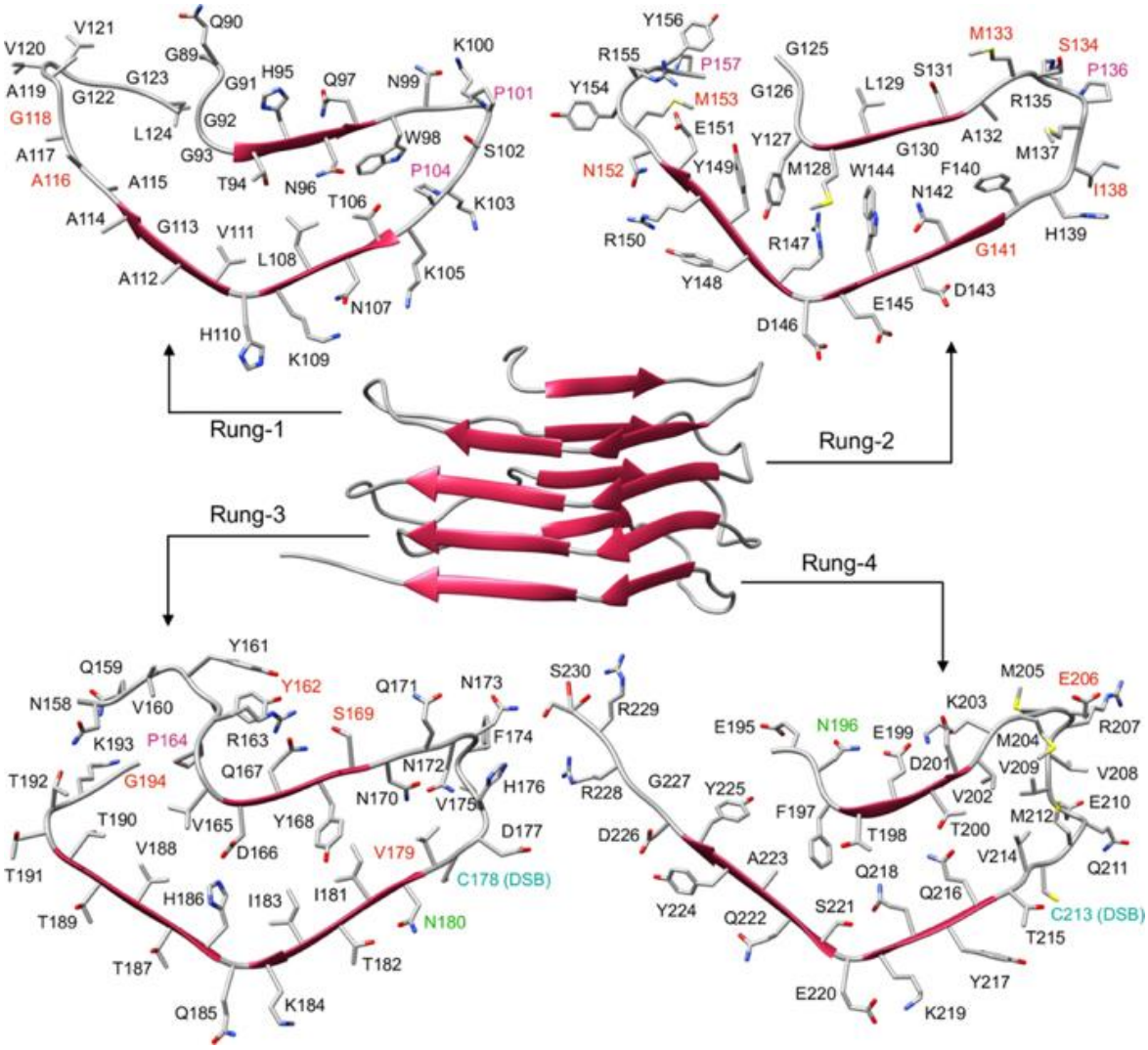

Fig 1.24. View of the 4RßS PrP^{Sc} Model. The structure of PrP^{Sc} modelled as a 4RßS (ß-strands represented as red arrows) is depicted in the center of the figure. Residues are displayed in each individual rung (1–4) with different colors. PK cleavage sites identified by mass spectrometry in two different previous reports are colored in red. Glycosylation sites are labelled in green. Prolines are colored in purple. Cystine is indicated in cyan. Adapted from Spagnolli et al. 2019 (Open access).

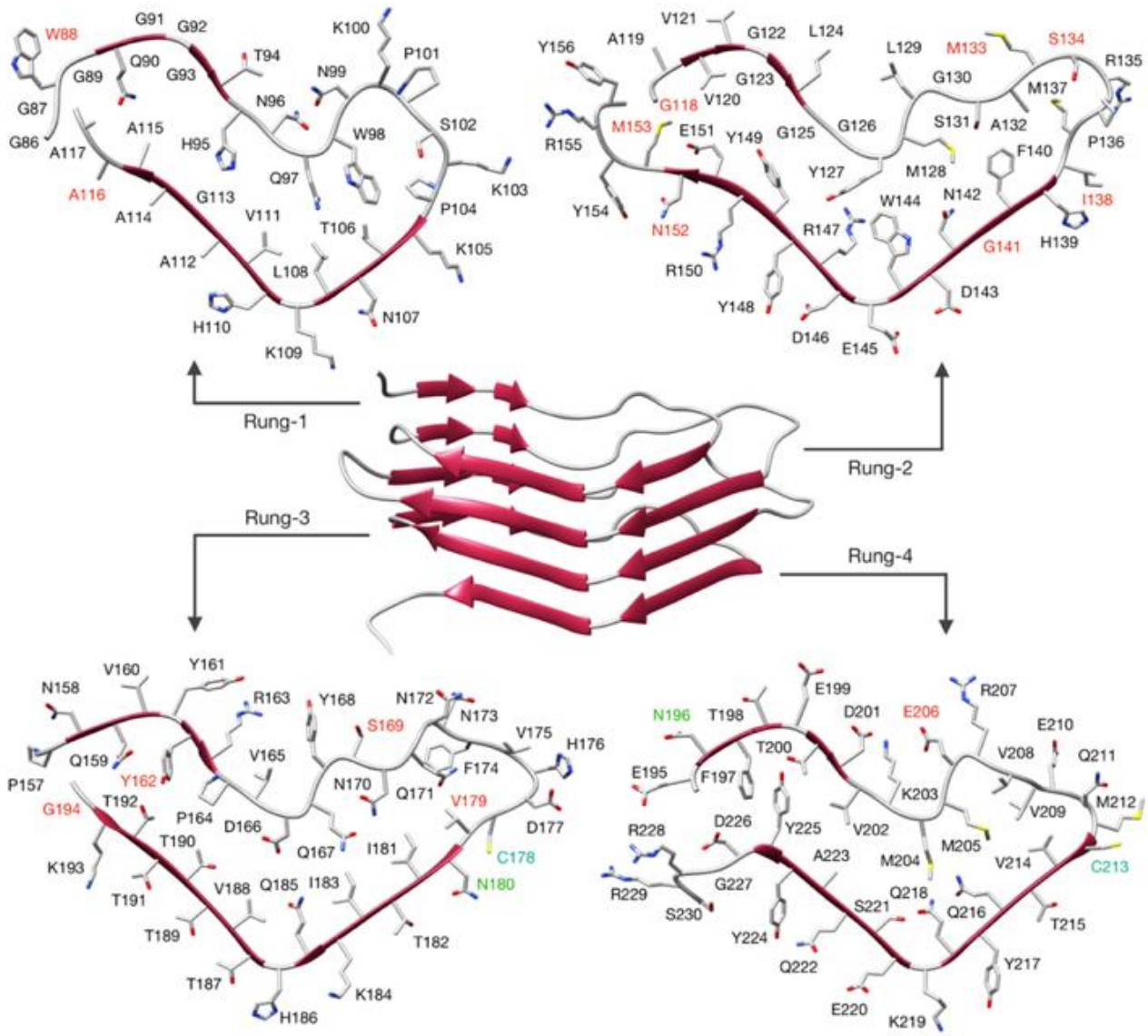

Fig 1.25. 4RbS model of mouse PrP^{Sc} compatible with deformed templating (see section 1.5.2). The structure of the deformed-templating-compatible PrP^{Sc} modeled as a 4RbS is shown in the figure center. Residues are depicted as sticks and displayed in each individual rung with labels in different colors. PK cleavage sites identified by mass spectrometry are labeled in red. Glycosylation sites are labeled in green and cystine in cyan. Residue numbering is relative to the mouse sequence. Adapted from Spagnolli et al. 2020 (Open access).

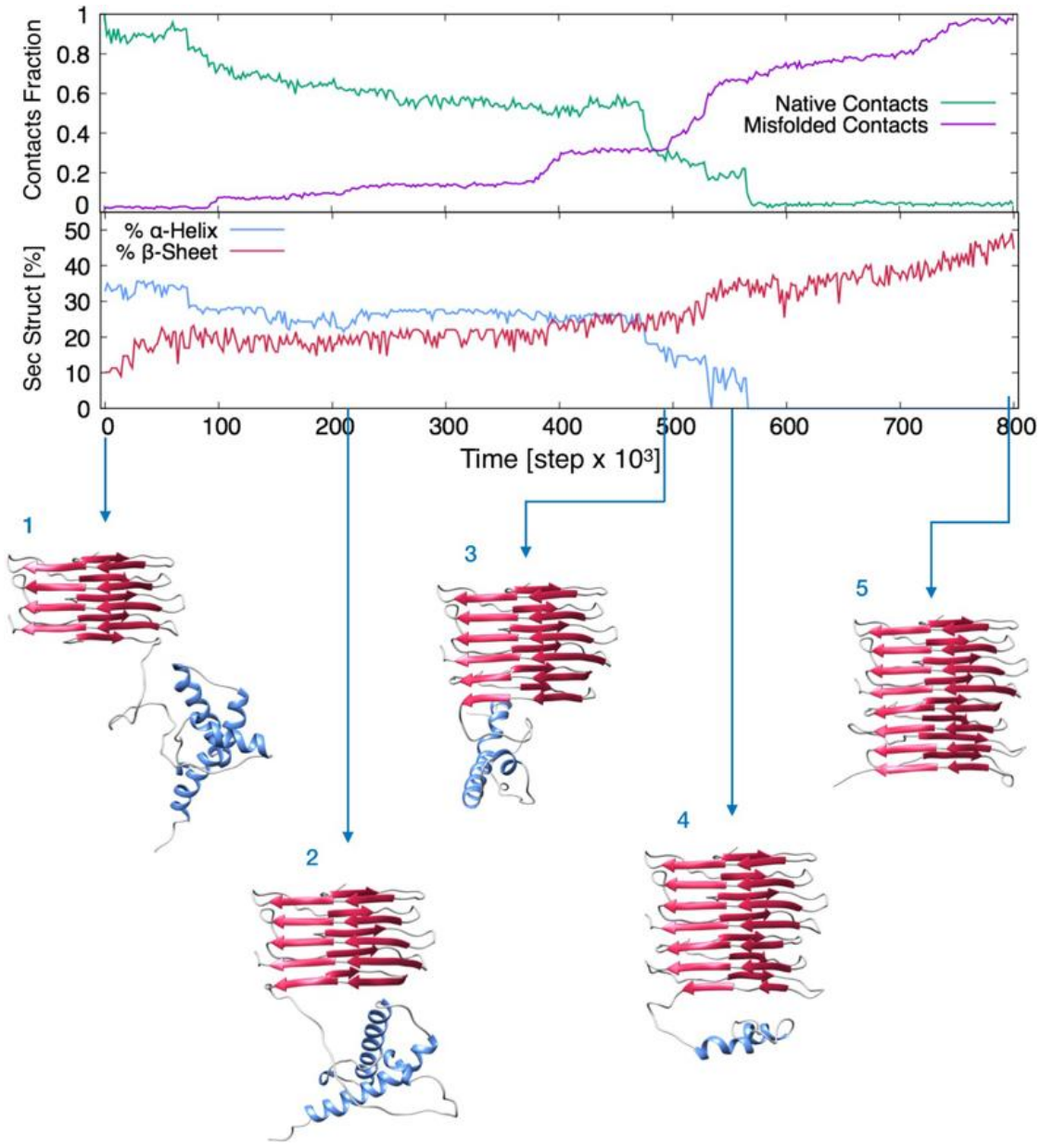

Fig 1.26 Graphs and Frames Extracted from the rMD Simulation of PrP^C to PrP^{Sc} Conversion. Upper graph reports the fraction of native and misfolded contacts of the instantaneous configurations of the PrP^C-PrP^{Sc} complex, starting from the initial modelled configuration (depicted in 1) in which PrPC contacts the 4RßS monomer, with respect to the final target configuration (4RßS dimer). Lower graph shows the secondary structure content. Pictures of the evolving complex represent frames extracted from the entire conversion simulation at precise rMD steps, corresponding to the refolding of PrPC as follow: (2) residues 89–115; (3) residues 89–151; (4) residues 89–190; (5) residues 89–230. The process highlights the progressive unfolding and refolding of PrPC onto the 4RßS template, which initially involves the unstructured region, followed by the loss of α-helices and a progressive formation of ß-sheets. Adapted from Spagnolli et al. 2019 (Open access).

1.5 Recombinant prions

The first recombinant infectious prions which were inoculated in animals showing the clinical signs of the prion disease were produced by Legname and colleagues in 2004. Recombinant mouse prion protein (recMoPrP) produced in *Escherichia coli* was polymerized into amyloid fibrils that represented a subset of β sheet–rich structures. Fibrils consisting of recMoPrP(89–230) were inoculated intracerebrally into transgenic (Tg) mice expressing MoPrP(89–231). The mice developed neurologic dysfunction between 380 and 660 days after inoculation. Brain extracts showed protease-resistant PrP by Western blotting; these extracts transmitted disease to wild-type FVB mice and Tg mice overexpressing PrP, with incubation times of 150 and 90 days, respectively. (Legname et al. 2004). However, this study was criticized because the prions obtained were very slow in producing infectivity and the mice used in the experiment were transgenic mice expressing a truncated version of PrP, MoPrP 89–230, in large quantities (about 16x the expression seen in wild type animals), meaning that possibly the PrP amyloid inoculated did not produced a prion disease but rather accelerated spontaneous development of a genetic form of neurodegeneration induced by overexpression of an aberrant form of PrP.

Shortly after the accomplishment of prion disease transmission with recPrP amyloids, Baskakov and colleagues made an unexpected discovery: while wild type Syrian hamsters (Sha) inoculated with recombinant ShaPrP amyloid did not develop any clinical signs of prion disease (in contrast with transgenic animals expressing a large amount, 16X, of PrP), some of them accumulated abnormally folded forms of PrP, and inoculation of their brain homogenates to wild type animals in a second passage induced a prion disease (Makarava et al., 2010). These authors have prepared over time different variants of PrP amyloid, all behaving in a similar fashion, with a silent propagative phase followed by emergence of clinical disease in second or even third passage (Makarava et al., 2011, 2012, 2015, 2016; Makarava and Baskakov, 2012; Klimova et al., 2015).

These studies have revealed that under most experimental conditions, upon first passage, a propagative, misfolded PrP species emerges that exhibits a peculiar, atypical pattern of PK-resistance. Namely, its main PK-resistant core spans from a position around 160 to the C-terminus and excludes the epitope recognized by antibody 3F4 (109–112) but includes the epitope of antibody SAF-84 (160–170). Such PK-resistant core is also characteristic of the PrP amyloid used for inoculation, and its size is related to the span of the PrP amyloid β-sheet-rich core (160-220). Such atypical, propagative PK-resistant PrP conformer is mostly monoglycosylated, although small fractions of diglycosylated and non-glycosylated conformer are also seen. With successive passages, classic PrP^{Sc} starts to emerge, eventually outcompeting the atypical propagative PK-resistant PrP conformer (Makarava et al., 2011, 2012, 2015, 2016; Makarava and Baskakov, 2012; Klimova et al., 2015).

Careful experiments were carried out to discriminate between two possibilities: 1. Minute amounts of PrP^{Sc} are present from the beginning in the first passage or 2.The atypical, propagative PK-resistant PrP conformer precedes PrP^{Sc}, which originates by a slow and progressive conversion of the former into the latter conformer. Baskakov and colleagues ruled out experimentally the first possibility, for example, with extremely sensitive PMCA-based analyses that would have detected even a small handful of PrP^{Sc} molecules

(Makarava and Baskakov, 2012; Makarava et al., 2012). Therefore, they coined the term "deformed templating" to refer to the second process, which they demonstrated to be taking place (Makarava and Baskakov, 2012; Makarava et al., 2012). Furthermore, these authors proposed a wider application of the term, which was defined as a process by which self-replicating protein conformational states with a given cross-β folding pattern can seed formation of an alternative self-replicating state with different cross-β folding pattern. Therefore, it could be concluded that recombinant PrP amyloid, which propagates *in vitro*, can also propagate in the brain, and, under extreme circumstances, show some infectivity. However, it could also be concluded that PrP amyloid was not equal to PrP^{Sc}. Furthermore, the non-infectious yet propagative recombinant PrP amyloid generated by RT-QuIC and analyzed by Groveman et al is not PrP^{Sc} either, and given its lack of infectivity cannot be called *stricto sensu* a prion.

However, recombinant PrP^{Sc}, long sought by researchers in the field, does exist. In fact, the ability of generating them revolutionized the field due to the easiness of obtaining the material with which to do research compared to having to isolate the prions from brain homogenates of infected animals. Many techniques raised which will be further explained. In fact, in 2010, Jiyan Ma produced for the first time recombinant prions by PMCA (see below) which, after intracerebral injection of the recombinant prion, wild-type mice developed neurological signs in ~130 days and reached the terminal stage of disease in ~150 days, similar to the classic prion strains. Characterization of diseased mice revealed classic neuropathology of prion disease, the presence of protease-resistant PrP, and the capability of serially transmitting the disease; these findings confirmed that the mice succumbed to prion disease (Wang 2010).

In the following sections, the different approaches to generate recombinant PrP^{Sc} will be discussed.

1.5.1 Protein misfolding cyclic amplification (PMCA)

Protein misfolding cyclic amplification is a technique by which to produce PrP^{Sc} from PrP^{C}. This method was developed by Soto and colleagues in 2001 (Saborio et al.).

Theoretically, it is similar to the polymerase chain reaction (PCR) by which a DNA sequence can be amplified millions of times in a cyclic reaction, being PMCA a cyclic reaction as well but used to amplify prions. This technique has two phases: first, there is an incubation of brain derived PrP^{C}, the substrate, with a small quantity of PrP^{Sc}, the seed, in which the PrP^{C} is misfolded into PrP^{Sc} forming aggregates; next, a sonication cycle by ultrasounds is applied which has been proposed to break down the newly formed amyloid PrP^{Sc} fibers, generating more nucleation centers for the next incubation phase. The initial PrP^{Sc} seed increases exponentially throughout the process.

It should be noted, nevertheless, that no biophysical or biochemical studies have been carrid out to demonstrate this mechanism of action, and it is very likely that sonication not only affects the newly formed PrP^{Sc} molecules but also the PrP^{C} substrate, perhaps partially unfolding it.

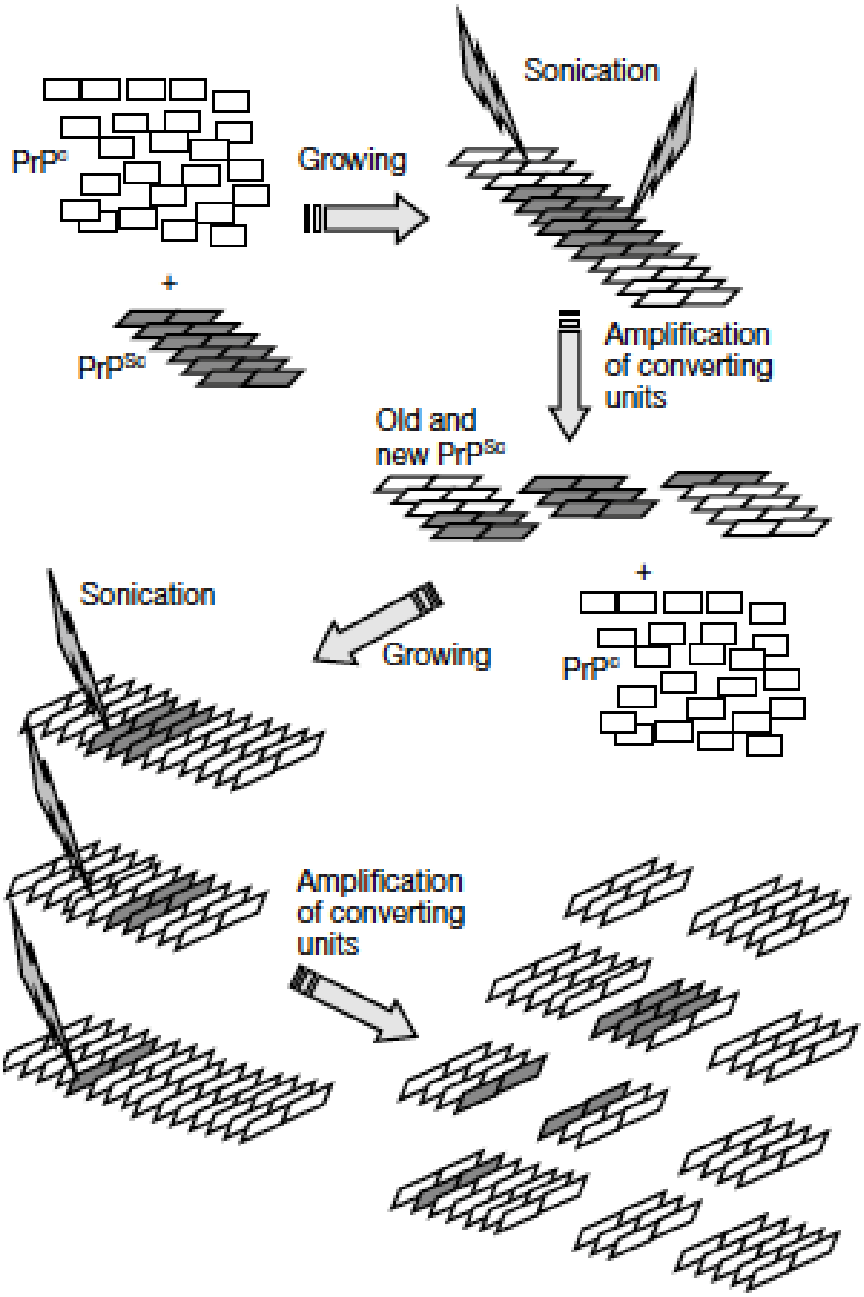

Fig 1.27 Diagrammatic representation of the PMCA procedure. Amplification is based on multiple cycles of PrP^{Sc} incubation in the presence of excess PrP^{C} followed by sonication. During the incubation periods, the size of oligomeric PrP^{Sc} is increased by incorporation of PrP^{C} into the growing aggregate, while during sonication the aggregates are disrupted, producing an expanded population of converting units. Adapted from Saborio et al.

In 2010, PMCA was adapted to the use of recombinant PrP as the substrate, rec-PMCA, which constituted a proof for the protein-only hypothesis (Wang 2010, Kim et al. 2010). However, other groups generated more infectious prions with the use of cofactors such as Supattapone's with RNA (Deleault et al. 2003) and phosphatidylethanolamine (Deleault et al., 2012) and Castilla's with dextran (Fernández-Borges et al., 2017).

1.5.2 Real Time – Quaking Induced Conversion (RT-QuIC)

In 2010, Caughey's group developed another in vitro technique to generate PrP amyloids.

The RT-QuIC assay incorporates $rPrP^C$ as a substrate, intermittent shaking of the reactions in 96-well plates, detergent and chaotrope-free reaction conditions, and ThT-based fluorescence detection - which uses thioflavin-T: a small molecule that gives strong fluorescence upon binding of amyloids which correlates with their concentration - of prion-seeded $rPrP^C$ amyloid fibrils. The advantage of using ThT detection is that it can be included in the reaction mixture. In the presence of amyloid fibrils, ThT undergoes an enhancement of fluorescence yield as well as a spectral shift in excitation/emission maxima that can be measured frequently over the RT-QuIC time course.

However, the material obtained with RT-QuIC, although propagative, is not infectious (Wilham et al., 2010).

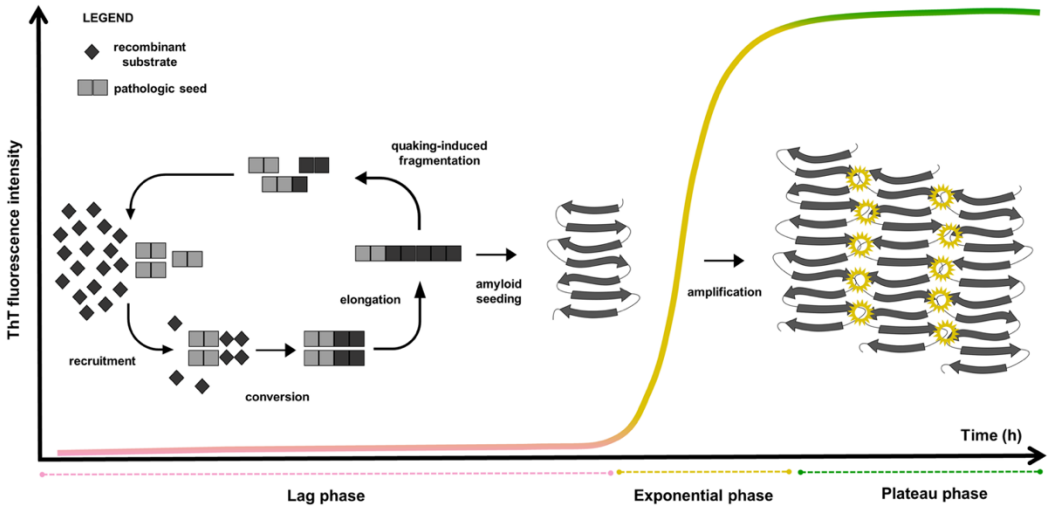

Fig 1.28 Schematic representation of the RT-QuIC reaction. The RT-QuIC reaction may be divided into temporal stages: the lag phase, the exponential phase and the plateau phase. The lag phase represents the time required for the reaction to take place. During this step, the seed is allowed to contact the substrate and to trigger the conformational change. Once enough energy is received by the system, ThT sensitive oligomers emerge, which incorporate the monomers into small aggregates (exponential phase). Eventually, when all the substrate is incorporated into fibrils, a plateau phase is observed Adapted from Candelise et al. 2020 (Permission granted by the journal).

1.5.3 Protein misfolding shaking amplification (PMSA)

In 2019, Castilla's group developed PMSA, a novel recombinant prion propagation system based on PMCA that substitutes sonication with shaking thereby allowing the production of unprecedented amounts of multi-labeled, infectious recombinant prions.

Shaking is generated by the use of shakers such as *Thermomixer* or *Monoshake* in a continuous mode. The substrate is composed of only recPrP and dextran sulfate in a buffer with a fixed composition that contains salts and detergents. This technique also requires the use of small zirconia-silica beads to improve the propagation efficiency.

The use of dextran sulfate, limits the structural heterogeneity of the *in vitro* propagated prions and makes possible, for the first time, the generation of infectious and likely homogeneous samples in sufficient quantities for studies with high-resolution structural techniques.

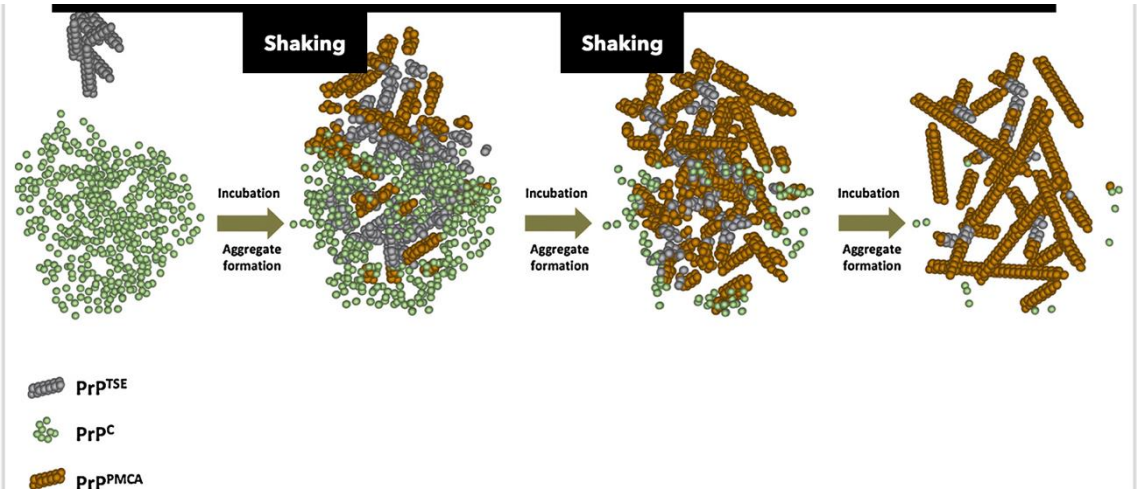

Fig 1.29 Diagrammatic representation of the PMSA procedure. Amplification is based on multiple cycles of PrP^{Sc} incubation in the presence of excess PrP^{C} followed by shaking. During the incubation periods, the size of oligomeric PrP^{Sc} is increased by incorporation of PrP^{C} into the growing aggregate, while during sonication the aggregates are disrupted, producing an expanded population of converting units. Adapted from Saá et Cervenakova 2015 (Permission requested by the journal).

1.6 Concluding remarks

After this brief overlook of the biology of prions and the historical evolution of the knowledge of the structure of PrP^{Sc}, since my thesis is centered around its structure I may say again that when I started in November 2017 there were only two contending models of PrP^{Sc}: the 4RβS and the PIRIBS. Both with their strong points and flaws. In this context, my purpose was to challenge both models in order to elucidate the structure of the most notorious prion, PrP^{Sc}, by acquiring and comparing different solid state nuclear magnetic resonance spectra.

2. OBJECTIVES

At the outset of this work, two contending plausible architectures had been proposed for the structure of PrP^{Sc} prion: a 4-rung-β-solenoid (4RβS) and a parallel-in register-intermolecular-β-sheet (PIRIBS). The main objective set for this thesis was to challenge both models in order to elucidate which is the real structure of PrP^{Sc}.

Such objective has been broken down into several specific tasks, some of which have been incorporated over time as new information arose from my own experiments and from the published results of others:

2.1 Preparation of non-infectious recPrP amyloid and infectious recBVPrP^{Sc}(109I) and analysis by FTIR to compare their secondary structures.

2.2 Acquisition and comparison of different ssNMR spectra (CP-HSQC, DREAM, DARR, INEPT-HSQC) of (U-^{13}C, ^{15}N)-recBVPrP^{Sc}(109I) to be able to distinguish between PIRIBS and 4RβS architectures.

2.3 Acquisition and comparison of PITHIRDS-CT spectra of ^{13}CO-Phe PrP amyloid, ^{13}CO-Tyr-Het-s (218-289) and ^{13}CO-Phe-recBVPrP^{Sc}(109I) as well as of ^{13}CO-Leu PrP amyloid, ^{13}CO-Tyr-Het-s (218-289) and ^{13}CO-Leu-recBVPrP^{Sc}(109I) to assess their intermolecular distances to be able to distinguish between PIRIBS and 4RβS architectures.

2.4 Acquisition and comparison of 1D-^{13}CP-MAS and PARIS spectra of ^{13}CO-PrP amyloid, ^{13}CO-Tyr-Het-s (218-289) and ^{13}CO-Phe-recBVPrP^{Sc}(109I) to obtain information about flexibility/rigidity of the samples.

2.5 Acquisition and comparison of $T_{1\rho}$ spectra of ^{13}CO-PrP amyloid, ^{13}CO-Tyr-Het-s (218-289) and ^{13}CO-Phe-recBVPrP^{Sc}(109I) to obtain further information about flexibility/rigidity of the samples.

2.6 Acquisition of ^{13}C-^{13}C DARR spectra of U-(^{13}C, ^{15}N)-Phe-recBVPrP^{Sc}(109I) to probe the chemical shifts of each one of the three Phe residues present in the sample.

3. HYPOTHESIS

Solid state nuclear magnetic resonance allows the study of the structure of PrP^{Sc} which we believed it was a 4-rung-β-solenoid at the beginning of my PhD in 2017.

4. MATERIALS AND METHODS

4.1 General reagents

All general reagents mentioned in the following sections were from Aldrich-Sigma unless otherwise indicated.

4.2 Production of recombinant protein

RecBVPrP(109I)23-231 was expressed by competent *E. coli* Rosetta (DE3) bacteria harboring pOPINE expression vector containing the wild type I109 bank vole Prnp gene whose sequence is shown next for the record with the insert in capital letters:

tcctgcatcttttaatcaaatcccaagatgtgtataaacgcgccggtatgtacaggaagaggtttatactaaactgttacattgcaa
acgtggtttcgtgtgccaagtgtgaaaaccgatgtttaatcaaggctctgacgcatttctacaaccacgactccaagtgtgtggg
tgaagtcatgcatcttttaatcaaatcccaagatgtgtataaaccaccaaactgccaaaaaatgaaaactgtcgacaagctctgtc
cgtttgctggcaactgcaagggtctcaatcctatttgtaattattgaataataaaacaattataaatgtcaaatttgtttttttattaacga
tacaaaccaaacgcaacaagaacatttgtagtattatctataattgaaaacgcgtagttataatcgctgaggtaatatttaaaatca
ttttcaaatgattcacagttaatttgcgacaatataatttttattttcacataaactagacgccttgtcgtcttcttcttcgtattccttctctt
tttcatttttctcttcataaaaattaacatagttattatcgtatccatatatgtatctatcgtatagagtaaatttttttgttgtcataaatatat
atgtctttttttaatggggtgtatagtaccgctgcgcatagtttttctgtaatttacaacagtgctattttctggtagttcttcggagtgtg
ttgctttaattattaaatttatataatcaatgaatttgggatcgtcggttttgtacaatatgttgccggcatagtacgcagcttcttctag
ttcaattacaccatttttttagcagcaccggattaacataactttccaaaatgttgtacgaaccgttaaacaaaaacagttcacctcc
cttttctatactattgtctgcgagcagttgtttgttgttaaaaataacagccattgtaatgagacgcacaaactaatatcacaaactg
gaaatgtctatcaatatatagttgctgatggccggccgtaatgagacgcacaaactaatatcacaaactggaaatgtctatcaat
atatagttgctctagttattaatagtaatcaattacggggtcattagttcatagcccatatatggagttccgcgttacataacttacgg
taaatggcccgcctggctgaccgcccaacgacccccgcccattgacgtcaataatgacgtatgttcccatagtaacgccaata
gggactttccattgacgtcaatgggtggagtatttacggtaaactgcccacttggcagtacatcaagtgtatcatatgccaagtac
gccccctattgacgtcaatgacggtaaatggcccgcctggcattatgcccagtacatgaccttatgggactttcctacttggcag
tacatctacgtattagtcatcgctattaccatgcatggtcgaggtgagccccacgttctgcttcactctccccatctccccccccctc
cccacccccaattttgtatttatttatttttttaattattttgtgcagcgatgggggcgggggggggggggggggcgcgcgccaggc
ggggcggggcggggcgaggggcggggcggggcgaggcggagaggtgcggcggcagccaatcagagcggcgcgctc
cgaaagtttccttttatggcgaggcggcggcggcggcggccctataaaaagcgaagcgcgcggcgggcgggagtcgctgc
gcgctgccttcgccccgtgccccgctccgccgccgcctcgcgccgcccgccccggctctgactgaccgcgttactcccaca
ggtgagcgggcgggacggcccttctccttcgggctgtaattagcgcttggtttaatgacggcttgtttcttttctgtggctgcgtg
aaagccttgaggggctccgggagggccctttgtgcgggggggagcggctcggggctgtccgcgggggggacggctgccttc
gggggggacggggcagggcggggttcggcttctggcgtgtgaccggcggctctagagcctctgctaaccatgttcatgcctt
cttctttttcctacagctcctgggcaacgtgctggttattgtgctgtctcatcattttggcaaagaattggatcggaccgaaattaat
acgactcactatagggaattgtgagcggataacaattcccctggagttaatccgggacctttaattcaacccaacacaatatatt
atagttaaataagaattattatcaaatcatttgtatattaattaaaatactatactgtaaattacattttatttacaatcaaaggagatata
ccatgAAGAAGCGGCCAAAGCCTGGAGGGTGGAACACTGGTGGAAGCCGATA
CCCTGGGCAGGGCAGCCCTGGAGGCAACCGGTACCCACCTCAGGGTGGTGG
TACCTGGGGACAGCCCCATGGCGGTGGCTGGGGACAGCCTCACGGTGGTGG
TTGGGGTCAGCCTCACGGTGGCGGTTGGGGTCAACCCCATGGCGGCGGCTG
GGGTCAAGGAGGTGGCACCCACAATCAGTGGAACAAGCCCAGTAAGCCAA
AAACCAACATGAAGCATGTGGCAGGCGCTGCCGCGGCTGGGGCAGTGGTGG
GGGGCCTGGGTGGCTACATGCTGGGAAGCGCCATGAGCAGGCCCATGATCC
ATTTCGGCAATGACTGGGAGGACCGCTACTACCGTGAAAACATGAACCGGT
ACCCTAACCAAGTGTACTACCGGCCGGTGGACCAGTACAACAACCAGAACA
ACTTCGTGCACGATTGCGTCAACATCACCATCAAGCAGCATACAGTCACCA
CTACCACCAAGGGGGAGAACTTCACGGAGACCGACGTCAAGATGATGGAG
CGCGTGGTGGAGCAGATGTGCGTCACCCAGTATCAGAAGGAGTCCCAGGCC

TACTACGAAGGGAGAAGTTCCTaacatcaccatcaccatcactaagtgattaacctcaggtgcaggctgc
ctatcagaaggtggtggctggtgtggccaatgccctggctcacaaataccactgagatcgatctttttccctctgccaaaaattat
ggggacatcatgaagccccttgagcatctgacttctggctaataaaggaaatttattttcattgcaatagtgtgttggaatttttgtg
tctctcactcggaaggacatatgggagggcaaatcatttaaaacatcagaatgagtatttggtttagagtttggcaacatatgccc
atatgtaactagcataaccccttggggcctctaaacgggtcttgaggggttttttgctgaaagcatgcggaggaaattctccttga
agtttccctggtgttcaaagtaaaggagtttgcaccagacgcacctctgttcactggtccggcgtattaaaacacgatacattgtt
attagtacatttattaagcgctagattctgtgcgttgttgatttacagacaattgttgtacgtattttaataattcattaaatttataatcttt
agggtggtatgttagagcgaaaatcaaatgattttcagcgtctttatatctgaatttaaatattaaatcctcaatagatttgtaaaata
ggtttcgattagtttcaaacaagggttgtttttccgaaccgatggctggactatctaatggattttcgctcaacgccacaaaacttg
ccaaatcttgtagcagcaatctagctttgtcgatattcgtttgtgttttgttttgtaataaaggttcgacgtcgttcaaaatattatgcg
cttttgtatttctttcatcactgtcgttagtgtacaattgactcgacgtaaacacgttaaatagagcttggacatatttaacatcgggc
gtgttagctttattaggccgattatcgtcgtcgtcccaaccctcgtcgttagaagttgcttccgaagacgattttgccatagccaca
cgacgcctattaattgtgtcggctaacacgtccgcgatcaaatttgtagttgagctttttggaattgcgatcgcataacttcgtatag
catacattatacgaagttataagctcggaacgctgcgctcggtcgttcggctgcggcgagcggtatcagctcactcaaaggcg
gtaatacggttatccacagaatcaggggataacgcaggaaagaacatgtgagcaaaaggccagcaaaaggccaggaaccg
taaaaaggccgcgttgctggcgtttttccataggctccgccccctgacgagcatcacaaaaatcgacgctcaagtcagaggtg
gcgaaacccgacaggactataaagataccaggcgtttccccctggaagctccctcgtgcgctctcctgttccgaccctgccgc
ttaccggatacctgtccgcctttctcccttcgggaagcgtggcgctttctcaatgctcacgctgtaggtatctcagttcggtgtag
gtcgttcgctccaagctgggctgtgtgcacgaacccccgttcagcccgaccgctgcgccttatccggtaactatcgtcttgag
tccaacccggtaagacacgacttatcgccactggcagcagccactggtaacaggattagcagagcgaggtatgtaggcggt
gctacagagttcttgaagtggtggcctaactacggctacactagaagaacagtatttggtatctgcgctctgctgaagccagtta
ccttcggaaaaagagttggtagctcttgatccggcaaacaaaccaccgctggtagcggtggtttttttgtttgcaagcagcagat
tacgcgcagaaaaaaaggatctcaagaagatcctttgttaccaatgcttaatcagtgaggcacctatctcagcgatctgtctattt
cgttcatccatagttgcctgactccccgtcgtgtagataactacgatacgggagggcttaccatctggccccagtgctgcaatg
ataccgcgagacccacgctcaccggctccagatttatcagcaataaaccagccagccggaagggccgagcgcagaagtgg
tcctgcaactttatccgcctccatccagtctattaattgttgccgggaagctagagtaagtagttcgccagttaatagtttgcgcaa
cgttgttgccattgctacaggcatcgtggtgtcacgctcgtcgtttggtatggcttcattcagctccggttcccaacgatcaaggc
gagttacatgatcccccatgttgtgcaaaaaagcggttagctccttcggtcctccgatcgttgtcagaagtaagttggccgcagt
gttatcactcatggttatggcagcactgcataattctcttactgtcatgccatccgtaagatgcttttctgtgactggtgagtactcaa
ccaagtcattctgagaatagtgtatgcggcgaccgagttgctcttgcccggcgtcaatacgggataataccgcgccacatagc
agaactttaaaagtgctcatcattggaaaacgttcttcggggcgaaaactctcaaggatcttaccgctgttgagatccagttcgat
gtaacccactcgtgcacccaactgatcttcagcatcttttactttcaccagcgtttctgggtgagcaaaaacaggaaggcaaaat
gccgcaaaaaagggaataagggcgacacggaaatgttgaatactcatactcttccttttcaatattattgaagcatttatcaggg
ttattgtctcatgtccgcgcgtt.

Bacteria from a glycerolate maintained at –80 °C were inoculated using a pipete tip into the growth media (LB) and subsequently were grown in a 250 ml Erlenmeyer flask containing 50 ml of LB broth, which had been previously prepared and frozen, overnight at 37 °C and 220 rpm. The next morning the turbidity was checked and if it has increased that means that has been bacterial growth. The turbidity increased thus the culture was then transferred to two 2 L Erlenmeyer flasks containing each 500 ml of minimal medium supplemented with 3 g/L glucose, 1 g/L NH_4Cl, 1 M $MgSO_4$ (1 ml/L), 0.1 M $CaCl_2$ (1 ml/L), 10 mg/ml thiamine (1 ml/L) and 10 mg/ml biotin (1 ml/L). For production of uniformly labelled (U-^{13}C,^{15}N)-PrP, glucose and NH_4Cl were substituted by (U-^{13}C)-glucose and $^{15}NH_4Cl$ (Cortecnet, Paris) as the sole carbon and nitrogen sources. When the culture reached an OD_{600} of ~0.9-1.2 AU, isopropyl β-D-1-thiogalactopyranoside (IPTG) was added to induce expression of PrP overnight under the same temperature and agitation conditions. Bacteria were then centrifuged in an Avanti J20 centrifuge using a rotor Beckman JA-10 5000 xg for 15 minutes at 4ºC, supernatant was then discarded by decantation and the pellets were frozen for 2h, or

alternatively overnight, at -80ºC. Pellets were resuspended in 60 mL of lysis buffer: 50 mM Tris-HCl, 5 mM EDTA, 20 mM $MgCl_2$, 1% Triton X-100, pH 8 previously prepared plus fresh addition of three previously thaw aliquots to a final concentration of 1 mM PMSF, 10 μg/mL lysozime, 30 u/mL DNase. All the pellets in the 60 mL of lysis buffer were combined in a single centrifuge tube and then it was shaken on a horizontal shaker 1h at room temperature at 225 rpm. Afterwards, it was sonicated using a tip sonicator with the sample on ice 3 times for 30 seconds at 30% power. Then it was transferred to two tubes for rotor Bekman JA-20 using again Avanti J20 centrifuge at 20,000 xg for 20 minutes at 4ºC. Next, the supernadant was discarded by decantation and the inclusion bodies pellets were resuspended in 15 mL of MQ water and centrifuged again under the same conditions. Later, the supernadant was discarded again by decantation and the inclusion bodies solubilized in 20 mM Tris-HCl, 0.5 M NaCl, 6 M Gdn/HCl, pH = 8 overnight at 37ºC and 225 rpm. The next day, they were centrifuged 20,000 xg, 1h, 4ºC in a Beckman rotor JA-20 using an Avanti J20 centrifuge. This time, supernadant was collected in a 30 mL tube and sonicated on ice using a tip sonicator (Roadrunner Buster model, Acme Brand, New México, USA) 3 times for 30 seconds at 30% of power. Then, it was filtered using a 0,45 μm filter and a 1 mL syringe. A 1:1000 aliquote was saved named "inclusion bodies". Although the protein does not contain a His-tag, purification of the protein was performed with a histidine affinity column (HisTrap FF crude 5 ml, GE Healthcare Amersham) taking advantage of the natural His present in the octapeptide repeat region of PrP. The column was conected to a peristaltic pump and equilibrated with binding buffer: 20 mM Tris-HCl, 500 mM NaCl, 5 mM imidazole, 2M Gnd/HCl, pH 8, 25 mL at 5 mL/min. Then the sample was loaded into the column at 2 mL/min and another aliquot 1:1000 of the eluted which was gathered was saved named "load". Next, the column was washed with 50 mL of binfing buffer at 5 mL/min and another aliquot 1:1000 of the eluted which was gathered was saved named "wash". After elution in five fractions (elution 1, elution 2, elution 3, elution 4 and elution 5) whose respectively aliquots were collected with 50 mL of buffer containing 20 mM Tris-HCl, 0.5 M NaCl, 500 mM imidazole and 2 M Gdn/HCl, pH = 8, at 2 mL/min the quality and purity of protein batches was assessed by BlueSafe (NZYTech, Lisbon) staining after electrophoresis in SDS-PAGE commercial gels 4-12% Bis-Tris from invitrogen, using the following conditions: 70 V for 10 min, 110 V for 10 min and 150 V for 40 min. Protein concentration was measured using the Nanodrop device without using the molar extinction coefficient for comparison purposes to another group which does not use it as well. Finally, Gdn/HCl was added, to a final concentration of 6 M, for long-term storage of purified protein preparations at –80 °C.

For production of (^{13}CO-Phe)-PrP, (^{13}CO-Leu)-PrP, (^{13}CO-Asp)-PrP and (U-^{13}C,^{15}N-Phe)-PrP the bacteria were first grown in a 250 ml Erlenmeyer flask containing 50 ml of LB broth overnight at 37 °C and 220 rpm. After checking the next morning for the increase in turbidity, the culture was then transferred to two 2 L Erlenmeyer flasks containing each 500 ml of minimal medium supplemented with all essential non-labelled L-amino acids except the target amino acid at a concentratiom of 0.1 g/L each, and the labelled target amino acid also at a concentration of 0.1 g/L, and transferred to two 2 L Erlenmeyer flasks. Whe preparing the suplement it is important to note that tyrosine must be added lastly as it does not solve until autoclavated. The cultures were incubated at 37 °C, 225 rpm, for 2-3 hours until OD was 0.8 or higher, after which expression was induced by addition of IPTG to a final concentration of 1 mM and the culture was then incubated for 3 hours at 37 °C, 225 rpm. Bacteria were afterwards pelleted and processed as described above.

4.3 Conversion of recBVPrP(109I)23-231 to recBVPrP(109I)^{Sc}

Conversion of recBVPrP(109I)23 231 to recBVPrP(109I)^{Sc} was achieved by PMSA as previously described (Eraña et al.). The procedure was carried out at the CIMUS BSL2 lab. The purified recPrP stored in buffer containing 6 M Gdn/HCl (*vide supra*) was diluted 1:5 in phosphate buffered saline (PBS) and dialyzed against PBS at 1:2000 ratio for 1 h at room temperature. The dialyzed sample was centrifuged at 19000 g for 15 min at 4 °C and the supernatant was used for PMSA substrate preparation. The concentration of recPrP in the supernatant was measured spectrophotometrically and adjusted to the working concentration, which was 20 μM, unless otherwise indicated. The protein was then mixed at a 1:9 ratio with conversion buffer (150 mM NaCl, 10 g/L Triton X-100, and 0.5% w/v of dextran sulfate sodium salt from *Leuconostoc spp*. with sizes ranging from 6500 to 10000, Sigma-Aldrich in PBS). The substrate was aliquoted either used immediately or stored at –80 °C until required. PMSA was performed by transferring 18 ml of the recPrP substrate to a 50 ml Falcon tube containing 2.8 g of washed 1 mm zirconia/silica beads (11079110Z, BioSpec Products Inc.) and 2 ml of recPrP^{Sc} seed obtained from a previous round of PMSA initially. Later on a new method was developed which consised in using 20 zirconia/silica beads previously embedded with the given PrP^{Sc} seed plus 20 mL of substrate. In order to obtain these embebbed beads 1 mL of previously washed with PBS and DNase free sterile water dried virgin zirconia beads were transferred to a 50 mL Falcon vial plus 1 mL of PrP^{Sc} PMSA product, enough so all beads were covered by it and it was shaked for 1 h at 39ºC 900 rpm. After this first round, embebed bead were already obtained and ir order to keep producing more the same protocol was reproduced but using previusly charged beads instead as seed instead of the PMSA product. The tube was placed in a Shaker and incubated at 39 °C and 900 rpm in a continuous mode for 16-24 h.

4.4 Proteinase K digestion and analysis of digestion products

Samples were digested by addition of PK (Roche) from a concentrated stock solution of 500 ug/mL to a final concentration of 25 μg/ml and incubation at 42 °C for 1 h. PK aliquots are prepared in advance as 100 μL each and thaw when needed; what is not used is thrown away. The sample was then immediately centrifuged at 19000 g at 4 °C for 30 min, the supernatant was discarded and the pellet resuspended and washed with 1 ml of PBS. After a further 30 min at 19000 g at 4 °C, the supernatant was discarded by careful pipetting.

For analysis of PK-induced fragmentation, PK-treated recBVPrP^{Sc}(109I) pellets were dissolved in reducing Laemmli buffer and heated at 95 °C for 10 min, followed by SDS-PAGE in commercial 4-12% Tris/glycine gels (NuPage, Thermo-Fisher). After electrophoresis, gels were stained with BlueSafe Coomassie stain (NZYTech, Lisbon). Alternatively, for mass spectrometry-based analysis, the pellets were resuspended in 50 μl of 6 M Gdn/HCl with 3 pulses (5 s each) of a tip sonicator and incubated at 37 °C for 1 h. TFA was carefully added in a chemical hood to a final concentration of 1%. Samples (4 μl) were injected to a micro liquid chromatography system (Eksigent Technologies nanoLC 400, SCIEX) coupled to a high speed Triple TOF 6600 mass spectrometer (SCIEX) with a micro flow source, and equipped with a silica-based reversed phase column Chrom XP C18 150 × 0.30 mm, 3 mm particle size and 120 Å pore size (Eksigent, SCIEX). A YMC-TRIART C18 trap column was connected prior to the separating column, on-line (3 mm particle size and 120 Å pore size, YMC Technologies, Teknokroma). After sample loading and washing with 0.1% formic acid in water to remove Gdn/HCl and other non-peptide components of the sample, the flow was

switched on to the analytical column and separation proceeded at a flow rate of 5 µl/min with a solvent system consisting of 0.1% formic acid in water as mobile phase A, and 0.1% formic acid in acetonitrile as mobile phase B. Peptides were separated over 40 min with a gradient ranging from 2% to 90% of mobile phase B. Data acquisition was performed in a TripleTOF 6600 System (SCIEX, Foster City, CA) using a Data dependent workflow. Source and interface conditions were the following: ionspray voltage floating (ISVF) 5500 V, curtain gas (CUR) 25, collision energy (CE) 10 and ion source gas 1 (GS1) 25. Instrument was operated with Analyst TF 1.7.1 software (SCIEX, USA). Switching criteria was set to ions greater than mass to charge ratio (m/z) 350 and smaller than m/z 1400 with charge state of 2-5, mass tolerance 250 ppm and an abundance threshold of more than 200 counts (cps). Former target ions were excluded for 15 s. The instrument was automatically calibrated every 4 hours using tryptic peptides from PepCalMix as external calibrant. For data analysis, the sample TIC was opened using the Peak View 2.2 software that allows protein reconstruction. The LC-MS Peptide Reconstruct feature uses a peak finding algorithm to identify groups of peaks that form isotope series and charge series. Protein deconvolution was carried out between 800 to 20000 Da.

4.5 Negative stain TEM

Sedimented recBVPrP23-231 amyloid fibers, recBVPrP^{Sc} or Het-s samples were adsorbed on Formvar carbon coated gold grids, washed with water thrice, negatively stained with freshly filtered 2% uranyl acetate, air dried and imaged using a JEOL JEM F200CF HR electron microscope.

4.6 Recombinant PrP amyloid fibers

(^{13}CO-Phe) and (U-^{13}C,^{15}N-Phe) recombinant non-infectious BVPrP(109I)23-231 fibers were prepared as described by (Torrent *et al)*. PrP is lyofilized and then a 10 ml solution of PrP 0.6 mg/ml in 50 mM MES buffer, pH 6.0 containing 2.4 M Gdn/HCl was placed in a 15 ml Falcon tube. The tube (arranged horizontally on the plate surface) was incubated with continuous orbital shaking at 30 rpm at 37 °C inside a heater. Fibril formation was monitored using a ThT binding assay: aliquots of the reaction mixture were withdrawn and diluted into 10 mM sodium acetate buffer, pH 5.0 to a final PrP concentration of 0.3 µM. Then ThT (Invitrogen) 1 mM in water stock solution stored in the dark at 4ºC was added to a final concentration of 10 µM and fluorescence measured at $\lambda_{ex.}$ 450 nm, $\lambda_{em.}$ 485 nm. When ThT fluorescence reached the plateau stage, samples were dialyzed in 10 mM sodium acetate, pH 5.0, and collected by ultracentrifugation for 45 min at 228147 g using a Beckman Optima TL100 Ultracentrifuge and TLA-100.3 rotor, and resuspended in 10 mM sodium acetate, pH 5.0. A washing step was performed by repeating the ultracentrifugation and resuspension steps. The final pellet was resuspended in deionized water. For TEM imaging, 10 uL of fibers were adsorbed on freshly glow discharged, Formvar carbon-coated grids, washed with water thrice, negatively stained with freshly filtered 2% uranyl acetate, air-dried and viewed using a JEOL JEM-F200CF-HR electron microscope.

4.7 Het-s fibers

The His$_6$-Het-s prion forming domain Het (218-289) (Sabate et al., Sabate et al. 2) was expressed in BL21 *E. coli* (bacteria with the plasmid incorporated generously provided by Raimon Sabaté, University of Barcelona), and purified using NTA affinity chromatography as described for PrP. The protein buffer was exchanged to 200 mM acetic acid (pH = 2.5) using a PD-10 gel filtration column. Protein concentration was

adjusted to 200 μM and an equal volume of 1 M Tris/HCl, pH 8 was added. The resulting sample was incubated at 37 °C with shaking at 1400 rpm in a Thermomixer for 24 h. A visible bulky sediment was visible at the end of the incubation period, which was collected by centrifugation and resuspended in the desired volume of deionized water. The sample was imaged by TEM as described (vide supra) for the PrP amyloid.

4.8 FTIR spectra acquisition

IR-MSP analysis of highly purified PrP^{Sc} extracts was carried out as previously described (Daus et al.). Mid-IR spectra were acquired in transmission mode using an IFS 28/B FT-IR spectrometer from Bruker (Bruker Optics GmbH, Ettlingen Germany) that was linked to an IRscope II infrared microscope (Bruker). IR microspectra
were recorded with a spatial resolution of approximately 80 μm. Nominal spectral resolution was 4 cm^{-1}, and the zero filling factor was 4. For each background and for
each sample spectrum, 512 individual interferograms were averaged, zero-filled and apodized using a Blackman-Harris 3-term apodization function. For the examined PrP^{Sc} and PrP amyloid infrared spectra were recorded at three different positions in PrP^{Sc} or PrP sample spots dried on CaF_2 windows. Data acquisition and spectral preprocessing was carried out by utilizing Bruker's instrument software OPUS v. 5.5. Second derivative spectra were obtained by means of a 9-smoothing point Savitzki-Golay derivative filter. Spectra from the PrP amyloid and the PrP^{Sc} samples were vector normalized in the wave number region between 1610 and 1700 cm^{-1}.

4.9 Solid-State NMR measurements (ssNMR).

(U-^{13}C,^{15}N)-recBVPrP^{Sc}(109I),(^{13}CO-Phe)-recBVPrP^{Sc}(109I),
(^{13}CO-Leu)-recBVPrP^{Sc}(109I),(^{13}CO-Asp)-recBVPrP^{Sc}(109I),(U-^{13}C,^{15}NPhe)-recBVPrP^{Sc}(109I) solutions, as obtained by PMSA, were treated to a final concentration of 10 μg/ml of PK from a freshly prepared PK stock solution of 500ug/mL and 10 mL. The samples were then centrifuged at 30,000 g for 1 h at 20 °C in 85 ml OAK polycarbonate (Nalgene) tubes using a Beckman 70.1 Ti 03E1372 rotor in an Optima Ultracentrifuge. The supernatant was carefully removed with a Pasteur pipette, and all the pellets were moved to one single tube by resuspending them in PBS then it was centrifuged under the same conditions for another hour. Next, the supernatant was again carefully removed and the pellet was resuspended in 1 mL of PBS and centrifuged inside a 1.5 mL eppendorf tube at 20,000 rpm for 15 minutes. Once again the supernatant was removed and the pellet resuspended in 1 mL of either MilliQ water or DNAse free water, centrifuged under the same conditions for additional 15 min and supernatant removed to obtain the final pellet. The sample was then loaded into a 1.3 mm rotor for ssNMR measurement using the Bruker solid sample preparation kit. The final pellet was resuspended in 50 μl water by repeated pipetting and transferred to the loading funnel with the 1.3 mm rotor inserted. This assembly was placed in a home-built desiccation chamber containing $CaCl_2$ until all the water evaporated, leaving thin PrP^{Sc} scales around the border of the 1.3 mm rotor. Using the Bruker loading rod, the scales were carefully introduced and compacted into the rotor, either together with 2 μl of milliQ water to obtain a hydrated sample or not. Alternatively, the final pellet was dried out inside the 1.5 mL eppendorf tube at 60ºC for a couple of hours and then overnight at 37ºC, the next morning the pellet was deattached from the wall of the eppendorf using a metal clip, overturned over the rotor and then pushed inside with a small metal wire. The rotor was capped and placed in the solid NMR probe. Solid-state NMR experiments were measured at 278 K in a Bruker NEO 17.6 T spectrometer (proton resonance 750 MHz and ^{13}C resonance 188 MHz) equipped with a

$^{1}H/^{13}C/^{15}N$ triple resonance solid probe for 1.3 mm zirconia rotors and an available range of MAS rates from 8 to 67 kHz.

The spectrometer control software was TopSpin 4.0. All spectra were processed with MestreNova v14.0 (Mestrelab Research Inc.). Carbon-13 chemical shifts were referenced to the CA signal of solid glycine at 43.5 ppm. Nitrogen-15 chemical shifts were referenced to the ^{15}N peak of a solid ^{15}N labelled sample of glycine at 35.0 ppm. Proton chemical shifts were referenced to the intense water peak at 4.7 ppm.

1D ^{13}C cross-polarization spectra (^{13}C CPMAS) were measured at a MAS rate of 40 kHz (pulse program *hC.cp* of the Bruker library) with an inter-scan delay (d_1) of 2 s. Cross-polarization was applied during 3 ms with a constant carbon field strength of 66.6 kHz; the power on the ^{1}H nucleus was linearly ramped from 70% to 100% with a peak field strength of 152 kHz. Heteronuclear decoupling during FID acquisition was performed with SPINAL-64 with a proton field strength of 170 kHz. The spectrum was acquired with 1500 scans.

1D ^{13}C PARISxy direct polarization spectra (^{13}C PARIS) were measured at a MAS rate of 40 kHz. At the end of the inter-scan relaxation delay, immediately before the ^{13}C excitation pulse, a train of PARISxy 12.5 μs pulses with 24 kHz field strength were applied to introduce modulation sidebands at half the rotation rate, causing ^{13}C enhancement. The pre-scan delay (d_1) was set to 0.5 s, which is followed by PARISxy irradiation during 3 s. The ^{13}C excitation pulse had a tilt angle of 90° and was applied with a B1 field strength of 62.5 kHz. Heteronuclear decoupling during acquisition of the FID was performed with SPINAL-64 with a proton field strength of 170 kHz. The spectrum was acquired with 1500 scans.

2D ^{1}H-^{13}C CP-HSQC spectra were measured at 50 kHz MAS (pulse sequence *hCH2D.dcp* of the Bruker library). The ^{1}H and ^{13}C carriers were placed at 2.27 and 80 ppm, respectively. The spectral widths in the ^{1}H and ^{13}C dimensions were 19.6 and 175 ppm, respectively. The initial proton/carbon cross polarization contact time was 0.7 ms and the proton contact pulse power used an ascending linear ramp of 50%. The final carbon/proton cross polarization contact time was 0.4 ms and the proton contact pulse power used a descending linear ramp of 50%. MISSISSIPPI water suppression pulses were applied on proton at 15 kHz during 7.66 ms. The number of complex points acquired in the t_2 and t_1 dimensions were 588 and 300, respectively. The FID was acquired under heteronuclear decoupling at 20 kHz with WALTZ-16 for both ^{13}C and ^{15}N nuclei. The inter-scan delay was 1.4 s and the number of scans per t_1 value was 16.

2D ^{13}C-^{13}C DARR spectra were measured at 20 kHz MAS (pulse sequence *cpSPINDIFF* of the Bruker library). The ^{13}C carrier was placed at 110 ppm and the spectrum covered a spectral width of 220 ppm in each carbon dimension. The ^{1}H carrier was set on the water resonance at 4.7 ppm. The initial proton/carbon cross polarization contact time was 2 ms and the proton contact pulse power used an ascending linear ramp of 50%. During the mixing time of the sequence, a DARR ^{1}H pulse was applied at 20 kHz. The number of complex points acquired in t_2 and t_1 dimensions were 1666 and 300, respectively. The FID was acquired under heteronuclear proton decoupling at 110 kHz with SPINAL-64. The inter-scan delay was 2.5 s and the number of scans per t_1 value was 88.

2D ^{13}C-^{13}C DREAM spectra were measured at MAS frequencies, ω_r, of 45 and 24 kHz (pulse sequence *hCC_dream2D-cp* of the Bruker library). The ^{13}C carrier was centered at 110 ppm and the spectrum covered a spectral width of 220 ppm in each carbon dimension. The ^{1}H and ^{15}N carriers were centered at 3.5 and 120 ppm, respectively. The DREAM mixing time was 3 ms and consisted in a ^{13}C adiabatic pulse of frequency given by $0.45 \cdot \omega_r$, which in our spectra correspond to a frequency of 20.3 (/10.8) kHz at 45 (/24) kHz MAS. The ^{13}C adiabatic pulse was applied at a frequency of 50 ppm and simultaneously with ^{1}H CW decoupling at 110 kHz. The number of complex points acquired in t_2 and t_1 dimensions were 1000 and 600, respectively. The FID was acquired under heteronuclear decoupling in ^{1}H at 110 kHz with SPINAL-64 and in ^{15}N at 20 kHz with WALTZ-16. The inter-scan delay was 2 s and the number of scans per t_1 value was 32.

2D ^{1}H-^{13}C INEPT-HSQC spectra were measured at 45 or 60 (pulse sequence hCH2D.hsqc of the Bruker library). The 1H and 13C carriers were centered at 2.27 and 75 ppm, respectively. The 1H and 13C spectral widths were 19.6 and 180 ppm, respectively. The INEPT delays were optimized for relaxation losses using a nominal value of scalar coupling 1JCH of 200 Hz, a value that is over the expected value of 145 Hz. MISSISSIPPI water suppression pulses were applied in proton at 15 kHz during 1.66 ms. The number of points acquired in t2 and t1 dimensions were 323 and 220, respectively. The FID was acquired under 13C and 15N heteronuclear decoupling at 20 kHz with WALTZ-16. The inter-scan delay was 1.6 s and the number of scans was 48.

PITHIRDS-CT (Shewmaker et al.) spectra were acquired on ^{13}CO selectively labelled samples at MAS 40 kHz with sensitivity enhancement using Pulse-Spin-Locking (PSL) acquisition (Petkova et al.) The conditions for the initial cross-polarization step were identical to the ^{13}C-CPMAS spectrum described above. The Constant-Time (CT) evolution period with ^{13}C PITHIRDS dipolar recoupling was applied for a total of 33.6 ms, as defined by Tycko (Shewmaker et al.). It comprises cycles of sixteen rotor periods occupied with 180° pulses of 8.33 μs duration ($\tau_r/3$) with displacements in time of 0, $\tau_r/3$ and $2\tau_r/3$, where τ_r is the rotor period duration. A series of effective dipolar evolution periods were explored in different spectra ranging from 0 to the maximum of 33.6 ms. During the PITHIRDS-CT sequence and acquisition periods, ^{1}H TPPM decoupling at 110 kHz field strenght was applied. Carbon-13 PSL π pulses had a duration of 7 μs and were applied with 20 rotor cycles per echo. The relaxation delay (d_1) was set to 4 s and each spectrum was acquired with 4096 scans in 4 h 36 min. Data analysis included natural abundance correction for the ^{13}C background. PITHIRDS-CT curves were simulated with in-house software written in Fortran, gently provided by Robert Tycko (Laboratory of Chemical Physics, NIDDK, NIH, Bethesda, USA). The simulation of PITHIRDS-CT intensity curves was performed for a system of five ^{13}C atoms arranged linearly at distances of 4, 5, 6 and 7 Å.

2D ^{13}C-^{13}C-TOCSY (Hung. et al) was acquired for sample (U-^{13}C,^{15}N-Phe)-recBVPrP^{Sc} at 16.9 kHz MAS. The initial cross-polarization was applied during 2 ms with a constant carbon field strength of 118 kHz; the power on the ^{1}H nucleus was linearly ramped from 50% to 100% with a peak field strength of 202 kHz. After t_1 evolution, spin-lock was applied during 3.55 ms with continous wave pulses simultaneous on ^{13}C and ^{1}H with field strengths of 51.4 and 100 kHz, respectively. In both ^{13}C dimensions the center was placed at 100 ppm and the spectral width was 221 ppm. Heteronuclear decoupling during FID acquisition was performed with SPINAL-64 with a proton field strength of 110 kHz. The

indirect dimension was acquired with 300 complex points in t_1 with the States-TPPI acquisition mode and 833 points in t_2. The number of scans per t_1 increment was 96 and the relaxation delay (d_1) was 2 s. The total measurement time was 16 h 25 min.

Carbon-13 Rotating frame relaxation time (*($^{13}C\_T_{1r}$*): were measured at 278 and 313K for the three ^{13}CO selectively labelled samples (sequence *cpxt1rho* of the Bruker library). The ^{13}C carrier was placed centered at the ^{13}CO signal at ~175 ppm and the ^{1}H carrier was set at 5.0 ppm. The MAS rate was set to 60 kHz to reduce CSA contributions and the ^{13}C spin-lock field strength was set to 70 kHz, a frequency that avoids the rotatory-resonance ill-conditions at $0.5 \cdot w_R$ and $1 \cdot w_R$. The initial ^{1}H-^{13}C cross-polarization used a contact time of 3 ms. A total of 16 durations of the spin-lock pulse (t_{SL}) were explored that were acquired as independent fids of a pseudo-2D spectrum. The durations of t_{SL} were: 1, 8, 16, 32, 50, 70, 86, 100, 120, 150, 180, 200, 230, 260, 280 and 320 ms. Heteronuclear decoupling during the spin-lock pulse and FID acquisition was performed with Spinal-64 with a proton field strength of 170 kHz. The interscan delay (d_1) was 5 s and each fid was acquired with 200 scans. The peak intensity at each t_{SL} duration was fitted to a mono-exponential function (eq. 1) using software Origin8.0 to determine the T_{1r} relaxation time.

$$M_{xy}(\tau_{SL}) = M_0 \cdot \exp(-\tau_{SL} / T_{1\rho}) \qquad \text{eq. 1}$$

Where M_{xy} is the signal intensity at a given τ_{SL} and M_0 is the intensity at the minimum duration of the spin-lock time.

5. RESULTS

5.1 Expression of BVPrP

BVPrP(109I)23-231 was expressed in *E. coli* and purified using NTA affinity chromatography.

Although lacking a His tag, the His residues in the octarepeat region of PrP result in its binding to the NTA matrix. Fig.5.1 shows the purification process with a yield of 80%: in lane 1 protein suspended in inclusion bodies buffer, then load, wash, first elution fraction, second elution fraction and third elution fraction.

As we can see BVPrP protein appears mainly in the first elution fraction with a purity of 90%. PrP protein has a theoretical average weight of almost 23,000 Da and an experimental one of 25,000 Da.

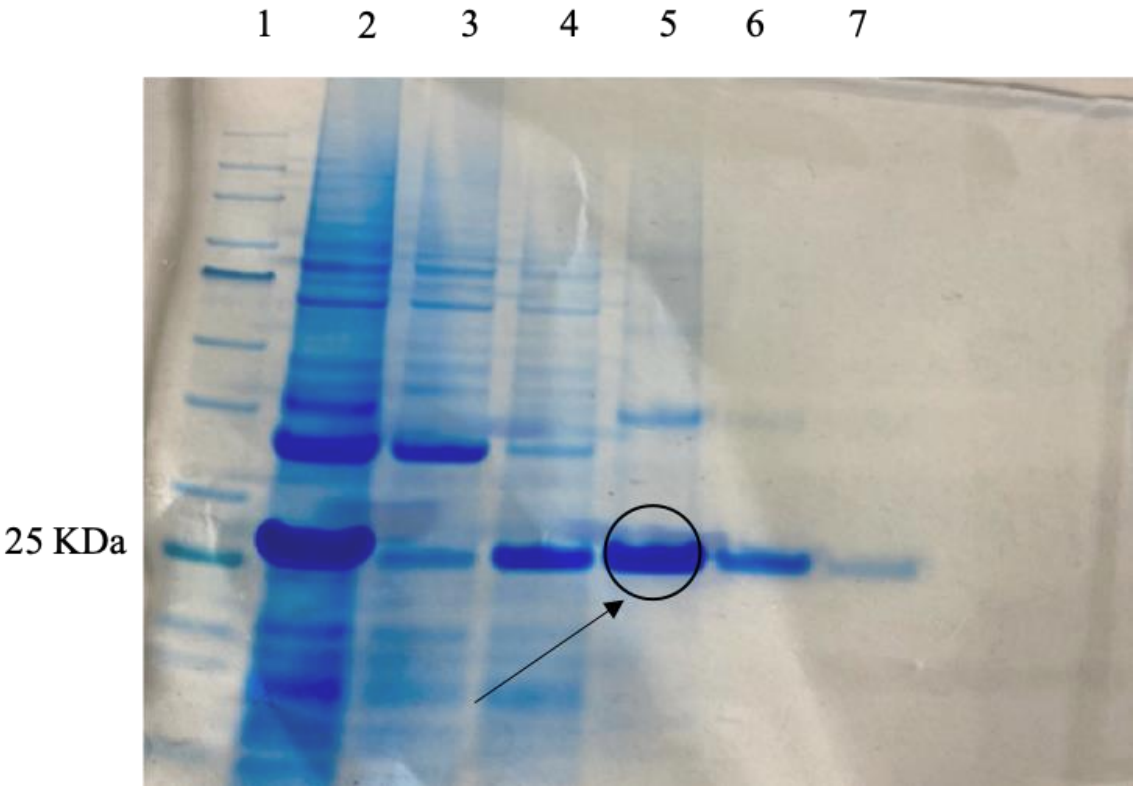

Fig.5.1. Generation of BV PrP. The resulting purification product using HisTrap immobilized metal affinity chromatography was subjected to SDS-PAGE using 4-12% Bis-Tris commercial gels, which were then stained with Coomassie blue. Protein has a weight of 23 kDa at ≅ 25 kDa in lane 5 and its dimer can also be seen at around 45 KDa.

5.2 Generation of recombinant BVPrP^{Sc}

PMSA-based procedure to prepare recBVPrP^{Sc}(109I)23-231 includes a PK-treatment step to ensure elimination of any non-converted PrP substrate. Such treatment also eliminates the amino-terminal tail ~23-96 of recBVPrP^{Sc}(109I)23-231 and introduces some internal nicks (Eraña et al.). PMSA plus PK treatment has an approximate yield of 1%. For simplicity, I will refer to this PK-treated recBVPrP^{Sc}(109I)23-231 as recBVPrP^{Sc}. This material has been described in a previous publication (Eraña et al.) and is highly infectious, with attack rates of 100% and titers of $6.34 \cdot 10^4$/µg of PrP in TgVole (1x).

A full biochemical characterization of this material was carried out to complete the partial one described in previous study (Eraña et al.). I first analyzed the pattern of PK-resistant fragments using the 4-12% commercial Tris/glycine SDS-PAGE gels. We detected the known main fragments with apparent MWs of 15.5 and 9.5 kDa and a faint, smeary band centered around ~6 kDa (Fig. 5.2).

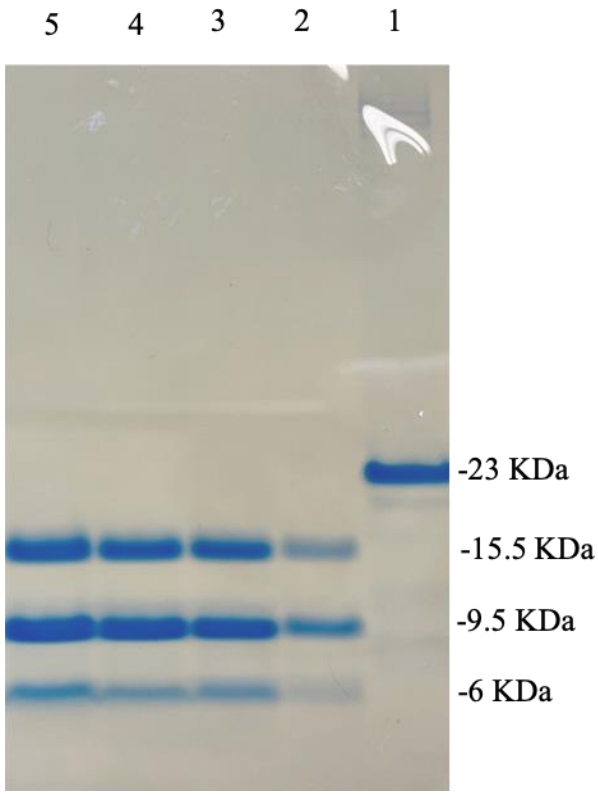

Fig. 5.2. Biochemical characterization of recBVPrP^{Sc}. RecBVPrP(109I) was converted to recBVPrP^{Sc}(109I) by PMSA; the procedure involves a final treatment with 25 µg/ml PK to eliminate any unconverted substrate. A: The resulting product was subjected to SDS-PAGE using 4-12% commercial gels and Precision Plus Protein Dual Xtra Standards marker from Bio-Rad. In lane 1 PrP undigested and lanes 2-5 different PrP^{Sc} preparations PK-treated 25 µg/mL.

GGGTHNQWNKPSKPKTNMKHVAGAAAAGAVVGGLGGYMLGSAMSR
PMIHFGNDWEDRYYRENMNRYPNQVYYRPVDQYNNQNNFVHDCVNI
TIKQHTVTTTTKGENFTETDVKMMERVVEQMCVTQYQKESQAYYEGRSS

Fig 5.3. Sequence of recBVPrP^{Sc}. PK cleavage sites: G92, N97, Q98, N153 and M154 are shown in red.

Next, a complete mass spectrometry-based analysis of the samples was carried out, which showed an agreement with the SDS-PAGE-based analyses since the three characteristic bands are found in the appropriate proportions.

PK-treated samples were pelleted by centrifugation, and the pellets denatured in 6 M Gdn/HCl and injected into a nanoHPLC coupled to an ESI-TOF detector.

Spectra (Fig. 5.4) showed fragments N97-S231, Q98-S231, and G92-S231 (the ~15 kDa band seen in the SDS-PAGE gels); fragments N153-S231 and M154-S231 (the ~9.5 kDa band seen in the gels) and N97-E152, Q98-N153 and Q98-E152 (the ~6 kDa band in the gels). These detected fragments are in well agreement with those described by Eraña and colleagues.

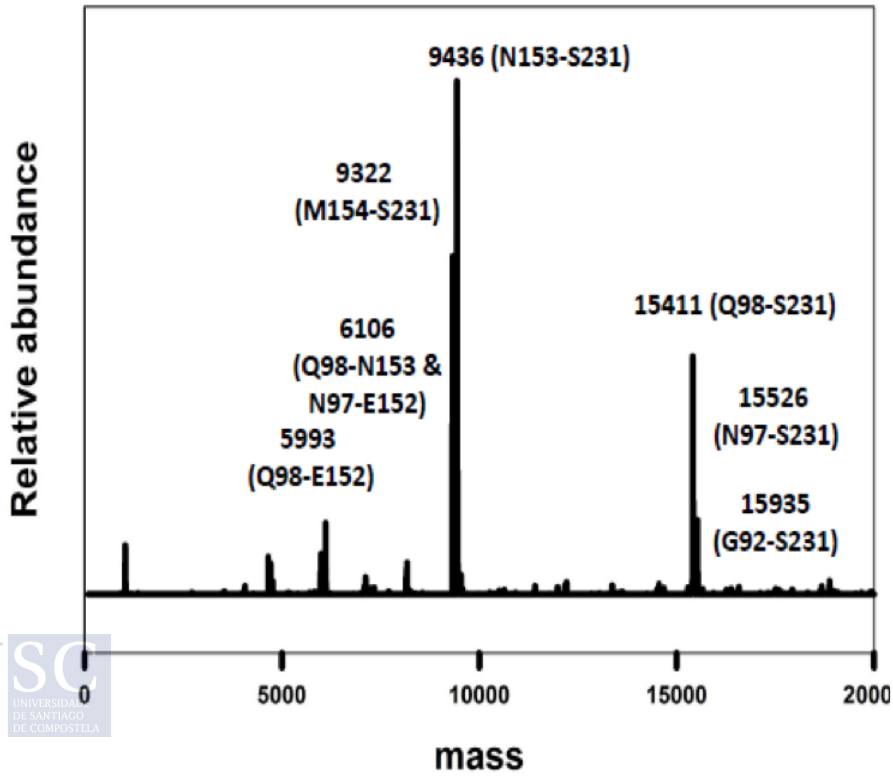

Fig.5.4. Mass spectral analysis of recBVPrP^{Sc}: Mass spectral analysis of the sample revealing three main fragments: N97-S231, Q98-S231, and G92-S231

5.3 Generation of non-infectious PrP amyloid

Non-infectious PrP amyloid was generated from recombinant PrP as previously described by Human Rezaei and colleagues (Torrent et al.) for FTIR and ssNMR measurements.

The thioflavin-T fluorescence reached its maximum at around 180 hours (≅ 7.5 days) of incubation, signaling the end of the fibrillation process (Fig. 5.5).

Plenty of fibers can be observed by atomic force microscopy and negative stain transmission electron microscopy which-are composed of two protofilaments. Such fibers were PK-treated as well and showed a partial PK resistance with a band of around 9 kDa as has been previously described (El Moustaine 2011) which corresponds to the weight of the PK-resistant core (residues 160-220) (Fig. 5.5).

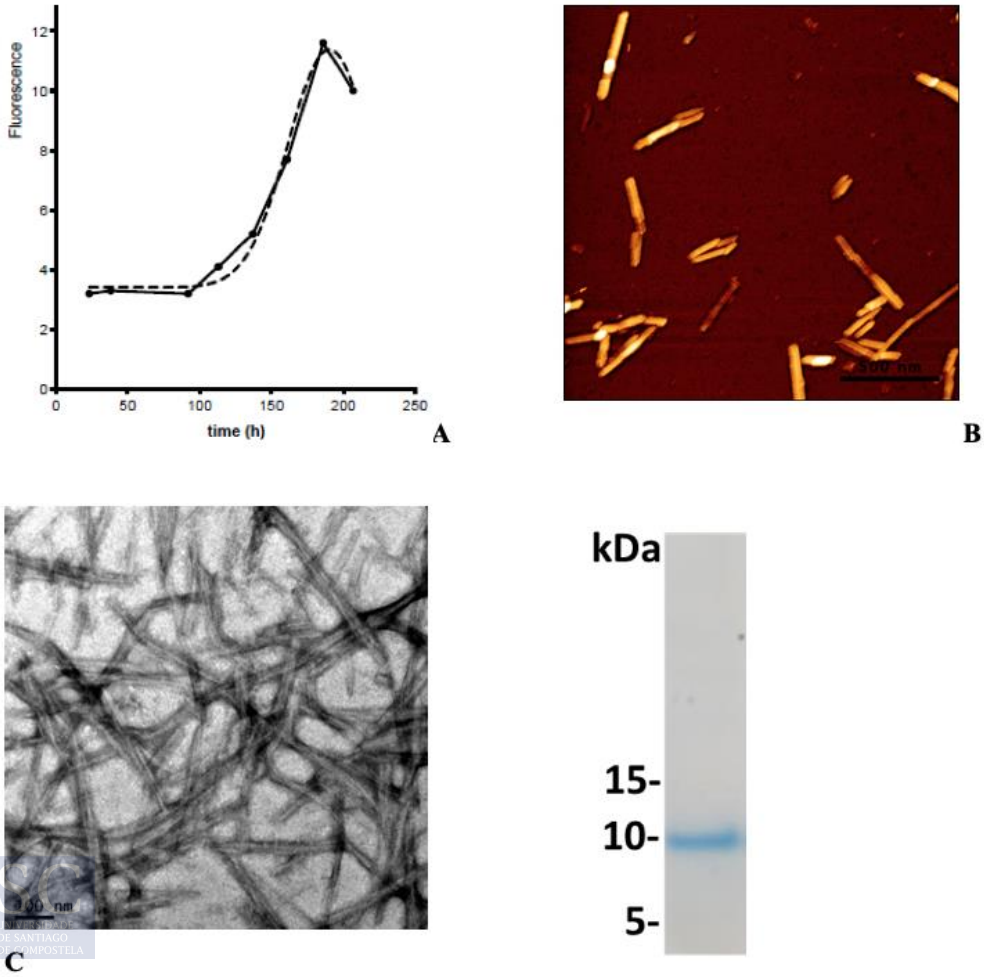

Fig.5.5. Characterization of the non-infectious recBVPrP(109I)23-231 amyloid sample. A: Thioflavin T (ThT) fluorescence obtained by Rezaei's group at INRA. B: Atomic force microscopy by Rezaei's group at INRA; C: negative stain TEM; D. Partial PK resistance.

5.4 Generation of Het-s amyloid

Het-s (218-289) was expressed and purified as usual.

The Coomassie stained figuring the protein in lane 5 at 10 KDa and the negative stain TEM image showing the fibrillar version of the protein can be observed below.

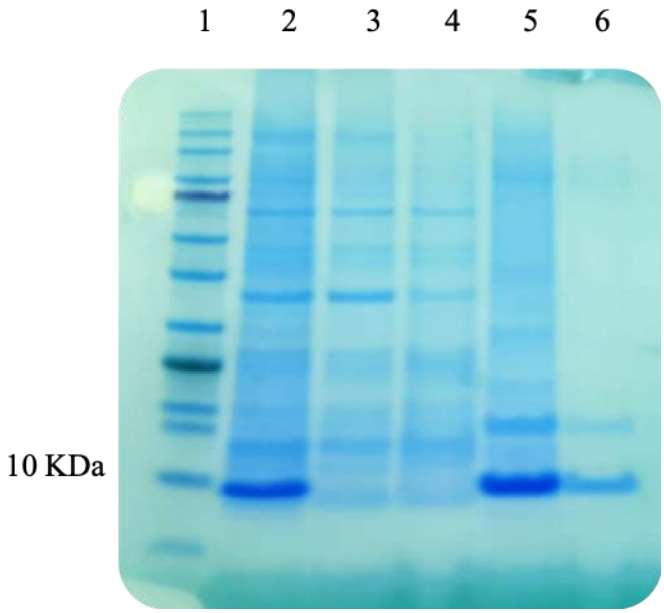

Fig 5.6. Biochemical characterization of the Het-s (218-289) sample. Coomassie stained showing the purification process of the protein at 10 kDa. b).

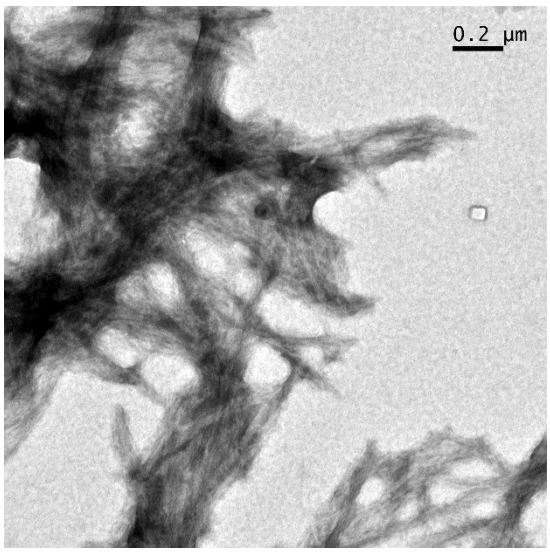

Fig 5.7. Characterization of the Het-s (218-289) sample. Negative stain TEM image of the fibrillar Het-s (218-289).

5.5 Fourier transform infrared spectroscopy (FTIR)

FTIR spectra of fully infectious recombinant Bank vole PrP^{Sc} (recBVPrP^{Sc}) have been compared with that of a non-infectious BVPrP amyloid during my short stay at Michael Beekes's group at the Robert Koch Institut in Berlin, Germany.

RecBVPrP^{Sc} was prepared using PMSA. In turn, BVPrP amyloid was prepared by unseeded incubation of recombinant BV PrP under denaturing conditions. RecBVPrP^{Sc} was treated with PK (25 µg/ml) before being subjected to FTIR analysis. This procedure ensures that any residual non-converted PrP, including any amorphous PrP aggregates, is destroyed. The PK treatment will also likely destroy a fraction of PK-sensitive recPrP^{Sc}, a price to pay to assure purity of the final sample. Centrifugal sedimentation after PK treatment allowed collection of PrP^{Sc}, which loses its intrinsically disordered N-terminal tail up to position ~97/98, cleaved off by PK.

The second derivative FTIR spectrum of the non-infectious BVPrP amyloid showed characteristic absorption bands in the Amide I/II region, with a peak exhibiting a maximum at 1626 cm-^{1} and a shoulder at 1630 cm-^{1}, typical of β-strands, and a group of peaks with maxima at 1674 and 1663 cm-^{1}, ascribed to loops and turns. In turn, the spectrum of recBVPrP^{Sc} exhibited a sharp peak with a maximum at 1632 cm-^{1}, that was slightly asymmetric, as if featuring an unresolved shoulder at a slightly lower wavenumber.

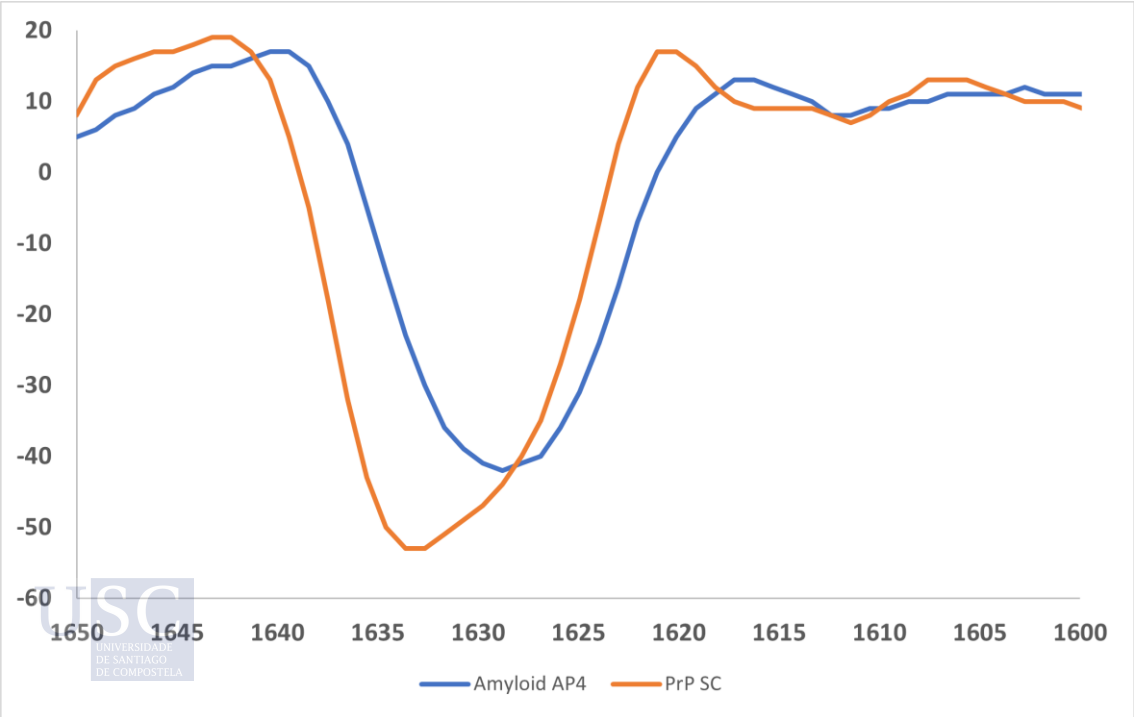

Fig 5.8.FTIR spectra. PrP Amyloid in **blue**, normalized average of 21 spectra with minimum at 1628,67 cm^{-1}. PrP^{Sc} in **orange**, normalized average of 4 spectra with minimun at 1633,28 cm^{-1}.

5.6 Solid state nuclear magnetic resonance (ssNMR)

Experiments were performed using non-infectious PrP amyloid known to present a parallel in register intermolecular beta sheet architecture (PIRIBS), infectious prion PrP^{Sc} amyloid of yet unknown structure and yeast prion Het-s amyloid which presents a two-rung beta solenoid architecture.

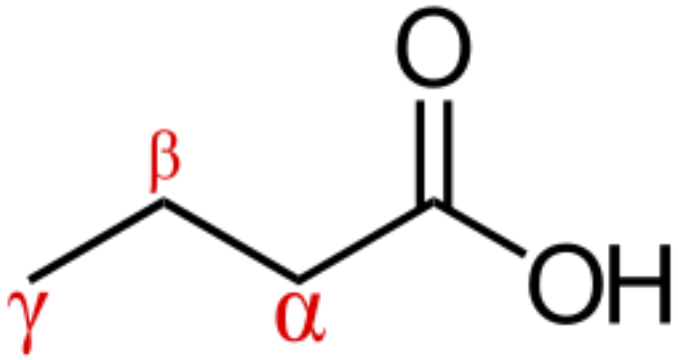

Fig 5.9.Chemical nomenclature of carbons.

A 2D ^{1}H-^{13}C CP-HSQC spectrum of PK-treated uniformly labeled (U-^{13}C,^{15}N)-recBVPrP^{Sc} was recorded to assess the general quality of the spectra it can be achieved with this sample. (Fig. 5.12). In this kind of spectra, essentially all ^{13}C atoms within a certain distance of one another are correlated by cross peaks in the spectrum. In practice this means that at short mixing times all carbon atoms within one spin-system (residue) are coupled to one another, giving rise to characteristic patterns in the spectrum.

Choosing a value of 4.6 ppm in the ^{1}H axis as the maximum for coil conformation and based on their chemical shifts (Zhang et al.), the majority of signals correspond to residues featuring β-sheet secondary structure (~85% β-sheet vs. ~15% coil, Fig. 5.12). This distribution should be considered very cautiously, given that the frontier between both types of chemical shifts is fuzzy; however, it is clear that the majority of signals detected derive from the β-stretches of the amyloid, with just a small fraction of signals arising from connecting loops with intermediate mobility, likely the shortest ones or positions within loops close to the rigid β-strands.

However, a proportion of ~50% β-sheet, ~50% coil and no α-helix is expected based on FTIR and CD spectroscopy measurements (Wille et al., Safar et al., Smirnorvas et al.). The lower proportion of coil in the NMR spectrum can be a result of the more mobile residues in the flexible loops becoming “invisible” to these NMR experiments, likely a consequence of their dynamics in the μs- ms time scale leading to relative short T_2 times which renders those spins completely out of the window of rotational frequencies that match the Hartman-Hahn condition for the Cross Polarization (CP) period and therefore they do not generate signals in any spectrum based on CP (Fig. 5.11).

It is also of note that the signals corresponding to β-strands showed a downfield spread, with signals reaching up to 7 ppm, something that to the best of our knowledge has not been reported. This might be a consequence of the high packing order and/or effects of

the cross-beta CO–HN hydrogen bonds in the chemical shifts of the Hα/Cα resonances. However, due to the unusual chemical shifts it might also be that we are seeing an artifact. In such case, the apparent ~85% β-sheet vs. ~15% coil proportion of signals would be an overestimation, and a much higher proportion of signals from coils would be present in the spectrum.

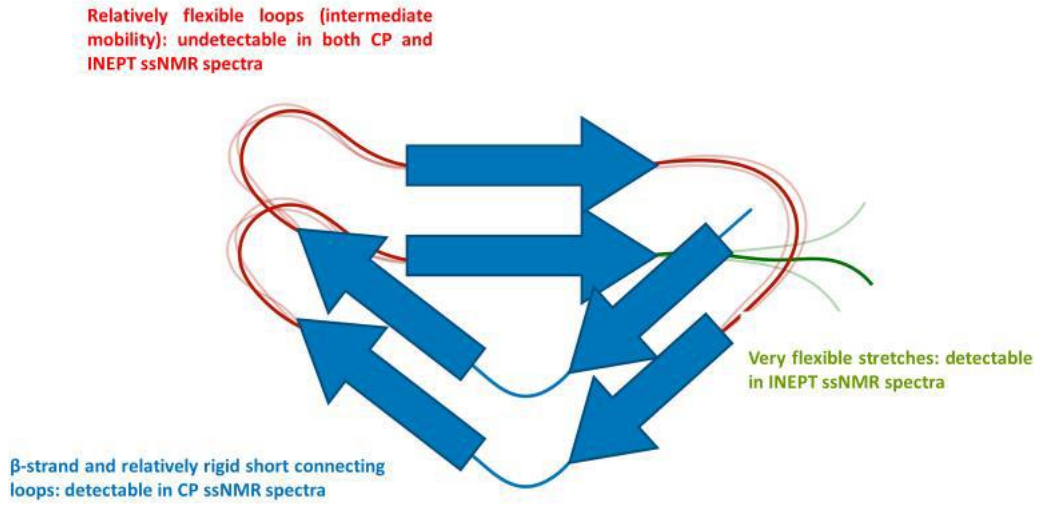

Fig 5.11. Schematic representation of the different molecular mobility regimes existing in an amyloid sample and its relationship with detectability in ssNMR spectra. Well-structured stretches have low mobility and are optimally detected in CP ssNMR spectra. Very flexible stretches (long loops or open ends) undergo fast motions even in the solid state in partially hydrated samples, which render them undetectable under standard CP ssNMR conditions; however, these residues can be detectable in INEPT-based experiments at high MAS rates. The intermediate case is that of segments with mobility at intermediate rates (i.e. with moderate flexibility); these residues may be undetectable both in CP and INEPT NMR experiments due to severe line broadening

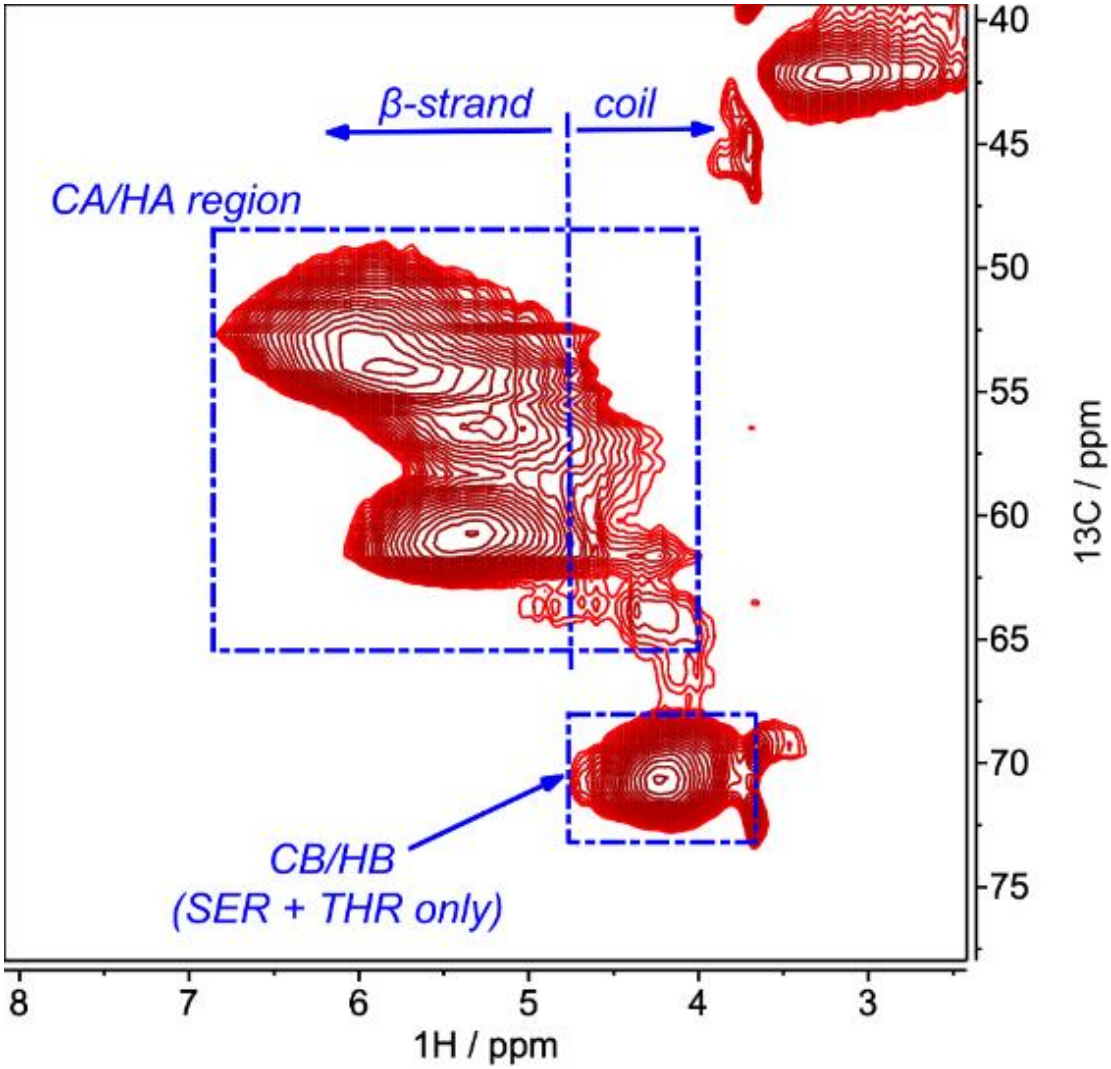

Fig 5.12. Hα/Cα and Hβ/Cβ regions of the 2D ^{1}H-^{13}C CP-HSQC spectrum of PK-treated, uniformly labelled (U-^{13}C,^{15}N)-recBVPrP^{Sc}.

DREAM (Fig. 5.13) and DARR (Fig. 5.14) experiments were performed to test for a variety of ^{13}C-^{13}C polarization transfer efficiencies that could enhance the detection of residues in a wide span of motional regimes. These experiments are similar to the HSQC, but at long mixing times the transfer of magnetization is more efficient and so one can expect to see more cross peaks, which is useful in order to obtain inter-residue contacts for assignment and structure calculations. Thus the objective was to obtain information compatible with only one of the two models.

Fig. 5.13A shows a DREAM spectrum in which cross-peaks arise primarily from one-bond, intra-residue spin polarization transfers. Both ^{13}C-^{13}C experiments include a period of CP and the signals observed in these experiments should arise from residues in the most rigid parts of the protein fold (e.g. the β-sheets and relatively short/rigid connecting loops), while residues that experience motions in the fast or intermediate time scale (e.g. residues in the more flexible loops or in the terminal ends) do not appear or have weak

intensities, a consequence of their dynamics in the μs- ms time scale leading to relative short T_2 times.
In other words, the fact that an amino acid is observed in these ^{13}C-^{13}C spectra can be interpreted as an evidence suggesting that the residue is in a β-sheet or, at least, in a relatively rigid segment; although the same amino acid can produce more than one signal in the spectra if it founds itself in more than one rigid environment, ie., if there is conformational heterogeneity.

In my sample signals are broad, as expected from an amyloid, previously seen in similar spectra from PrP amyloid samples (Tycko et al 2010., Müller et al. 2014) and preliminary reported by ourselves (Eraña et al.) This completely precluded assignment of specific residues.

However, a wealth of relevant amino acid-class information could be extracted: (i) A minimum of four Ala peaks are observed in the 48-51/19-25 ppm chemical shift region of the DREAM spectrum, characteristic of β-strand secondary structure (Zhang et al.) (Fig 5.13C). No signals are observed for Ala residues with chemical shifts characteristic of coil secondary structure. There are 8 Ala residues in $BVPrP^{Sc}$(97-231), one in the C-terminal region(Ala224) and the other 7 in the N-terminal region: Ala113, Ala115, Ala116, Ala117, Ala118, Ala120 and Ala133 (Fig. 5.3). If one rules out the very unlikely possibility that all four signals detected correspond to Ala224 in four different conformational variants, with all other Ala residues being invisible as a result of being located in flexible stretches (vide supra), this observation means that at least some, and likely 3 of these N-terminal Ala residues must feature a β-strand conformation, or, in other words, there are β-strands in the N-terminal region of $BVPrP^{Sc}$(97-231), reaching a position as N-terminal as Ala116. This has never been reported for any PrP amyloid, whose β-strands are confined to the 165-231 region (Tycko et al. 2010, Müller et al. 2014). (ii) There are two sets of signals corresponding to Cβ/Cγ2correlations of Ile residues, in the 36-42/13-18 ppm region of the spectrum, featuring chemical shifts that are characteristic of β-strand and coil secondary structure, respectively (Zhang et al.) (Fig. 5.13B). Based on the relative intensities of the signals, and the fact that there are 4 Ile residues in $BVPrP^{Sc}$(97-231), it seems reasonable to conclude that 3 of these Ile residues are likely located in β-strands (δC ≈ 40/17 ppm) while 1 (δC ≈ 38.5/14 ppm) is located either in a short coil or at the edge of a long coil, near a β-strand. Once again, the probability that some of the signals correspond to different conformational variants of a single Ile while other Ile residues are "invisible" is extremely unlikely. (iii) Despite the fact that there are 13 Gly residues in $BVPrP^{Sc}$(97-231), few CO/Cα signals corresponding to Gly residues are observed. These signals should appear around the characteristic 45/175 ppm region in the DARR spectrum (Figs. 5.14B, 5.15) (Zhang et al.). The DARR spectrum obtained shows only 6 weak signals in this region. In general, Gly residues are conspicuously absent from β-strands (Minor et al. 1994). We recorded a second DREAM spectrum with 24 kHz MAS rate and 3 ms mixing time. Under these conditions, cross-peaks arising from Gly Cα /CO and Gly Cα/Cα correlations appear with opposite phase to the other cross peaks (Fig. 5.15) because of the particular sensitivity of DREAM to the experimental conditions. As seen in Fig. 5.15, we detected a clear group of signals corresponding to more than one Gly residue. Furthermore, in this spectrum we detected a few additional cross-peaks at 53/45 ppm that correspond to inter-residue correlations between Gly Cα and the Cα of contiguous residues. (iv) There is an intense signal corresponding to the Cα/Cβ correlation of several unresolved Thr residues at 61/70 ppm, with a weak neighboring signal corresponding to 1 Thr residue (Fig. 5.13A). Their chemical shifts values are compatible with both β-sheet and coil secondary structure. It is

reasonable to conclude that the signals forming the intense unresolved peak come from a majority of Thr residues featuring β-sheet secondary structure. (v) There are 3 clear, well resolved Ser Cα/Cβ cross-peaks in the 55-59/64-68 ppm region of the spectrum (Fig. 5.13D). Their distribution suggests that two of them might feature β-sheet conformation, while the other is likely more compatible with coil conformation (Zhang et al), although this interpretation must be taken cautiously (vide supra). Two additional well resolved peaks above these three are also compatible with the chemical shifts of Serine residues but might also correspond to Prolines (Fig. 5.13D). (vi) Two regions of the DARR spectrum display cross-peaks corresponding to aromatic amino acid residues: region 115-163 ppm for C-aromatic/C-aromatic correlations and region 30-60/115-138 ppm for correlations of the aliphatic Cα and Cβ carbons with the aromatic carbons. Signals corresponding to ~6-8 Tyr residues could be unequivocally discerned from the diagonal peaks of Tyr carbons Cε (δC ~117 ppm) and Cζ (δC ~157 ppm), as these chemical shift values are privative of Tyr. Other peak groups in the aromatic subspectrum confirm this assignment, like those correlations between the Cδ/ Cε and the Cε/Cζ carbons (Fig. 5.14C). Besides, a small number of additional, non-Tyr aromatic amino acid residues (Phe, Trp or His) can be discerned at 125-140 ppm (Fig. 5.14C)

In summary, although some relevant amino acid-class information could be extracted, it did not suffice to support one of the two contending models (4RβS vs. PIRIBS) since all these constraints are compatible with both models.

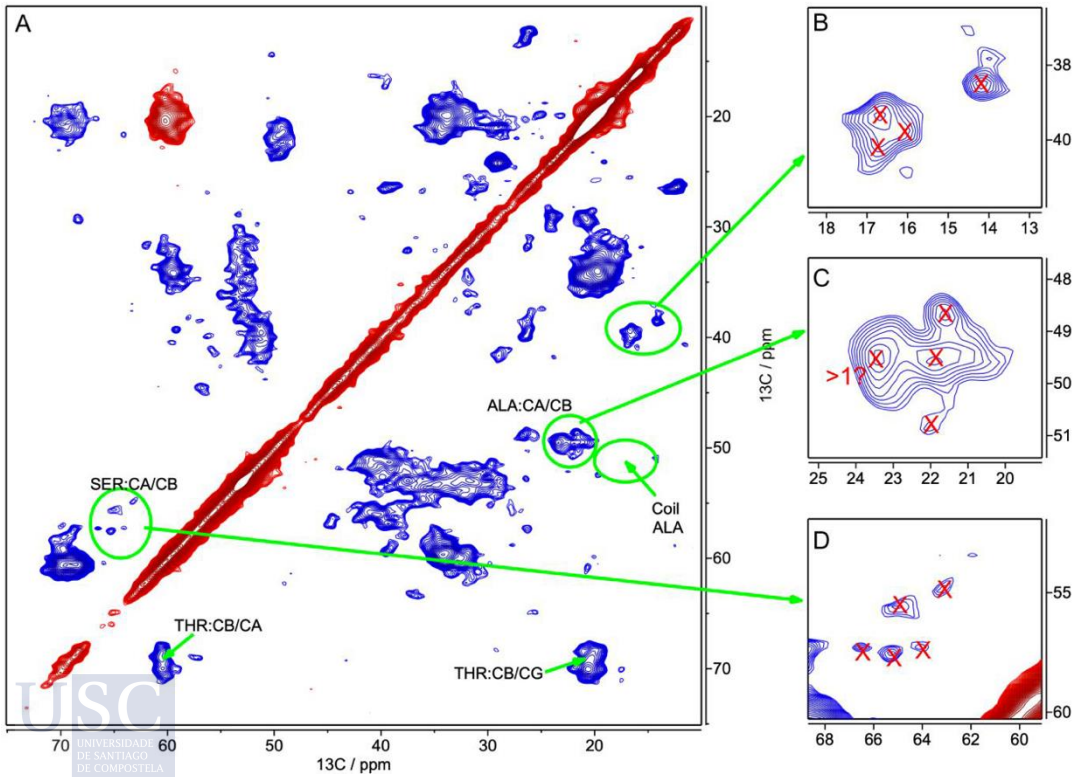

Fig. 5.13. 2D ^{13}C-^{13}C DREAM spectrum (45 kHz MAS, 3 ms mixing time) of PK-treated, uniformly labelled (U-^{13}C,^{15}N)-BVPrP^{Sc}(109I). (A) Expansion of the aliphatic region (Cα, Cβ, Cγ...). (B) Expanded 36-42/13-18 ppm region, where Ile Cβ/Cγ2 correlation cross-peaks appear. (C) Expanded 48-51/19-25 ppm region, where Ala Cα/Cβ correlation cross-peaks appear. (D) Expanded 52-60/59-68 ppm region, where Ser Cα/Cβ correlation cross-peaks appear

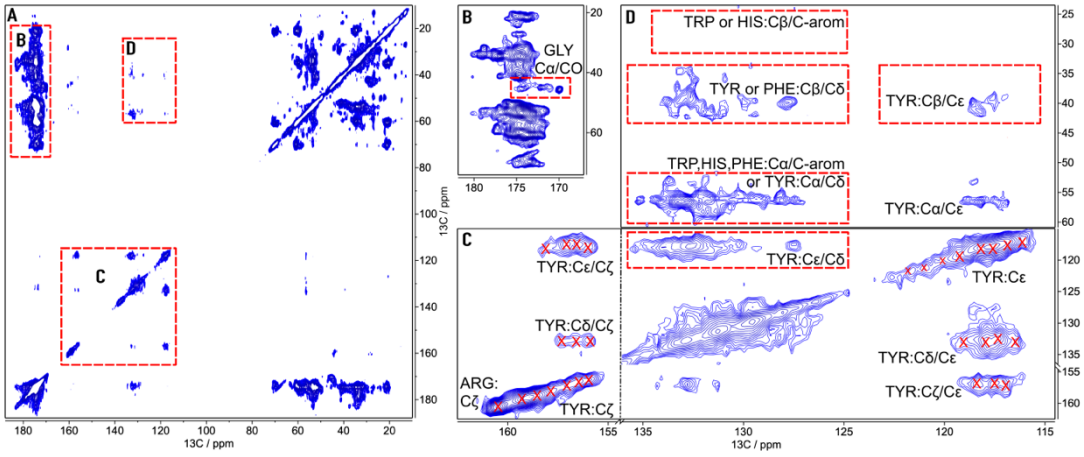

Fig.5.14. 2D ^{13}C-^{13}C DARR spectrum of PK-treated, uniformly labelled (U-^{13}C,^{15}N)-BVPrP(109I)^{Sc}, recorded at 20 kHz MAS rate with 80 ms mixing time. (A) Full spectrum: red rectangles contain the expanded regions. (B) Expansion of the C-aliphatic/CO region. Red rectangle contains the GLY:CA/CO correlations (≈3-5 peaks). (C) Expansion of the C-aromatic/C-aromatic region. A minimum of 6 TYR residues can be deduced from diagonal peaks and correlations of their Cδ, Cε and Cζ atoms. It is unclear if diagonal peaks in the range δC ~ 120-123 ppm are additional TYR:Cε resonances or if they correspond to aromatic carbons from TRP and HIS residues. Contribution of other aromatic residues (PHE, HIS, TRP) to peaks in the region 125-130 ppm cannot be discarded, nor confirmed, due to overlap of their typical chemical shift ranges (Zhan et al). (D) Expansion of the C-aliphatic/C-aromatic correlations. Cross-peaks in the δC ~ 115-120 ppm region (Cε) can be unequivocally assigned to TYR:Cα/Cε (δCα ~ 57 ppm) and TYR:Cβ/Cε (δCβ ~ 41 ppm).

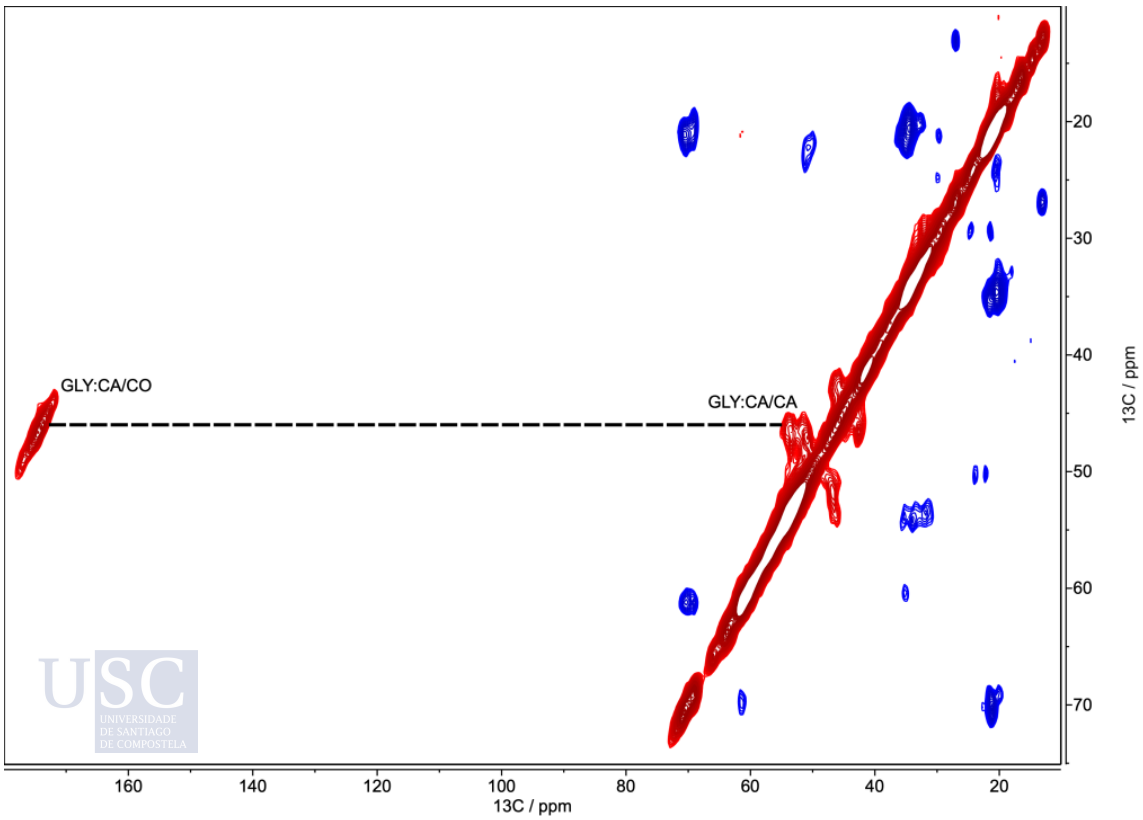

Fig. 5.15. 2D ^{13}C-^{13}C DREAM spectrum (24 kHz MAS, 3 ms mixing time) of PK-treated, uniformly labelled (U-^{13}C,^{15}N)-BVPrP^{Sc}(109I).

Uniformly labelled PK-treated (U-^{13}C,^{15}N)-BVPrP^{Sc} sample was also subjected to ssNMR analysis with methods based on INEPT magnetization transfer and rotation at high MAS rates (2D ^{1}H-^{13}C and ^{1}H-^{15}N INEPT-HSQC experiments). Differently to what occurs with experiments based in CP, INEPT based experiments are more suitable to detect the resonances of the most mobile or flexible stretches or domains of the solid sample thus we were expecting to see the residues we were not able to see with CP (Fig.5.11)

Under these conditions, a small number of signals were detected in spectra of (U-^{13}C,^{15}N)-BVPrP^{Sc} when the sample was rotated at ≅ 60 kHz MAS rate. Some of the peaks in the 2D ^{1}H-^{13}C INEPT-HSQC spectrum such as δC ~70 ppm and δH ~3.5 ppm were identified as originating from natural abundance ^{13}C of Triton X-100 molecules, which is used as co-factor during preparation of recBVPrP^{Sc} by PMSA, that are tightly bound to the recBVPrP^{Sc} (Fig 5.13). Therefore the focus of attention was moved to the ^{1}H-^{15}N INEPT-HSQC spectra (Fig. 5. 14), as all their signals unequivocally derive from amino acid residues in recBVPrP^{Sc} because neither Triton nor dextran, another compound used as cofactor, have nitrogen atoms.

Based on the distinctive chemical shift values of the side-chain H-N atoms, peaks can be identified corresponding to 2 Gln/Asn residues (δN ~110-112 ppm and δH ~ 7.1 and 7.8 ppm) and 1 Arg (δNε ~83 ppm and δHε ~ 7.4 ppm). Furthermore, cross-peaks in the 117-120 ppm/8.1-8.8 ppm area are compatible with backbone HN of 2-3 Ser and/or Thr residues. A group of a minimum of 4-5 additional unresolved signals is also present in the δN ~119-127 ppm/ δH ~ 8.0-8.5 ppm region (Fig. 5. 14). Finally, an intense signal centered at 129.5 ppm/7.8 ppm, which is a chemical shift value typical of N atoms in C-terminal amino acid residues was also seen.

Thus, all these residues are located in areas with very high mobility such as turns and unpacked coils, but again, the information retrieved is compatible with both PIRIBS and 4RβS models therefore we cannot state which one is correct from these results.

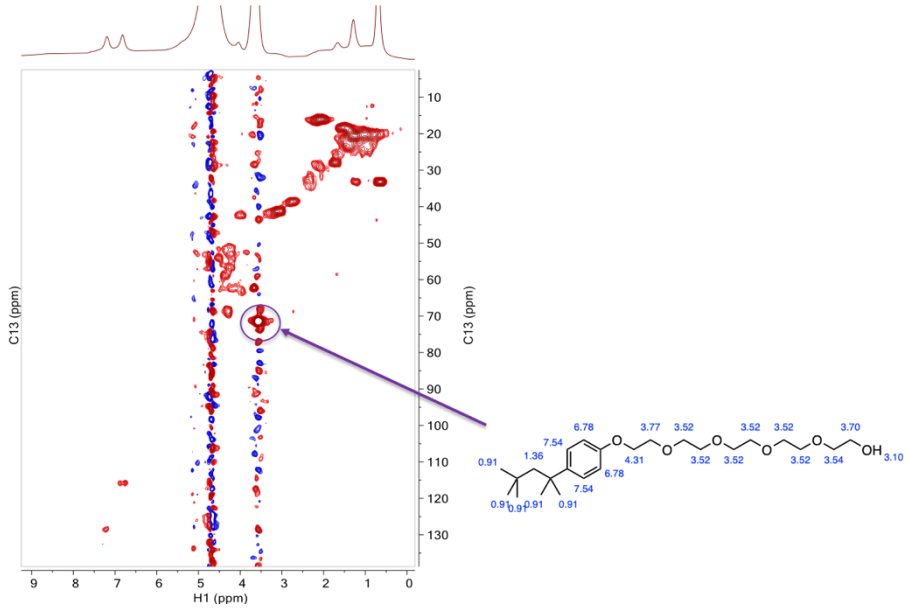

Fig 5.16. ^{1}H-^{13}C INEPT-HSQC spectrum of PK treated (U-^{13}C, ^{15}N)- BVPrP^{Sc}.

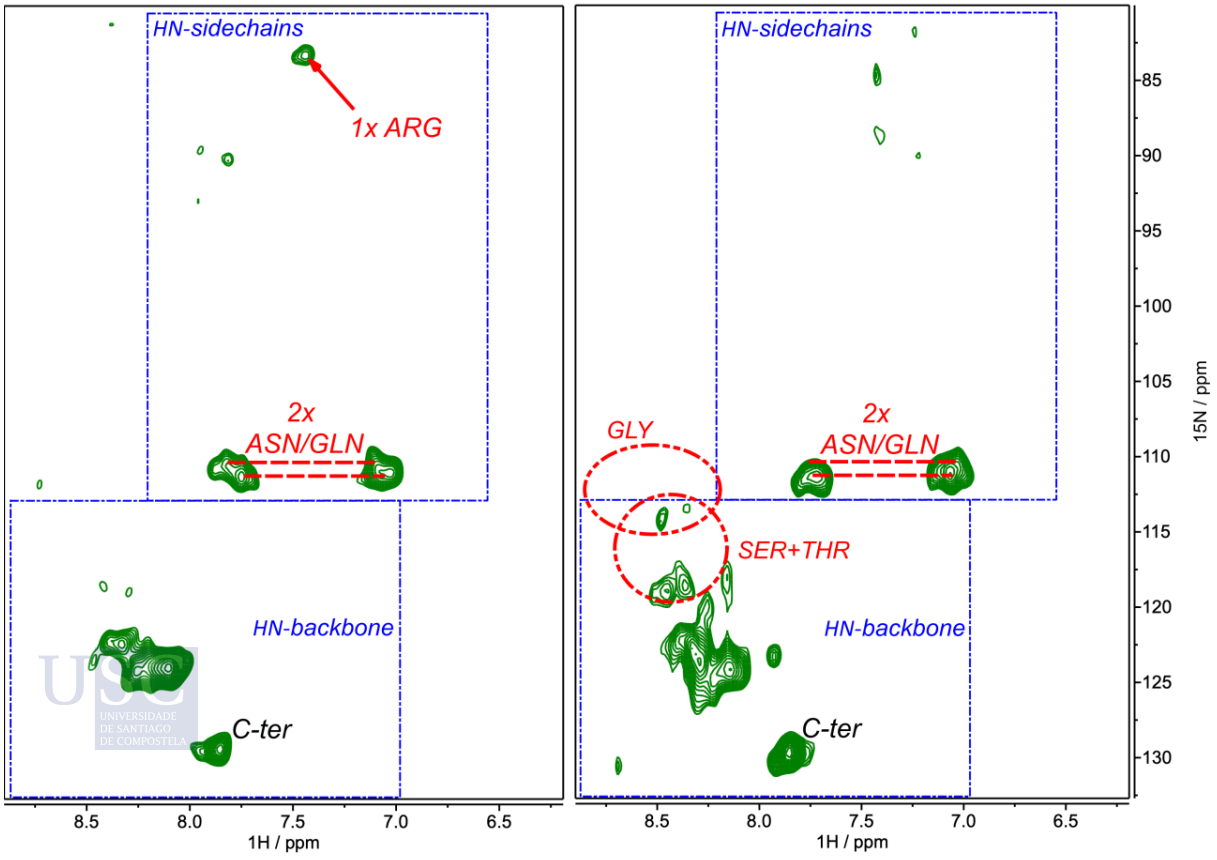

Fig.5. 17. Sections of 2D ^{1}H-^{15}N INEPT-HSQC spectra of PK-treated, uniformly labelled (U-^{13}C,^{15}N)-BVPrP^{Sc}(109I) obtained at a MAS rate of (a) 45 kHz, and (b) 60 kHz.

5.7 PITHIRDS

In the absence of a substantial residue-specific assignment, the data obtained from 2D, C-C spectra, while of great descriptive interest, are not sufficient to discriminate between a 4RβS and a PIRIBS architecture. Thus, an experiment capable of distinguishing between both architectures without the requirement of extensive assignment and extensively used to probe the architecture of amyloids, namely the PITHIRDS-CT developed by Tycko and colleagues (Tycko, Tycko et al, Shewmaker et al.), was performed.

During the evolution period of this NMR pulse sequence, rotor-synchronized π pulses that occupy one third of the magic angle spinning (MAS) rotor period are applied on ^{13}C to recouple (restore) the ^{13}C-^{13}C dipole-dipole interactions that otherwise average out by MAS. The experiment is repeated for a series of effective recoupling times that modulate the signal intensity. Relaxation and other factors that also modulate signal intensity, in particular during the recoupling period, are kept constant by the use of constant time conditions (CT) for the whole series of experiments (Tycko). Thus, the curve of ^{13}C signal intensity *vs*. effective recoupling time is primarily modulated by the ^{13}C-^{13}C dipole-dipole interaction and, due to its $1/r^3$ dependence, ^{13}C-^{13}C distances can be deduced by numerical simulations (Groveman et al.,Tycko, Shewmaker et al.). The pulse sequence and some of the experimental conditions originally developed for a 9.4 T spectrometer were adapted to the 17.6 T instrument available at the university and 40 kHz MAS.

To understand this experiment it is important to know that β-sheet structures include (i) antiparallel sheets in which adjacent strands run in the opposite direction, (ii) parallel sheets with the adjacent strands running in the same direction which can be in-registered, with identical residues aligned or out of register, (iii) β-helices, a coil whose strands are in β-configuration. These different structures predict dramatically different results in the PITHIRDS-CT experiment. If a molecule is carbonyl-^{13}C-labelled at a single amino acid residue, the nearest neighbor ^{13}C is in another molecule. In a parallel in-register β-sheet, this distance is 0.48 nm, namely the same amino acid residue in the preceding and following molecules in the same β-sheet (Fig. 5.18A). In an antiparallel structure, most carbonyl ^{13}C labels will be no closer than 0.96 nm (Fig. 5.18B). In a singly labeled β-helix, the next nearest ^{13}C would probably be many-fold the distance (0.48 nm) between two β-strands, and the precise distance would be determined by intermolecular orientation (Fig. 5.18D). With several scattered residues labeled (2-5 per molecule in our experiments), if most exhibit a nearest neighbor distance of about 0.5 nm, the parallel in-register structure is likely (Shewmaker et al. 2008).

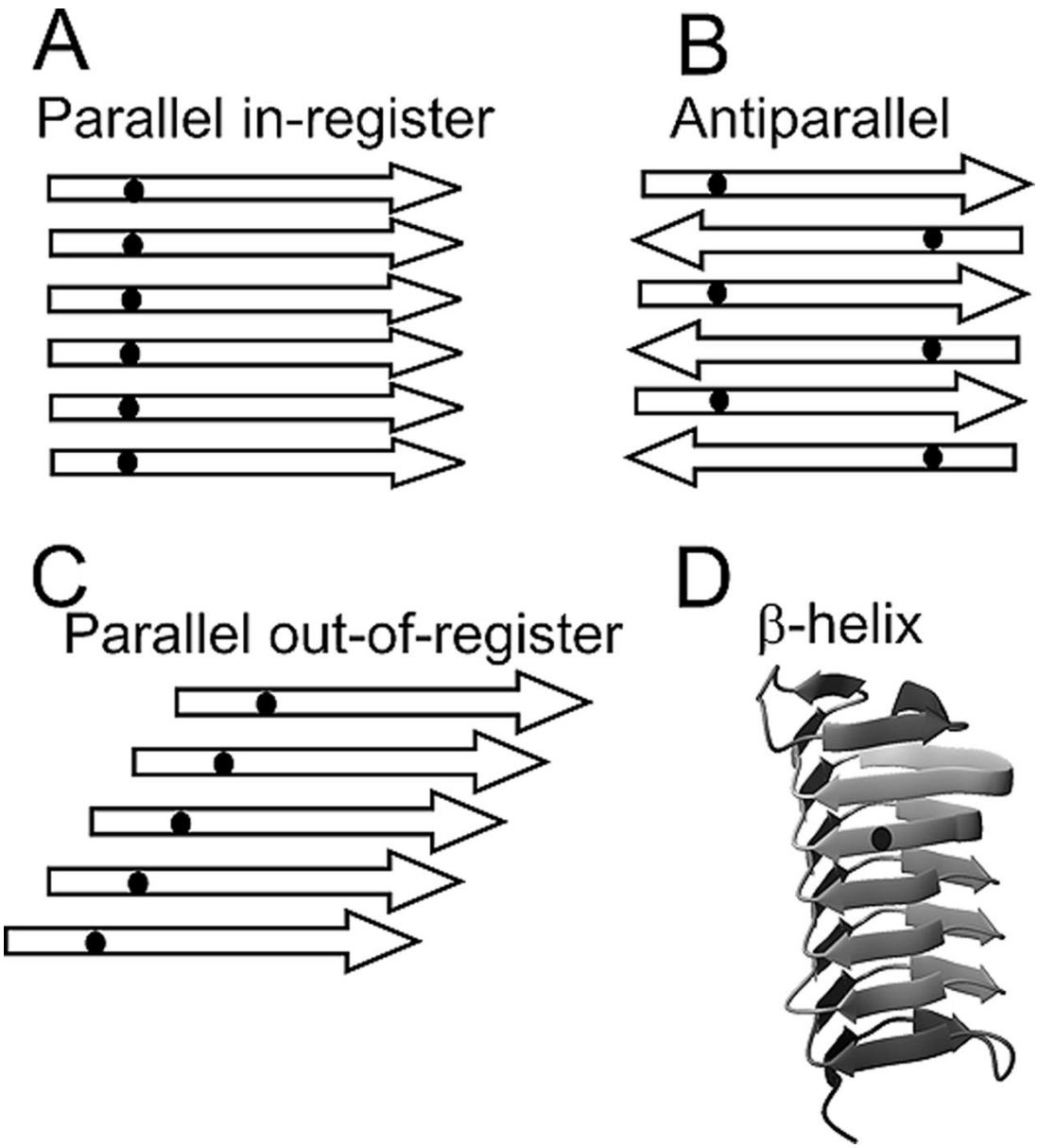

Fig 5.18. Possible ß-sheet amyloid structures. Model structures of parallel in-register, antiparallel and ß-helix structures are shown. The black dot shows the position of a single residue. Adapted from Shewmaker et al. 2008.

The PITHIRDS-CT experiment was performed on a ^{13}CO-Phe and ^{13}CO-Leu labelled recBVPrP^{Sc} sample to probe the intermolecular carbonyl-carbonyl distances, both are residues with a high tendency of being in β-sheets; there are three Phe in recBVPrP^{Sc} (Phe141, Phe175 and Phe198) and two Leu (Leu124 and Leu129). Two amyloids of known architecture were used as controls: a ^{13}CO-Phe labelled recBVPrP non-infectious amyloid sample, known to feature a PIRIBS architecture (Tycko et al., Wang et al 2020) and a sample of ^{13}CO-Tyr labelled HET-s(218-289) fibrils, known to consist of 2-rung β-solenoids (Shewmaker et al.,Wasmer et al.). Tycko et al. reported a slightly longer than expected mean distance of 5.0-5.5 Å for the Phe residues in the PrP amyloid (Fig 5.19) (Tycko 2010), explained as a consequence of Phe141 being likely located outside the PIRIBS core. A recent cryo-EM study has confirmed this (Wang et al. 2020) (Fig 5.20)

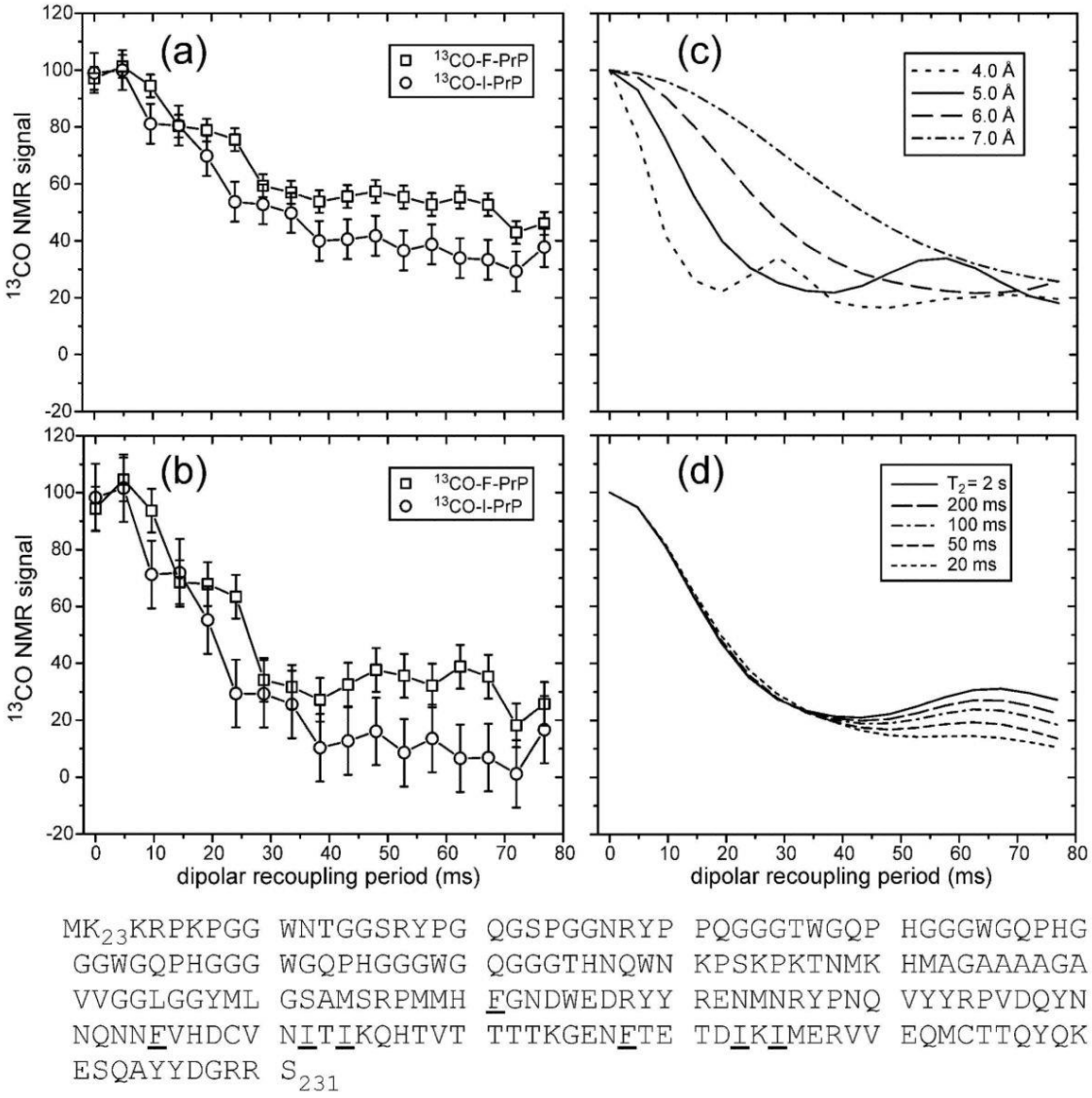

Fig 5.19. PITHIRDS experiments with ^{13}CO-Phe and ^{13}CO-Ile BV PrP by Tycko. (a) Experimental measurement of intermolecular 13C-13C dipole-dipole couplings using the PITHIRDS-CT solid state NMR technique, for ^{13}CO-F-PrP and ^{13}CO-I-PrP fibrils (squares and circles, respectively). Positions of labeled Phe and Ile residues are underlined in the PrP23-231 sequence at the bottom of the figure. Error bars represent the root-mean-squared noise in the NMR signals. Lines are guides to the eye. (b) Experimental PITHIRDS-CT data after correction for natural-abundance 13C signal contributions as explained in the text. (c) Simulated PITHIRDS-CT curves for linear chains of dipole-coupled 13C nuclei with the indicated spacings. T2 relaxation is not included. (d) Simulated PITHIRDS-CT curves for dipole-coupled 13C nuclei with a 4.8 Å spacing and with indicated values of the transverse relaxation time T2. Adapted from Tycko 2010. Shown in this section for clarity.

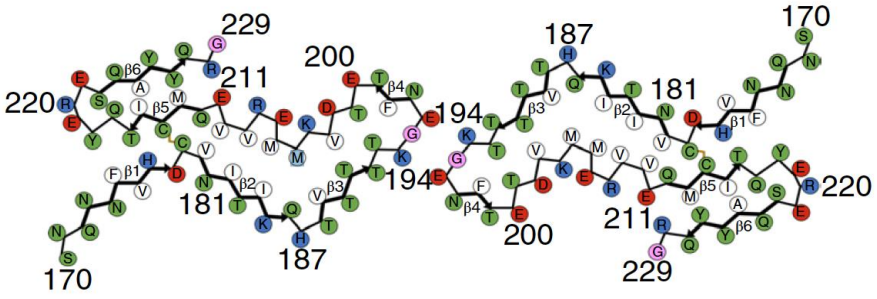

Fig 5.20. PrP amyloid structure as solved by Cryo-EM. As we can see Phe141 is located outside of the PIRIBS core. Adapted from Wang et al. 2020.

In our experiment, the ^{13}C carbonyl signal decay for PrP amyloid confirmed a PIRIBS architecture with a mean Phe-Phe distance of 5-6 Å, in excellent agreement with Tycko's results (Fig. 5.21 and 5.22). Also as expected, the signal decay for the HET-s(218-289) prion sample was negligible (Fig. 5.21 and 5.22), in agreement with the >>7 Å distances between its Tyr residues (Shewmaker et al., Wasmer et al). Surprisingly, the ^{13}C decay curve of recBVPrP^{Sc} fitted to a mean distance of ~6-7 Å between Phe and Leu residues (Fig. 5.21, 5.22 and 5.23). This strongly suggests that the architecture of recBVPrP^{Sc} conforms to a PIRIBS, and not to a 4RβS as it had been expected by us (Wille et al., Safar et Wille, Spagnolli et al.,Vázquez-Fernández).

We hypothesized that perhaps one or two of the three Phe residues and one of the two Leu might be located outside canonical β-strands featuring an ideal cross-β architecture, perhaps loops connecting β-strands, as has been proposed by others (Gorkovskiy et al.), since the measured mean Phe-Phe distance is even larger than that seen in the PrP amyloid, with just one Phe outside the PIRIBS core (Tycko 2010 ,Wang 2020). We reasoned that such arrangement might result in local flexibility leading to an overestimation of distances in the PITHIRDS experiment due to imperfect ^{13}C-^{13}C dipolar recoupling.

An additional control PITHIRDS-CT experiment was performed with crystalline ^{13}CO-Phe in which the closest distance of ^{13}CO carbons in the X-ray structure is 3.15 Å. As expected, the mean measured distance obtained by PITHIRDS between ^{13}CO carbons was of <4 Å (Fig. 5.23).

We also performed experiments with ^{13}CO-Asp BVPrP^{Sc} where the mean distance in ^{13}CO-Asp BVPrP^{Sc} was slightly longer than 7 Å (Fig 5.24); we hypothesized that maybe the mean intermolecular distance was so long due to the residues being in loops since Asp is not a residue with a high β-sheet tendency; therefore we reasoned that if the sample was hydrated the mobility of the more flexible residues located outside of the β-sheet core would increase thereby reducing the natural abundance signal. However, after hydrating we obtained a distance of longer than 7 Å again (Fig. 5.25).

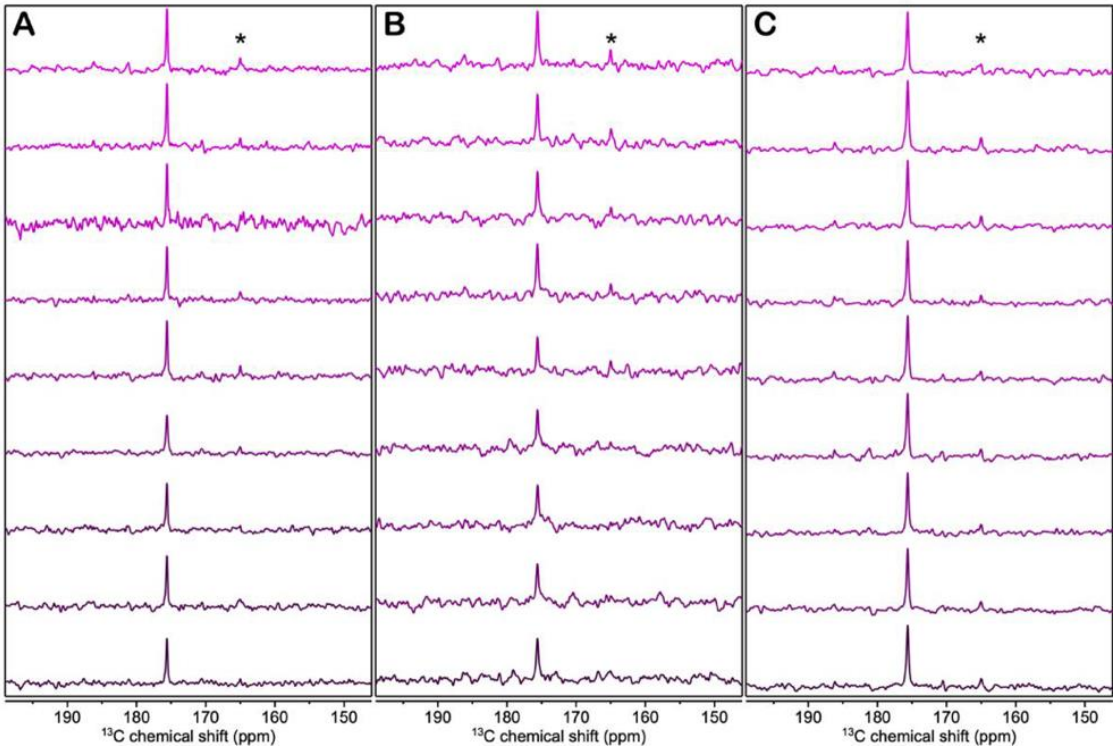

Fig.5.21. 1D PITHIRDS-CT spectra showing the intensity of the ^{13}CO signal. A: (^{13}CO-Phe)-recBVPrP(23-231) amyloid. B: (13CO-Phe)-recBVPrP^{Sc}. C: (13CO-Tyr)-HET-s(218-289). From top to bottom, the effective recoupling evolution time is 0.0, 2.4, 4.8, 9.6, 14.4, 19.2, 24.0, 26.4, and 33.6 ms. All spectra of a given sample were acquired with the same number of scans, processed identically and are represented with the same vertical scale. The asterisk denotes a small artefact at the carrier frequency due to pulsed-spin-lock acquisition.

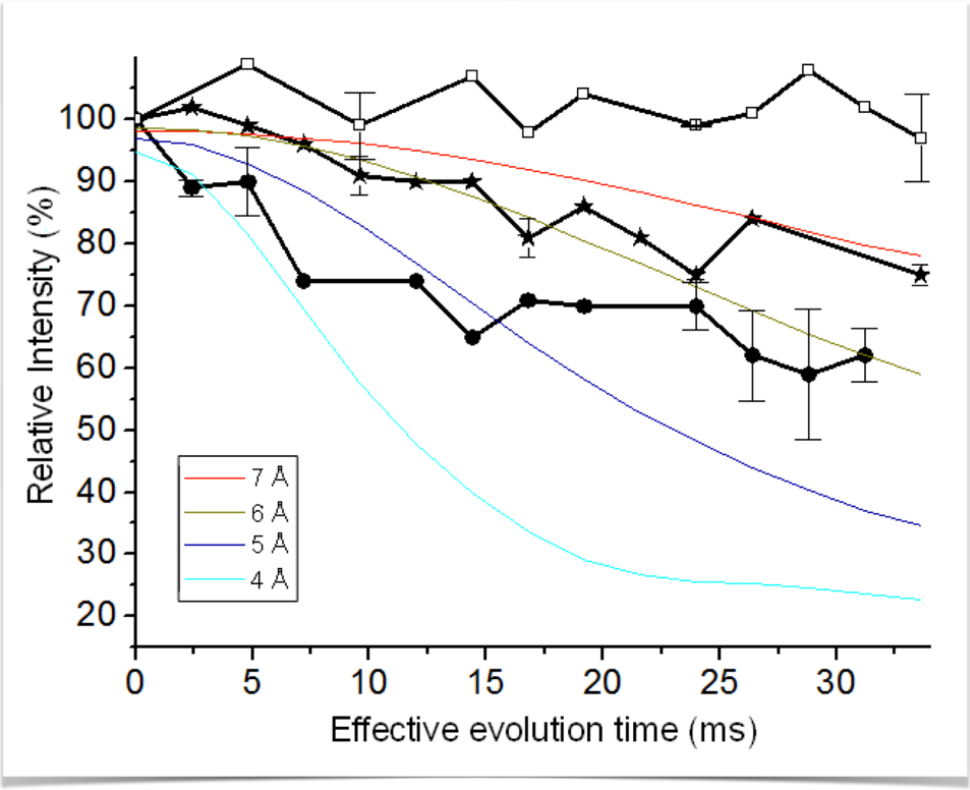

Fig.5.22. Measurement of intermolecular ^{13}C-^{13}C dipole-dipole couplings using PITHIRDS-CT. Data are shown after correction of natural abundance ^{13}C contributions. Symbols are: • (^{13}CO-Phe)-recBVPrP^{Sc}, ★ (^{13}CO-Phe)-recBVPrP(23-231) amyloid, and □ (^{13}CO-Tyr)-HET-s(218-289) and represent means of 2 independent experiments —3 for (^{13}CO-Phe)-recBVPrP^{Sc}—, with bars representing standard errors of the mean. Black segments connecting the symbols are drawn to guide the eye. Solid coloured lines are simulated curves for specific distances in Å.

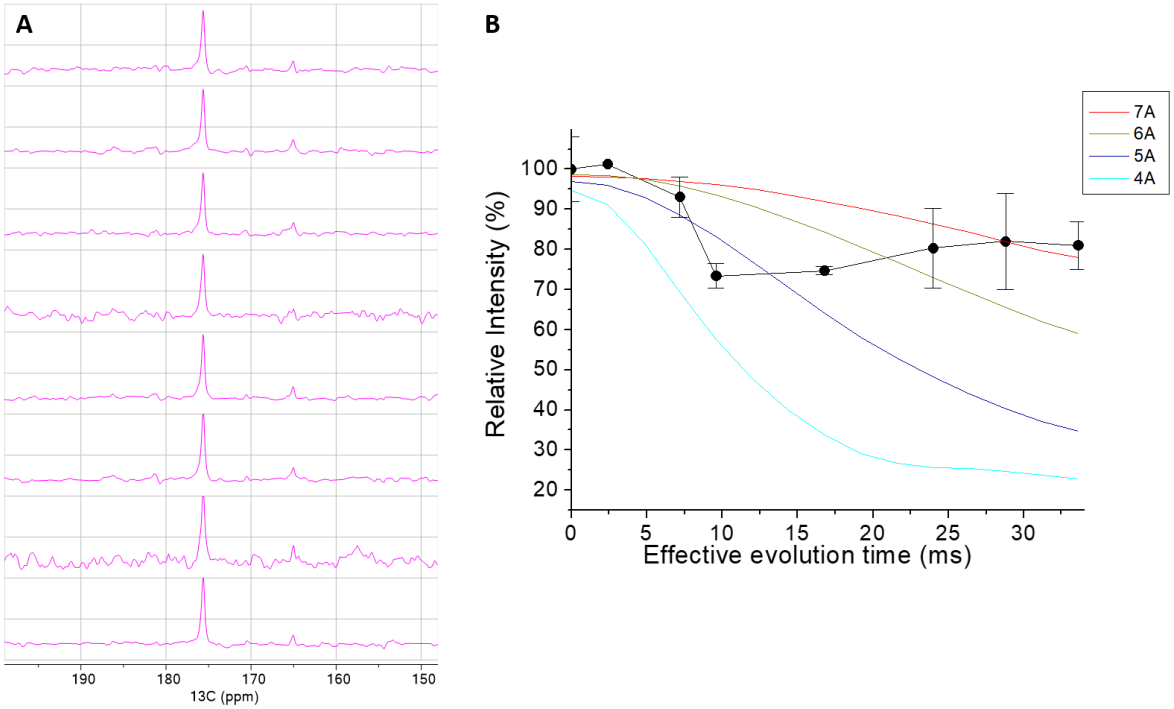

Fig. 5.23. Measurement of intermolecular ^{13}C-^{13}C dipole-dipole couplings in ^{13}CO-Leu recBVPrP^{Sc} using PITHIRDS-CT. A) PITHIRDS spectra. From top to bottom the effective recoupling evolution time is 0.0, 2.4, 7.2, 9.6, 16.8, 24.0, 28.8 and 33.6 ms. B) PITHIRDS plot. The black points represent means of two independent experiments after correction of natural abundance ^{13}C contributions and the bars represent standard errors of the mean. Black segments connecting the symbols are draqn to guide the eye. Solid colored lines are similutaed curves for specific distances in Å.

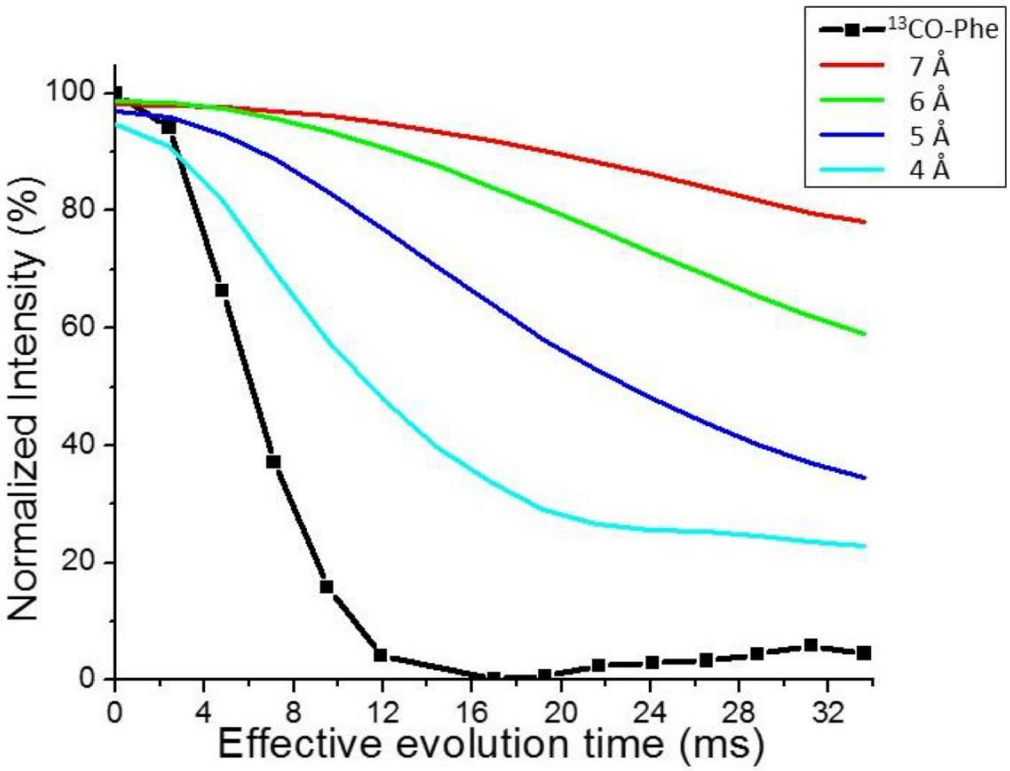

Fig. 5.23. Measurement of intermolecular ^{13}C-^{13}C dipole-dipole couplings in ^{13}CO-Phe using PITHIRDS-CT.

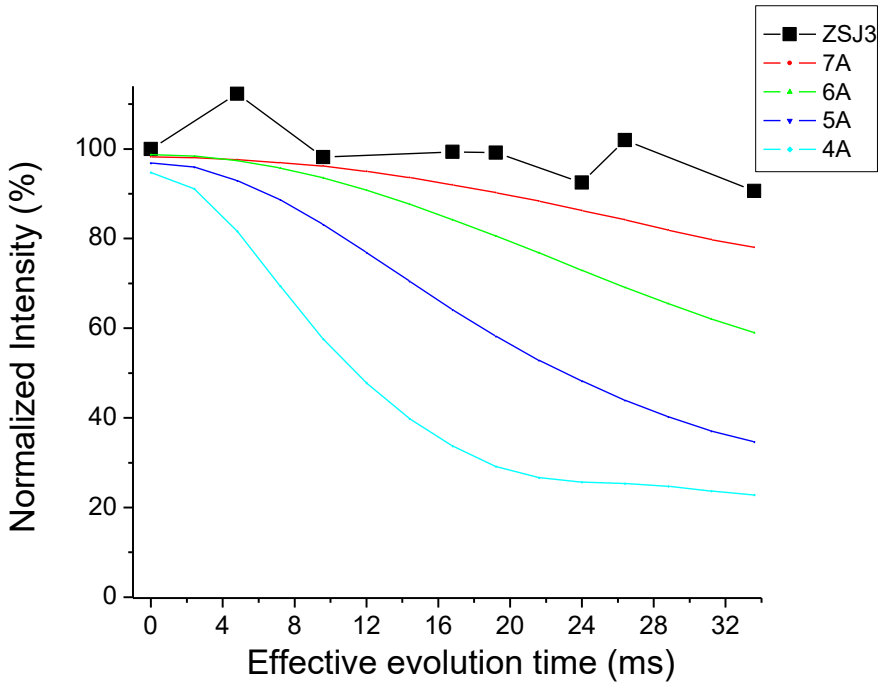

Fig. 5.24. Measurement of intermolecular ^{13}C-^{13}C dipole-dipole couplings in ^{13}CO-Asp recBVPrP^{Sc} using PITHIRDS-CT.

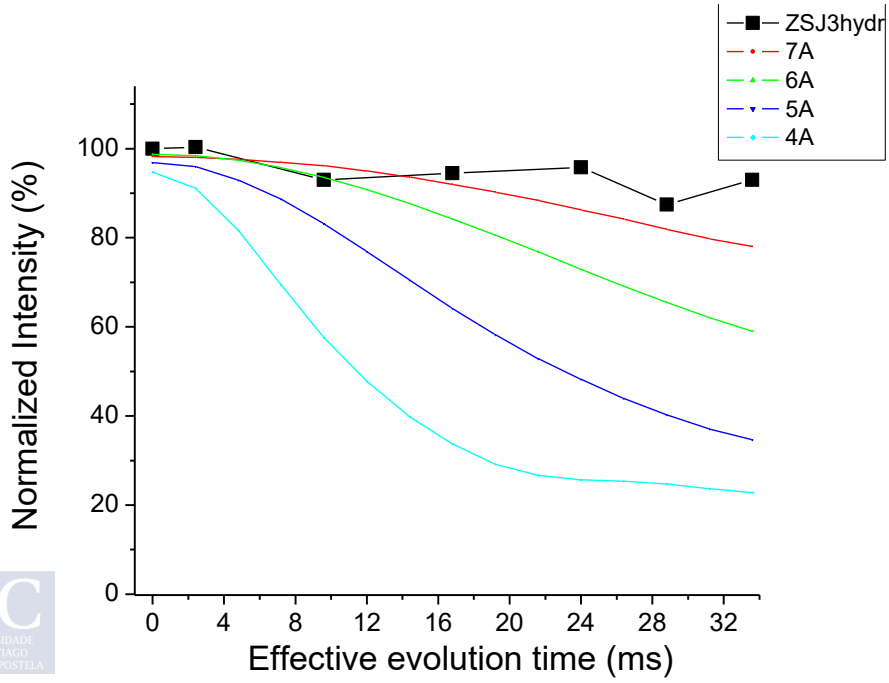

Fig. 5.25. Measurement of intermolecular ^{13}C-^{13}C dipole-dipole couplings in ^{13}CO-Asp recBVPrP^{Sc} after hydrating the sample using PITHIRDS-CT.

5.8. CP-MAS and PARIS

To comparatively assess the flexibility of the three structures, since we had hypothesized that several of our chosen Phe and Leu residues were in loops or short and flexible β-sheets in the PrP^{Sc} structure thus it should be more flexible, the peak intensities were measured in 1D ^{13}C CP-MAS and PARIS spectra of the samples (Figure 5.27).

The PARIS experiment relies on ^{1}H-^{1}H recoupling and direct polarization from ^{1}H to ^{13}C. It employs a long proton recoupling period of a few seconds synchronized with MAS to polarize nearby ^{13}C atoms, it is followed by a hard pulse on ^{13}C of just a few microseconds, a duration that is much shorter than the usual contact times (e.g. 0.5 to 5 ms) required for a ^{13}C CP-MAS experiment. Therefore, PARIS is less affected by ^{13}C transversal relaxation and enhances the intensity of nuclei located in moderately flexible stretches (moderate dynamic heterogeneity in the microsecond to low millisecond time scale) characterized by short T_2 times. Under our experimental conditions, CP-MAS provided higher sensitivity than PARIS with a rigid crystalline sample of glycine with long T2 times and signals with rather similar intensities for a sample of amorphous ubiquitin (Figure 5.26).

In practice, taking as reference the intensities in the CP-MAS spectra, we interpreted that signals that are intense in the PARIS spectrum originate from mobile atoms in relatively flexible stretches, while signals that are very attenuated originate from more rigid stretches (Figure 5.27). Resonances of the PARIS spectrum of recBVPrP^{Sc} are heavily attenuated in comparison with the CP-MAS spectrum, reflecting that most of the aliphatic and CO carbons are not experiencing fast dynamics in the ms time scale. In particular, the CO resonance drops to <10%. Of the total CO intensity, 62% is due to ^{13}CO-Phe spins while the other 38% originates from natural abundance ^{13}C background. The CO intensity of the PARIS may originate from those natural abundance residues (not Phe) displaying some mobility, likely in connecting loops since those have a higher flexibility than β-strands. Similarly fibrillary HET-s, that has a higher percentage of residues in β-sheet stretches, is even more attenuated in the PARIS. In contrast, in the PARIS spectrum of the recBVPrP23-231 amyloid, about 50% of the intensity is conserved both in the aliphatic and carbonyl regions of the spectrum, reflecting residual mobility all over, and agreeing with a higher mobility of Phe141 in this sample (Tycko et al.,Wang et al.)

All in all, these results show that the mean mobility of Phe residues in recBVPrP^{Sc} is very limited in the millisecond time scale, substantially lower than that of Phe141 in the BVPrP(23-321) amyloid, and in the same range of that of the Tyr residues in the HET-s prion domain.

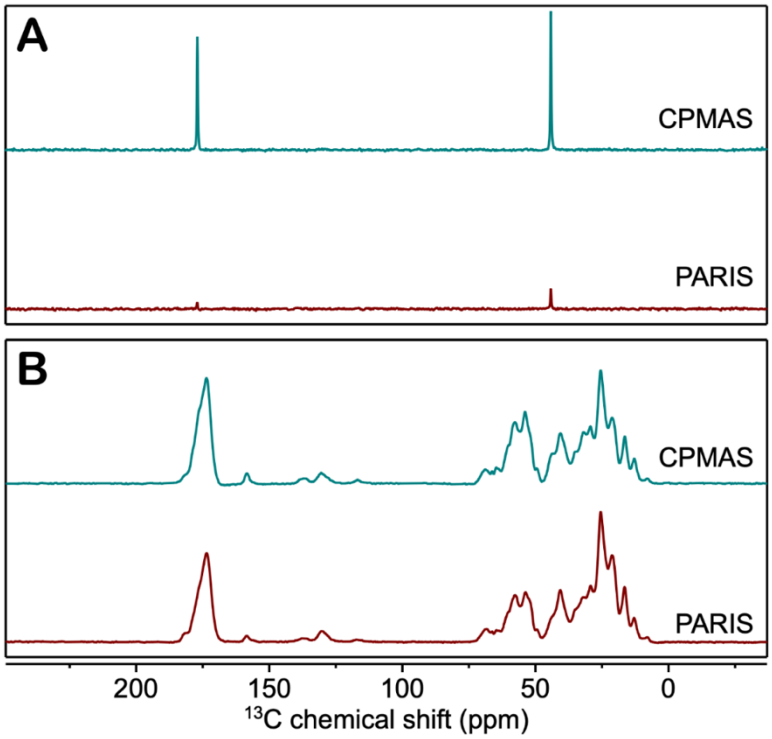

Fig. 5.26. 1D 13C CP vs PARIS ssNMR spectra of (A) microcrystalline glycine in the α-form at natural abundance, and (B) amorphous U-(^{13}C-^{15}N) labelled ubiquitin.

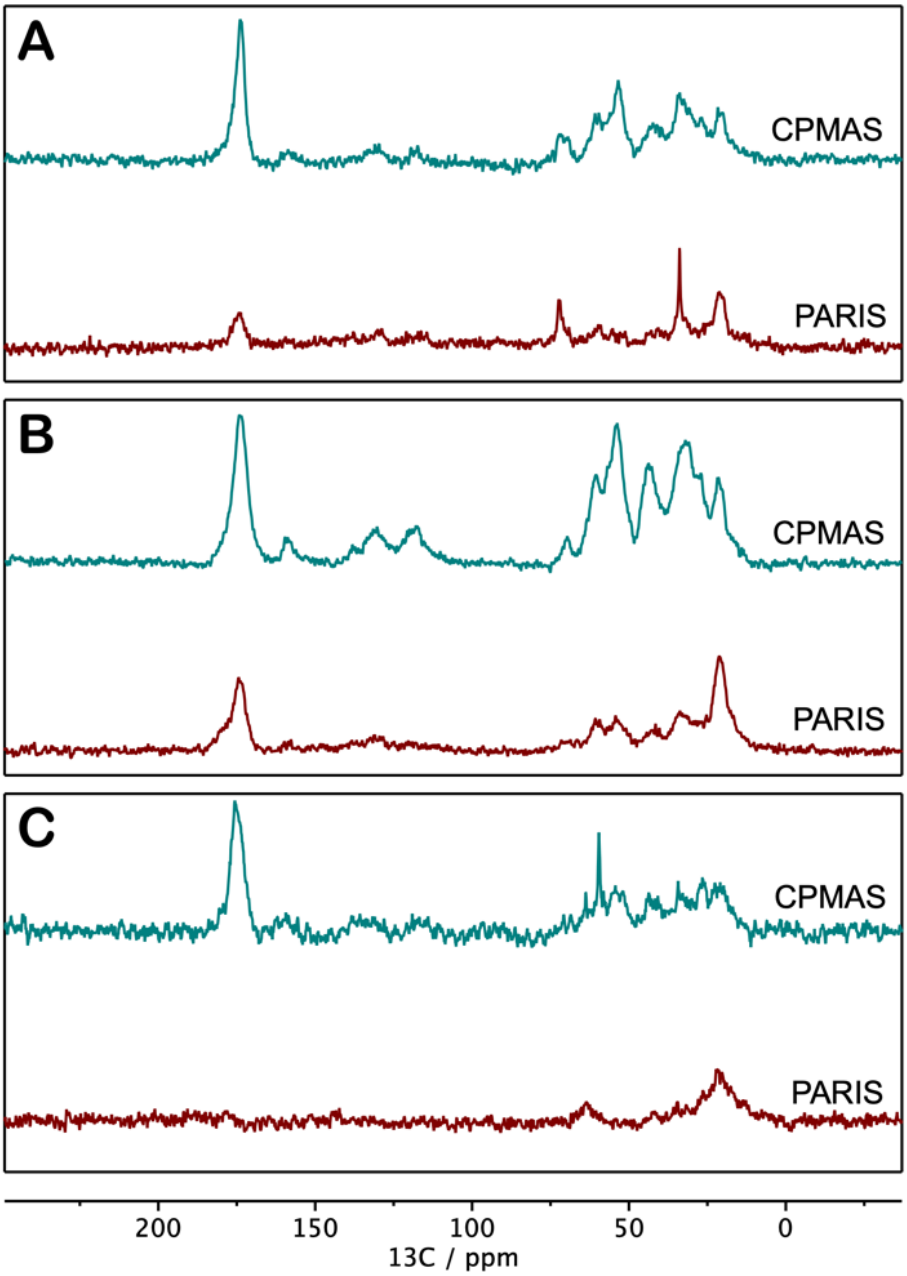

Fig. 5.27. CP-MAS (upper traces) and PARIS (lower traces) spectra of samples (A) the (^{13}CO-Phe)-recBVPrP^{Sc} prion, (B) the (^{13}CO-Phe)-recBVPrP(23-231) amyloid, and (C) the fibrillary (^{13}CO-Tyr)-HET-s(218-289) prion domain. Aliphatic peaks (0-80 ppm) originate from the ^{13}C natural abundance background of the Cα and side chains. The carbonyl band (≈174 ppm) has contributions from the ^{13}C labeled residues (A and B, 3× Phe; C, 2× Tyr) and the ^{13}C natural abundance background of all the backbone and side chain carbonyl groups. The theoretical contributions of the ^{13}C natural abundance to the carbonyl band are: A 38%, B 48%, C 33%.

5.9. $T_{1\rho}$ experiments

In order to further assess the flexibility of our recBVPrP^{Sc} sample, this time in the us time scale, relaxation $T_{1\rho}$ experiments were performed with ^{13}CO-Phe-recBVPrP^{Sc}, ^{13}CO-Phe-PrP amyloid and ^{13}CO-Phe-Het-s. The measurement of relaxation times of low abundance heteronuclei such as ^{13}C or ^{15}N, or of abundant heteronuclei but efficiently diluted in the molecular structure can provide valuable dynamic information at the levels of just one nucleus (i.e. CSA), a dipole defined by a pair of NMR active nuclei, a molecular fragment and/or the full molecule (Kurbanov et al. 2011) (Fig. 5.28).

Different from relaxation parameters such as T_1 and T_2 that only permit to explore a single frequency of motions at a given spectrometer magnetic field, the measurement of the rotating frame T_{1r} relaxation time allows to explore a range of motions which in the case of ss-NMR correspond to correlation times (t_c) between 0.1 ms and ms (Krushelnitsky13). The experimental conditions used here to measure ^{13}C_T_{1r} relaxation times were chosen to maximize the sensitivity to motions with a correlation time t_c of 2.27 ms, that is a region of mobility in which large amplitude motions such as loop motions and domain motions occur in solid proteins at temperatures close to the ambient (Fig. 5.29).

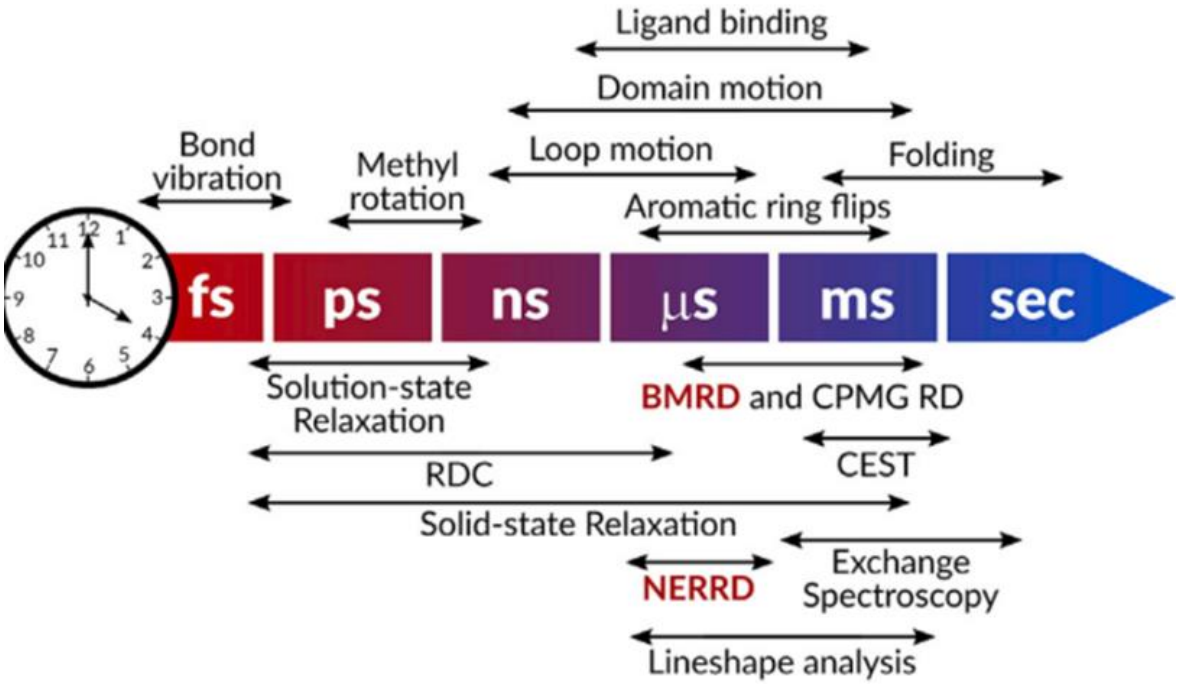

Fig. 5.28 NMR time scale for molecular motions and its observation by ss-NMR. Adaptem from Rovó20.

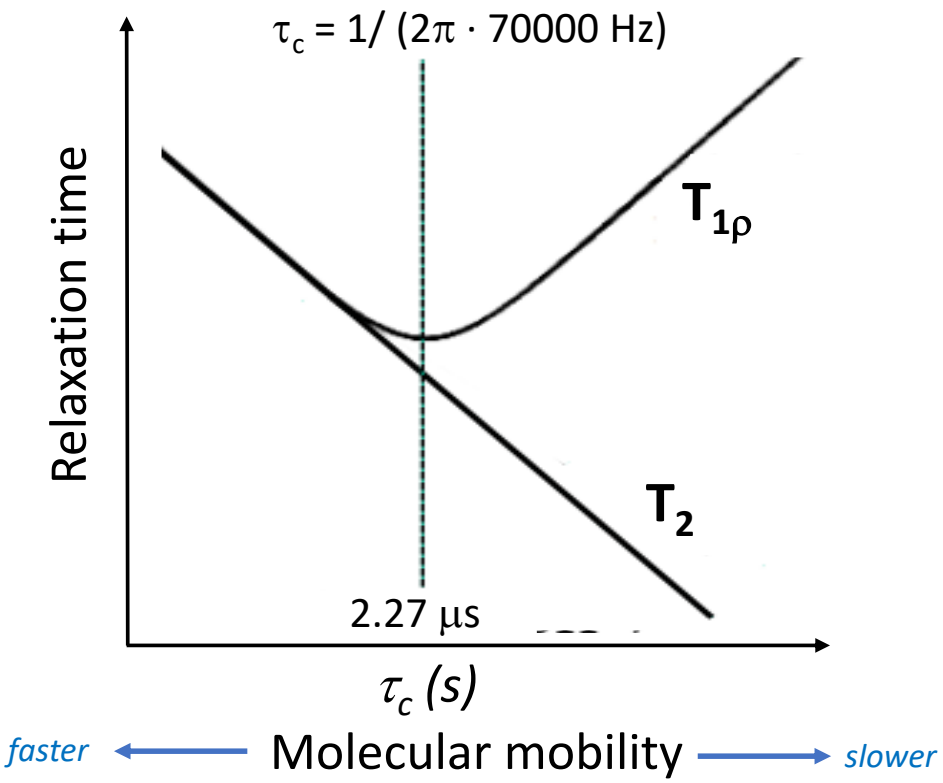

Fig. 5.29. Scheme of the dependence of T_{1r} and T_2 with the correlation time (t_c) for the dipolar relaxation mechanism based in [Kurbanov11]. Regardless the sample, the absolute minimum of the T_{1r} curve occurs exactly at a specific correlation time given by the effective B_1 field strength of the spin-lock pulse applied in the experiment which under our experimental conditions correspond to a t_c of 2.27 ms. A molecule may experience one or several types of internal motions simultaneously and the finally observed T_{1r} depends on the proximity of their correlation time/s to the specific value of t_c that is selected by the T_{1r} experiment (i.e. t_c = 2.27 ms).

Under the relative fast-MAS conditions used of 60 kHz, the CSA mechanism can be neglected, and the only relaxation mechanism contributing to the T_{1r} is the dipolar interaction of ^{13}C with the adjacent protons. The ^{13}C-T_{1r} measurements were carried out at two temperatures of 278 and 313K (Fig. 5.30). It can be seen that the ^{13}C-T_{1r} obtained for the three samples are relative similar at 278 K and more different at 313K. Prior to the interpretation of this data it is important to remark here that the CO signal that is observed in the spectrum of these three samples does not correspond to a single carbonyl nucleus but to the contribution of several carbonyl nuclei that were selectively ^{13}CO labelled in each prion sequence. There is the additional contribution due to the natural abundance of ^{13}C (1.1%) of the non-labelled carbonyls of the backbone as well as the carbonyls in the side chain of amino acids. of types Q, E, N and D. It implies that the $^{13}C\_T_{1r}$ obtained here are sensitive to the motions experienced by an average of all these contributions to the observed carbonyl signal in these $^{13}C\_T_{1r}$ experiments.The effect of increasing the temperature in the sample is reducing the correlation time so that in these experiments one evaluates the effect on $^{13}C\_T_{1r}$ when moving along the horizontal axis of the scheme of Fig. 5.29 (i.e. the axis for t_c).

It can be seen in Fig. 5.30 and Table 5.1 that the three samples PrP amyloid, recBVPrP^{Sc} and HET-s increase its $^{13}C\_T_{1r}$ when raising the temperature from 278 to 313K and the corresponding relative increments are 21, 52 and 29% for PrP amyloid, recBVPrP^{Sc} and HET-s, respectively.

	PrP^{sc} (ZSJ1)	***Amyloid (AP3)***	***Het-s (HET S1b)***
$^{13}C_T_{1r}$_278K (s)	0.031 s	0.037 s	0.029 s
$^{13}C\_T_{1r}$ _313K (s)	0.065 s	0.047 s	0.041 s
VT_$^{13}C_T_{1r}$_variation (%)	52 %	21 %	29 %
Detached carbonyl signal mobility			
Rigid labelled aas. (%) (1)	64 %	36 %	53 %
Slow dynamic labelled aas. (%) (2)	0 %	18 %	0 %
Fast motions (%) (3)	7 %	8 %	9 %
Unknown dynamic natural abund. (%) (4)	29 %	38 %	38 %

(1) 13CO selectively labelled aas. in b-strand, (2) 13CO selectively labelled aas. flexible, (3) QEND side chains, (4) natural abundance backbone aas.

Table 5.1. $^{13}C\_T_{1r}$ relaxation times obtained for the carbonyl signal (~174 ppm) for the three samples studied at VT of 278 and 313 K. A detachment of the dynamic contributions to the carbonyl signal is provided taking into account the selective ^{13}CO labelling and the natural abundance of each sample. These contributions are hypothesized based in our biochemical data [to be explained, maybe in another section].

According to the scheme of Fig. 5.26 this behavior observed for $^{13}C\_T_{1r}$ at the two temperatures studied could be expected when at least some of ^{13}CO labelled nuclei in these samples experience motions that are faster than t_c 2.27 ms (i.e. the relevant dynamic of the three samples is located to the left side of the $^{13}C\_T_{1r}$ curve at the two temperatures).

Qualitatively, the aforementioned observation of a change in $^{13}C\_T_{1r}$ of 52% for recBVPrP^{Sc} which can be interpreted that this sample has a larger contribution of motions in the us-scale than the other two at the lower temperature of 278 K. Therefore, that recBVPrP^{Sc} is more flexible in the us time scale, which includes loop's motions, as we had expected and that can be the explanation for the unusual long intermolecular distance of 6.5 Å.

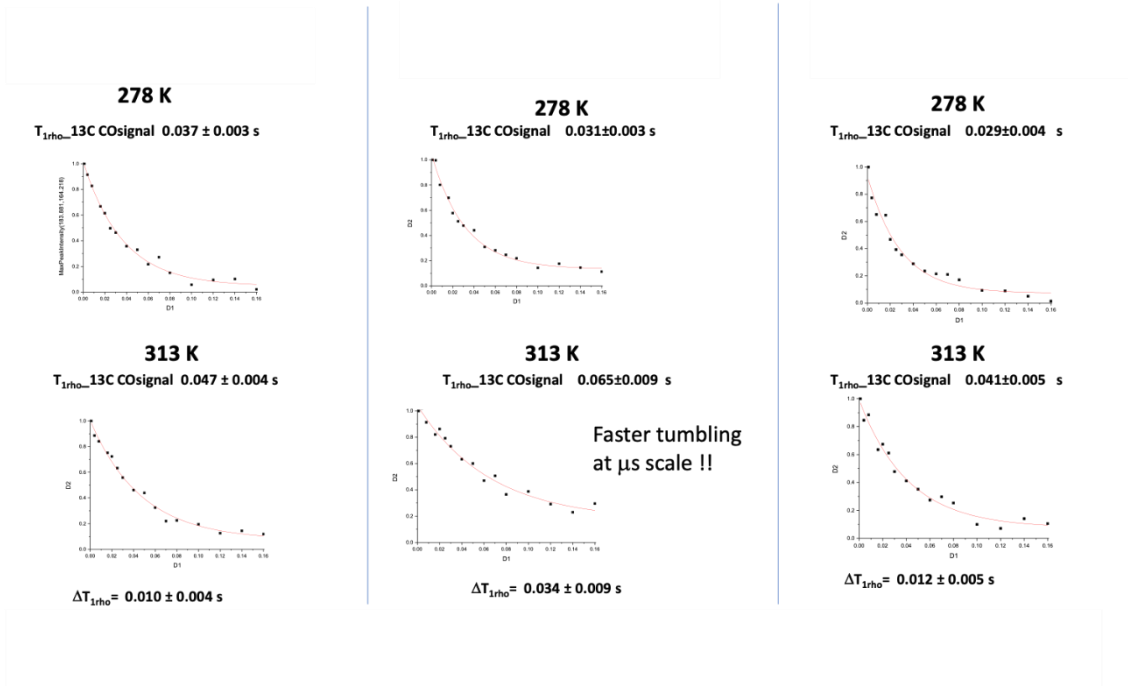

Fig. 5.30 Measurement of $^{13}C\_T_{1r}$ relaxation times. Plot of the experimental intensity of the ^{13}CO peak vs. the spin-lock time (s) for samples PrP amyloid, recBVPrP^{Sc} and HET-s at 278 and 313K. The points were fitted to eq. 1 to determine the $^{13}C\_T_{1r}$ relaxation time of the signal.

An alternative explanation for the longer than 5 Å measured distance would be a mixture of conformers featuring PIRIBS and 4RβS architectures. Such possibility is extremely unlikely and defies Occam's razor.

However, we reasoned that the possibility of the presence of more than one conformer in the recBVPrP^{Sc} sample, even if not necessarily featuring disparate architectures, could not be discounted and merited experimental evaluation. Structural heterogeneity has in fact been reported in Sup35p and PrP23-144 amyloid preparations generated in vitro (Gorkovskiy et al., Helmus et al.). In PrP23-144 infectious amyloid fibers, specific residues located in connecting loops within the PIRIBS core were shown to exhibit conformational heterogeneity (Helmus et al. 2008, Helmus et al. 2010). In our case, putative conformationally distinct residues could be located in PrP monomers belonging to different PrP stacks but also to the same stack, in which case they would feature CO-CO distances longer than 5 Å. However, it is known for a fact that this cannot be since such mixture would be unstable and our recBVPrP^{Sc} is completely stable: upon several PMSA passages it keeps showing the same PK resistance pattern (Eraña 2019).

5.10. ^{13}C-^{13}C DARR spectra

To gather further information on the conformational environment of Phe residues, we were expecting to find that some residues presented chemical shifts characteristic of coil secondary structure, recBVPrP^{Sc} with uniformly labelled (U-^{13}C,^{15}N)-Phe was prepared and its C-C DARR spectrum recorded (Fig. 5.25). It should be remembered that in the 2D 13C-13C DARR spectrum the signals corresponding to Phe could not be unequivocally distinguished from signals arising from other aromatic amino acid residues (Fig. 5.12). This is in contrast with the Ile Cβ/Cγ2 peaks, which could be unequivocally ascribed to Ile (Fig. 5.11B) and showed no evidence of conformational heterogeneity, as only 4 peaks were seen.

The cross-peaks in the CO/CA region, which showed the best dispersion (Fig. 5.31), are particularly informative: one cross-peak is expected from each one of the Phe residues, unless their chemical shifts completely overlap. Instead of the 3 expected, we detected two sets of two distinct signals each in the CO/CA region. One with a chemical shift characteristic of β-secondary structure, whereas the other set displayed a chemical shift typical of coils (Zhang et al.).

This raises several possibilities. One is that our recBVPrP^{Sc} sample is a mixture of two main conformers. For instance, in one of such conformers all of its three Phe residues are located in coils, whereas all three Phe residues in the other conformer are located in stretches featuring β-sheet secondary structure (Zhang et al.). Alternatively, they might feature Phe residues in different combinations of secondary structure, for example two in β-sheets and one in a coil, etc. Another option is that the various signals are due to Phe residues presenting static heterogeneity, hence there being just one conformer.

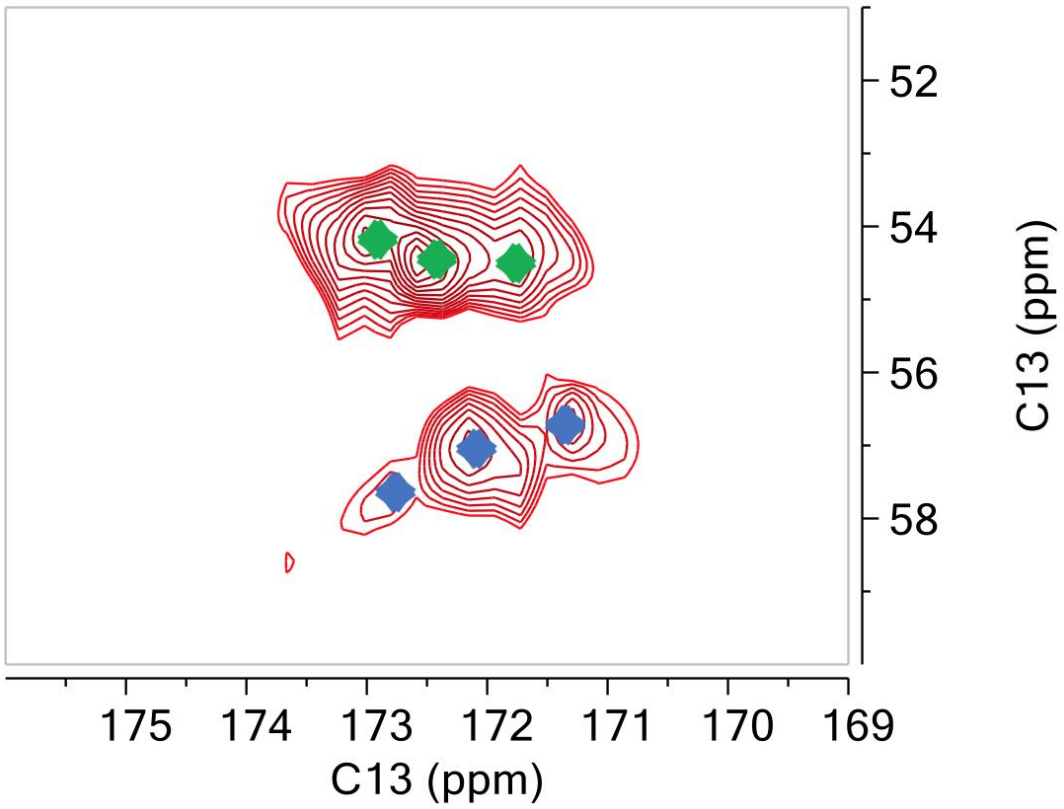

Fig. 5.31. ^{13}C-^{13}C DARR (□mix=100 ms, MAS 20 kHz) of a (U-^{15}N,^{13}C-Phe)-recBVPrP^{Sc} sample. Crosses indicate some of the peaks identified. Crosses are colored according to the CA and CB chemical shifts characteristic of ß-sheet (blue) or coil (green).

6. DISCUSSION

Recombinant PrP^{Sc} was prepared which presented high titers of infectivity ($6.34 \cdot 10^4$ LD50/μg of PrP in TgVole (1x) mice) and was characterized by SDS-PAGE and MS showing both techniques an agreement since the three characteristic bands of around 6, 9.5 and 15.5 KDa appear. Spectra (Fig. 5.4) showed fragments N97-S231, Q98-S231, and G92-S231 (the ~15.5 kDa band seen in the SDS-PAGE gels); fragments N153-S231 and M154-S231 (the ~9.5 kDa band seen in the gels) and N97-E152, Q98-N153 and Q98-E152 (the ~6 kDa band in the gels) which are all in perfect agreement with the identification of the PMSA product by Eraña et al. The larger N97-S231 PK-resistant core is reminiscent of Drowsy-type PrP^{Sc} strains (Bessen et al.). Cleavage at N153 and M154 is also seen in brain-derived PrP^{Sc} albeit at a substantially lower proportion (Vázquez-Fernández et al, Silva et al.).

All in all, by PMSA we obtained a recombinant PrP^{Sc} which can be concluded as being *bona fide* thus all the experiments we shall perform with it should yield results also transferable to brain PrP^{Sc}, although interpreted with due caution.

6.1 FTIR analysis

The spectral characteristics of our non-infectious PrP sample, a minimun at 1626 cm^{-1} and a shoulder at 1630 cm^{-1}, is consistent with data found in the literature (Bocharova et al., 2005a, Bocharova et al. 2005b, Makarava et al. 2009, Jones and Surewicz, 2005), showing absorption bands typical of β-strands with maxima in the 1616 and 1626 region, sometimes seen as a single peak, sometimes as a peak with a shoulder at a slightly higher wavenumber value. The maxima of amyloids in general, and PrP amyloids in particular, are lower than the typical minima of non-amyloid soluble proteins containing β-strands, typically found around 1630 cm^{-1} (Zandomeneghi et al. 2004), although overlap exists. This has been interpreted as a consequence of the particular strength and rigidity of the cross- β arrangement of β-strands in amyloids. Furthermore, the presence of shoulders in the main absorption peak always suggests the existence of two types of β-strands in the sample with slightly different characteristics: parallel vs. antiparallel, longer vs. shorter, etc., as the frequencies of absorption of β-sheet carbonyls can be modulated by factors, such as strength/length of hydrogen-bonding, distortions of sheet structure, or solvent exposure (Caughey et al. 1998). Non-infectious PrP amyloids are known to feature a parallel-in-register stacked (PIRIBS) architecture, a conclusion based on ssNMR, EPR and cryo-EM (Cobb et al. 2007, Tycko et al., 2010, Wang 2020). This means that they contain only parallel β-strands and the presence of shoulders in their β-structure associated band must perhaps be ascribed to subpopulations of β-strands with differences in length or compactness. Thus, when a PrP amyloid sample was partially unfolded by heating, the maximum of the absorption β band shifted from 1620 cm-^{1} to a higher wavenumber (Bocharova et al., 2005a).

The maximum of the β-structure-associated absorption peak in the infectious recBVPrP^{Sc} sample is at 1632, shifted to upper wavenumbers with respect to the values seen in the spectrum of the amyloid sample. Similar upshifted maxima have been described in the literature for brain-derived PrP^{Sc} samples. Thus, Spassov et al. reported spectra with maxima at 1629-1634 cm-^{1} for different strains of murine scrapie PrP^{Sc}, in some cases with tenuous shoulders of a slightly lower value (Spassov 2006). In another study, the

shoulders of these β bands separated into independent peaks with maxima at 1636/1626 cm-1 for Hyper and 263K PrP^{Sc} and a single peak with a maximum at 1629 cm^{-1} for Drowsy PrP^{Sc} (Caughey et al., 1998). In a more recent study, the same group showed spectra of GPI-anchorless (which are also underglycosylated) PrP^{Sc} samples of different strains with single maxima at 1630/1634 cm^{-1} or doublets at 1630/1634 and 1622/1626 cm^{-1} (Baron et al. 2011). These higher absorption maxima overlap with the values seen in spectra of β-strand-containing soluble proteins (Khurana and Fink 2000).

At this point, it is noteworthy to consider that both recBVPrP^{Sc} and PrP amyloid present PIRIBS architectures although our experiments showed that the FTIR spectrum of infectious recBVPrP^{Sc} exhibits a distinct difference with respect to that of a non-infectious BV PrP amyloid, with a β band in the amide I region whose maximum is upshifted. The only possible explanation is that both conformers have PIRIBS architectures with key differences in the length of β strands, their flexibility, water accessibility, etc. Taking into account our other experiments (NMR) this difference is probably due to our recBVPrP^{Sc} being a PIRIBS whose β-sheets are over all less rigid than those of non-infectious PrP amyloid.

6.2 ssNMR studies of uniformly labelled recPrP^{Sc}

Up to recently, it was not possible to investigate rec PrP amyloids with high resolution techniques due to the general challenge posed to structure analysis by insoluble, non-crystalline, and heterogeneous samples but also to the impossibility of preparing NMR-sufficient amounts of homogeneous brain-purified samples.

In 2010, Tycko and collaborators reported for the first time the results of solid state NMR measurements on recombinant PrP 23-231amyloid fibers, previously only experiments with fragments of PrP (PrP 106-126, PrP 109-122, PrP 89-143 and PrP 23-144) had been performed. Their principal conclusions are that recPrP 23-231 fibers contain in-register parallel β-sheets and that the structurally ordered fibril core includes the C-terminal segment, approximately residues 175-225, which includes the second and third α-helices of monomeric PrP. Only a subset of residues within this segment contribute to solid state NMR signals, however, suggesting that structurally ordered sub-segments (presumably β-strands) coexist with disordered and dynamic sub-segments (presumably loops). (Tycko 2010).

Mueller and colleagues in 2014 reproducibly prepared two kinds of samples containing sheep full-length recPrP(25-233) amyloid, one which was formed by spontaneous conversion and another one by nucleation with scrapie brain seeds purified using PTA purification, in high yield and purity, and characterized them by solid state NMR. The seeded sample was prepared using PrP^{Sc} seed and had an attack rate of 100%, however the authors did not eliminate the PrP^{Sc} seed which was in high enough quantities in the inoculum to render it infectious, and the one prepared by spontaneous conversion which had an attack rate very low in the first passage, of a maximum of 2/8, and an attack rate of 100% in the second passage.

They carefully selected this sample of ovine ARQ full-length recombinant PrP(25-233) for several reasons: (i) Only full-length recPrP encompasses the entire brain PrP^{Sc} sequence containing all prion disease-related polymorphism sites. Only fibrils from full-

length PrP closely resemble structures formed in vivo. (ii) Scrapie is the biochemically most investigated as well as the most widespread prion disease. (iii) The well-defined set of sheep PrP-polymorphisms at positions 136 (A/V), 154 (R/H), and 171 (Q/R/H) governs scrapie susceptibility and allows further study of structure infectivity relationships. The homozygous combination A136R154Q171 is associated with highest scrapie susceptibility and frequency.(iv) RecPrP-fibrils can be generated either under partially denaturing conditions or by protein misfolding cyclic amplification (PMCA) and they believed that it was better to use denaturing conditions, probably because it is considerably easier to prepare than the PMCA-samples due to the intrinsic difficulty of such technique. However, because they used the first method their samples were either non-infectious or infectious due to the PrP^{Sc} seed originally added.

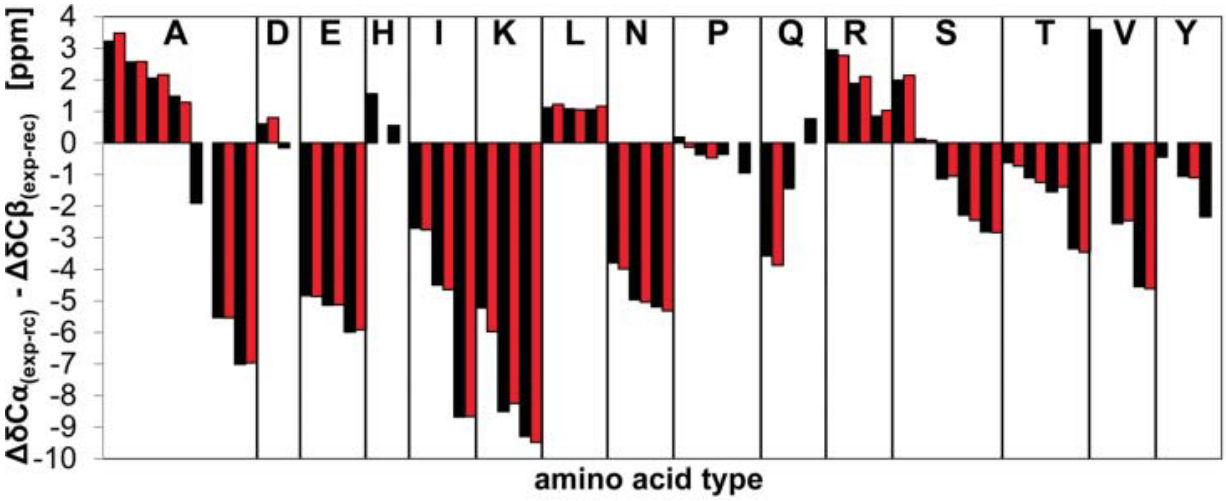

Figure 6.1. Secondary chemical shifts. A comparison of secondary chemical shifts of ovrecPrP(25-233) after spontaneous (black) or PrP^{Sc}-seeded (red) conversion suggests that both amyloid types share a similar overall arrangement of secondary structure elements. All amino acid residues are listed in alphabetic order. Adapted from Mueller 2014. Shown for clarity.

Mueller and collaborators compared its NMR data with that of previous studies using non-infectious recombinant PrP samples like his but from mouse (Tycko 2010), which allowed them to draw several conclusions; some of which will be delineated here: (i) The secondary chemical shifts of ovrecPrP(25-233) after spontaneous conversion or PrP^{Sc}-seeding are similar though not identical (Fig. 6.1), indicating similar underlying conformational motifs. An overlay of solid-state NMR spectra of both preparations, however, visualizes slightly different cross peak patterns and intensities suggesting the presence of deviating structural features. Since site-specific information was missing, however, it could not be decided whether slightly different cross peak positions indicate local structural differences only. (ii) The number of identified residues in solid-state NMR spectra is apparently smaller than the number of amino acid residues in the ovrecPrP(25-233)-sequence as it is the case of our recBVPrP^{Sc} which is mainly due to a severe spectral overlap, particularly in highly populated chemical shift regions. In addition, it could not be excluded that line broadening effects further reduce the number of identifiable residues. The complete lack of INEPT-signals confirms that all segments in ovrecPrP-conformers after spontaneous conversion or PrP^{Sc}-seeding are rigid on a sub-

microsecond time scale which differs from our results, as we saw some residues (Gln/Asp, Arg) in our ^{1}H-^{15}N- INEPT spectrum. Apart from spectral overlap, a smaller than expected number of rigid residues may additionally be due to exchange broadening by molecular motions on the NMR-time scale or due to extensive inhomogeneous line broadening beyond detectability as a result of a high degree of disorder in completely rigid segments. (iii) The segment C-terminal of sequence position 100 contains only 10 out of 43 glycine residues. They observed, however, the up to twofold number of glycine cross. A number of 10 glycine residues represent only 7.5 % of all 133 residues C-terminal of sequence position 100. The integrals of the glycine-specific N-Cα-region in 2D-(^{15}N-$^{13}C\alpha$)-spectra (without any following mixing) and the glycine-specific CO-Cα -region in 2D-(^{13}C-^{13}C)-correlation spectra, however, constitute on average 14.6 ± 1.5 % of the entire Cα-region in the respective spectrum. This indicates that either a small fraction of the N-terminus does contribute to solid-state NMR-spectra or that glycine-containing regions C-terminal of sequence position 100 are disordered to some extent this is in line with our results as we only detected a few rigid Gly residues in our DARR spectrum. (iv) A sequentially assigned minimum of 3 consecutive b-sheet residues or 4 consecutive a-helical residues are required to define a β-strand or an α-helix, respectively, at a distinct sequence position. Although Mueller and colleagues lacked site-specific assignments, they found some hints for the position of secondary structure elements by combining the secondary structure information for individual amino acid types with information about the primary sequence. The 3 ovrecPrP (25-233)-leucine residues are at positions 128, 133, and 141, i.e., clustered in the middle region. All of them are characterized by α-helical chemical shift signatures. Seven out of 9 alanine residues in ovrecPrP(25-233) are clustered at positions 116, 118, 119, 120, 121, 123, and 136 like in our recBVPrP^{Sc} sample. At least 4 alanine residues identified in their spectra have chemical shifts indicative of α-helical secondary structure. Eight out of 11 arginine residues in ovrecPrP(25-233) are N-terminal of position 168. All signals assigned to arginine residues have chemical shifts indicative of α-helical secondary structure but now we now this cannot be so they were shifts indicative of loops (Zhang 1994). These observations suggested that this middle region of fibrillated ovrecPrP(25-233) contains several closely adjacent β-turns secondary structure. All resonances with an α-helical chemical shift signature could be assigned to this region, either unambiguously (Leu128, Leu133, Leu141) or tentatively (Ala116, Ala118, Ala119, Ala120, Ala121, Ala123, Ala136, Asp147, Asp150, Arg139, Arg151, Arg154, His114, His143, Gln101, Ser135, Ser138, Val124, and Val125). (v) All other secondary chemical shifts were indicative of amino acid residues in a β-sheet conformation. A semi-mobile N-terminus and loops and β-turns segments between residues 115 and 155 imply that the majority of these β-strand residues are confined to the segment C-terminal of residue 155 (Mueller 2014) as had already been stated by Tycko and collaborators in 2010 (Tycko 2010).

When comparing our data to Mueller's, we saw some resemblance, however, we employed a different protocol to prepare infectious material for NMR analysis, PMSA, which generates inherently infectious recombinant PrP^{Sc}, unlike Mueller's and Tycko's samples. Moreover, our material had an attack rate of 100% and PK resistance. Thanks to the development of PMSA which allows for the production of high quantities of recombinant PrP^{Sc} we were able to perform ssNMR experiments with (U-^{13}C, ^{15}N)-BV PrP^{Sc} (109I). We obtained ^{1}H-^{13}C CP-HSQC, ^{13}C-^{13}C-DREAM, ^{13}C-^{13}C-DARR, ^{1}H-^{13}C-INEPT-HSQC and ^{1}H-^{15}N-INEPT-HSQC spectra which permitted us to gather some structural information but not to effectively distinguish between the PIRIBS and the 4RβS models which was not known at the time of these experiments.

The spectra we obtained with U-^{13}C, ^{15}N)-BV PrP^{Sc} (109I) showed, as expected, broad signals, as seen for other amyloids, all featuring some degree of conformational diversity within a given sample (Mueller 2014, Tycko 2010). The exception to this is the functional Het-s prion domain, whose conformation has been subjected to natural selection and is therefore very well defined, which results in spectra with sharp peaks (Wasmer 2008). However, clearly that is not the case for PrP^{Sc}, an amyloid conformer with no expected function, and without the stringent selective pressures associated to one. Nevertheless, in spite of the severe signal overlapping and the high number of signals in the spectra, we were able to glean a substantial amount of useful structural information from the spectra.

One important and new conclusion at the time derived from the spectra is that β-strands extend into the N-terminus of the recPrP^{Sc} PK-resistant core, as at least three of the Ala in the Ala113, Ala115, Ala116, Ala117, Ala118, Ala120 sequential stretch are in β-sheet conformation since we see a minimum of four Ala peaks in the DREAM spectrum (Fig. 5.11C) with chemical shift characteristic of β-strand secondary structure (Zhang et al.) and we know that we cannot assume that one amino acid just produces one peak in the spectra as such amino acid may present heterogeneity but we also know that three residues in a row are needed to form a β-strand; this is why we can conclude that in the Ala 113-Ala120 where there are nearly only Ala there must be three residues in a β-sheet conformation. This conclusion that β-strands extend into the N-terminus of the recPrP^{Sc} PK-resistant core disagrees with that of Mueller's and Tycko's non-infectious material (Mueller 2014, Tycko 2010) whose resistant β-core starts around position 160, therefore those Ala residues do not contribute to it. Moreover, since brain-derived 263 K PrP^{Sc}'s structure was solved last year by cryo-EM (Kraus 2021) we know that it indeed has those Ala in a β-sheet conformation, precisely in a giant β-arch from residues 125 up to 168.

In addition, before the structure of brain-derived PrP^{Sc} was known, we were able to obtain more relevant data from the DARR and DREAM spectra. Our spectroscopic data suggest that at least one Ile residue out of the four present is the PrP^{Sc} sequence is not located in a β-strand since there are two sets of signals featuring two kinds of chemical shifts, one characteristic of β-strand and the other of coil secondary structure (Fig. 5.11B), despite the fact that Ile has the second highest propensity to participate in β-strands (Minor Jr), whereas in Mueller's work with the non-infectious sample, all Ile are located within β-strands (Mueller 2014). Moreover, Gly which has a low propensity to be in β-strands (Minor 2014) is barely observed in our spectrum (Fig. 5.12B) as well as in Mueller's spectra (Mueller 2014) which is expected and of no surprise to us.

Furthermore, analysis under conditions more suitable for soluble state samples were performed, i.e., 2D ^{1}H-^{15}N INEPT-HSQC experiments (Fig. 5.15), showed that a few amino acid residues of PK-treated BVPrP^{Sc} are located in regions with a very high mobility since as already stated in INEPT experiments the cross peaks that appear are the one corresponding to amino acid residues which have a high mobility in the scale of ns, in contrast with the CP experiments we performed before. While sequential information could not be obtained, based on their distinct chemical shift values, these include 2 Gln and/or Asn residues, 1 Arg and 2-3 Ser and/or Thr residues among a total of ~10-12 residues. Smirnovas et al. and Noble et al. have reported deuterium/hydrogen exchange studies suggesting that a short C-terminal (but not N-terminal) sequential stretch is substantially flexible, with high exchange rates (Smirnovas, Noble). The C-terminal stretch of BVPrP is: Ser231-Ser-Arg-Gly-Glu-Tyr-Tyr225. Our ^{1}H-^{15}N INEPT-HSQC spectra contained unequivocal signals corresponding to a minimum of 2 Serines and one

Arginine. A possible weak Glycine was also seen (Fig. 5.13). A sizeable fraction of our PK-treated recBVPrP^{Sc} sample has a nick at positions Asp153 and Met154 which we believed could be evidence of a putative small tail might become loose after the PK treatment.

To sum up our ssNMR experiments gathered some relevant amino acid secondary structure information which, sadly, was not enough to fulfill its main objective which was distinguishing between the PIRIBS and the 4RBS models. Contrary to desires, since hypothesized that PrP^{Sc} presented a 4RBS architecture, the data we were able to extract from ssNMR is compatible with a PIRIBS architecture that had been proposed for recBVPrP^{Sc} (Groveman 2014). More specifically, a PIRIBS structure in which several Ala residues within the A114-A121 region are part of a β-strand, one of the 4 Ile residues within the Q97-S231 main PK-resistant core is located within a loop, and the majority, but not all Gly residues are excluded from β-strands. In 2021 it would be confirmed that indeed at least the structure of brain-derived PrP^{Sc} is a PIRIBS.

6.3 PITHIRDS experiments

As it has already been described, attempt of solving the structure of PrP^{Sc} by performing experiments with the uniformly labeled PrP^{Sc} sample was not successful. We needed something different: an experiment that was able to distinguish between both proposed architectures. Therefore, we used PITHIRDS-CT developed by Tycko et al. to probe the architecture of recBVPrP^{Sc}. This experiments allowed us to know whether PrP^{Sc} presents a PIRIBS structure or not.

As already indicated, during the evolution period of this NMR pulse sequence, rotor-synchronized π pulses that occupy one third of the magic angle spinning (MAS) rotor period are applied on ^{13}C to recouple the ^{13}C-^{13}C dipole-dipole interactions that otherwise average out by MAS. The experiment is repeated for a series of effective recoupling times that modulate the signal intensity. Relaxation and other factors that also modulate signal intensity, in particular during the recoupling period, are kept constant by the use of constant time conditions (CT) for the whole series of experiments (Tycko 2007). Thus, the curve of ^{13}C signal intensity vs. effective recoupling time is primarily modulated by the ^{13}C-^{13}C dipole-dipole interaction and, due to its $1/r^3$ dependence, ^{13}C-^{13}C distances can be deduced by numerical simulations (Groveman 2014, Shewmaker 2006, Baxa 2007, Shewmaker 2009a, Gorkovskiy 2014, Tycko 2010, Shewmaker 2009b). We adapted the pulse sequence and some of the experimental 366 conditions originally developed for a 9.4 T spectrometer to our 17.6 T instrument and to 40 kHz MAS.

We chose these to measure mean Leu-Leu and Phe-Phe residues following previous studies (Groveman 2014, Shewmaker 2006, Baxa 2007, Shewmaker 2009a, Gorkovskiy 2014, Tycko 2010, Shewmaker 2009b) because they typically appear in β-strands (Minor 1994). Other possible choices such as Tyr or Ile were discarded given the existence of sequential pairs or very close neighbors (Tyr224-Tyr225, Ile181-Ile183) that can introduce intra-molecular artifacts into the purportedly inter-molecular ssNMR-distance measurements.

Before discussing our PITHIRDS results, it is important to describe Gorkovskiy and collaborators´ work from 2014. They used PITHIRDS to probe the architecture of the

Sup35p prion domain which is a yeast eukaryotic translation release factor that consists of a Q/N-rich N-terminal domain (N, residues 1–123), a highly charged middle domain (M, residues 124–253), and the C-terminal domain essential for translation termination(C, residues 254–685). The Sup35p prion domain includes the N domain (residues 1–123) and an unknown part of the M domain, depending on how "prion domain" is defined (Gorkovskiy 2014). Gorkovskiy and collaborators converted the three Ile residues in Sup35NM to Leu and subsequently replaced 16 single residues with Ile, one by one, and prepared the ^{13}CO-Ile amyloid of each mutant. In order to test the in-register parallel model for amyloid of Sup35NM, it would be ideal to have singly ^{13}C-labeled molecules so that nearest neighbor distances would necessarily be intermolecular and Ile is a suitable choice for performing scanning mutagenesis. They also had the same problem as us of relatively broad peaks found in 2D solid-state NMR experiments (Gorkovskiy 2014).

PITHIRDS measurements showed ten of the residues examined to have a ~5 Å distance; however, five residues (Y29I, I239, G51I, G58I and Y73I), interspersed among these, showed longer apparent distances (Fig. 6.2), which was interpreted in terms of their possible location in turns or loops within the PIRIBS core, because, as stated by the authors, residues in turns or loops are not as tightly constrained by main chain H-bonds to the neighboring molecules to be close to the corresponding residues (Gorkovskiy 2014). As an example, residues I239 and Y731 have an apparent distance of way longer than 7 Å , like our Het-s sample,(Fig. 6.2), and would be located in short connecting loops (Fig. 6.3) This may also be our case and the explanation of why we obtained a 6.5 intermolecular distance with Phe and Leu. It would be interesting in the future to explore the possibility of doing scanning mutagenesis with Phe or Leu in recBVPrP^{Sc}.

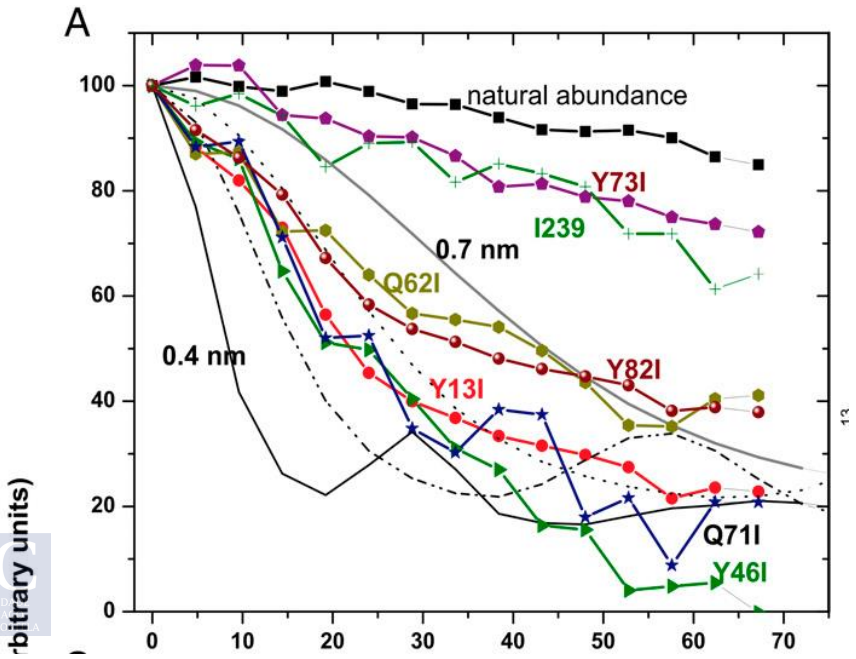

Figure 6.2. Measurements of ^{13}C-^{13}C dipole-dipole couplings of Sup35NM samples singly labeled with Ile-1-^{13}C. Amyloid filaments of Sup35NM Y13I, Y46I, Q62I, Q71I, Y73I, Y82I, and I239 (each having the I152L, I220L, and I239L, except for the I239 sample) singly labeled with Ile-1-^{13}C are compared with unlabeled filaments. Adapted from Gorkovskiy 2014.

Figure 6.3. Gorkovskiy's model of Sup35NM amyloid. Residues in blue are found to have in-register parallel structure and those in red are not. The Ile residues in green were changed to Leu in all mutants as was Ile239, except when labeling Ile239 itself. The data suggest that each molecule in the in-register ß-sheet contributes several ß-strand segments and several turns or loops. The underlined regions may be ß-strands and possible loop/turn regions are shown. Adapted from Gorkovskiy 2014.

Our PITHIRDS studies show that infectious recBVPrP^{Sc} features the characteristics of a PIRIBS, albeit with unusually long measured mean Phe-Phe and Leu-Leu distances. One possible explanation for these discrepancy with the expected 5 Å ^{13}CO-^{13}CO intermolecular distance is that only some of the three Phe and two Leu are located in canonical β-strands, being the other remaining residues in short β-archs and/or loops connecting the canonical β-strands which might result in apparent > 5 Å mean distances, since that is the case with the non-infectious PrP amyloid whose Phe 141 is outside of the β-core showing its PITHIRDS an intermolecular distance of 5.5 Å, and as this also happens to residues Q621 and Y821 from the Sup35p prion domain which have a 6.5 Å mean distance (Gorkovskiy). With a 7Å mean intermolecular ^{13}CO-^{13}CO distance, our ^{13}CO-Asp-recBVPrP^{Sc} sample did not yield a result compatible with a PIRIBS architecture. However, taking into account Phe-Phe and Leu-Leu results, it is likely than most Asp residues are not located in β-strands as this residue has a low propensity of being in β-strands, which is the case in Kraus's structure (Fig.6.6B)

Furthermore, it is also important to consider PrP 23-144 amyloid. Recombinant C-terminally truncated prion protein PrP23-144 which corresponds to the Y145Stop PrP variant associated with a Gerstmann–Sträussler–Scheinker-like prion disease spontaneously forms amyloid fibrils with a parallel in-register β-sheet architecture and β-sheet core mapping to residues ~112–139. Mouse PrP 23-144 fibers were found to be infectious by Choi and colleagues in 2016 when inoculated into both transgenic and wild type mice with a 100% attack rate which was a complete surprise at the time; however, it

was not given too much importance as it was interpreted as a transmission that in the brain evolved towards PrP^{Sc} *boda fide* in a deformed-templating-like mechanism (Choi 2016).

Later, in 2017, Theint and collaborators performed experiments with solid-state NMR spectroscopy with the aim of solving the structures of PrP23-144 amyloids from three different species: human, mouse and Syrian hamster. The unique advantage of PrP23-144 amyloid fibrils is that, unlike other mammalian prions, this system is readily amenable to high-resolution structural analysis by solid-state NMR spectroscopy (Theint 2017), given the much smaller number of signals in spectra of uniformly labelled PrP 23-144 amyloid which in turned resulted to be a consequence of just a small number of residues conforming the resistant β-core.

Moreover, Theint and colleagues found other features of PrP 23-144 amyloid which are in line with our observations that residues in amyloids located in loops render by PITHIRDS an intermolecular distance considerably longer than the expected 5 Å. Namely, they found that some amino acid residues located in tentative short loops connecting canonical β-strands within the PIRIBS core of infectious PrP 23-144 fibers are flexible enough so as to not being detectable in two-dimensional NCA spectra. This would be a consequence of motions in the microsecond-millisecond time scale. Namely, Tyr128 and Met129 in HuPrP23-144 and Met129 in MoPrP23-144 amyloid fibers were undetectable (Theint 2017).

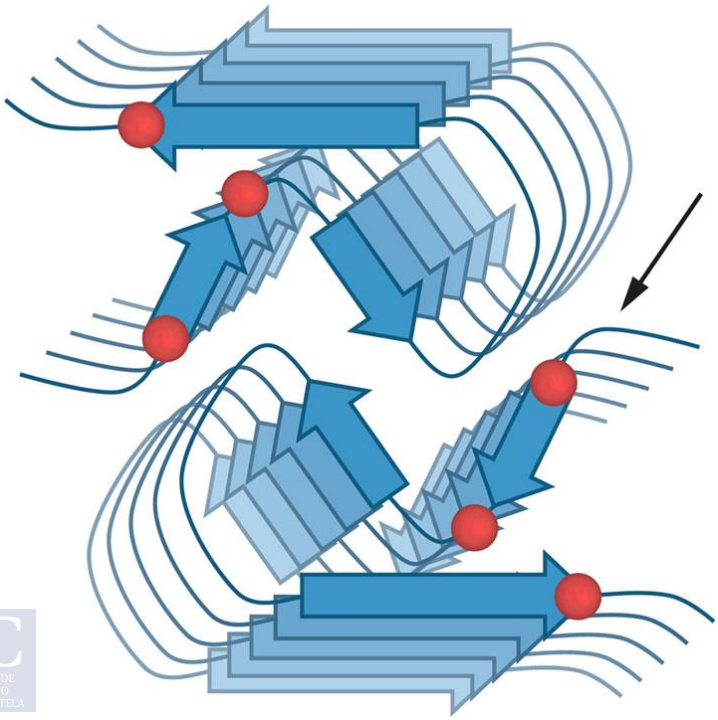

Figure 6.4. Schematic model for the human amyloid core based on the combination of solid-state NMR and tilted-beam transmission electron microscopy data. Adapted from Theint 2017.

Surprisingly, it turned out that the PrP 23-144 amyloid's architecture proposed based on ssNMR (Fig. 6.4) was erroneous: not long after its proposal, the same group (Li 2021) published a density map for the ordered amyloid core with a nominal resolution of 2.86 Å obtained by cryo-EM (Fig. 6.5a and b). This core shows a parallel, in-register architecture, in which each fibril consists of four identical protofilaments with a C2 symmetry (Fig. 6.5b and c). A near-atomic model was built for the fibril core that maps to residues 108-141 (Fig. 6.5d and e).

The identity of this core region is similar to that suggested by previously reported solid-state NMR studies, though the fibril samples in those studies appear to be composed of two protofilaments not four. In their cryo-EM-based model, each subunit has an "S" shape, largely extended backbone geometry and encompasses three relatively short β-strands (residues 109-112, 133-135, and 138-140) (Fig. 6.5c and e). The 113-125 region is rich in rigid turns, with numerous solvent-inaccessible hydrophobic residues participating in intramolecular interactions involving side chains of M112/A116/A117 and A115/A118/V121/L125 (Fig. 6 d and f), in line with those previously observed by solid-state NMR by the authors. Another cluster of solvent-inaccessible hydrophobic side chains maps to the C-terminal part of the core and includes M129, A133, I139, and F141 (Fig. 1d and f).

These two clusters of hydrophobic resides play a key role in stabilizing the four-protofilament structure of the fibrils. In this structure, protofilaments A and B (as well as C and D) are arranged in a head-to-tail manner, with a large dry interface between them that is stabilized largely by intermolecular interaction between the N-terminal hydrophobic residues (M112, A116, A117, A120, and V122) and C-terminal hydrophobic residues (M129, A133, I139, and F141) (Fig.6.5e and f). The above-described intermolecular interactions, together with intramolecular interactions involving hydrophobic residues within the 112-125 region, result in a structure in which most (13 out of 18) hydrophobic side chains are buried within the amyloid core interior.

The interface between inner protofilaments B and C is much shorter, with intermolecular hydrogen bonds involving only L130 and S132. The latter interface is additionally stabilized by side chain-side chain interactions involving nearby residues Y128, L130, M133, and R136 (Fig. 5.6 e and g). It is again important to notice that Y128 was not detected in two-dimensional NCA spectra either.

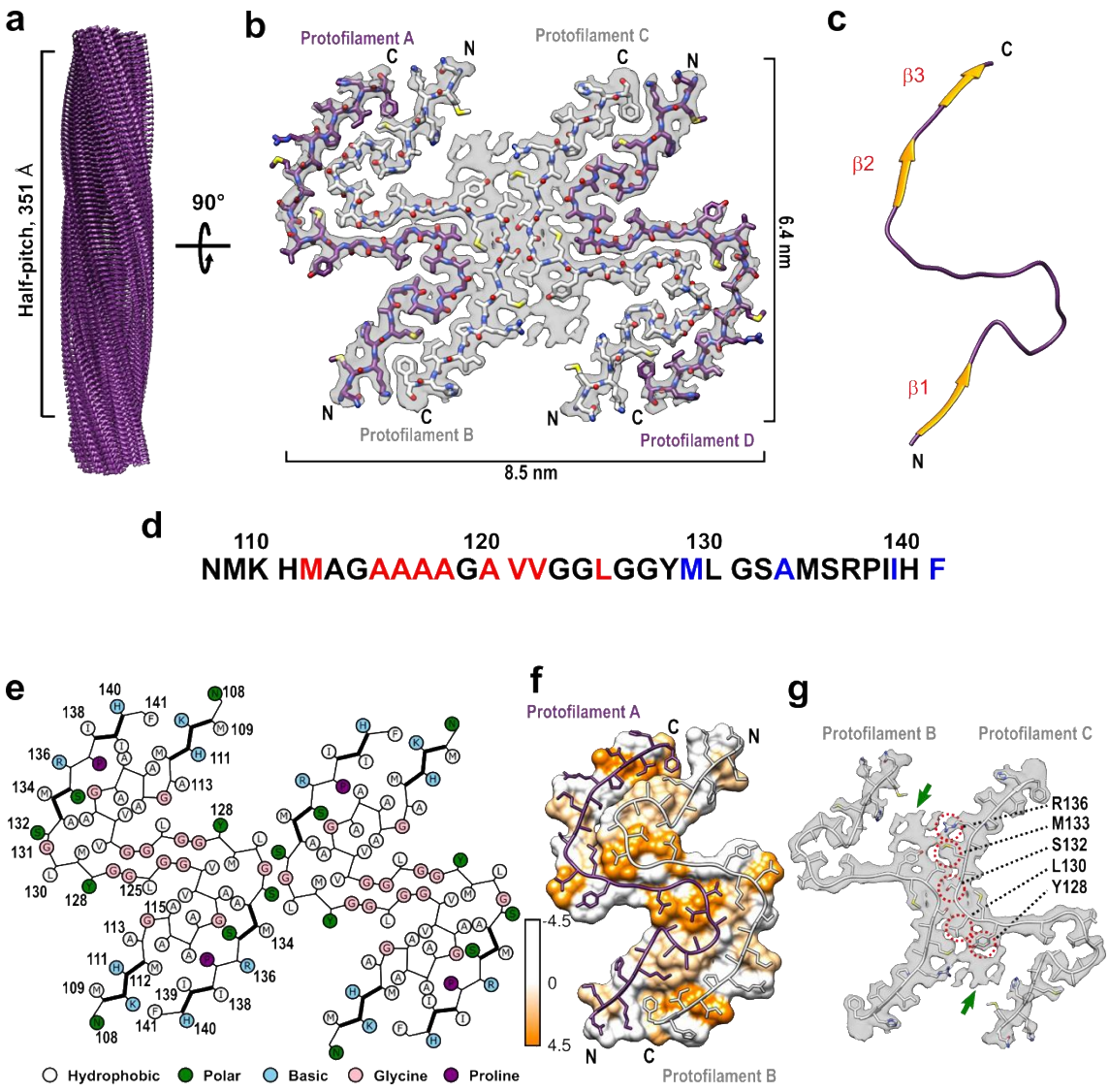

Figure 6.5. Cryo-EM structure of huPrP23-144 amyloid fibrils. a Cryo-EM density map showing a left-handed twisted helix with a half-pitch of 351 and a classical parallel, in-register ß-sheet architecture. b The top view of the atomic model superimposed on the cryo-EM density map. The amyloid core contains four identical protofilaments. Two outer protofilaments with greater accessibility to water are depicted in purple; two inner protofilaments are depicted in white. c One representative subunit of the fibril core with ß-strands shown in orange. d Amino acid sequence for the highly ordered core of huPrP23-144 fibrils. N- and C-terminal solvent-inaccessible hydrophobic residues are shown in red and blue, respectively. e Schematic representation of one cross-sectional layer of the amyloid core, with ß-strands shown as thicker lines. f Hydrophobicity of the cross-section of protofilaments A and B, with hydrophobicity levels colored according to Kyte-Doolittle19 (top view). g One cross-sectional layer of protofilaments B and C shown as atomic model superimposed on the cryo-EM map (top view). Extra unassigned densities (likely representing side chains of residues outside the core region) are indicated by green arrows; residues within the amyloid core involved in the inter-protofilament interactions are indicated by red circles. Adapted from Li 2021.

Coming back to our hypothesis that we obtained using PITHIRDS an intermolecular distance of 6.5 Å for our recBVPrP^{Sc} sample due to the selected residues being in coils, the fact that residues M129 and Y128, which are undetectable in ssNMR NCA experiments, are proved by cryo-EM to be located in a stretch spanning Ala112-Ser132 that does not feature a canonical β-strand conformation, although interestingly they are part of the PIRIBS core of the fibers, supports our hypothesis.

Furthermore, relaxation dispersion ssNMR experiments showed that residues located in that stretch have excited-state populations somewhat higher than those of residues located in the most rigid and solvent excluded parts of the PIRIBS core (~5-15% vs.2%), corresponding to protein backbone motions in the timescale of ~100-300 μs (Shannon 2019). This degree of mobility is relatively low, except for the Tyr128-Met129 "center" of the stretch; however, it might have a substantial effect on PITHIRDS-based measurements of distances between ^{13}CO carbons of stacked residues located in such loop stretches, because then the outcome of the experiment is a weighted average of the available conformations and populations. In a PIRIBS structure, such distance averaging likely introduces a bias in the experimental CO-CO distances towards longer values than the canonical of 5 Å which is in principle the shortest distance for the inter-chain arrangement (Gorkovskiy 2014, Theint 2017, Li 2021, Shannon 2019).

To explore further possibilities of why we obtained such a large mean intermolecular ^{13}CO-^{13}CO distance it is important to also consider the case of the non-infectious PrP amyloid: its Phe141 is completely out of the PIRIBS core, which spans ~170-230 (Tycko 2010, Wang 2020, Müller 2014), while Phe175 and Phe198 (BV numbering) are located in β-strands that are part of it (Tycko 2010, Wang 2020, Müller 2014). Data obtained from ssNMR show that all three Phe residues exhibit chemical shifts typical of β-sheet secondary structure (Tycko 2010); however, Phe141 is located in a short stretch whose global chemical shift signature is suggestive of a β-arch (Minor 1994).

In a recent, from last year, cryo-EM based structure of the HuPrP E196K amyloid, an "island" comprising residues Arg136-Gly142 was resolved (Fig. 6.6) as a density independent of the main Asn171-Ser222 PIRIBS core (Wang 2021). Such island would be connected to the main PIRIBS core by a flexible coil stretch spanning from the N-terminus to Asn171 (Wang 2021). This island therefore forms a "mini-PIRIBS" stack outside the main core, yet despite theoretically perfect stacking of its Phe141 CO atoms at 5 Å, their contribution to the mean distance measured by PITHIRDS must be of >>5. While such island was not detected in the cryoEM-based reconstruction of wt HuPrP amyloid (Wang 2020), its existence as a general feature of PrP amyloids seems likely, given for example the β-strand signature of all three CP signals of ^{13}CO-Phe-labelled wt PrP amyloid with two slightly distinct peaks at a 1:2 proportion (Tycko 2010).

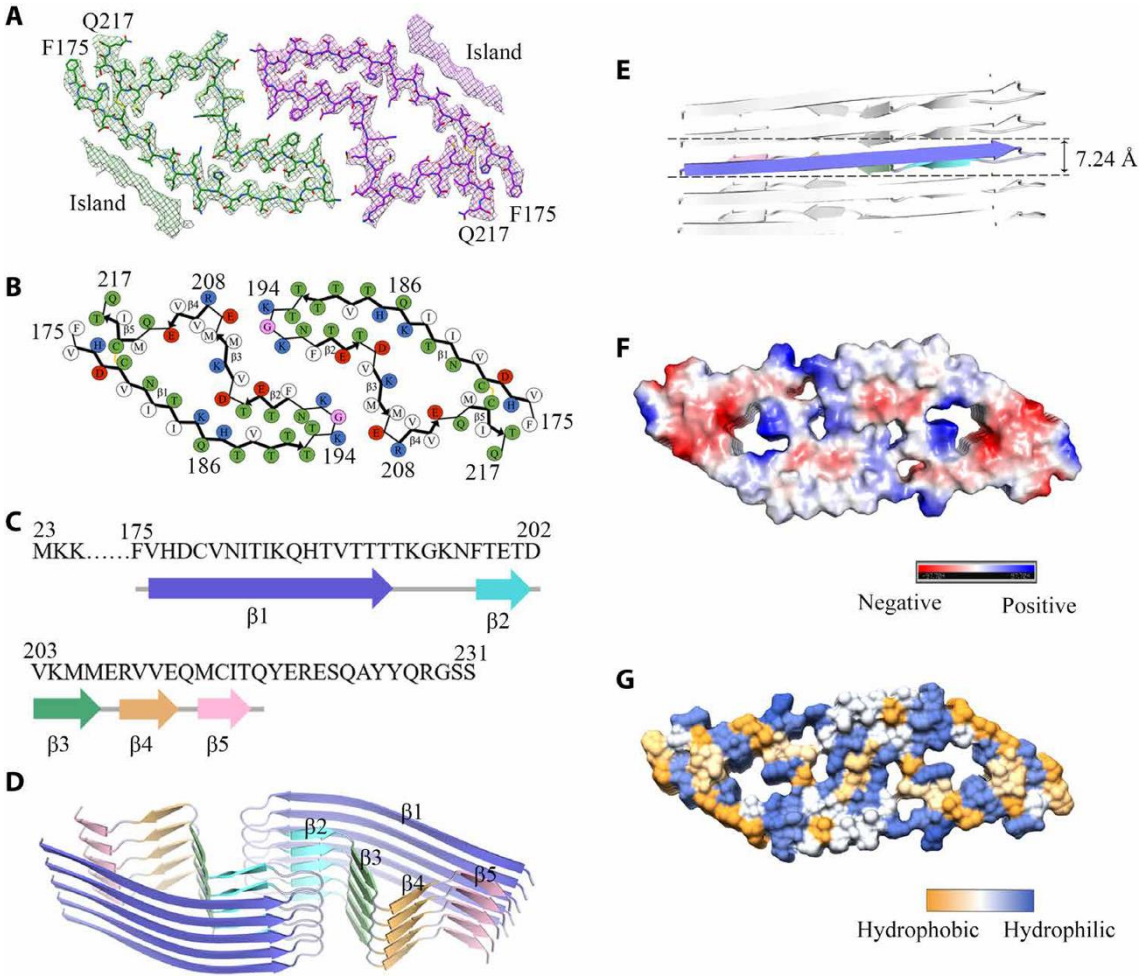

Figure 6.6. Atomic structure of E196K fibrils. (A) Cryo-EM map of E196K fibrils with the atomic model overlaid. Two identical densities (termed two islands) flanking the two protofibrils, which are colored green and purple, respectively. Each island is located on the opposing side of hydrophobic side chains of Val180, Ile182, and Ile184 in each monomer. (B) Schematic view of the E196K fibril core. Residues are colored as follows: white, hydrophobic; green, polar; red and blue, negatively and positively charged, respectively; and magenta, glycine. ▫ strands are indicated with bold lines. E196K fibrils are stabilized by a disulfide bond (yellow line) formed between Cys179 and Cys214 in each monomer, also visible in (A). (C) Sequence of the fibril core comprising residues 175 to 217 from E196K, with the observed five ▫ strands colored blue (ß1), cyan (ß2), green (ß3), orange (ß4), and pink (ß5). The dotted line corresponds to residues 23 to 174 not modeled in the cryo-EM density. (D) Ribbon representation of the structure of an E196K fibril core containing five molecular layers and a dimer. (E) As in (D), but viewed perpendicular to the helical axis, revealing that the height of one layer of the subunit along the helical axis is 7.24 Å. (F) Electrostatic surface representation of the structure of an E196K fibril core containing five molecular layers and a dimer. (G) Hydrophobic surface representation of the structure of an E196K fibril core as in (D). (F and G) Two pairs of amino acids (Lys194 and Glu207; Lys196 and Glu200) from opposing subunits form four salt bridges at the zigzag interface of the two protofibrils. The surface of two opposing subunits is shown according to the electrostatic properties (F) or the hydrophobicity (G) of the residues. Adapted from Wang 2021.

Alternatively, the PITHIRDS, C-C-DARR, CPMAS and PARIS data presented herein could also be explained, as already mentioned, if our sample comprises a mixture of components with PIRIBS and 4RβS architectures since the estimated mean ^{13}CO-^{13}CO intermolecular distance is exactly 6.5 Å as the one for Phe-Phe and Leu-Leu (Fig. 6.7).

However, such a possibility, for which we do not have any evidence, is not parsimonious at all and seems extremely unlikely that two different structural species coexist, which are propagative and that they do so at the same speed since our recBVPrP^{Sc} is stable throughout several PMSA passages. Thus it will be dismissed.

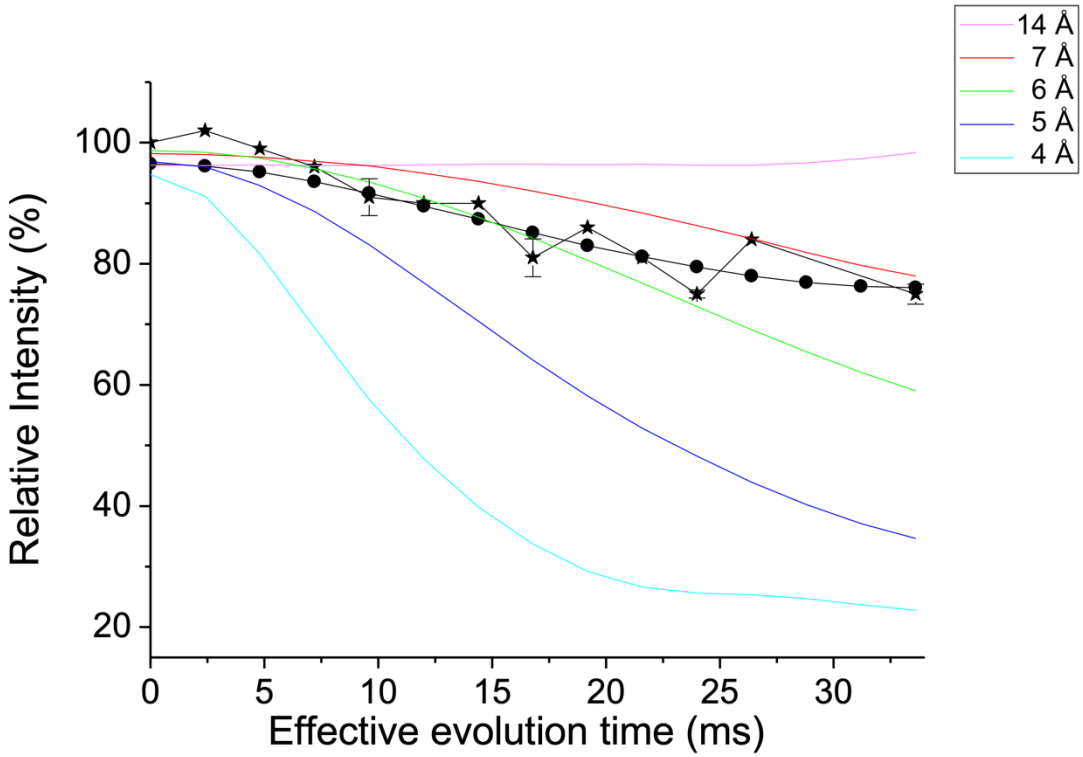

Fig 6.7. Measurement of intermolecular 13C-13C dipole-dipole couplings using PITHIRDS-CT. Symbols are: ★ experimental (13CO-Phe)-recBVPrPSc PITHIRDS-CT intensities with correction of the natural abundance, and ● simulated averaged PITHIRDS-CT intensities for a model of two structures with no exchange among them consisting in a mixture of 65% of 4RβS and 35% PIRIBS. Black segments connecting the symbols are drawn to guide the eye. Solid colored lines are simulated curves for a linear arrangement of 5 atoms separated by the given distances (4, 5, 6, 7 and 14 Å), as indicated in the main text. Experimental values (★) represent the mean of two independent experiments. Simulated points (●) were calculated as the weighted average of two PITHIRDS-CT simulations carried out for a linear arrangement of 5 atoms separated by distances of 14 Å and 5 Å. The weighting factors were manually adjusted for fitting the experimental curve in steps of 5% and the best fit was obtained with factors 0.65 and 0.35, respectively. The intensities simulated for the distance of 5 Å are consistent with the canonical 5 Å 13CO-13CO cross-β distance characteristic of a PIRIBS structure.15,18 The intensities simulated for the distance of 14 Å were very close to those experimentally obtained in Figure 2 (main text) for (13CO-Tyr)-HET-s(218-289), which is known to adopt a 2RβS structure.18,20

6.4 Experiments to assess the flexibility of recBVPrP^{Sc}

With the aim of assessing a putative mobility of Phe residues in recBVPrP^{Sc} sample we performed 1D CP-MAS and PARIS experiments, which should give us the signals of the rigid and the flexible residues, respectively, of ^{13}CO-Phe-BVPrP^{Sc}, ^{13}CO-Phe-PrP amyloid and ^{13}CO-Tyr-Het-s (218-289) in the ms timescale. We were expecting to see the highest PARIS signal for BVPrP^{Sc}, then for BVPrP amyloid and lastly for Het-s (218-289).

However, as already stated, our results yielded that the mean mobility of Phe residues in recBVPrP^{Sc} is very limited, substantially lower than that of Phe141 in the BVPrP(23-321) amyloid, and in the same range of that of the Tyr residues in the HET-s prion domain. Therefore, the putative Phe residues located in loops do not have a high mobility perceptible in the ms timescale.

Since the PARIS experiments results did not shed any light into our residues being in flexible stretches hypothesis and by comparison with the results from residues from other PIRIBS amyloids, we tended to believe that such was our case as well, T_{1rho} relaxation experiments were performed with all three ^{13}CO-Phe samples at two different temperatures, 278 and 313 K, in order to probe such residue flexibility.

We saw that recBVPrP^{Sc} had a faster tumbling in the us scale which leads to believe that indeed there are several residues, possibly Phe, that besides being in β-strands have high flexibility. It was surprising to us to see that PrP amyloid and Het-s had yield a similar result when Het-s is considerably more rigid than PrP amyloid because it has both Tyr in β-sheets (Wasmer 2008) whereas it is known for a fact that PrP amyloid has one out of three Phe, Phe141, in one loop and the other two in β-sheets. This can be explain because the relaxation experiment's results are an average of all the ^{13}CO-labelled residues in the sample and it can easily be for the PrP amyloid that one Phe is indeed very flexible, Phe 141 in a β-arch, but the other two which are in β-sheets are in very rigid environments thus the average is equal to that of the two Tyr of Het-s, being one in the middle of a β-strand and the other at the end of one.

6.5 Experiments with U-(^{15}N, ^{13}C)-Phe recBVPrP^{Sc}

In parallel to these experiments, we decided to explore the three Phe residues and prepared a U-(^{15}N, ^{13}C)-Phe recBVPrP^{Sc} sample, thinking that it would be possible to identify if some of the three had chemical shifts more typical of coil. Then, we were planning to perhaps carry out 2D PARIS to show how those with coil chemical shifts had stronger PARIS signals.

To our surprise, instead of 3 signals, one per Phe residue, we detected six, three indeed with chemical shifts of coil and three with chemical shifts characteristic of β-strands (Fig 5.29). This result was completely unexpected and besides not providing a clear answer to our question, it raised the possibility of the existence of a mixture of amyloid conformations.

Such mixture might take the form of PrP^{Sc} monomers in a stack with variations in the local conformation of loops, or two/three completely different coexisting but segregated

stacks. The latter makes more spectroscopic sense because the signals are sharp, characteristic of stable conformational states. However, the former makes more biochemical sense, since the biochemical properties of our recBVPrP^{Sc} strain are solid because they are stable throughout several PMSA passages with the same PK resistance pattern, being it not possible that two or more different subspecies exist with the same exact propagative speed (Eraña 2019). Moreover, exploring the option of the conformers, it is important to note that if conformer A is on top of conformer B, and they are not perfectly aligned as in a canonical PIRIBS, this would also lead to abnormally long distances which would agree with our results. However, it seems odd to imagine that one loop in PIRIBS conformer A would not have a 5 Å intermolecular distance with a lower loop in the arrangement from conformer B.

However, one additional piece of information is that in the DREAM spectra, the Cβ/Cγ2 signals of Ile residues are perfectly isolated: there is one Ile signal for each residue being a total of four signals for the four residues, meaning that there is no heterogeneity. Therefore, this information strongly supports the idea of a stuck of only conformer A being the micro static heterogeneity only an asset of Phe.

6.6 Concluding remarks

In the midst of the quest for solving the structure of recBVPrP^{Sc}, in 2021, Kraus and collaborators reported on the structure of Syrian hamster 263K PrP^{Sc} resolved by cryo-EM at 3.2 Å resolution (Kraus 2021). The structure of the main, if not only, fibrillary component in the sample is a PIRIBS. They used the same experimental approach as Vázquez-Fernández and collaborators did, which I have described in depth in the introduction. However, from 2016 to 2021, cryo-EM's resolution improved down to 3.2 Å , massively, as for instance now the camera takes videos instead of photos, named tomographs. I will explain the structure in detail based on the model they constructed, quoting Kraus's work.

In this structure, the cross-section is asymmetric about the fibril axis (Fig. 6.8 C,D, and Fig. 6.9B–2F). The well-resolved fibril core, which primarily represents residues 95–227, was around 13 nm in its longest dimension and around 3.5 nm at its narrowest (Fig. 6.8D and E). They inferred from the known attachment sites of the glycans (N181 and N197) and GPI anchor (S231) that these moieties project into the solvent. However, these structures were largely unresolved in the averaged image reconstruction, presumably because of their heterogeneity in sequence (Rudd et al., 1999) and conformation. Nonetheless, the first unit of N-linked glycans, N-acetylglucosamine, is consistent with the densities that are adjacent to N181 and N197 (Fig. 6.9 B and C). Surface hydrophobicity maps show hydrophobic zones in both halves, as well as a hydrophobic bridge across the interface between the two halves (Fig 6.9F).

Other major features of the 263K structure include the following: (i) Hydrophobic ''Greek key'' motif: a particularly hydrophobic stretch of residues 112–134 is reminiscent of the ''Greek key'' topology in α-synuclein fibrils. (ii) Middle (125–168) β-arch: residues 125–168 form a major hairpin or, more conventionally, β-arch (Fig. 6.9B–2D) that is related to what they had termed the ''127–161 hairpin'' in earlier in silico modeling. (iii) Disulfide β-arch: 263K fibrils also have a disulfide-linked β-arch of residues between C179 and C214 (Figures 6.9B–2D). This β-arch is reminiscent of motifs

that have been predicted for PIRIBS-based prions and observed in rhuPrP23–231 fibrils by cryo-EM. However, in contrast to recombinant PrP fibrils, the disulfide β-arch in 263K prions contains two N-linked glycans. Also, the flanks of this arch are straighter than the β-arch in rhuPrP23– 231 fibrils, except for a notable kink at M206–R208, and the presumably hydrated gap between flanks near the tip of the arch is larger. The extreme C-terminal residues fold back against the flank of the disulfide loop at Y218, whereas in rhuPrP23–231 fibrils, this fold occurs at R220. A key structural difference that might influence these conformational differences is the presence of a GPI anchor at the C-terminus of the 263K fibrils. (iv) Staggered interface between N- and C-terminal domains: lateral views of the 263K fibril show that residues of each monomer are not entirely coplanar across the fibril cross-section and ends (Fig 6.9F). At the interface between the Greek key domain and more C-terminal residues, residues 119–135 of one monomer are most closely opposed to residues 158–177 of the i-1 and i-2 monomers. This results in uneven fibril ends, with the hydrophobic Greek key motif protruding at one end and receding at the other (Kraus 2021).

Of note, 263K features a 90-230 PIRIBS core in which only 33% of the residues are located in canonical β-strands, and the rest make up tight connecting coils (Kraus 2021). In particular, two of the three Phe residues (Phe141 and Phe198) and the two Leu residues, Leu124 and Leu129 (mouse numbering) are located in coil stretches. These abundant β-strand connecting coils, which had been predicted long ago (Vázquez-Fernández 2012, Silva 2015) while featuring rigidity resulting in relatively weak PARIS signals, may well drift from the ideal 5 Å CO-CO distance typical of canonical cross-β stacks. Furthermore, there is reason to believe that recBVPrP^{Sc} is overall less compact than brain-derived 263K PrP^{Sc}, as surmised from its relative sensitivity to PK cleavage, particularly within the 130-160 region, (Figure 5.1), so that coils might be even more abundant.

All in all, we believe that in our recBVPrP^{Sc} sample there is only one single kind of PIRIBS stack with only one kind of conformers, not a mixture, although the residues we have scanned by PITHIRDS behave as if they were not in a canonical cross-β distance as previously shown with Sup35 (Gorkovskiy 2014). Furthermore, there is some conformational heterogeneity affecting some residues as Phe or perhaps some loops in the individual monomers. Over all, the β-core is relatively rigid with no main movements in the ms time scale that PARIS detects, although there is flexibility in the us time scale as seen by the $T_{1\rho}$ experiments we performed, thus explaining the mean intermolecular ^{13}CO-^{13}CO distance larger than the canonical 5 Å.

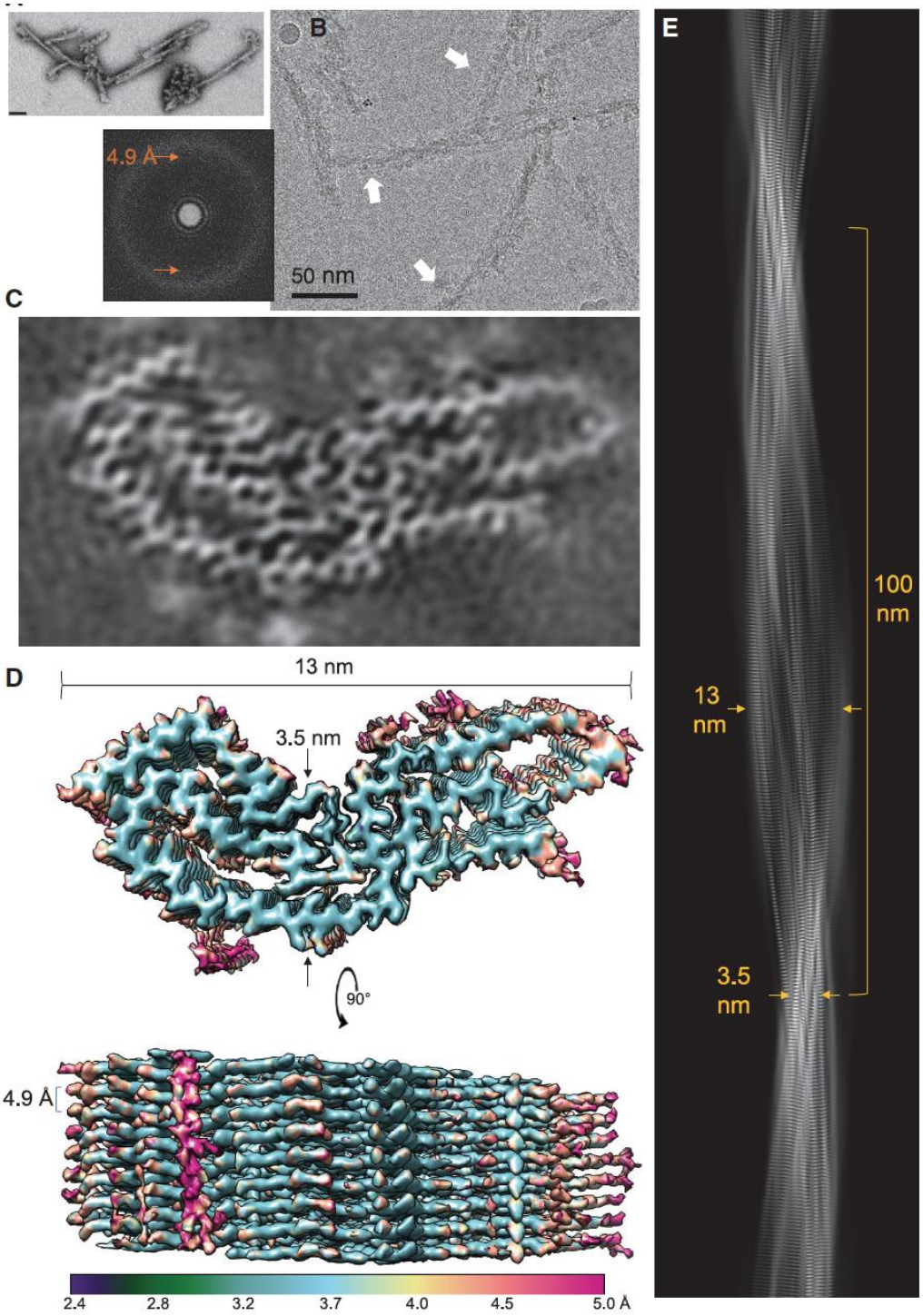

Fig. 6.8. EM images and density maps of 263K prion fibrils. (A) Negatively stained transmission EM image (bar, 50 nm). (B) Raw 2D cryo-EM image (cropped representation) with associated fast Fourier transform showing signals for regular 4.9-A spacings (orange arrows). White arrows indicate fibril-associated peripheral globular features that were frequently observed. (C) Projection of density map of fibril cross-section derived from single-particle cryo-EM analysis. (D) Surface depictions of density map with indicated dimensions and colors showing local resolutions according to bar. (E) Projection of the fibril density map.

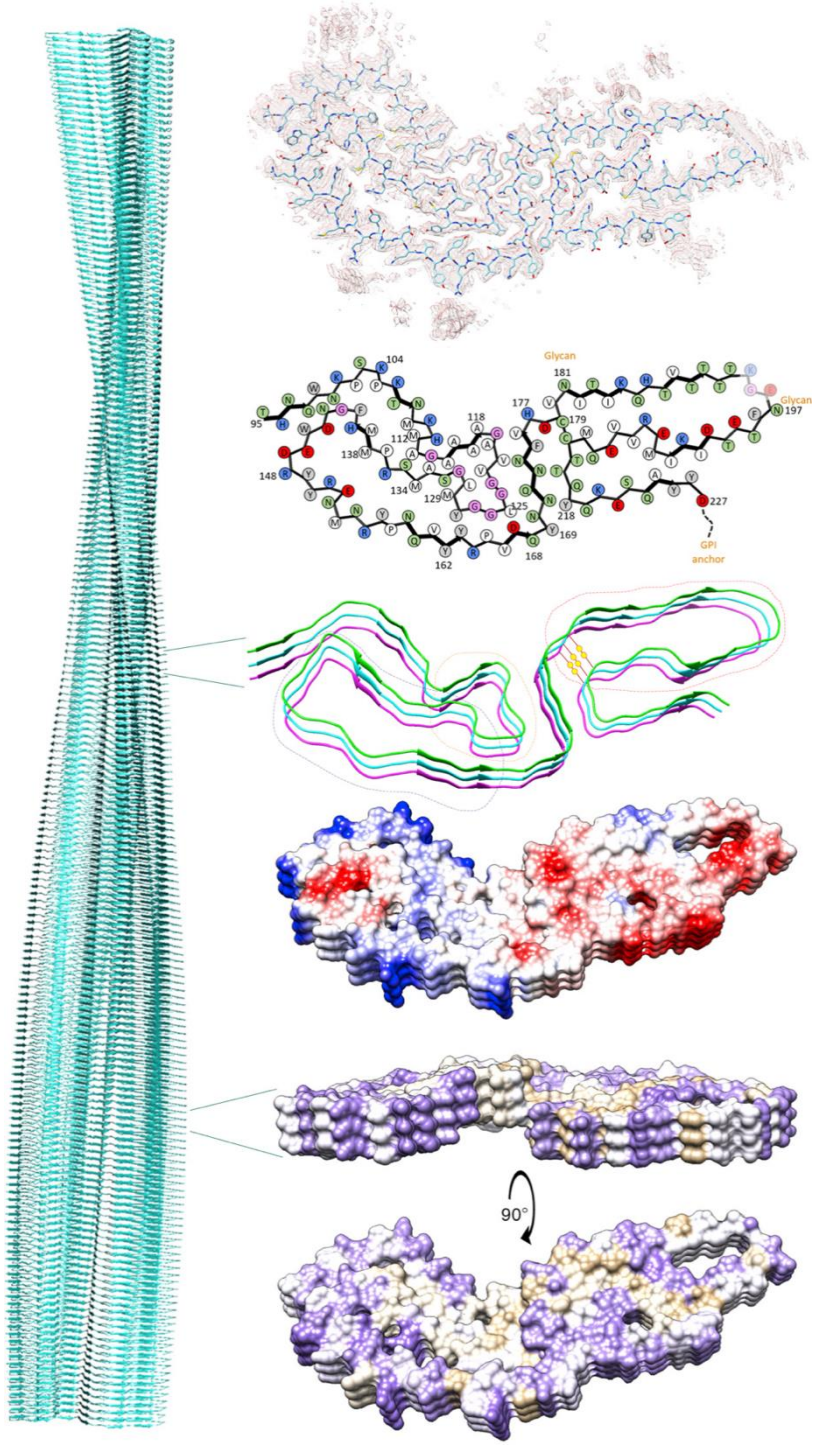

Fig. 6.9. 263K prion model based on cryo-EM density map
(A) Extended fibril model as a ribbon diagram. (B) PrP residues 95–227 threaded through a crosssectional density map (mesh). Blue arrows indicate peripheral densities outside of the core polypeptide, some of which are likely attributable to glycans and GPI anchors attached at sites labeled in (C).(C) Schematic depiction of fibril core showing side-chain orientations relative to the polypeptide backbone. Residues assigned to b-sheets in Chimera are marked by thicker backbones with arrowheads. Side chains of residues 194–196(faded) were poorly resolved. Green, polar; blue, basic; red, acidic; white, aliphatic; gray, aromatic;pink - glycine.(D) b sheets in a stacked trimeric segment of the fibril. Structural elements are as labeled, and disulfide bond is indicated by a pair of yellow spheres. (E) Coulombic charge representation. (F) Kyte-Doolittle hydrophobicity surface of fibril ends (templates) showing the protruding (green arrowhead) and receding (magenta arrowheads) hydrophobic Greek key motif at opposite ends.

7. CONCLUSIONS

I obtained large enough quantities of recBVPrP^{Sc} which allowed us for the first time to be able to perform several different ssNMR experiments with this material and to compare it with the non-infectious PrP amyloid by FTIR. From such results, the following conclusions were drawn:

7.1 According to PITHIRDS experiments the ^{13}C decay curves of PK treated ^{13}CO-Phe-recBVPrP$^{Sc(}$109) and ^{13}CO-Leu-recBVPrP^{Sc}(109) fitted to a mean distance of 6.5 Å between Phe-Phe and Leu-Leu residues, which strongly suggests that the architecture of recBVPrP^{Sc} conforms to a PIRIBS, and not to a 4RβS as it had been expected.

7.2 According to $T_{1\rho}$ experiments performed with ^{13}CO-Phe-Het-s, ^{13}CO-Phe-PrP amyloid and ^{13}CO-Phe-recBVPrP^{Sc}, Phe residues in recBVPrP^{Sc} present higher mobility than the other samples in the us time scale which is due to one or more of such residues being located in β-archs and/or loops.

7.3 According to the ^{13}C-^{13}C-TOCSY and ^{13}C-^{13}C -DARR spectra of PK treated (U-^{13}C, ^{15}N)-Phe-recBVPrP^{Sc}(109) there are a minimum of six distinct Phe signals in the Cα /Cβ region and only three Phe, indicating that this residue presents static heterogeneity.

7.4 According to PARIS experiments performed with ^{13}CO-Phe-Het-s, ^{13}CO-Phe-PrP amyloid and ^{13}CO-Phe-recBVPrP^{Sc}, Phe residues in recBVPrP^{Sc} present a low mobility due to their movement not being detected in the ms time scale that PARIS measures.

7.5 Although now this information is not new, it was so back when we retrieved the data. According to the 2D ^{13}C-^{13}C DREAM spectrum of PK treated, uniformly labelled (U-^{13}C, ^{15}N)-recBVPrP^{Sc}(109I): (i) there are four Ala Cα /Cβ correlation cross peaks in the 48-51/19-25 ppm chemical shift region of the spectrum characteristic of β-strand secondary structure which span as N-terminal as A116 and (ii), there are two sets of signals corresponding to Cβ/Cγ2 correlations of Ile residues, in the 36-42/13-18 ppm region of the spectrum, featuring chemical shifts that are characteristic of β-strand and coil secondary structure, respectively. However, all these data did not allow us to distinguish between the PIRIBS and the 4RβS model as they are compatible with both.

7.6 According to the second derivative FTIR spectra of the non-infectious BVPrP amyloid and recBVPrP^{Sc}(109I), there are secondary structural differences between them, despite both being PIRIBS, possibly due to differences in the rigidity of their β-sheets.

8. REFERENCES

Aguzzi A, Calella AM. Prions: protein aggregation and infectious diseases. Physiol Rev. 2009 Oct;89(4):1105-52.

Allison WT, DuVal MG, Nguyen-Phuoc K, Leighton PLA. Reduced Abundance and Subverted Functions of Proteins in Prion-Like Diseases: Gained Functions Fascinate but Lost Functions Affect Aetiology. Int J Mol Sci. 2017 Oct 24;18(10):2223.

Alper T, Haig DA, Clarke MC. The exceptionally small size of the scrapie agent. Biochem Biophys Res Commun. 1966 Feb 3;22(3):278-84.

Alper T, Cramp WA, Haig DA, Clarke MC. Does the agent of scrapie replicate without nucleic acid? Nature. 1967 May 20;214(5090):764-6.

Baron GS, Hughson AG, Raymond GJ, Offerdahl DK, Barton KA, Raymond LD, Dorward DW, Caughey B. Effect of glycans and the glycophosphatidylinositol anchor on strain dependent conformations of scrapie prion protein: improved purifications and infrared spectra. Biochemistry. 2011 May 31;50(21):4479-90.

Bartz JC. Prion Strain Diversity. Cold Spring Harb Perspect Med. 2016 Dec 1;6(12):a024349.

Baskakov IV, Katorcha E. Multifaceted Role of Sialylation in Prion Diseases. Front Neurosci. 2016;10:358.

Baskakov IV, Byron C, Requena JR, Sevillano AM, Surewicz WK, Wille H. The prion 2018 round tables (I): the structure of PrP^{Sc}. Prion. 2019 Jan;13(1):46-52.

Basler K, Oesch B, Scott M, Westaway D, Walchli M, Groth DF, et al. Scrapie and cellular PrP isoforms are encoded by the same chromosomal gene. Cell. 1986;46(3):41728.

Baxa U, Wickner RB, Steven AC, Anderson DE, Marekov LN, Yau WM, Tycko R. Characterization of beta-sheet structure in Ure2p1-89 yeast prion fibrils by solid-state nuclear magnetic resonance. Biochemistry. 2007;46(45):13149-62.

Bessen RA, Marsh RF. Distinct PrP properties suggest the molecular basis of strain variation in transmis-sible mink encephalopathy. J Virol. 1994; 68: 7859-68.

Bocharova OV, Breydo L, Parfenov AS, Salnikov VV, Baskakov IV. In vitro conversion of full-length mammalian prion protein produces amyloid form with physical properties of PrP(Sc). J Mol Biol. 2005 Feb 18;346(2):645-59.

Bocharova OV, Breydo L, Salnikov VV, Gill AC, Baskakov IV. Synthetic prions generated in vitro are similar to a newly identified subpopulation of PrP^{Sc} from sporadic Creutzfeldt-Jakob Disease. Protein Sci. 2005 May;14(5):1222-32.

Bolton DC, McKinley MP, Prusiner SB. Identification of a protein that purifies with the scrapie prion. Science. 1982 Dec 24;218(4579):1309-11.

Bremer J, Baumann F, Tiberi C, Wessig C, Fischer H, Schwarz P, Steele AD, Toyka KV, Nave KA, Weis J, Aguzzi A. Axonal prion protein is required for peripheral myelin maintenance. Nat Neurosci. 2010 Mar;13(3):310-8.

Candelise N, Baiardi S, Franceschini A, Rossi M, Parchi P. Towards an improved early diagnosis of neurodegenerative diseases: the emerging role of in vitro conversion assays for protein amyloids. Acta Neuropathol Commun. 2020 Jul 25;8(1):117. doi: 10.1186/s40478-020-00990-x. PMID: 32711575; PMCID: PMC7382043.

Castle A.R., Gill A.C. Physiological functions of the cellular prion protein. Front Mol Biosci, 4 (2017), p. 19.

Caughey BW, Dong A, Bhat KS, Ernst D, Hayes SF, Caughey WS. Secondary structure analysis of the scrapie-associated protein PrP 27-30 in water by infrared spectroscopy. Biochemistry. 1991 Aug 6;30(31):7672-80.

Caughey B, Raymond GJ, Bessen RA. Strain-dependent differences in beta-sheet conformations of abnormal prion protein. J Biol Chem. 1998 Nov 27;273(48):32230-5.

Cobb NJ, Sönnichsen FD, McHaourab H, Surewicz WK. Molecular architecture of human prion protein amyloid: a parallel, in-register beta-structure. Proc Natl Acad Sci U S A. 2007 Nov 27;104(48):18946-51.

Cuillé, J.; Chelle, P.-L. La maladie dite tremblante du mouton est-elle inoculable? C. R. Acad. Sci. 1936, 203, 1552–1554

Cuillé, J.; Chelle, P.-L. Transmission experimentale de la tremblante a la chevre. C. R. Acad. Sci. 1939, 208, 1058–1060.

Daus, M.L.; Beekes, M. Chronic wasting disease: Fingerprinting the culprit in risk assessments. Prion 2012, 6, 17–22.

Daus ML, Wagenführ K, Thomzig A, Boerner S, Hermann P, Hermelink A, Beekes M, Lasch P. Infrared microspectroscopy detects protein misfolding cyclic amplification (PMCA)-induced conformational alterations in hamster scrapie progeny seeds. J Biol Chem. 2013 Dec 6;288(49):35068-80.

Deleault NR, Lucassen RW, Supattapone S. RNA molecules stimulate prion protein conversion. Nature. 2003 Oct 16;425(6959):717-20.

Deleault NR, Piro JR, Walsh DJ, Wang F, Ma J, Geoghegan JC, Supattapone S. Isolation of phosphatidylethanolamine as a solitary cofactor for prion formation in the absence of nucleic acids. Proc Natl Acad Sci U S A. 2012 May 29;109(22):8546-51.

Eraña H, Charco JM, Di Bari MA, Díaz-Domínguez CM, López-Moreno R, Vidal E, González-Miranda E, Pérez-Castro MA, García-Martínez S, Bravo S, Fernández-Borges N, Geijo M, D'Agostino C, Garrido J, Bian J, König A, Uluca-Yazgi B, Sabate R, Khaychuk V, Vanni I, Telling GC, Heise H, Nonno R, Requena JR, Castilla J. Development of a new largely scalable in vitro prion propagation method for the

production of infectious recombinant prions for high resolution structural studies. PLoS Pathog. 2019 Oct 23;15(10):e1008117.

Escobar LE, Pritzkow S, Winter SN, Grear DA, Kirchgessner MS, Dominguez-Villegas E, Machado G, Townsend Peterson A, Soto C. The ecology of chronic wasting disease in wildlife. Biol Rev Camb Philos Soc. 2020 Apr;95(2):393-408.

Fernández-Borges N, Di Bari MA, Eraña H, Sánchez-Martín M, Pirisinu L, Parra B, Elezgarai SR, Vanni I, López-Moreno R, Vaccari G, Venegas V, Charco JM, Gil D, Harrathi C, D'Agostino C, Agrimi U, Mayoral T, Requena JR, Nonno R, Castilla J. Cofactors influence the biological properties of infectious recombinant prions. Acta Neuropathol. 2018 Feb;135(2):179-199.

Gajdusek, D.C.; Zigas, V. Degenerative disease of the central nervous system in New Guinea; The endemic occurrence of “kuru”in the native population. N. Engl. J. Med. 1957, 257, 974–978.

Gajdusek, D.C.; Zigas, V. Kuru—Clinical, pathological and epidemiological study of an acute progressive degenerative disease of the central nervous system among natives of the eastern highlands of New Guinea. Am. J. Med. 1959, 26, 442–469.

Gajdusek, D.C.; Gibbs, C.J., Jr.; Alpers, M. Experimental transmission of a kuru-like syndrome to chimpanzees. Nature 1966, 209,794–796.

Gibbs CJ Jr, Gajdusek DC, Asher DM, Alpers MP, Beck E, Daniel PM, Matthews WB. Creutzfeldt-Jakob disease (spongiform encephalopathy): transmission to the chimpanzee. Science. 1968 Jul 26;161(3839):388-9.

Gill AC, Castle AR. The cellular and pathologic prion protein. Handb Clin Neurol. 2018;153:21-44.

Greenlee J.J., M.H. West Greenlee, The Transmissible Spongiform Encephalopathies of Livestock, ILAR Journal, Volume 56, Issue 1, 2015, Pages 7–25.

Gong B, Ramos A, Vázquez-Fernández E, Silva CJ, Alonso J, Liu Z, Requena JR. Probing structural differences between PrP(C) and PrP(Sc) by surface nitration and acetylation: evidence of conformational change in the C-terminus. Biochemistry. 2011 Jun 7;50(22):4963-72.

Gonzalez-Montalban N, Makarava N, Ostapchenko VG, Savtchenk R, Alexeeva I, Rohwer RG, Baskakov IV. Highly efficient protein misfolding cyclic amplification. PLoS Pathog. 2011 Feb 10;7(2):e1001277.

Gough, K.C.; Maddison, B.C. Prion transmission: Prion excretion and occurrence in the environment. Prion 2010, 4, 275–282.

Gorkovskiy A, Thurber KR, Tycko R, Wickner RB. Locating folds of the in-register parallel β-sheet of the Sup35p prion domain infectious amyloid. Proc Natl Acad Sci U S A. 2014 Oct 28;111(43):E4615-22

Govaerts C, Wille H, Prusiner SB, Cohen FE. Evidence for assembly of prions with left-handed beta-helices into trimers. Proc Natl Acad Sci U S A. 2004 Jun 1;101(22):8342-7.
Groveman BR, Dolan MA, Taubner LM, Kraus A, Wickner RB, Caughey B. Parallel in-register intermolecular β-sheet architectures for prion-seeded prion protein (PrP) amyloids. J Biol Chem. 2014; 289: 24129-42.

Hadlow,W.J. Scrapie and kuru. Lancet 1959, 274, 289–290.

Helmus JJ, Surewicz K, Surewicz WK, Jaroniec CP. Conformational flexibility of Y145Stop human prion protein amyloid fibrils probed by solid-state nuclear magnetic resonance spectroscopy. J Am Chem Soc. 2010; 132:2393–2403.

Houston, F.; Andréoletti, O. Animal prion diseases: The risks to human health. Brain Pathol. 2019, 29, 248–262.

Hung, I.; Gan, Z. Spin-locking and cross-polarization under magic-angle spinning of uniformly labeled solids. J. Magn. Reson. 2015, 256, 23-29.

Jones EM, Surewicz K, Surewicz WK. Role of N-terminal familial mutations in prion protein fibrillization and prion amyloid propagation in vitro. J Biol Chem. 2006 Mar 24;281(12):8190-6.

Kim JI, Cali I, Surewicz K, Kong Q, Raymond GJ, Atarashi R, Race B, Qing L, Gambetti P, Caughey B, Surewicz WK. Mammalian prions generated from bacterially expressed prion protein in the absence of any mammalian cofactors. J Biol Chem. 2010 May 7;285(19):14083-7.

Klimova N, Makarava N, Baskakov IV. The diversity and relationship of prion protein self-replicating states. Virus Res. 2015 Sep 2;207:113-9.

Kocisko DA, Come JH, Priola SA, Chesebro B, Raymond GJ, Lansbury PT, Caughey B. Cell-free formation of protease-resistant prion protein. Nature. 1994 Aug 11;370(6489):471-4

Kraus A, Hoyt F, Schwartz CL, Hansen B, Artikis E, Hughson AG, Raymond GJ, Race B, Baron GS, Caughey B. High-resolution structure and strain comparison of infectious mammalian prions. Mol Cell. 2021 Aug 24:S1097-2765(21)00651-1.

R. Kurbanov, T. Zinkevich, A. Krushelnitsky, "The nuclear magnetic resonance relaxation data analysis in solids: General R1/R1ρ equations and the model-free approach", J. Chem. Phys., 2011, 135, 184104.

A. Krushelnitsky et al., "Slow motions in microcrystalline proteins as observed by MAS-dependent 15N rotating-frame NMR relaxation" J. Magn. Reson., 2014, 248, 8-12

Latarjet, R.; Muel, B.; Haig, D.A.; Clarke, M.C.; Alper, T. Inactivation of the scrapie agent by near monochromatic ultraviolet light. Nature 1970, 227, 1341–1343.

Leighton PL, Allison WT. Protein Misfolding in Prion and Prion-Like Diseases: Reconsidering a Required Role for Protein Loss-of-Function. J Alzheimers Dis. 2016 Jul 6;54(1):3-29.

Legname G, Baskakov IV, Nguyen HO, Riesner D, Cohen FE, DeArmond SJ, Prusiner SB. Synthetic mammalian prions. Science. 2004 Jul 30;305(5684):673-6.

Legname G. Prions and Neurodegenerative Diseases. 1st edition. Progress in molecular biology and translational science. Academic Press 2020. September 19, 2020. Chapter 1.

Li Q, Wang F, Xiao X, Kim C, Bohon J, Kiselar J, et al. Structural attributes of mammalian prion infectivity: Insights from studies with synthetic prions. J Biol Chem. 2018; 293: 18494-18503.

Li Q, Jaroniec CP, Surewicz WK. Cryo-EM structure of disease-related prion fibrils provides insights into seeding barriers. bioRxiv 2021.08.10.455830.

Lu X, Wintrode PL, Surewicz WK (2007) Beta-sheet core of human prion protein amyloid fibrils as determined by hydrogen/deuterium exchange. Proc. Natl. Acad. Sci. U.S.A. 104: 1510–1515.

Makarava N, Kovacs GG, Bocharova O, Savtchenko R, Alexeeva I, Budka H, Rohwer RG, Baskakov IV. Recombinant prion protein induces a new transmissible prion disease in wild-type animals. Acta Neuropathol. 2010 Feb;119(2):177-87.

Makarava N, Kovacs GG, Savtchenko R, Alexeeva I, Budka H, Rohwer RG, Baskakov IV. Genesis of mammalian prions: from non-infectious amyloid fibrils to a transmissible prion disease. PLoS Pathog. 2011 Dec;7(12):e1002419.

Makarava N, Baskakov IV. Genesis of tramsmissible protein states via deformed templating. Prion. 2012 Jul 1;6(3):252-5.

Makarava N, Kovacs GG, Savtchenko R, Alexeeva I, Ostapchenko VG, Budka H, Rohwer RG, Baskakov IV. A new mechanism for transmissible prion diseases. J Neurosci. 2012 May 23;32(21):7345-55.

Makarava N, Savtchenko R, Baskakov IV. Two alternative pathways for generating transmissible prion disease de novo. Acta Neuropathol Commun. 2015 Nov 10;3:69.

Martin-Pastor M, Stoyanov E. New insights into the use of hydroxypropyl cellulose for drug solubility enhancement: An analytical study of sub-molecular interactions with fenofibrate in solid state and aqueous solutions. J Polym Sci. 2021.

Merz PA, Somerville RA, Wisniewski HM, Iqbal K. Abnormal fibrils from scrapie-infected brain. Acta Neuropathol. 1981;54(1):63-74.

Minor DL Jr1, Kim PS. 1994. Measurement of the beta-sheet-forming propensities of amino acids. Nature 367:660-3.

Müller H, Brener O, Andreoletti O, Piechatzek T, Willbold D, Legname G, Heise H. 2014. Progress towards structural understanding of infectious sheep PrP-amyloid Prion. 8:344-58.

Nazabal A, Hornemann S, Aguzzi A, Zenobi R. Hydrogen/deuterium exchange mass spectrometry identifies two highly protected regions in recombinant full-length prion protein amyloid fibrils. J Mass Spectrom. 2009 Jun;44(6):965-77.

Nemani SK, Myskiw JL, Lamoureux L, Booth SA, Sim VL. Exposure Risk of Chronic Wasting Disease in Humans. Viruses. 2020 Dec 17;12(12):1454.

Nguyen JT, Inouye H, Baldwin MA, Fletterick RJ, Cohen FE, Prusiner SB, Kirschner DA. X-ray diffraction of scrapie prion rods and PrP peptides. J Mol Biol. 1995 Sep 29;252(4):412-22.

Ostapchenko VG, Sawaya MR, Makarava N, Savtchenko R, Nilsson KP, Eisenberg D, Baskakov IV. Two amyloid States of the prion protein display significantly different folding patterns. J Mol Biol. 2010 Jul 23;400(4):908-21.

Osterholm, M.T.; Anderson, C.J.; Zabel, M.D.; Scheftel, J.M.; Moore, K.A.; Appleby, B.S. Chronic wasting disease in cervids: Implications for prion transmission to humans and other animal species. mBio 2019, 10.

Pan KM, Baldwin M, Nguyen J, Gasset M, Serban A, Groth D, Mehlhorn I, Huang Z, Fletterick RJ, Cohen FE, et al. Conversion of alpha-helices into beta-sheets features in the formation of the scrapie prion proteins. Proc Natl Acad Sci U S A. 1993 Dec 1;90(23):10962-6.

Pastrana MA, Sajnani G, Onisko B, Castilla J, Morales R, Soto C, Requena JR. Isolation and characterization of a proteinase K-sensitive PrPSc fraction. Biochemistry. 2006 Dec 26;45(51):15710-7.

Petkova, A. T.; Tycko, R. Sensitivity enhancement in structural measurements by solid state NMR through pulsed spin locking. J. Magn. Reson. 2002, 155, 293-299.

Prusiner, S.B. Novel proteinaceous infectious particles cause scrapie. Science 1982, 216, 136–144.

Prusiner SB, McKinley MP, Bowman KA, Bolton DC, Bendheim PE, Groth DF, Glenner GG. Scrapie prions aggregate to form amyloid-like birefringent rods. Cell. 1983 Dec;35(2 Pt 1):349-58.

Prusiner, S.B. Scrapie prions. Annu. Rev. Microbiol. 1989, 43, 345–374.

Prusiner SB. Molecular biology of prion diseases. Science. 1991 Jun 14;252(5012):1515-22.

Prusiner SB. Prion diseases and the BSE crisis. Science. 1997 Oct 10;278(5336):245-51.

Prusiner, S.B. Prions. Proc. Natl. Acad. Sci. USA 1998, 95, 13363–13383.

Prusiner, S.B. (Ed.) Prion Biology; Cold Spring Harbor Laboratory Press: Cold Spring Harbor, NY, USA, 2017; p. 456.

Purusottam, R. N.; Bodenhausen, G.; Tekely, P. Quantitative one- and two-dimensional 13C spectra of microcrystalline proteins with enhanced intensity. J. Biomol. NMR 2013, 57, 11-19.

Requena JR, Wille H. The structure of the infectious prion protein: experimental data and molecular models. Prion. 2014; 8(1):60–6. Epub 2014/03/04.

Riek R, Hornemann S, Wider G, Billeter M, Glockshuber R, Wüthrich K. NMR structure of the mouse prion protein domain PrP(121-231). Nature. 1996 Jul 11;382(6587):180-2.

Riek R, Hornemann S, Wider G, Glockshuber R, Wüthrich K. NMR characterization of the full-length recombinant murine prion protein, mPrP(23-231). FEBS Lett. 1997 Aug 18;413(2):282-8.

P. Rovó, "Recent advances in solid-state relaxation dispersion techniques", Solid State Nucl. Magn. Reson., 2020, 108, 101665.

Saá P, Cervenakova L. Protein misfolding cyclic amplification (PMCA): Current status and future directions. Virus Res. 2015 Sep 2;207:47-61. doi: 10.1016/j.virusres.2014.11.007. Epub 2014 Nov 13. PMID: 25445341.

Sabaté, R.; Baxa, U.; Benkemoun, L.; Sánchez de Groot, N.; Coulary-Salin, B.; Maddelein, M. L.; Malato, L.; Ventura, S.; Steven, L. C.; Saupe, S. J. Prion and non-prion amyloids of the HET-s prion forming domain. J. Mol. Biol. 2007, 370(4), 768-83.

Sabaté, R.; Castillo, V.; Espargaró, A.; Saupe, S. J.; Ventura, S. Energy barriers for HET-s prion forming domain amyloid formation. F.E.B.S. J. 2009, 276, 18, 5053-5064.

Safar J, Roller PP, Gajdusek DC, Gibbs CJ Jr. Scrapie amyloid (prion) protein has the conformational characteristics of an aggregated molten globule folding intermediate. Biochemistry. 1994; 33: 8375-83.

Safar J, Wille H, Itri V, Groth D, Serban H, Torchia M, et al. Eight prion strains have PrP(Sc) molecules with different conformations. Nat Med. 1998; 4: 1157-65.

Sajnani G, Pastrana MA, Dynin I, Onisko B, Requena JR. Scrapie prion protein structural constraints obtained by limited proteolysis and mass spectrometry. J Mol Biol. 2008 Sep 26;382(1):88-98.

Sajnani G, Silva CJ, Ramos A, Pastrana MA, Onisko BC, Erickson ML, Antaki EM, Dynin I, Vázquez-Fernández E, Sigurdson CJ, Carter JM, Requena JR. PK-sensitive PrP is infectious and shares basic structural features with PK-resistant PrP. PLoS Pathog. 2012;8(3):e1002547.

Sakudo, A. Chronic wasting disease: Current assessment of transmissibility. Curr. Issues Mol. Biol. 2019, 36, 13–22

Sawaya MR, Sambashivan S, Nelson R, Ivanova MI, Sievers SA, Apostol MI, Thompson MJ, Balbirnie M, Wiltzius JJ, McFarlane HT, Madsen AØ, Riekel C, Eisenberg D. Atomic structures of amyloid cross-beta spines reveal varied steric zippers. Nature. 2007 May 24;447(7143):453-7.

Sevillano AM, Fernandez-Borges N, Younas N, Wang F, S RE, Bravo S, et al. Recombinant PrP^{Sc} shares structural features with brain-derived PrPSc: Insights from limited proteolysis. PLoS Pathog. 2018; 14(1):e1006797

Sigurdsson B., RIDA, A Chronic Encephalitis of Sheep: With General Remarks on Infections Which Develop Slowly and Some of Their Special Characteristics, British Veterinary Journal, Volume 110, Issue 9,1954, 341-354,0007-1935,

Silva CJ, Vázquez-Fernández E, Onisko B, Requena JR. Proteinase K and the structure of PrPSc: The good, the bad and the ugly. Virus Res. 2015; 207,120-6.

Sim VL, Caughey B. Ultrastructures and strain comparison of under-glycosylated scrapie prion fibrils. Neurobiol Aging. 2009 Dec;30(12):2031-42.

Shannon MD, Theint T, Mukhopadhyay D, Surewicz K, Surewicz WK, Marion D, et al. Conformational dynamics in the core of Human Y145Stop prion protein amyloid probed by relaxation dispersion NMR. Chemphyschem. 2019; 20:311-31.

Shewmaker F, Wickner RB, Tycko R. Amyloid of the prion domain of Sup35p has an in-register parallel beta-sheet structure. Proc Natl Acad Sci U S A. 2006;103(52):19754-9.

Shewmaker F, Kryndushkin D, Chen B, Tycko R, Wickner RB. Two prion variants of Sup35p have in-register parallel beta-sheet structures, independent of hydration. Biochemistry. 2009;48(23):5074-82.

Shewmaker, F.; McGlinchey, R. P.; Thurber, K. R.; McPhie, P.; Dyda, F.; Tycko, R.; Wickner, R. B. The functional curli amyloid is not based on in-register parallel beta-sheet structure. J Biol. Chem. 2009, 284, 25065-76

Smirnovas V, Baron GS, Offerdahl DK, Raymond GJ, Caughey B, Surewicz WK. Structural organization of brain-derived mammalian prions examined by hydrogen-deuterium exchange. Nat Struct Mol Biol. 2011; 18: 504-6.

Smith JF, Knowles TP, Dobson CM, Macphee CE,Welland ME. Characterization of the nanoscale properties of individual amyloid fibrils. Proc Natl Acad Sci U S A. 2006 Oct 24;103(43):15806-11.

Soto C, Satani N. The intricate mechanisms of neurodegeneration in prion diseases. Trends Mol Med. 2011 Jan;17(1):14-24.

Spagnolli G, Rigoli M, Orioli S, Sevillano AM, Faccioli P, Wille H, et al. Full atomistic model of prion structure and conversion. PLoS Pathog. 2019; 15:(7), e1007864.

Spagnolli G, Rigoli M, Novi Inverardi G, Codeseira YB, Biasini E, Requena JR. Modeling PrP^{Sc} Generation Through Deformed Templating. Front Bioeng Biotechnol. 2020 Oct 6;8:590501

Stahl N, Baldwin MA, Teplow DB, Hood L, Gibson BW, Burlingame AL, Prusiner SB. Structural studies of the scrapie prion protein using mass spectrometry and amino acid sequencing. Biochemistry. 1993 Mar 2;32(8):1991-2002.

Sunde M, Serpell LC, Bartlam M, Fraser PE, Pepys MB, Blake CC. Common core structure of amyloid fibrils by synchrotron X-ray diffraction. J Mol Biol. 1997 Oct 31;273(3):729-39.

Supattapone S, Bosque P, Muramoto T, Wille H, Aagaard C, Peretz D, Nguyen HO, Heinrich C, Torchia M, Safar J, Cohen FE, DeArmond SJ, Prusiner SB, Scott M. Prion protein of 106 residues creates an artifical transmission barrier for prion replication in transgenic mice. Cell. 1999 Mar 19;96(6):869-78.

Tattum MH, Cohen-Krausz S, Thumanu K, Wharton CW, Khalili-Shirazi A, Jackson GS, Orlova EV, Collinge J, Clarke AR, Saibil HR. Elongated oligomers assemble into mammalian PrP amyloid fibrils. J Mol Biol. 2006 Mar 31;357(3):975-85.

Telling GC, Parchi P, DeArmond SJ, Cortelli P, Montagna P, Gabizon R, Mastrianni J, Lugaresi E, Gambetti P, Prusiner SB. Evidence for the conformation of the pathologic isoform of the prion protein enciphering and propagating prion diversity. Science. 1996 Dec 20;274(5295):2079-82.

Theint T, Nadaud PS, Aucoin D, Helmus JJ, Pondaven SP, Surewicz K, et al. Species-dependent structural polymorphism of Y145Stop prion protein amyloid revealed by solid-state NMR spectroscopy. Nat Commun. 2017;8(1):753.

Torrent, J.; Martin, D.; Noinville, S.; Yin, Y.; Doumic, M.; Moudjou, M.; Béringue, V.; Rezaei, H. Pressure reveals unique conformational features in prion protein fibril diversity. Sci. Rep. 2019**,** *9*(1), 2802.

Tranulis MA, Gavier-Widén D, Våge J, Nöremark M, Korpenfelt SL, Hautaniemi M, Pirisinu L, Nonno R, Benestad SL. Chronic wasting disease in Europe: new strains on the horizon. Acta Vet Scand. 2021 Nov 25;63(1):48.

Tycko R. Symmetry-based constant-time homonuclear dipolar recoupling in solid state NMR. J Chem Phys. 2007; 126: 064506.

Tycko R, Savtchenko R, Ostapchenko VG, Makarava N, Baskakov IV. The α-helical C-terminal domain of full-length recombinant PrP converts to an in-register parallel β-sheet structure in PrP fibrils: evidence from solid state nuclear magnetic resonance. Biochemistry. 2010; 49: 9488-97.

Tycko R, Wickner RB. Molecular structures of amyloid and prion fibrils: consensus versus controversy. Acc Chem Res. 2013 Jul 16;46(7):1487-96.

Uehlinger, F.D.; Johnston, A.C.; Bollinger, T.K.; Waldner, C.L. Systematic review of management strategies to control chronic wasting disease in wild deer populations in North America. BMC Vet. Res. 2016, 12.

Vázquez-Fernández E, Alonso J, Pastrana MA, Ramos A, Stitz L, Vidal E, et al. Structural organization of mammalian prions as probed by limited proteolysis. PLoS One. 2012; 7(11):e50111.

Vázquez-Fernández E, Vos MR, Afanasyev P, Cebey L, Sevillano AM, Vidal E, Rosa I, Renault L, Ramos A, Peters PJ, Fernández JJ, van Heel M, Young HS, Requena JR, Wille H. The Structural Architecture of an Infectious Mammalian Prion Using Electron Cryomicroscopy. PLoS Pathog. 2016 Sep 8;12(9):e1005835.

Wang F, Wang X, Yuan CG, Ma J. Generating a prion with bacterially expressed recombinant prion protein. Science. 2010 Feb 26;327(5969):1132-5.

Wang, L. Q.; Zhao, K.; Yuan, H. Y.; Wang, Q.; Guan, Z.; Tao, J.; Li, X. N.; Sun, Y.; Yi, C. W.; Chen, J.; Li, D.; Zhang, D.; Yin, P.; Liu, C.; Liang, Y. Cryo-EM structure of an amyloid fibril formed by full-length human prion protein. Nat. Struct. Mol. Biol. 2020, 27 (6), 598-602.

Westfeld T, Verel R, Ernst M, Beckmann A, Meier BH. 2012. Properties of the DREAM scheme and its optimization for application to proteins. J Biomol. NMR. 53:103-112

Wasmer C, Lange A, Van Melckebeke H, Siemer AB, Riek R, Meier BH. Amyloid fibrils of the HET-s(218-289) prion form a beta solenoid with a triangular hydro-phobic core. Science. 2008; 319: 1523-6.

Welker E, Raymond LD, Scheraga HA, Caughey B. Intramolecular versus intermolecular disulfide bonds in prion proteins. J Biol Chem. 2002; 277(36):33477–81.

Wiegand T, Malär AA, Cadalbert R, Ernst M, Böckmann A, Meier BH. Asparagine and Glutamine Side-Chains and Ladders in HET-s(218-289) Amyloid Fibrils Studied by Fast Magic-Angle Spinning NMR. Front Mol Biosci. 2020 Sep 30;7:582033.

Wickner RB, Edskes HK, Son M, Bezsonov EE, DeWilde M, Ducatez M. Yeast Prions Compared to Functional Prions and Amyloids. J Mol Biol. 2018 Oct 12;430(20):3707-3719.

Wilham JM, Orrú CD, Bessen RA, Atarashi R, Sano K, Race B, Meade-White KD, Taubner LM, Timmes A, Caughey B. Rapid end-point quantitation of prion seeding activity with sensitivity comparable to bioassays. PLoS Pathog. 2010 Dec 2;6(12):e1001217.

Wille H, Zhang GF, Baldwin MA, Cohen FE, Prusiner SB. Separation of scrapie prion infectivity from PrP amyloid polymers. J Mol Biol. 1996 Jun 21;259(4):608-21.

Wille H, Michelitsch MD, Guenebaut V, Supattapone S, Serban A, Cohen FE, Agard DA, Prusiner SB. Structural studies of the scrapie prion protein by electron crystallography. Proc Natl Acad Sci U S A. 2002 Mar 19;99(6):3563-8.

Wille H, Bian W, McDonald M, Kendall A, Colby DW, Bloch L, Ollesch J, Borovinskiy AL, Cohen FE, Prusiner SB, Stubbs G. Natural and synthetic prion structure from X-ray fiber diffraction. Proc Natl Acad Sci U S A. 2009 Oct 6;106(40):16990-5.

Wille H, Requena JR. The structure of PrP^{Sc} prions. Pathogens 2018; 7: E20.

Zhang H, Neal S, Wishart DS. RefDB: A database of uniformly referenced protein chemical shifts. J Biomol NMR. 2003; 25: 173–195.

Zattoni M & Legname G.Tackling prion diseases: a review of the patent landscape, Expert Opinion on Therapeutic Patents, 2021.

Zigas V. (Ed.) Laughing Death: The Untold Story of Kuru. Humana Press; Totowa, NJ, USA, 1990.

Annex

This thesis has produced a pre-print in BioRxiv (no impact factor).

Solid state NMR reveals a parallel in register architecture for an infectious recombinant prion
Manuel Martín-Pastor, Yaiza B. Codeseira, Giovanni Spagnolli, Hasier Eraña, Leticia C. Fernández, Davy Martin, Susana Bravo, Nuria López-Lorenzo, Alba Iglesias, Rafael López-Moreno, Raimon Sabaté, Sonia Veiga, Human Rezaei, Emiliano Biasini, Víctor M. Sánchez-Pedregal, Joaquín Castilla, Jesús R. Requena
bioRxiv 2021.07.20.453078; doi: https://doi.org/10.1101/2021.07.20.453078

My contribution to this work has been preparing the samples and analyzing the spectra acquired by Martín-Pastor.

Prion diseases, i.e. Creutzfeld-Jakob disease (CJD), are rare, fatal neurodegenerative ailments. Their worldwide yearly incidence is of about one case per million people. They are caused by the autopropagative misfolding of the prion protein, PrP, namely PrPSc. This thesis proposal aims at elucidating the structure of such prion. The main technique employed is solid state nuclear magnetic resonance (ssNMR) by which we were able to analyze for the first time labelled recombinant BV PrPSc samples produced in large quantities by the protein misfolding shaking amplification (PMSA) method. The most important piece of information obtained was that recBVPrPSc presents a parallel-in-register-intermolecular-β-sheet (PIRIBS) secondary structure.